Statistical Studies of Fluid, Passive-Scalar, and Burgers Turbulence

A thesis submitted for the degree of
Doctor of Philosophy
in the Faculty of Science

Samriddhi Sankar Ray

IISc

Department of Physics
Indian Institute of Science
Bangalore - 560012
India

March 2010

Declaration

The work reported in this thesis is original and was carried out by me during my tenure as a PhD student at the Department of Physics, Indian Institute of Science, Bangalore. This thesis has not formed the basis for the award of any degree, diploma, associateship, membership or similar title of any university or institution.

(Samriddhi Sankar Ray)
March, 2010

Department of Physics,
Indian Institute of Science,
Bangalore - 560012,
India

Acknowledgements

It gives me great pleasure to place on record my love and gratitude for a number of people who have brought me joy and sorrow in unequal measure.

It will not be an exaggeration to say that possibly the only reason I am writing this Thesis, and this acknowledgement, today is because of my thesis advisor, Professor Rahul Pandit. Looking back I find it improbable that I, a nervous academic wreck, would actually have finished a PhD without his support. Rahul has been not only a mentor and an advisor, but also a friend and, often, a confidante. At the risk of stating the obvious I would like to place on record my debt to him for my training in turbulence and for allowing me to work with others independent of him. Apart from being an example of how an academic should approach his work, Rahul has shown me what it means to have infinite patience, propriety and encouragement for all. And always with a smile. These are virtues I can only admire and, hard as I try, never imbibe. I would also like to thank his wonderful family, Shobha and Mrinalika, for their affection, warmth, and for making me feel at home whenever I meet them. It has been a pleasure to know them and I am sure we will stay in touch in the years to come.

A significant portion of my PhD work was carried out in collaboration with Professor Uriel Frisch at the Observatoire in Nice. It has been fascinating to work with someone as uninhibited as Uriel. My thanks to Helene Frisch as well for being so supportive; it is always such a pleasure to talk to her. Some of my fondest memories are the long walks with Uriel along the slopes of the Observatoire or with Helene and Uriel along the coastline skirting the Mediteranean. We have had quarrels, debates, and agreements on a wide variety of subjects and I have always come back enriched and, sometimes, annoyed.

Let me now place on record my gratitude for my first teacher in turbulence – Dhrubaditya Mitra. It was at his insistence that I joined Rahul and since my early days in research Dhruba has been my constant tutor. It has been a pleasure working with him and I look back with great fondness at the times we have spent together discussing things wholly unrelated to fluid motion! Thanks a lot for everything.

My grateful thanks to my colleague Prasad Perlekar. I am quite certain that without his patient teaching of the intricacies of simulations many of the Chapters in this Thesis would never have seen the light of day.

I have been fortunate to work with some very fine collaborators over the last three years. I would like to thank my co-authors Susan Kurien, Jiang-Zhou Zhu, Achim Wirth, Walter Pauls, Claude Bardos, Edriss Titi, and Sagar Chakraborty.

I was fortunate to be a part of a wonderful group working with Rahul. My early initiations into the pitfalls of coding were by Apratim Chatterji. I would like to thank Abhik Basu for being a friend and a collaborator. In recent times it has been my privilege to work with Ganapati Sahoo, Anupam Gupta, and Debarghya Baner-

dignity and a reassuring presence which I dare say has helped each and everyone of us. I have my doubts if I would ever have come to grips with either Fortran or Matlab without Smarajit's tireless tutorials. His almost child-like enthusiasm for sports and the gym was a constant source of amusement for all of us. Sumilan and I started out as Integrated PhD batchmates. I remember being in awe of his academic prowess back then. I still am. Its only later when I started sharing the office with him that the other side of his persona emerged – humour, humility, and a respect for individuals and individuality without compromising on his own set of values. Subhro, a year junior to me, came to IISc with a formidable reputation for being one of the finest undergraduate students at Presidency College in recent memory. I am no judge, but I am sure his prowess has increased many folds in the last few years. Gentle and kind to a fault, it is his honesty, both intellectual and otherwise, which I really envy. He taught me, by example and not words, that it is possible to be a courteous and respectful mischief-maker. I will miss his infectious enthusiasm for everything he does. In short, I will miss the old gang of 117, the endless pranks, the endless arguments, the endless laughter and noise. And inspite of our devilish delights, to set the records straight, I am certain that none can say that our doors were closed to people who sought counsel or help.

Just outside this old boys club is a bunch of people whose company I will miss. To begin with it, was fantastic to have Debraj Choudhury, Chinkhanlun Guite, Vijay Kumar K., Vishal Saraogi, Sankha Subhra Sarkar, Purbasha Halder, Suresh Kumar Vasa, and Sumilan Banerjee as my batchmates in the IPhD programme of the Physics Department. I also cherish the happy times I spent with Ketki Verkhedkar, Jayashree Nagesh, Pralay Kumar Santra, Arnab China, and Kanishka Biswas. It has been a pleasure to know Debarshini Chakraborty and I cherish all the times we have spent together. She certainly played her part in getting me to read Douglas Adams! Arjun Joshua, now in Israel, is a dear friend of mine. His quiet dignity coupled with a sense of humour often hid the sensitive, caring and considerate man that he really is. Kalyan Sundar Chakrabarti is of similar stock. Even as I write this I remember all the good times we had and with Kalyan I always find myself agreeing on most occassions. Although he is in the US now we still find time to talk. It was also my great fortune to know Tirthankar Dutta; it is rare to find a nicer and more trusting person than him. Whenever I am on the roads on Campus I miss Ananda Ghosh's laughter and his simplicity. I would also like to place on record my gratefulness to Natasha Mhatre and Vivek Nityananda for their love and criticism in equal measure. I often miss them whenever I feel the need for a second, if not balanced, opinion on a range of issues. Sincere thanks to Harikrishna Reddy and B. Padmanabhan as well for bearing with me over the years. Vijay Narayan, with

Finally, its time to express my love and gratitude to people, very dear to my heart, and whom I have known for as long as I can remember. One of the joys of growing up was being close to friends of my parents. I recall with much fondness the love and friendship of Subhas*kaka* and Uttara*maashi*, Subir*kaka* and Rinku*kakima*, Lama*kaka* and Manju*maashi*, Dipanjan*kaka* and Arati*maashi*, Dipak*kaka* and Nanda*maashi*, Kumar*kaka* and Ira*kakima*, Swapan*kaka* and Bhaswati*maashi*, Amitava*kaka*, and Rajkumar*kaka*. Anil*mesho* and Manjula*maashi* are gratefully acknowledged for their warmth, affection, and, to be perfectly honest, the many fabulous lunches and dinners. And Samir*kaka* for all the love that I could possibly wish for. A special word of thanks to Suchi*di* and especially Subir*da* with his delightfully concoted anecdotes, his wit, and above all his love and care.

I thank Shameek Ray for being such a loyal friend and cousin over all these years. Having grown older, I miss the fist-fights of our younger days. I would like to thank Sagar for his encouragement and good cheer. Sunandan Chakraborty has been one of my closest friends and we share a common love for a variety of things. Time spent with him is rarely dull. He is a keen observer, possesing a rare sensitivity. Suranjan Chakraborty, although much older and wiser to me, is thanked for his bundle of good humour. I would also like to express my love and affection for Meghna and Rukmini; I have known them all my life and its always a pleasure to meet them. I wish them all the very best.

Having grown up on a diet of Wodehouse, I have always had the odd suspicion of aunts and uncles. Strangely enough it has been rather different with my set of aunts and uncles. My thanks and love to all of them, and especially to *Jethi*, *Mamima* and *Mamamoni*, *Mashimoni* and Goradash for always being there.

A special thanks to *Boudi* and Tinni for their unfailing love and trust all through these years. Lama*da* for being my mentor, friend, guardian, and a wonderful *nephew*. My thanks to Sucharita*di* for being such a patient listener and for all your love. And all my love for my two super-talented and lovely *granddaughters*, Rajashee and Sreemoyee.

Some of my happiest memories are those spent with my grandparents. I am grateful for their unconditional love and affection.

It is always difficult to express my love and gratefulness for my family. Trying to do so is at best embarrassing and at worst inadequate. I would happily settle for the latter. So a thank you to my brother Riddhi Sankar and my sister Mrinmayee for being with me always; my brother-in-law, Arnab, for your quiet understanding; Poppy for being on my mind most of the time and brightening up my day. And my parents. I could never ever wish for more than what I have got from all of you.

Contents

Preface

CHAPTER 1 We present an introductory overview of several challenging problems in the statistical characterisation of turbulence. We provide examples from fluid turbulence in three and two dimensions, from the turbulent advection of passive scalars, and turbulence in the one-dimensional Burgers equation.

CHAPTER 2 In this chapter we systematise the study of dynamic multiscaling of time-dependent structure functions in different models of passive-scalar and fluid turbulence. We show that, by suitably normalising these structure functions, we can eliminate their dependence on the origin of time at which we start our measurements and that these normalised structure functions yield the same linear bridge relations that relate the dynamic-multiscaling and equal-time exponents for statistically steady turbulence. We show analytically, for both the Kraichnan Model of passive-scalar turbulence and its shell model analogue, and numerically, for the GOY shell model of fluid turbulence and a shell model for passive-scalar turbulence, that these exponents and bridge relations are the same for statistically steady and decaying turbulence. Thus we provide strong evidence for dynamic universality, i.e., dynamic-

multiscaling exponents do not depend on whether the tur-
bulence decays or is statistically steady.

CHAPTER 3 In this Chapter we show that for two-dimensional
turbulence there exist different ways of extracting time
scales from time-dependent vorticity structure functions.
These lead to different dynamic-multiscaling exponents
which are related to equal-time multiscaling exponents by
different classes of bridge relations. We also show that the
dynamic exponents of the Eulerian and quasi-Lagrangian
fields are the same since the presence of air-drag induced
Ekman friction eliminates sweeping in two dimensions.
We check this explicitly by detailed numerical simulations
of forced two-dimensional turbulence with air-drag-induced
Ekman friction.

CHAPTER 4 In this Chapter we show that the use of a high
power α of the Laplacian in the dissipative term of hydro-
dynamical equations leads asymptotically to truncated in-
viscid *conservative* dynamics with a finite range of spatial
Fourier modes. Those at large wavenumbers thermalize,
whereas modes at small wavenumbers obey ordinary vis-
cous dynamics. The energy bottleneck observed for finite
α may be interpreted as incomplete thermalization. Arti-
facts arising from models with $\alpha > 1$ are discussed.

CHAPTER 5 In this Chapter we explore the real-space man-
ifestation of the bottleneck in the energy spectrum of the
hyperviscous Burgers equation for moderately large de-

grees of dissipativity. We show that the bottleneck in the energy spectrum is related to the oscillations which develop in the velocity field in a thin boundary layer around the shock region. By a careful DNS of the hyperviscous Burgers equation we have been able to show that a bottleneck develops at wavenumbers which correspond to the wavenumber of these oscillations. Moreover we show that these oscillations have amplitudes which decay exponentially and the characteristic length scale of the decay is related inversely to the full-width-at-half-maximum of the bottleneck bump.

CHAPTER 6 Extended Self-Similarity (ESS), a procedure that remarkably extends the range of scaling for structure functions in Navier–Stokes turbulence and thus allows improved determination of intermittency exponents, has never been fully explained. In this Chapter, we show that ESS applies to Burgers turbulence at high Reynolds numbers and we give the theoretical explanation of the numerically observed improved scaling at both the infrared and ultraviolet end, in total a gain of about three quarters of a decade: there is a reduction of subdominant contributions to scaling when going from the standard structure function representation to the ESS representation. We conjecture that a similar situation holds for three-dimensional incompressible turbulence and suggest ways of capturing subdominant contributions to scaling.

CHAPTER 7 In this chapter we consider a modification of
the three-dimensional Navier–Stokes equations and other
hydrodynamical evolution equations with space-periodic
initial conditions in which the usual Laplacian of the dis-
sipation operator is replaced by an operator whose Fourier
symbol grows exponentially as $e^{|k|/k_d}$ at high wavenumbers
$|k|$. Using estimates in suitable classes of analytic func-
tions, we show that the solutions with initially finite en-
ergy become immediately entire in the space variables and
that the Fourier coefficients decay faster than $e^{-C(k/k_d)\ln(|k|/k_d)}$
for any $C < 1/(2\ln 2)$. The same result holds for the one-
dimensional Burgers equation with exponential dissipa-
tion but can be improved: heuristic arguments and very
precise simulations, analyzed by the method of asymp-
totic interpolation of van der Hoeven, indicate that the
leading-order asymptotics is precisely of the above form
with $C = C_\star = 1/\ln 2$. The same behavior with a univer-
sal constant $C_\star$ is conjectured for the Navier–Stokes equa-
tions with exponential dissipation in any space dimension.
This universality prevents the strong growth of intermit-
tency in the far dissipation range which is obtained for
ordinary Navier–Stokes turbulence. Possible applications
to improved spectral simulations are briefly discussed.

List of Publications

1. *Dynamic Multiscaling in Turbulence*, R. Pandit, **Samriddhi Sankar Ray**, and D. Mitra, European Physics Journal B **64**, 463 (2008).

2. *The Universality of Dynamic Multiscaling in Homogeneous, Isotropic Navier-Stokes and Passive-Scalar Turbulence*, **Samriddhi Sankar Ray**, D. Mitra, and R.Pandit, New Journal of Physics, **10**, 033003 (2008).

3. *Hyperviscosity, Galerkin truncation and bottlenecks in turbulence*, U. Frisch, S. Kurien, R. Pandit, W. Pauls, **Samriddhi Sankar Ray**, A. Wirth, and J-Z Zhu, Physical Review Letters, **101**, 144501 (2008).

4. *Entire solutions of hydrodynamical equations with exponential dissipation*, C. Bardos, U. Frisch, W. Pauls, **Samriddhi Sankar Ray**, E. S. Titi, Communications in Mathematical Physics, in press (DOI 10.1007/s00220-009-0916-z) (2009).

5. *Statistical Properties of Turbulence: An Overview*, R. Pandit, P. Perlekar, **Samriddhi Sankar Ray**, Pramana – Journal of Physics, **73**, 157 (2009).

6. *Extended Self-Similarity Works and Why*, S. Chakraborty, U. Frisch, and **Samriddhi Sankar Ray**. Journal of Fluid Mechanics, *Fast Track*, in press. Available at http://arxiv.org/abs/0912.2406.

Manuscripts in Preparation

1. *Dynamic Multiscaling in Two-dimensional Turbulence*, **Samriddhi Sankar Ray**, P. Perlekar, D. Mitra, and R. Pandit.

2. *Bottlenecks in Hyperviscous Burgers Equation: Theory and Numerical Results*, **Samriddhi Sankar Ray**, U. Frisch, and R. Pandit.

3. *Persistence of Topological Structures in Two-dimensional Turbulence*, P. Perlekar, **Samriddhi Sankar Ray**, D. Mitra, and R. Pandit.

4. *Scaling and Multiscaling in Binary Fluids*, **Samriddhi Sankar Ray** and A. Basu.

5. *Route to Thermalisation in the Galerkin-truncated Burgers equation*, **Samriddhi Sankar Ray**, U. Frisch, S. Nazarenko, and T. Matsumuto.

Chapter 1

Introduction

1.1 Introduction

Physicists have often described turbulence as the last great unsolved problem of classical physics [1, 2, 3]. However, it is difficult to precisely formulate what would constitute a solution of the problem. This is mainly because turbulence is not *one problem* but a collection of *several* important problems which range from the characterisation and control of turbulent flows [4, 5], to mathematical questions which are concerned with the smoothness, or lack thereof, of solutions of the Navier-Stokes and related equations [6, 7, 8, 9, 10]. Besides turbulence also assumes central importance in fluid dynamics [5, 11, 12, 13], astrophysics [14, 15, 16, 17], geophysics [18, 19], climate science [20], plasma physics [15, 16, 17, 21, 22], and statistical physics [23, 24, 25, 26, 27, 28, 29, 30, 31, 32]. In this introductory chapter, we concentrate on the statistical characterisation of fluid turbulence [33] in three dimensions, the turbulence of passive scalars such as pollutants [34], two-dimensional turbulence in thin films or soap films [35, 36], and turbulence in the Burgers equation [37, 38, 39]. Our choice of topics is dictated by the contents of subsequent chapters and the discussion shall closely follow Ref. [40]. Keeping in mind the central problems studied in this Thesis, we will restrict ourselves mostly to

homogeneous, isotropic turbulence [33, 41, 42] and, where possible, we will highlight some similarities between the statistical properties of systems at a critical point and those of turbulent fluids [31, 43, 44].

This Chapter is organised as follows: Section 1.2 gives an overview of some of the experiments of relevance to statistical characterization of turbulence. In Section 1.3 we introduce some of the equations that we shall study in detail later in this Thesis. Section 1.4 provides a summary of phenomenological approaches, due to Richardson [45] and Kolmogorov (K41) [46], that have been developed to understand the behaviour of velocity and other structure functions in *inertial ranges*. In Section 1.5 we introduce the ideas of multiscaling that provides an understanding of the deviations from the predictions of K41-type phenomenology. In Section 1.6 we give a background to the kind of numerical simulations that will be explored in greater details in later chapters. Thus we devote this Section to (a) three-dimensional fluid turbulence, (b) shell models, (c) two-dimensional turbulence in soap films, and (d) turbulence in the one-dimensional Burgers equation.

1.2 Experimental Overview

Turbulent flows are commonplace in nature. They include the flow of water in rivers and pipes, the flow of air over moving cars or aeroplanes, jets that are formed when a fluid is forced through an orifice, the turbulent advection of pollutants and pollen grains, terrestrial and Jovian storms, turbulent convection in the sun, and turbulent shear flows in the arms of spiral galaxies. A wide variety of experimental studies have been carried out to understand the properties of such turbulent flows; we concentrate on those that are designed to elucidate the statistical properties of turbulence, especially turbulence that is, at small spatial scales and far away from boundaries,

homogeneous and isotropic. Most of our discussion will be devoted to incompressible flows, i.e., low-Mach-number cases in which the fluid velocity is much less than the velocity of sound in the fluid.

In laboratories such turbulence is generated in many different ways. A common method uses a grid in a wind tunnel [47]; the flow downstream from this grid is homogeneous and isotropic, to a good approximation. Another technique use the von Kármán swirling flow, i.e., flow generated in a fluid contained in a cylindrical tank with two coaxial, counterrotating discs at its ends [48, 49, 50]; in the middle of the tank, far away from the discs, the turbulent flow is approximately homogeneous and isotropic. Electromagnetically forced thin films and soap films [1, 35, 36] have yielded very useful results for two-dimensional turbulence. Turbulence data can also be obtained from atmospheric boundary layers [51, 52, 53, 54], oceanic flows [55], and astrophysical measurements [14]; experimental conditions cannot be controlled as carefully in such natural settings as they can be in a laboratory, but a far greater range of length scales can be probed than is possible in laboratory experiments.

Traditionally, experiments have measured the velocity $\mathbf{u}(\mathbf{x}, t)$ at a single point $\mathbf{x}$ at various times t by using hot-wire anemometers; these anemometers can have limitations in (a) the number of components of the velocity that can be measured and (b) the spatial and temporal resolutions that can be obtained [56, 57]. Such measurements yield a time series for the velocity; if the mean flow velocity $U >> u_{rms}$, the root-mean-square fluctuations of the velocity, then Taylor's frozen-flow hypothesis [5, 33] can be used to relate temporal separations δt to spatial separations δr, along the mean flow direction via $\delta r = U\delta t$. The Reynolds number $Re = UL/\nu$, where U and L are typical velocity and length scales in the flow and ν is the kinematic viscosity, is a convenient dimensionless control parameter; at low Re flows are laminar; as it increases there is a transition to turbulence often via a variety

of instabilities that we will not cover here; and at large Re fully developed turbulence sets in. To compare different flows it is often useful to employ the Taylor-microscale Reynolds number $Re_\lambda = u_{rms}\lambda/\nu$, where the Taylor microscale λ can be obtained from the energy spectrum as described later in Sec. 1.6.

Refinements in hot-wire anemometry [53, 58] and flow visualisation techniques such as laser-doppler velocimetry (LDV) [56], particle-image velocimetry (PIV) [56, 57], particle-tracking velocimetry (PTV) [56, 57], tomographic PIV [59], holographic PIV [60], and digital holographic microscopy [61] have made it possible to obtain reliable measurements of the Eulerian velocity $\mathbf{u}(\mathbf{x}, t)$ (see Sec. 1.3) in a turbulent flow. In the simplest forms of anemometry a time series of the velocity is obtained at a given point in space; in PIV two components of the velocity field can be obtained in a sheet at a given time; holographic PIV can yield all components of the velocity field in a volume. Components of the velocity derivative tensor $A_{ij} \equiv \partial_j u_i$ can also be obtained [53] and thence quantities such as the energy dissipation rate per unit mass per unit volume $\epsilon \equiv -\nu \sum_{i,j}(\partial_i u_j + \partial_j u_i)^2$, the vorticity $\omega = \nabla \times \mathbf{u}$, and components of the rate of strain tensor $s_{ij} \equiv (\partial_i u_j + \partial_j u_i)/2$, where the subscripts i and j are Cartesian indices. A discussion of the subtleties and limitations of these measurement techniques lies beyond the scope of this Chapter; we refer the reader to Refs. [53, 56, 57] for details. Significant progress has also been made over the past decade in the measurement of Lagrangian trajectories (see Sec. 1.3) of tracer particles in turbulent flows [48, 49]. Given such measurements, experimentalists can obtain several properties of turbulent flows. We give illustrative examples of the types of properties we consider.

Flow-visualisation methods often display large-scale coherent structures in turbulent flows. Examples of such structures are plumes in Rayleigh-Bérnard convection [62], structures behind a splitter plate [63], and large vortical structures in two-dimensional or stratified flows [1,

35, 36]. In three-dimensional flows, as we will see in greater detail later, energy that is pumped into the flow at the injection scale L cascades, as first suggested by Richardson [45], from large-scale eddies to small-scale ones till it is eventually dissipated around and beyond the dissipation scale η_d. By contrast, two-dimensional turbulence [35, 36, 64, 65] displays a dual cascade: there is an inverse cascade of energy from the scale at which it is pumped into the system to large length scales and a direct cascade of enstrophy $\Omega = \langle \frac{1}{2}\omega^2 \rangle$ to small length scales. The inverse cascade of energy is associated with the formation of a few large vortices; in practical realisations the sizes of such vortices are controlled finally by Ekman friction that is induced, e.g., by air drag in soap-film turbulence.

Measurements of the vorticity ω in highly turbulent flows show that regions of large ω are organised into slender tubes. The first experimental evidence for this was obtained by seeding the flow with bubbles that moved preferentially to regions of low pressure [66] that are associated with large-ω regimes. For recent experiments on vortex tubes we refer the reader to Ref. [67].

The time series of the fluid velocity at a given point $\mathbf{x}$ shows strong fluctuations. It is natural, therefore, to inquire into the statistical properties of turbulent flows. From the Eulerian velocity $\mathbf{u}(\mathbf{x}, t)$ and its derivatives we can obtain one-point statistics, such as probability distribution functions (PDFs) of the velocity and its derivatives. Velocity PDFs are found to be close to Gaussian distributions. However, PDFs of ω^2 and velocity derivatives show significant non-Gaussian tails; for a recent study, which contains references to earlier work, see Ref. [53]. The PDF of ϵ is non-Gaussian too and the time series of ϵ is highly intermittent [68]; furthermore, in the limit $Re \to \infty$, i.e., $\nu \to 0$, the energy dissipation rate per unit volume ϵ approaches a positive constant value (see, e.g., Fig. 2 of Ref. [69]), a result referred to as a *dissipative anomaly* or the *zeroth law of turbulence*.

Two-point statistics are characterised conventionally by studying the equal-time, order-p, longitudinal velocity structure function

$$S_p(\mathbf{r}) = \langle [(u(\mathbf{x} + \mathbf{r}) - u(\mathbf{x})) \cdot (\mathbf{r}/r)]^p \rangle, \tag{1.1}$$

where the angular brackets indicate a time average over the nonequilibrium statistical steady state that we obtain in forced turbulence. Experiments [33, 70] show that, for separations r in the *inertial range* $\eta_d \ll r \ll L$,

$$S_p(\mathbf{r}) \sim r^{\zeta_p}, \tag{1.2}$$

with exponents ζ_p that deviate significantly from the simple scaling prediction [46] $\zeta_p^{K41} = p/3$, especially for $p > 3$, where $\zeta_p < \zeta_p^{K41}$. This prediction, made by Kolmogorov in 1941 (hence the abbreviation K41), is discussed in Sec. 1.4; the deviations from this simple scaling prediction are referred to as multiscaling (Sec. 1.5) and they are associated with the intermittency of ϵ mentioned above. We mention, in passing, that the log-Poisson model due to She and Leveque provides a good parametrisation of the plot of ζ_p versus p [71].

The second-order structure function $S_2(\mathbf{r})$ can be related easily by Fourier transformation to the energy spectrum $E(k) = 4\pi k^2 \langle |\tilde{\mathbf{u}}(k)|^2 \rangle$, where the tilde denotes the Fourier transform, $k = |\mathbf{k}|$, $\mathbf{k}$ is the wave vector, we assume that the turbulence is homogeneous and isotropic, and, for specificity, we give the formula for the three-dimensional case. Since $\zeta_2^{K41} = 2/3$, the K41 prediction is

$$E^{K41}(k) \sim k^{-5/3}, \tag{1.3}$$

a result that is in good agreement with a wide range of experiments [see, e.g., Refs. [33, 72]].

The structure functions $S_p(r)$ are the moments of the PDFs of the longitudinal velocity increments $\delta u_{\parallel} \equiv [(u(\mathbf{x} + \mathbf{r}) - u(\mathbf{x})) \cdot (\mathbf{r}/r)]$. [In the argument of S_p we use r instead of $\mathbf{r}$ when we consider homogeneous, isotropic turbulence.] These PDFs have been measured directly [73]

and they show non-Gaussian tails; as r decreases, the deviations of these PDFs from Gaussian distributions increases.

Recently, there have been experiments on Lagrangian measurements [48, 49] that have been designed to track tracer particles in, e.g., the von Kármán flow at large Reynolds numbers. By employing state-of-the-art measurement techniques, such as silicon strip detectors [49], used in high-energy-physics experiments, or acoustic-doppler methods [48], these experiments have been able to attain high spatial resolution and high sampling rates and have, therefore, been able to obtain good data for acceleration statistics of Lagrangian particles and the analogues of velocity structure functions for them.

Order-p Lagrangian velocity structure functions are defined along a Lagrangian trajectory as

$$S_{i,p}^L(\tau) = \langle [v_i^L(t + \tau) - v_i^L(t)]^p \rangle, \qquad (1.4)$$

where the superscript L denotes Lagrangian and the subscript i the Cartesian component. If the time lag τ lies in the temporal analogue of the inertial range, i.e., $\tau_\eta \ll \tau \ll T_L$, where τ_η is the viscous dissipation time scale and T_L is the time associated with the scale L at which energy is injected into the system, then it is expected that

$$S_{i,p}^L(\tau) \sim \tau^{\zeta_{i,p}^L}. \qquad (1.5)$$

The analogue of the dimensional K41 prediction is $\zeta_{i,p}^{L,K41} = p/2$; experiments and simulations [50] indicate that there are corrections to this simple dimensional prediction.

The best laboratory realisations of two-dimensional turbulence are (a) a thin layer of a conducting fluid excited by magnetic fields, varying both in space and time and applied perpendicular to the layer [74], and (b) soap films [75] in which turbulence can be generated either by electromagnetic forcing or by the introduction of a comb, which plays the role of a grid, in a rapidly flowing soap film. In the range of

parameters used in typical experimental studies [1, 35, 36, 76] both
these systems can be described quite well [77, 78] by the 2D Navier
Stokes equation (see Sec. 3) with an additional Ekman-friction term,
induced typically by air drag; however, in some cases we must also
account for corrections arising from fluctuations of the film thickness,
compressibility effects, and the Marangoni effect. Measurement tech-
niques are similar to those employed to study three-dimensional tur-
bulence [1, 35, 36]. Two-dimensional analogues of the PDFs described
above for 3D turbulence have been measured [see, e.g., Refs. [76]];
we will touch on these briefly when we discuss numerical simulations
of 2D turbulence in Sec. 1.6. Velocity and vorticity structure func-
tions can be measured as in 3D turbulence; however, inertial ranges
associated with inverse and forward cascades must be distinguished;
the former shows simple scaling with an energy spectrum $E(k) \sim k^{-5/3}$
whereas the latter has an energy spectrum $E(k) \sim k^{-(3+\delta)}$, with $\delta = 0$ if
there is no Ekman friction and $\delta > 0$ otherwise. In the forward cas-
cade velocity structure functions show simple scaling [76]; we are not
aware of experimental measurements of vorticity structure functions
(we will discuss these in the context of numerical simulations in Sec.
1.6).

1.3 Models

Before we discuss the statistical characterization of turbulence, we
provide a brief description to the models we consider. We start with
the basic equations of hydrodynamics, in three and two dimensions,
that are central to this Thesis. We also introduce the Burgers equa-
tion in one dimension and the advection-diffusion equation for passive
scalars. We end this Section with a description of shell models that
are often used as highly simplified models for homogeneous, isotropic
turbulence.

At low Mach numbers, fluid flows are governed by the Navier-Stokes (NS) Eq. (1.6) augmented by the incompressibility condition

$$\partial_t \mathbf{u} + (\mathbf{u}.\nabla)\mathbf{u} = -\nabla p + \nu\nabla^2\mathbf{u} + \mathbf{f},$$
$$\nabla \cdot \mathbf{u} = 0, \tag{1.6}$$

where we use units in which the density $\rho = 1$, the Eulerian velocity at point $\mathbf{r}$ and time t is $\mathbf{u}(\mathbf{r}, t)$, the external body force per unit volume is $\mathbf{f}$, and ν is the kinematic viscosity. The pressure p can be eliminated by using the incompressibility condition [5, 33, 41] and it can then be obtained from the Poisson equation $\nabla^2 p = -\partial_{ij}(u_i u_j)$. In the unforced, inviscid case, the momentum, the kinetic energy, and the helicity $H \equiv \int d\mathbf{r}\,\omega \cdot \mathbf{u}/2$ are conserved; here $\omega \equiv \nabla \times \mathbf{u}$ is the vorticity. The Reynolds number $Re \equiv LV/\nu$, where L and V are characteristic length and velocity scales, is a convenient dimensionless control parameter: The flow is laminar at low Re and irregular, and eventually turbulent, as Re is increased.

In the vorticity formulation the Navier-Stokes equation (1.6) becomes

$$\partial_t \omega = \nabla \times \mathbf{u} \times \omega + \nu\nabla^2\omega + \nabla \times \mathbf{f}; \tag{1.7}$$

the pressure is eliminated naturally here. This formulation is particularly useful is two dimensions since ω is a pseudo-scalar in this case. Specifically, in two dimensions, the NS equation can be written in terms of ω and the stream function ψ:

$$\partial_t \omega - J(\psi, \omega) = \nu\nabla^2\omega + \alpha_E\omega + f;$$
$$\nabla^2\psi = \omega;$$
$$J(\psi, \omega) \equiv (\partial_x\psi)(\partial_y\omega) - (\partial_x\omega)(\partial_y\psi). \tag{1.8}$$

Here α_E is the coefficient of the air-drag-induced Ekman-friction term. The incompressibility constraint

$$\partial_x u_x + \partial_y u_y = 0 \tag{1.9}$$

ensures that the velocity is uniquely determined by ψ via

$$\mathbf{u} \equiv (-\partial_y\psi, \partial_x\psi). \tag{1.10}$$

In the inviscid, unforced case we have more conserved quantities in two dimensions than in three; the additional conserved quantities are $\langle \frac{1}{2}\omega^n \rangle$, for all powers n, the first of which is the mean enstrophy, $\Omega = \langle \frac{1}{2}\omega^2 \rangle$.

In one dimension (1D) the incompressibility constraint leads to trivial velocity fields. It is fruitful, however, to consider the Burgers equation [37], which is the NS equation without pressure and the incompressibility constraint. This has been studied in great detail as it often provides interesting insights into fluid turbulence. In 1D the Burgers equation is

$$\partial_t u + u\partial_x u = \nu\nabla^2 u + f, \tag{1.11}$$

where f is the external force and the velocity u can have shocks since the system is compressible. In the unforced, inviscid case the Burgers equation has infinitely many conserved quantities, namely, $\int u^n dx$ for all integers n. In the limit $\nu \to 0$ we can use the Cole-Hopf transformation, $u = \partial_x\Psi$, $f \equiv -\partial_x F$, and $\Psi \equiv 2\nu \ln \Theta$, to obtain

$$\partial_t\Theta = \nu\partial_x^2\Theta + F\Theta/(2\nu), \tag{1.12}$$

a linear partial differential equation (PDE) that can be solved explicitly in the absence of any boundary [38, 39].

Passive scalars such as pollutants can be advected by fluids. These flows are governed by the advection-diffusion equation

$$\partial_t\theta + \mathbf{u}.\nabla\theta = \kappa\nabla^2\theta + \mathbf{f}_\theta, \tag{1.13}$$

where θ is the passive-scalar field, the advecting velocity field $\mathbf{u}$ satisfies the NS equation (6.1), and $\mathbf{f}_\theta$ is an external force. The field θ is *passive* because it does not act on or modify $\mathbf{u}$. Note that Eq.(1.13) is linear in θ. It is possible, therefore, to make considerable analytical

progress in understanding the statistical properties of passive-scalar turbulence for the simplified model of passive-scalar advection due to Kraichnan [34, 86]; in this model each component of $\mathbf{f}_\theta$ is a zero-mean Gaussian random variable that is white in time; furthermore, each component of $\mathbf{u}$ is taken to be a zero-mean Gaussian random variable that is white in time and which has the covariance

$$\left\langle u_i(\mathbf{x}, t) u_j(\mathbf{x} + \mathbf{r}, t')\right\rangle = 2D_{ij}\delta(t - t'); \tag{1.14}$$

the Fourier transform of D_{ij} has the form

$$\tilde{D}_{ij}(\mathbf{q}) \propto (q^2 + \frac{1}{L^2})^{-(d+\xi)/2} e^{-\eta q^2} [\delta_{ij} - \frac{q_i q_j}{q^2}]; \tag{1.15}$$

$\mathbf{q}$ is the wave vector, L is the characteristic large length scale, η is the dissipation scale, and ξ is a parameter. In the limit of $L \to \infty$ and $\eta \to 0$ we have, in real space,

$$D_{ij}(\mathbf{r}) = D^0 \delta_{ij} - \frac{1}{2} d_{ij}(\mathbf{r}) \tag{1.16}$$

with

$$d_{ij} = D_1 r^\xi [(d - 1 + \xi)\delta_{ij} - \xi \frac{r_i r_j}{r^2}]. \tag{1.17}$$

D_1 is a normalization constant and ξ a parameter; for $0 < \xi < 2$ equal-time passive-scalar structure functions show multiscaling [34].

The hydrodynamical partial differential equations (PDEs) discussed above are difficult to solve, even on computers via direct numerical simulation (DNS), if we want to resolve the large ranges of spatial and temporal scales that become relevant in turbulent flows. It is useful, therefore, to consider simplified models of turbulence that are numerically more tractable than these PDEs. *Shell models* are important examples of such simplified models; they have proved to be useful testing grounds for the multiscaling properties of structure functions in turbulence. We will consider, as illustrative examples,

the Gledzer-Ohkitani-Yamada (GOY) shell model [88] for fluid turbulence in three dimensions and a shell model for the advection-diffusion equation [89].

Shell models cannot be derived from the NS equation in any systematic way. They are formulated in a discretised Fourier space with logarithmically spaced wave vectors $k_n = k_0 \tilde{\lambda}^n, \tilde{\lambda} > 1$, associated with shells n and dynamical variables that are the complex, scalar velocities u_n. Note that k_n is chosen to be a scalar: spherical symmetry is implicit in GOY-type shell models since their aim is to study homogeneous, isotropic turbulence. Given that k_n and u_n are scalars, shell models cannot describe vortical structures or enforce the incompressibility constraint.

The temporal evolution of such a shell model is governed by a set of ordinary differential equations that have the following features in common with the Fourier-space version of the NS equation [12]: they have a viscous-dissipation term of the form $-\nu k_n^2 u_n$, they conserve the shell-model analogues of the energy and the helicity in the absence of viscosity and forcing, and they have nonlinear terms of the form $\imath k_n u_n u_{n'}$ that couple velocities in different shells. In the NS equation all Fourier modes of the velocity affect each other directly but in most shell models nonlinear terms limit direct interactions to shell velocities in nearest- and next-nearest-neighbour shells; thus direct *sweeping effects*, i.e., the advection of the largest eddies by the the smallest eddies, are present in the NS equation but not in most shell models. This is why the latter are occasionally viewed as a highly simplified, quasi-Lagrangian representation (see later) of the NS equation.

The GOY-model evolution equations have the form

$$[\frac{d}{dt} + \nu k_n^2]u_n = i(a_n u_{n+1} u_{n+2} b_n u_{n-1} u_{n+1} + c_n u_{n-1} u_{n-2})^* + f_n, \qquad (1.18)$$

where complex conjugation is denoted by $*$, the coefficients are chosen to be $a_n = k_n$, $b_n = -\delta k_{n-1}$, $c_n = -(1-\delta)k_{n-2}$ to conserve the shell-model

analogues of the energy and the helicity in the inviscid, unforced case; in any practical calculation $1 \leq n \leq N$, where N is the total number of shells and we use the boundary conditions $u_n = 0 \ \forall n < 1$ or $\forall n > N$; as mentioned above $k_n = \tilde{\lambda}^n k_0$ and many groups use $\tilde{\lambda} = 2$, $\delta = 1/2$, $k_0 = 1/16$, and $N = 22$. The logarithmic discretisation here allows us to reach very high Reynolds number, in numerical simulations of this model, even with such a moderate value of N. For studies of decaying turbulence we set $f_n = 0, \forall n$; in the case of statistically steady, forced turbulence [43] it is convenient to use $f_n = (1+\iota)5 \times 10^{-3}$. For such a shell model the analogue of a velocity structure function is $S_p(k_n) = \langle |u(k_n)|^p \rangle$ and the energy spectrum is $E(k_n) = |u(k_n)|^2 / k_n$.

It is possible to construct other shell models, by using arguments similar to the ones we have just discussed, for other PDEs such as the advection-diffusion equation. Its shell-model version is

$$[\frac{d}{dt} + \kappa k_n^2]\theta = i[k_n(\theta_{n+1}u_{n-1} - \theta_{n-1}u_{n+1}) -$$
$$\frac{k_{n-1}}{2}(\theta_{n-1}u_{n-2} + \theta_{n-2}u_{n-1}) -$$
$$\frac{k_{n-1}}{2}(\theta_{n+2}u_{n+1} + \theta_{n+1}u_{n+2})]^* \qquad (1.19)$$

For this model, the advecting velocity field can either be obtained from the numerical solution of a fluid shell model, like the GOY model above, or by using a shell-model version of the type of stochastic velocity field introduced in the Kraichnan model for passive-scalar advection [44].

1.3.1 Eulerian, Lagrangian, Quasi-Lagrangian frameworks

The Navier-Stokes Eq.(1.6) is written in terms of the Eulerian velocity **u** at position **x** and time t; i.e., in the Eulerian case we use a frame of reference that is fixed with respect to the fluid; this frame can be used for any flow property or field. The Lagrangian framework [5] uses

a complementary point of view in which we fix a frame of reference to a fluid *particle*; this fictitious particle moves with the flow and its path is known as a Lagrangian trajectory. Each Lagrangian particle is characterised by its position vector $\mathbf{r_0}$ at time t_0; its trajectory at some later time t is $\mathbf{R} = \mathbf{R}(t; \mathbf{r_0}, t_0)$ and the associated Lagrangian velocity is

$$\mathbf{v} = \left(\frac{d\mathbf{R}}{dt}\right)_{\mathbf{r_0}}. \tag{1.20}$$

We will also employ the quasi-Lagrangian [91, 92] framework that uses the following transformation for an Eulerian field $\psi(\mathbf{r}, t)$:

$$\hat{\psi}(\mathbf{r}, t) \equiv \psi[\mathbf{r} + \mathbf{R}(t; \mathbf{r_0}, 0), t]; \tag{1.21}$$

here $\hat{\psi}$ is the quasi-Lagrangian field and $\mathbf{R}(t; \mathbf{r_0}, 0)$ is the position at time t of a Lagrangian particle that was at point $\mathbf{r_0}$ at time $t = 0$.

As we have mentioned above, sweeping effects are present when we use Eulerian velocities. However, since Lagrangian particles move with the flow, such effects are not present in Lagrangian and quasi-Lagrangian frameworks. In experiments neutrally buoyant tracer particles are used to obtain Lagrangian trajectories that can be used to obtain statistical properties of Lagrangian particles.

1.4 Homogeneous Isotropic Turbulence: Phenomenology

In 1941 Kolmogorov [46] developed his classic phenomenological approach to turbulence that is often referred to as K41. He used the idea of the Richardson cascade to provide an intuitive, though not rigorous, understanding of the power-law behaviours we have mentioned in Sec. 1.2. We give a brief introduction to K41 phenomenology and related ideas; for a detailed discussion the reader should consult Ref. [33].

First we must recognise that there are two important length scales: (a) The large *integral length scale L* that is comparable to the system

size and at which energy injection takes place; flow at this scale depends on the details of the system and the way in which energy is injected into it; (b) and the small *dissipation length scale* η_d below which energy dissipation becomes significant. The inertial range of scales, in which structure functions and energy spectra assume the power-law behaviours mentioned above (Sec. 1.2), lie in between L and η; as Re increases so does the extent of the inertial range.

In K41 Kolmogorov made the following assumptions: (a) Fully developed 3D turbulence is homogeneous and isotropic at small length scales and far away from boundaries. (b) In the statistical steady state, the energy dissipation rate per unit volume ϵ remains finite and positive even when $Re \to \infty$ (the dissipative anomaly mentioned above). (c) A Richardson-type cascade is set up in which energy is transferred by the breakdown of the largest eddies, created by inherent instabilities of the flow, to smaller ones, which decay in turn into even smaller eddies, and so on till the sizes of the eddies become comparable to η_d where their energy can then be degraded by viscous dissipation. As $Re \to \infty$ all inertial-range statistical properties are uniquely and universally determined by the scale r and ϵ and are independent of L, ν and η_d.

Dimensional analysis then yields the scaling form of the order-p structure function

$$S_p^{K41}(r) \approx C\epsilon^{p/3}r^{p/3}, \tag{1.22}$$

since ϵ has dimensions of $(length)^2(time)^{-3}$. [It is implicit here that the eddies, at any given level of the Richardson cascade, are space filling; if not, ϵ is intermittent and scale dependent as we discuss in Sec. 1.5 on multiscaling.] Thus $\zeta_p^{K41} = p/3$; for $p = 2$ we get $S_2^{K41}(r) \sim r^{2/3}$ whose Fourier transform is related to the K41 energy spectrum $E^{K41}(k) \sim k^{-5/3}$ [Fig. (1.1)].

The prediction $\zeta_3^{K41} = 1$, unlike all others K41 results, can be derived exactly for the NS equation in the limit $Re \to \infty$. In particular, it can

be shown that [33, 42]

$$S_3(\ell) \approx -\frac{4}{5}\epsilon\ell, \tag{1.23}$$

an important result, since it is both exact and nontrivial.

It is often useful to discuss K41 phenomenology by introducing v_ℓ, the velocity associated with the inertial-range length scale ℓ; clearly

$$v_\ell \sim \epsilon^{1/3}\ell^{1/3}. \tag{1.24}$$

The time scale $t_\ell \sim \frac{\ell}{v_\ell}$, the typical time required for the transfer of energy from scales of order ℓ to smaller ones. This yields the rate of energy transfer

$$\Pi \sim \frac{v_\ell^2}{t_\ell} \sim \frac{v_\ell^3}{\ell}. \tag{1.25}$$

Given the assumptions of K41, there is neither direct energy injection nor molecular dissipation in the inertial range. Therefore, the energy flux Π becomes independent of ℓ and is equal to the mean energy dissipation rate ϵ, which can now be written as

$$\epsilon \sim v_\ell^3/\ell. \tag{1.26}$$

A similar prediction, for the two-point correlations of a passive-scalar advected by a turbulent fluid is due to Obukhov and Corsin; we shall not discuss it here but refer the reader to Ref. [93, 94].

As we have mentioned above, the cascade of energy in 3D turbulence is replaced in 2D turbulence by a dual cascade: an inverse cascade of energy from the injection scale to larger length scales and a forward cascade of enstrophy [35, 36, 64, 65]. In the inverse cascade the energy accumulation at large length scales is controlled eventually by Ekman friction. The analogue of K41 phenomenology for this case is based upon physical arguments due to Kraichnan, Leith and Batchelor [65]. Given that there is energy injection at some intermediate length scale, kinetic energy get redistributed from such intermediate scales to the largest length scale. The scaling result for the
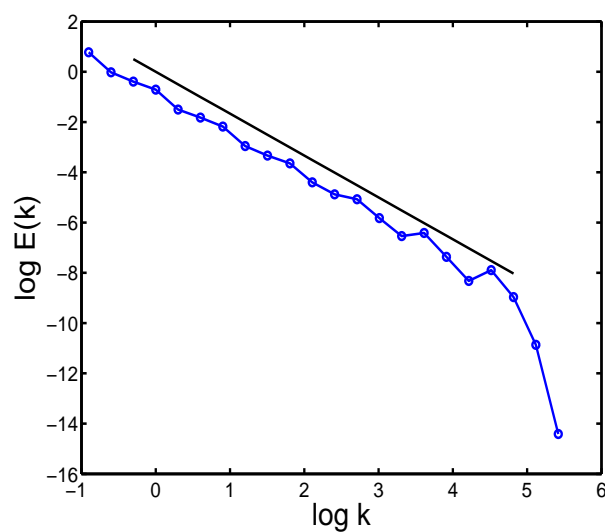
Figure 1.1: A representative log-log plot of the energy spectrum $E(k)$ versus k, from a numerical simulation of the GOY shell model with 22 shells. The straight black line is a guide to the eye indicating K41 scaling $k^{-5/3}$.
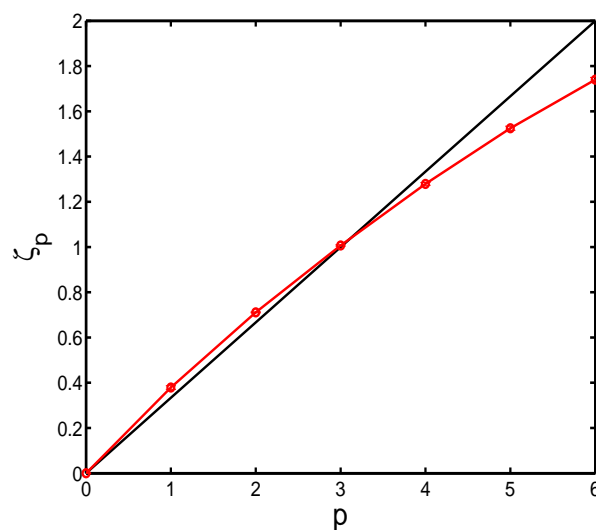
Figure 1.2: A plot of the equal-time scaling exponents ζ_p versus p, with error bars, obtained from the GOY shell model. The straight black line (color online) indicates K41 scaling $p/3$.

two cascades gives us a kinetic energy spectrum that has a $k^{-5/3}$ form in the inverse-cascade inertial range and a $k^{-3+\delta}$ form in the forward-cascade inertial range.

1.5 From scaling to multiscaling

In equilibrium statistical mechanics, equal-time and time-dependent correlation functions, in the vicinity of a critical point, display scaling properties that are well understood. For example, for a spin system in d dimensions close to its critical point, the scaling forms of the equal-time correlation function $g(r; \bar{t}, h)$ and its Fourier transform $\tilde{g}(k; \bar{t}, h)$, for a pair of spins separated by a distance r, are as follows:

$$g(r; \bar{t}, h) \approx \frac{G(r\bar{t}^{(\bar{\nu})}, h/\bar{t}^{(\bar{\Delta})})}{r^{d-2+\bar{\eta}}};\tag{1.27}$$

$$\tilde{g}(k; \bar{t}, h) \approx \frac{\tilde{G}(k/\bar{t}^{(\bar{\nu})}, h/\bar{t}^{(\bar{\Delta})})}{k^{2-\bar{\eta}}}.\tag{1.28}$$

Here the reduced temperature $\bar{t} = (T - T_c)/T_c$, where T and T_c are, respectively, the temperature and the critical temperature, and the reduced field $h = H/k_B T_c$, with H the external field and k_B the Boltzmann constant. The equal-time critical exponents $\bar{\eta}$, $\bar{\nu}$ and $\bar{\Delta}$ are universal for a given universality class (the unconventional overbars are used to distinguish these exponents from the kinematic viscosity, etc.). The scaling functions G and $\tilde{G}$ can be made universal too if two scale factors are taken into account [95]. Precisely at the critical point ($\bar{t} = 0, h = 0$) these scaling forms lead to power-law decays of correlation functions; and, as the critical point is approached, the correlation length ξ diverges [e.g., as $\xi \sim \bar{t}^{(-\bar{\nu})}$ if $h = 0$]. Time-dependent correlation functions also display scaling behaviour; e.g., the frequency (ω) dependent correlation function has the scaling form to Eq. (1.28).

$$\tilde{g}(k, \omega; \bar{t}, h) \approx \frac{\tilde{\mathcal{G}}(k^{-z}\omega, k/\bar{t}^{(\bar{\nu})}, h/\bar{t}^{(\bar{\Delta})})}{k^{2-\bar{\eta}}}.\tag{1.29}$$

This scaling behaviour is associated with the divergence of the relaxation time

$$\tau \sim \xi^z, \tag{1.30}$$

referred to as critical slowing down; here z is the dynamic scaling exponent.

In most critical phenomena in equilibrium statistical mechanics we obtain the simple scaling forms summarised in the previous paragraph. The inertial-range behaviours of structure functions in turbulence are similar to the power-law forms of these critical-point correlation functions. This similarity is especially strong at the level of K41 scaling; however, as we have mentioned earlier, experimental and numerical work suggests significant *multiscaling* corrections to K41 scaling with the equal-time multiscaling exponents $\zeta_p \neq \zeta_p^{K41}$; in brief, multiscaling implies that ζ_p is not a linear function p; indeed [33] it is a monotone increasing nonlinear function of p [Fig. (1.2)]. The multiscaling of equal-time structure functions seems to be a common property of various forms of turbulence, e.g., 3D turbulence and passive-scalar turbulence.

The multifractal model [33, 96, 97] provides a way of rationalising multiscaling corrections to K41. First we must give up the K41 assumption of only one relevant length scale ℓ and the simple scaling form of Eq.(1.21). Thus we write the equal-time structure function as

$$S_p(\ell) = C_p(\epsilon\ell)^{p/3}(\frac{\ell}{L})^{\delta_p}, \tag{1.31}$$

where $\delta_p \equiv \zeta_p - p/3$ is the anomalous part of the scaling exponent. We start with the assumption that the turbulent flow possesses a range of scaling exponents h in the set $I = (h_{min}, h_{max})$. For each h in this range, there is a set Σ_h (in real space) of fractal dimension $D(h)$, such that, as $\ell/L \to 0$,

$$\delta v_\ell(\mathbf{r}) \sim \ell^h, \tag{1.32}$$

if $\mathbf{r} \in \Sigma_h$. The exponents (h_{min}, h_{max}) are postulated to be independent of the mechanism responsible for the turbulence. Hence

$$S_p(\ell) \sim \int_I d\mu(h)(\ell/L)^{ph+3-D(h)}, \qquad (1.33)$$

where the ph term comes from p factors of (ℓ/L) and the $3 - D(h)$ term comes from an additional factor of $(\ell/L)^{3-D(h)}$, which is the probability of being within a distance of $\sim \ell$ of the set Σ_h of dimension $D(h)$ that is embedded in three dimensions. The co-dimension $D(h)$ and the exponents h_{min} and h_{max} are assumed to be universal [33]. The measure $d\mu(h)$ gives the weight of the different exponents. In the limit $\ell/L \to 0$ the method of steepest descent yields

$$\zeta_p = inf_h[ph + 3 - D(h)]. \qquad (1.34)$$

The K41 result follows if we allow for only one value of h, namely, $h = 1/3$ and set $D(h) = 3$. For more details we refer the reader to [33, 96, 97]; the extension to time-dependent structure functions is given in Refs. [43, 44, 98] and in Chapter 2.

Exact results for multiscaling can be obtained for the Kraichnan model of passive-scalar turbulence. We outline the essential steps below; details may be found in Ref. [34] and in Chapter 2.

The second-order correlation function is defined as

$$C_2(\mathbf{l}, \mathbf{t}) = \langle \theta(\mathbf{x}, \mathbf{t})\theta(\mathbf{x} + \mathbf{l}, \mathbf{t}) \rangle. \qquad (1.35)$$

Here the angular brackets denote averaging over the statistics of the velocity and the force which are assumed to be independent of one another [34]. This equation of motion

$$\partial_t C_2(\mathbf{l}, t) = \langle \partial_t \theta(\mathbf{x}, t)\theta(\mathbf{x} + \mathbf{l}, t) \rangle + \langle \theta(\mathbf{x}, t)\partial_t \theta(\mathbf{x} + \mathbf{l}, t) \rangle \qquad (1.36)$$

is easy to solve by first by using the advection-diffusion equation and then using Gaussian averages to obtain [34]

$$\partial_t C_2(l) = D_1 l^{1-d}\partial_l[(d-1)l^{d-1+\xi}C_2(l)] + 2\kappa l^{1-d}\partial_l[l^{d-1}\partial_l C_2(l)] + \Phi(\frac{l}{L_1}), \quad (1.37)$$

where $\Phi(\frac{l}{L_1})$ is the spatial correlation of the force [34] (notice that we now work with just the scalar l for the isotropic case). In the stationary state the time derivative vanishes on the left hand side. We impose the boundary conditions that, as $l \to \infty$, $C_2(l) = 0$, and $C_2(l)$ remains finite when $l \to 0$, whence

$$C_2(l) = \frac{1}{(d-1)D_1} \int_l^\infty \frac{r^{1-d}}{r^\xi + l_d^\xi} dr \int_0^r \Phi(\frac{r}{L_1})y^{d-1}dy. \qquad (1.38)$$

In the limit $l_d << l << L_1$, the second-order structure function has the following scaling form,

$$S_2(l) \equiv 2[C_2(0) - C_2(l)] \approx \frac{2}{(2-\xi)(d-1)D_1}\Phi(0)l^{2-\xi}, \qquad (1.39)$$

i.e., equal-time exponents $\zeta_2^\theta = 2 - \xi$; this result follows from dimensional arguments as well. For order-p correlation functions the equivalent of Eq. (1.37) can be written symbolically as [34]

$$\partial_t C_p = -M_p C_p + D_p C_p + F \otimes C_{p-2} \qquad (1.40)$$

where the operator M_p is determined by the advection term, D_p is the dissipative operator, and F is the spatial correlator of the force. In the limit of vanishing diffusivity, and in stationary state, the above equation reduces to

$$M_p C_p = F \otimes C_{p-2}. \qquad (1.41)$$

The associated homogeneous and inhomogeneous equations can be solved separately. By assuming scaling behaviour, we can extract the scaling exponent from simple dimensional analysis (superscript dim) to obtain

$$\zeta_p^{dim} = \frac{p}{2}(2-\xi). \qquad (1.42)$$

The solution $Z_p(\lambda\mathbf{r}_1, \lambda\mathbf{r}_2...\lambda\mathbf{r}_p)$ of the homogeneous part of Eq. (43) are called the zero-mode of the operator M_p. The zero-modes have the scaling property

$$Z_p(\lambda\mathbf{r}_1, \lambda\mathbf{r}_2...\lambda\mathbf{r}_p) \sim \lambda^{\zeta_p^{zero}} Z_p(\mathbf{r}_1, \mathbf{r}_2...\mathbf{r}_p). \qquad (1.43)$$

Their scaling exponents ζ_p^{zero} cannot be determined from dimensional arguments. The exponents ζ_p^{zero} are also called anomalous exponents. And for a particular order-p the actual scaling exponent is

$$\zeta_p = \min(\zeta_p^{zero}, \zeta_p^{dim}) \tag{1.44}$$

This is how multiscaling arises in Kraichnan model of passive-scalar advection. The principal difficulty lies in solving the problem with a particular boundary condition. In recent times the following results have been obtained: Although the scaling exponents for the zero-modes has not been obtained exactly for any p, except for $p = 2$ (in which case the anomalous exponent is actually subdominant), perturbative methods have yielded the anomalous exponents. Also, it has been shown that the multiscaling disappears for $\xi > 2$ or $\xi < 0$ and that, although the scaling exponents are universal, the amplitudes depend on the force correlator and hence the structure functions themselves are not universal. These results have been well supported by numerical simulations.

Several studies of the multiscaling of equal-time structure functions have been carried out as outlined above. By contrast there are fewer studies of the multiscaling of time-dependent structure functions. In Chapter 2 we explore this question in detail, both numerically, as well as, analytically for the Kraichnan model of passive-scalar turbulence.

1.6 Numerical Simulations

Numerical studies of the models described in Sec. 1.3 have contributed greatly to our understanding of turbulence. In this Section we introduce numerical studies of the 3D Navier-Stokes equation (Sec. 1.6.1), GOY and advection-diffusion shell models (Sec. 1.6.2) which are studied extensively in Chapter 2, the 2D Navier-Stokes equation (Sec.

1.6.3) whose dynamic scaling properties are studied in Chapter 3, and the 1D Burgers equation (Sec. 1.6.4), various facets of which are studied in Chapters 4, 5 and 6. Much of what we introduce here through illustrative examples will be discussed in detail with respect to specific problems in subsequent chapters.

1.6.1   3D Navier-Stokes Turbulence

We concentrate on the statistical properties of homogeneous, isotropic turbulence, so we restrict ourselves periodic boundary conditions. Even with these simple boundary conditions, simulating these flows is a challenging task as a wide range of length scales has to be resolved. Therefore, state-of-the-art numerical simulations use pseudo-spectral methods that solve the Navier-Stokes equations via Fast Fourier transforms [100, 101] typically on supercomputers. For a discussion on the implementation of the pseudo-spectral method we refer the reader to Refs. [100, 101].

We give illustrative results from a direct numerical simulation DNS with 1024^3 that we have carried out in our group [40]. This study uses the stochastic forcing of [103] and has attained a Taylor microscale Reynolds number $Re_\lambda \sim 100$, where $Re_\lambda = u_{rms}\lambda/\nu$; $u_{rms} = \sqrt{2E/3}$ is the root-mean-square velocity and the Taylor microscale $\lambda = \sqrt{\sum E(k)/\sum k^2 E(k)}$. For state-of-the-art simulations with up to 4096^3 collocation points we refer the reader to Ref.[69]. As we had mentioned in Sec. 1.2, regions of high vorticity are organised into slender tubes. These can be visualised by looking at isosurfaces of $|\omega|$ as shown in the representative plots of Figs. (1.3) and (1.4). The structure of high-$|\omega|$ vorticity tubes shows up especially clearly in the plots of Fig. (1.4), the second and third panels of which show successively magnified images of the central part of the first panel (for a 4096^3 version see Ref. [69]).
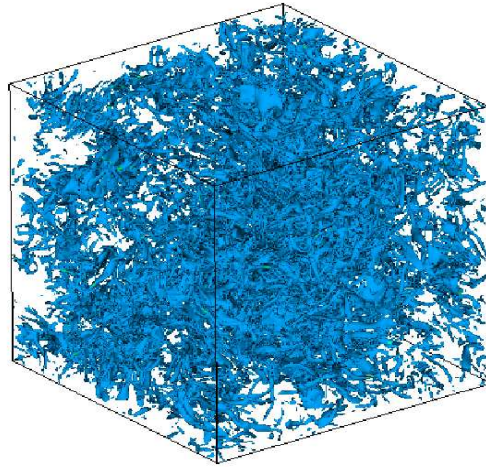
Figure 1.3: Isosurface plot of $|\omega|$ with $|\omega|$ equal to its mean value.

Figure (1.5) shows a plot of the compensated energy spectrum $k^{5/3}E(k)$ versus $k\eta$ (η is the dissipation scale in our DNS). The flat portion at low $k\eta$ indicates agreement with the K41 form $E^{K41}(k) \sim k^{-5/3}$. There is a slight bump after that; this is referred to as a bottleneck (see Ref. [105] and Sec 1.6.4, Chapters 4 and 5); the spectrum then falls in the dissipation range.

We do not provide data for the multiscaling of velocity structure functions in the 3D Navier-Stokes equation. We refer the reader to Ref. [50] for a recent discussion of such multiscaling. Often the inertial range is quite limited in such studies. This range can be extended somewhat by using the extended-self-similarity (ESS) procedure [106] in which the slope of a log-log plots of the structure function S_p versus S_q yields the exponent ratio ζ_p/ζ_q; this procedure is especially useful if $q = 3$ since $\zeta_3 = 1$ for the 3D Navier-Stokes case. In Chapter 6 we provide an explanation of ESS in the context of the Burgers equation and conjecture possible explanations of

The methods of statistical field theory have been used with some success to study the statistical properties of a randomly forced Navier-
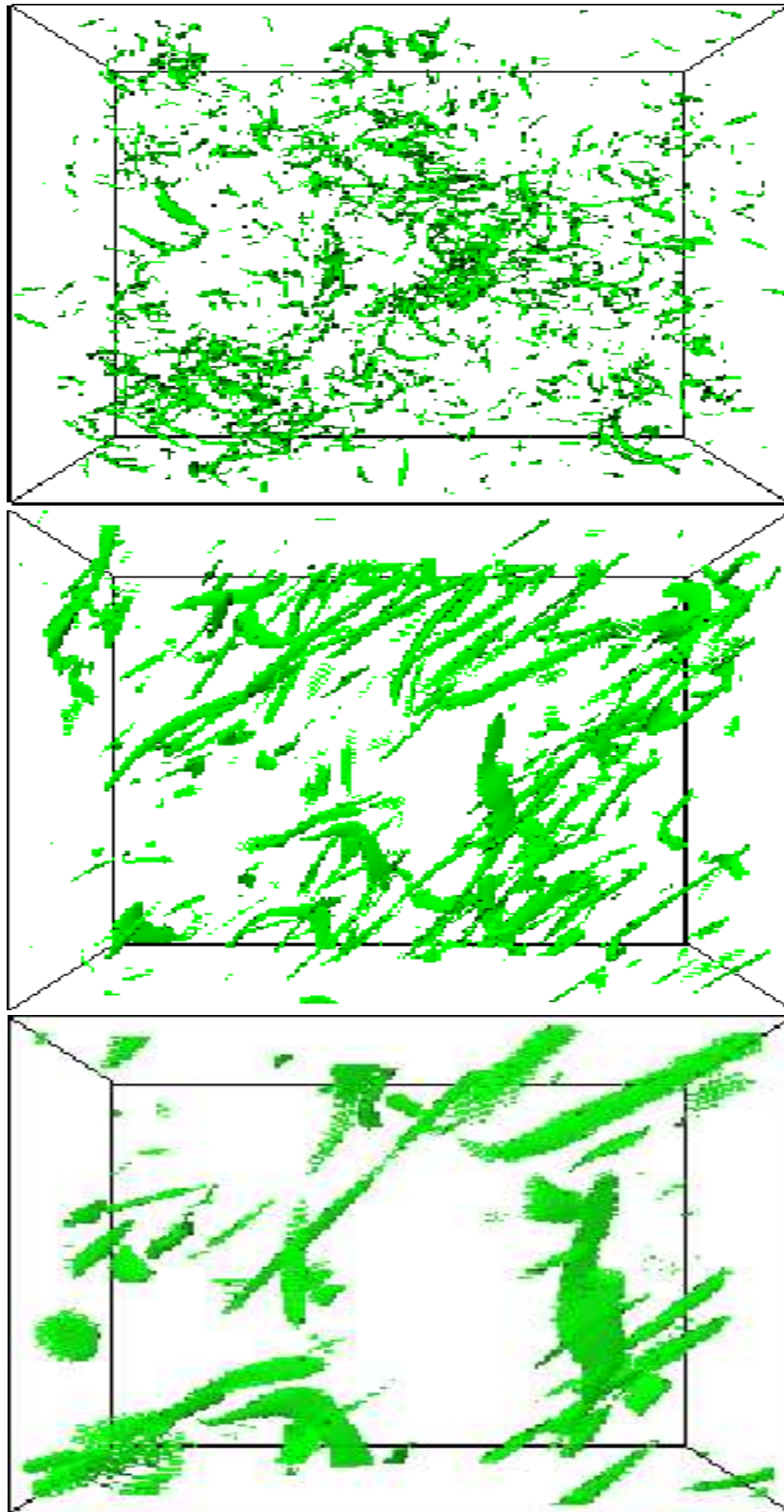
Figure 1.4: (Top) Isosurface plot of $|\omega|$ with $|\omega|$ equal to one standard deviation more than its mean value. (Center) A magnified version of the central part of the panel on the left. (Bottom) A magnified version of the central part of the panel in the middle.
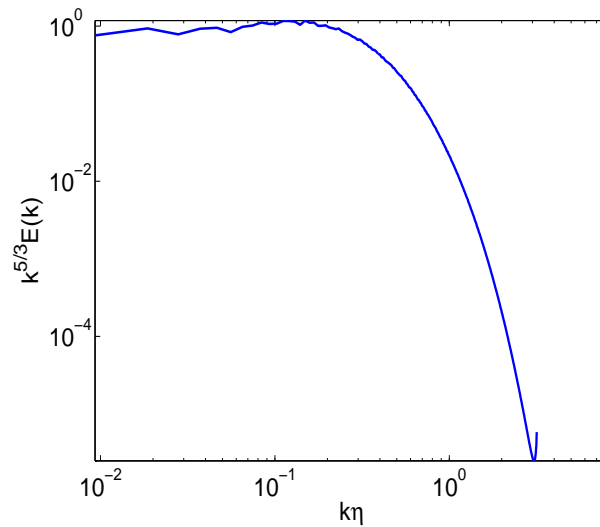
Figure 1.5: The compensated energy spectrum $k^{5/3}E(k)$ versus $k\eta$, where η is the dissipation scale from our DNS (see text).

Stokes equation [25, 26, 30, 31]. The stochastic force here acts at all length scales; it is Gaussian and has a Fourier-space covariance proportional to k^{1-y}. For $y \geq 0$, a simple perturbation theory leads to infrared divergences; these can be controlled by a dynamical renormalization group for sufficiently small y; for $y = 4$ this yields a K41-type $k^{-5/3}$ spectrum at the one-loop level. This value of y is too large to trust a low-y, one-loop result; also, for $y \geq 3$, the sweeping effect leads to another singularity [107]. Nevertheless, this randomly forced model has played an important role historically. Thus it has been studied numerically via the pseudo-spectral method [108, 109]. These studies have shown that, even though the stochastic forcing destroys the vorticity tubes that we have described above, it yields multiscaling of velocity structure that is consistent, for $y = 4$, with the analogous multiscaling in the conventional 3D Navier-Stokes equation, barring logarithmic corrections. We will discuss the analogue of this problem for the stochastically forced Burgers equation in Sec. 1.6.4.

1.6.2 Shell Models

Even though shell models are far simpler than their parent partial differential equations (PDEs), they cannot be solved analytically. The multiscaling of equal-time structure functions in such models has been investigated numerically by several groups; an overview of earlier work and details about numerical methods for the stiff shell-model equations can be found in Refs. [43, 44, 110]; chapter 2 is dedicated to our studies in dynamic multiscaling using shell models. An illustrative plot of equal-time multiscaling exponents for the GOY shell model is given in the right panel of Fig. (1.2).

We devote the rest of this Section to an introductory discussion of the dynamic multiscaling of time-dependent shell-model structure functions that has been elucidated recently [43, 44, 98, 99]. This will be covered in detail in the next Chapter. So far, detailed numerical studies of such dynamic multiscaling has been possible only in shell models. We concentrate on time-dependent velocity structure functions in the GOY model and their passive-scalar analogues in the advection-diffusion shell model.

In a typical decaying-turbulence experiment or simulation, energy is injected into the system at large length scales (small k); it then cascades to small length scales (large k); eventually viscous losses set in when the energy reaches the dissipation scale. We will refer to this as cascade completion. Energy spectra and structure functions show power-law forms like their counterparts in statistically steady turbulence. It turns out [44] that the multiscaling exponents for both equal-time and time-dependent structure functions are universal in so far as they are independent of whether they are measured in decaying turbulence or the forced case in which we get statistically steady turbulence.

Furthermore, the distinction between Eulerian and Lagrangian frameworks assumes special importance in the study of dynamic multiscal-

ing of time-dependent structure functions in three-dimensional flows. Eulerian-velocity structure functions are dominated by the sweeping effect that lies at the heart of Taylor's frozen-flow hypothesis; this relates spatial and temporal separations linearly (see Sec. 1.2) whence we obtain trivial dynamic scaling with dynamic exponents $z_p^{\mathcal{E}} = 1$ for all p, where the superscript $\mathcal{E}$ stands for Eulerian. By contrast, we expect nontrivial dynamic multiscaling in Lagrangian or quasi-Lagrangian measurements. Such measurements are daunting in both experiments and direct numerical simulations; however, they are possible in shell models. As we have mentioned in Sec. 1.3, shell models have a quasi-Lagrangian character since they do not have direct sweeping effects. Thus we expect nontrivial dynamic multiscaling of time-dependent structure functions in them.

Indeed, we find that [43, 44, 92] that, given a time-dependent structure function, we can extract an infinity of time scales from it. The dynamic scaling Ansätze can then be used to extract dynamic multiscaling exponents. A generalisation of the multifractal model then suggests linear relations, referred to as bridge relations, between these dynamic multiscaling exponents and their equal-time counterparts. In Chapter 2 we show how these bridge relations are derived.

The order-p, time-dependent, structure functions, for longitudinal velocity increments, $\delta u_{\parallel}(\mathbf{x}, \mathbf{r}, t) \equiv [\mathbf{u}(\mathbf{x} + \mathbf{r}, t) - \mathbf{u}(\mathbf{x}, t)]$ and passive-scalar increments, $\delta\theta(\mathbf{x}, t, \mathbf{r}) = \theta(\mathbf{x} + \mathbf{r}, t) - \theta(\mathbf{x}, t)$ are defined as

$$\mathcal{F}_p^u(r, \{t_1, \ldots, t_p\}) \equiv \left\langle [\delta u_{\parallel}(\mathbf{x}, t_1, r) \ldots \delta u_{\parallel}(\mathbf{x}, t_p, r)] \right\rangle \tag{1.45}$$

and

$$\mathcal{F}_p^{\theta}(\mathbf{r}, t_1, ..., t_p) = < [\delta\theta(\mathbf{x}, t_1, \mathbf{r}) ... \delta\theta(\mathbf{x}, t_p, \mathbf{r})] >; \tag{1.46}$$

i.e., fluctuations are probed over a length scale r which lies in the inertial range. For simplicity, we consider $t_1 = t$ and $t_2 = \ldots = t_p = 0$. Given $\mathcal{F}^u(r, t)$ and $\mathcal{F}^{\theta}(r, t)$, we can define the order-p, degree-M, integral-time

scales and derivative-time scales as follows [44]:

$$\mathcal{T}_{p,M}^{I,u}(r,t) \equiv \left[\frac{1}{\mathcal{S}_p^u(r)} \int_0^\infty \mathcal{F}_p^u(r,t) t^{(M-1)} dt \right]^{(1/M)}; \tag{1.47}$$

$$\mathcal{T}_{p,M}^{I,\theta}(r,t) \equiv \left[\frac{1}{\mathcal{S}_p^\theta(r)} \int_0^\infty \mathcal{F}_p^\theta(r,t) t^{(M-1)} dt \right]^{(1/M)}; \tag{1.48}$$

$$\mathcal{T}_{p,M}^{D,u}(r,t) \equiv \left[\frac{1}{\mathcal{S}_p^u(r)} \frac{\partial^M \mathcal{F}_p^u(r,t)}{\partial t^M} \right]^{(-1/M)}; \tag{1.49}$$

$$\mathcal{T}_{p,M}^{D,\theta}(r,t) \equiv \left[\frac{1}{\mathcal{S}_p^\theta(r)} \frac{\partial^M \mathcal{F}_p^\theta(r,t)}{\partial t^M} \right]^{(-1/M)}. \tag{1.50}$$

Integral-time dynamic multiscaling exponents $z_{p,M}^{I,u}$ for fluid turbulence can be defined via $\mathcal{T}_{p,M}^{I,u}(r,t) \sim r^{z_{p,M}^{I,u}}$ and the derivative-time ones $z_{p,M}^{D,u}$ by $\mathcal{T}_{p,M}^{D,u}(r,t) \sim r^{z_{p,M}^{D,u}}$. They satisfy the following bridge relations [44]:

$$z_{p,M}^{I,u} = 1 + [\zeta_{p-M} - \zeta_p]/M; \tag{1.51}$$

$$z_{p,M}^{D,u} = 1 + [\zeta_p - \zeta_{p+M}]/M. \tag{1.52}$$

For passive-scalars advected by a turbulent velocity field, the corresponding dynamic multiscaling exponents are defined as $\mathcal{T}_{p,M}^{I,\theta}(r,t) \propto r^{z_{p,M}^{I,\theta}}$ and $\mathcal{T}_{p,M}^{D,\theta}(r,t) \propto r^{z_{p,M}^{D,\theta}}$; they satisfy the following bridge relations involving the scaling exponents ζ_M of equal-time, order-M structure functions of the advecting velocity field:

$$z_{p,M}^{I,\theta} = 1 - \frac{\zeta_M}{M}; \tag{1.53}$$

$$z_{p,M}^{D,\theta} = 1 - \frac{\zeta_{-M}}{M}. \tag{1.54}$$

These bridge relations, unlike the ones for fluid turbulence, are independent of p. [Recall that, for the Kraichnan model, we get simple dynamic scaling.]

GOY-model equal-time structure functions and their associated inertial-range exponents are defined as follows:

$$S_p^u(k_n) \equiv \left\langle [u_n(t)u_n^*(t)]^{p/2} \right\rangle \sim k_n^{-\zeta_p}. \tag{1.55}$$

The time-dependent structure function are

$$F_p^u(k_n, t_0, t) \equiv \left\langle [u_n(t_0)u_n^*(t_0 + t)]^{p/2} \right\rangle. \tag{1.56}$$

We evaluate these numerically for the GOY shell model [numerical details may be found in Refs. [43, 44]], extract integral and derivative time scales from them and thence the exponents $z_{p,1}^{I,u}$ and $z_{p,2}^{D,u}$, respectively, from slopes of log-log plots of $T_{p,1}^{I,u}(n)$ versus k_n and of $T_{p,2}^{D,u}(n)$ versus k_n.

For the passive-scalar case, the equal-time order-p structure functions is

$$S_p^\theta(k_n) \equiv \left\langle [\theta(t)\theta_n^*(t)]^{p/2} \right\rangle \sim k_n^{-\zeta_p^\theta} \tag{1.57}$$

and its time-dependent version is

$$F_p^\theta(k_n, t_0, t) = < [\theta_n(t_0)\theta_n^*(t_0 + t)]^{p/2} > . \tag{1.58}$$

For the case of passive-scalars advected by a velocity field which is turbulent (a solution of the GOY model), we calculate the integral (for $M = 1$) and derivative time scales (for $M = 2$), respectively. The slope of a log-log plot of $T_{p,1}^{I,\theta}(n)$ vs k_n yields the integral time scale exponent, $z_{p,1}^{I,\theta}$, since $T_{p,1}^{I,\theta}(n) \propto k_n^{-z_{p,1}^{I,\theta}}$. Likewise, from plots of the derivative time scales we extract the exponent $z_{p,2}^{D,\theta}$. For a detailed discussion on dynamic multiscaling, for both fluids and passive-scalars, we refer the reader to Refs. [44, 98] and Chapter 2 of this Thesis.

1.6.3 2D Navier-Stokes Turbulence

Two-dimensional turbulence is markedly different from turbulence in three dimensions. This is partly because, as we have noted before,

that unlike in three dimensions the two-dimensional Navier-Stokes admits an additional conserved quantity, namely the enstrophy, in the limit of viscosity going to zero. As a result of this additional invariant, 2D Navier-Stokes turbulence admits a dual cascade: An inverse cascade of kinetic energy from the forcing scale to the large spatial scales and a direct or forward cascade of enstrophy from the forcing scale to the small spatial scales [65]. In decaying turbulence, in the absence of forcing and Ekman friction, only the forward enstrophy cascade persists. We show this via an illustrative pseudo-spectral DNS of the 2D NS equations with periodic boundary conditions and 1024^2 collocation points. In Fig. (1.6) we show an example of a compensated energy spectrum $k^3 E(k)$; the horizontal region corresponds to the inertial range. For a state-of-the-art simulation, with forcing and Ekman friction, that resolves both forward and inverse cascades we refer the reader to Ref. [112]; such DNS studies have also investigated the scaling properties of structure functions and have provided some evidence for conformal invariance in the inverse cascade inertial range [113].
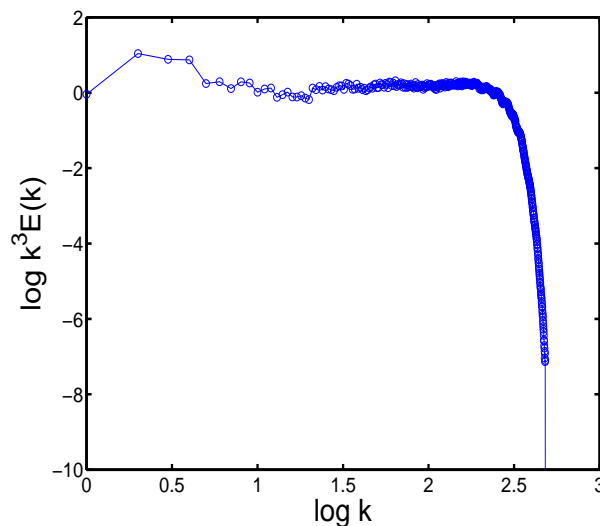
Figure 1.6: A log-log plot of the compensated energy spectrum $k^3 E(k)$ versus k from our DNS, of resolution 1024^2, of two dimensional decaying turbulence with periodic boundary conditions. The flat region indicates a scaling form $E(k) \sim k^{-3}$.

In Chapter 3 of this Thesis we study equal-time and time-dependent structure functions in homogeneous, isotropic turbulence in great detail. To put our work in context, we end this Section with a short review of a recent DNS study [78] that sheds light on the effect of the Ekman friction on the statistics of the forward cascade in wall-bounded flows that are directly relevant to laboratory soap-film experiments [114, 115, 116, 117]. The details of this DNS are given in Ref. [78]. In brief, ω is driven to a statistical steady state by a deterministic Kolmogorov forcing $F_\omega \equiv k_{inj}F_0\cos(k_{inj}x)$, with F_0 the amplitude and k_{inj} the wavenumber on which the force acts; no-slip and no-penetration boundary conditions are imposed on the walls. The important non-dimensional control parameters are the Grashof number $\mathcal{G} = 2\pi\|F_\omega\|_2/(k_{inj}^3\rho v^2)$ and the non-dimensional Ekman friction $\gamma = \alpha_E/(k_{inj}^2 v)$, where we non-dimensionalize F_ω by $2\pi/(k_{inj}\|F_\omega\|_2)$, with $\|F_\omega\|_2 \equiv (\int_A |F_\omega|^2 d\mathbf{x})^{1/2}$ and the length and time scales are made non-dimensional by scaling $\mathbf{x}$ by k_{inj}^{-1} and t by k_{inj}^{-2}/v. A fourth-order Runge-Kutta scheme is used for time marching and spatial derivatives are evaluated via second-order and fourth-order, centered, finite differences, respectively, for points adjacent to the walls and for points inside the domain. The Poisson equation is solved by using a fast-Poisson solver [102] and ω is calculated at the boundaries by using Thom's formula [78].

Since Kolmogorov forcing is inhomogeneous, it is useful to use the decomposition $\psi = \langle\psi\rangle + \psi'$ and $\omega = \langle\omega\rangle + \omega'$, where the angular brackets denote a time average and the prime the fluctuating part to calculate the order-p velocity and vorticity structure functions. Since this is a wall-bounded flow, it is important to extract the isotropic parts of these structure functions [78, 118]. Furthermore, given the resolution (2049^2), it becomes necessary to use the ESS procedure to extract exponent ratios. Illustrative log-log ESS plots for velocity, $S_p(R)$, and vorticity, $S_p^\omega(R)$, structure functions are shown in the Fig.

(1.7) and Fig. (1.8); respectively; their slopes yield the exponent ratios that are plotted versus the order p in Fig. (1.9) and Fig. (1.10). The Kraichnan-Leith-Batchelor (KLB) predictions [65] for these exponent ratios, namely, $\zeta_p^{KLB}/\zeta_2^{KLB} \sim r^{p/2}$ and $\zeta_p^{\omega,KLB}/\zeta_2^{\omega,KLB} \sim r^0$, agree with our values for ζ_p/ζ_2 but not $\zeta_p^{\omega}/\zeta_2^{\omega}$: velocity structure functions do not display multiscaling [left panel of Fig. (1.9)] whereas their vorticity analogs do [note the curvature of the plot in the right panel of Fig. (1.10)]. Similar results have been seen in DNS studies with periodic boundary conditions [119, 112]. Additional results for PDFs of several properties can be obtained [78]; these are in striking agreement with experimental results [115].

In Chapter 3, we will return to the issue of dynamic multiscaling in two-dimensional flows with friction and periodic boundary conditions.
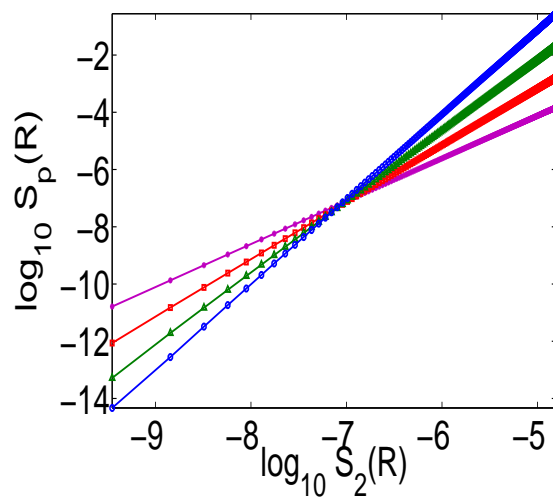
Figure 1.7: Log-log ESS plots of the isotropic parts of the order-p velocity structure functions $S_p(R)$ versus $S_2(R)$; $p = 3$ (purple line with dots), $p = 4$ (red line with square), $p = 5$ (green line with triangles), and $p = 6$ (blue line with circles). According to the KLB prediction $S_p(R) \sim R_p^{\zeta}$.
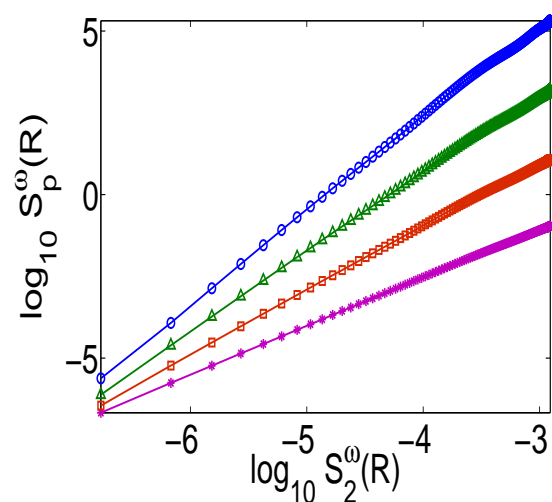
Figure 1.8: Log-log ESS plots of the isotropic parts of the order-p vorticity structure functions $S_p(R)$ versus $S_2(R)$; $p = 3$ (purple line with stars), $p = 4$ (red line with square), $p = 5$ (green line with triangles), and $p = 6$ (blue line with circles).
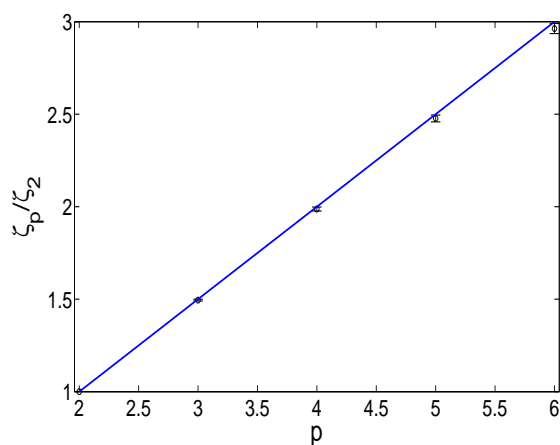
Figure 1.9: Plots of the exponent ratios ζ_p/ζ_2 versus p for the velocity differences.
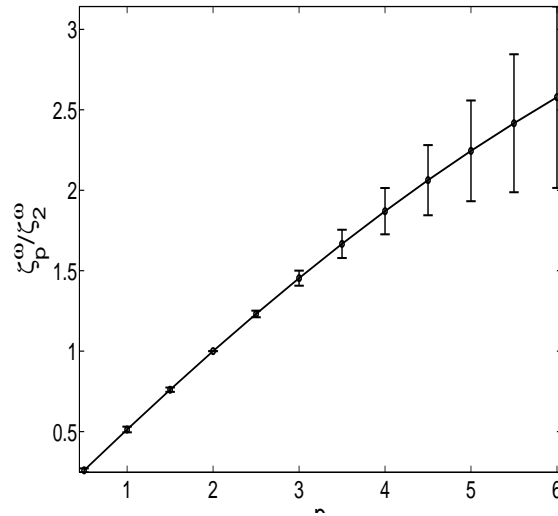
Figure 1.10: Plots of the exponent ratios $\zeta_p^\omega / \zeta_2^\omega$ versus p for the vorticity differences.

1.6.4 The One dimensional Burgers Equation

In this Section we introduce studies of the 1D Burgers equation by using two different examples. The first of these uses a pseudo-spectral method with 2^{14} collocation points, the $2/3$ dealising rule, and a fourth-order Runge-Kutta time-marching scheme. In the second study of a stochastically forced Burgers equation (see below) we use a fast-Legendre method that yields results in the zero-viscosity limit [120].

For the Burgers equation with no external forcing and sufficiently well-behaved initial conditions, the velocity field develops *shocks*, or jump discontinuities, which merge into each other with time. The time at which the first shock appears is usually denoted by t_*. For all times greater than t_*, it is possible to calculate, analytically, the scaling exponents ζ_p for the equal-time structure functions via

$$S_p \equiv \langle [u(x+r,t) - u(x)]^p \rangle \sim C_p |r|^p + C'_p |r|, \qquad (1.59)$$

where the first term comes from the *ramp*, and the second term comes from the probability of having a shock in the interval $|r|$. As a consequence of this we have *bifractal* scaling : for $0 < p < 1$ the first term

dominates leading to $\zeta_p = p$ and for $p > 1$ the second one dominates giving $\zeta_p = 1$. This leads to an energy spectrum $E(k) \sim k^{-2}$. Representative plots from our pseudo-spectral DNS, with $\nu = 10^{-3}$ and an initial condition $u(x) = \sin(x)$ (for which $t_* = 1$) are shown in Figs. (1.11) and (1.12); the former shows plots of the velocity field at times $t = 0$, 1, and $t = 1.5$ and the latter the energy spectrum at $t = 1$.
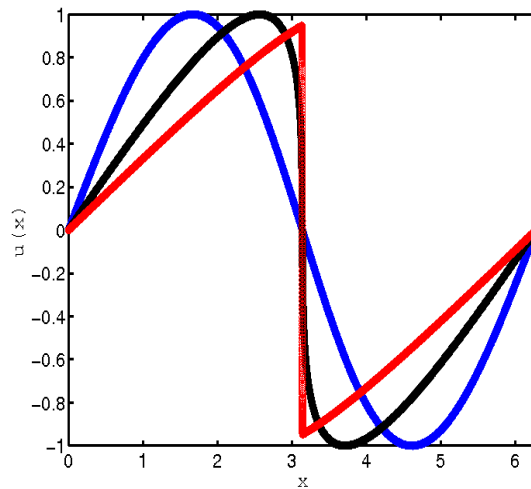
Figure 1.11: Snapshots of the solution of the Burgers equation obtained from our DNS with initial condition $u(x) = \sin x$ at times $t = 0$ (blue), $t = 1$ (black) and $t = 2$ (red).

The stochastically forced Burgers equation has played an important role in renormalization-group studies [120]. In particular, consider a Gaussian random force $f(x, t)$ with zero mean and the following covariance in Fourier space:

$$\langle \hat{f}(k_1, t_1)\hat{f}(k_2, t_2)\rangle = 2D_0|k|^\beta \delta(t_1 - t_2)\delta(k_1 + k_2); \qquad (1.60)$$

here $\hat{f}(k, t)$ is the spatial Fourier transform of $f(x, t)$, D_0 is a constant, and the scaling properties of the forcing is governed by the exponent β. For positive values of β, the Burgers equation can be studied by using renormalization-group techniques; specifically, for $\beta = 2$ one recovers
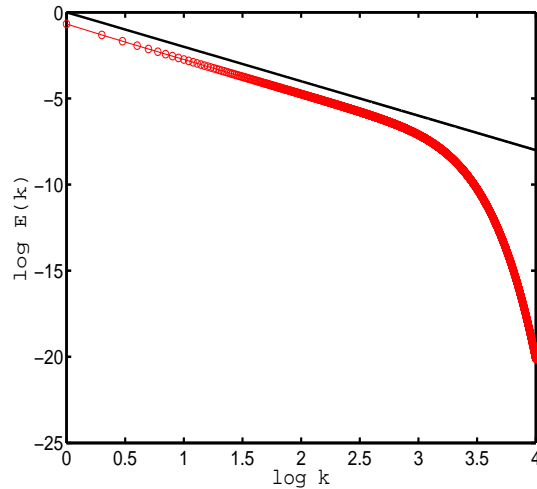
Figure 1.12: A representative log-log plot of $E(k)$ versus k, at time $t = 1$ for the Burgers equation with initial conditions $u(x) = \sin x$.

simple (Kardar-Parisi-Zhang or KPZ) scaling with the equal-time exponent $\zeta_p = p$. It was hoped that forcing with negative values of β (in particular $\beta = -1$), which cannot be studied by renormalization-group methods, might yield multiscaling of velocity structure functions.

However, high-resolution study [120], which uses a fast-Legendre method, has shown that the apparent multiscaling of structure functions in this stochastic model might arise because of numerical artifacts. The general consensus is that this stochastically forced Burgers model should show bifractal scaling. In Fig. (1.13) we present representative plots of the velocity field (blue curve) and the scaling exponents in Fig. (1.14) for this model. We have obtained the data for these figures by using a fast-Legendre method with 2^{18} collocation points.

Numerical studies of the Burgers equation have also proved useful in elucidating bottleneck structures in energy spectra [121, 122] It turns out that such a bottleneck does not occur in the conventional Burgers equation. However, it does [123] occur in the hyperviscous
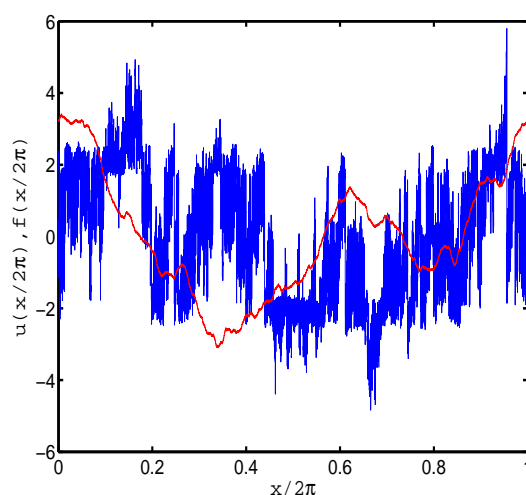
Figure 1.13: (A snapshot of the velocity field (jagged line in blue) in steady state and the force in red from our fast-Legendre method DNS of the stochastically forced Burgers equation.
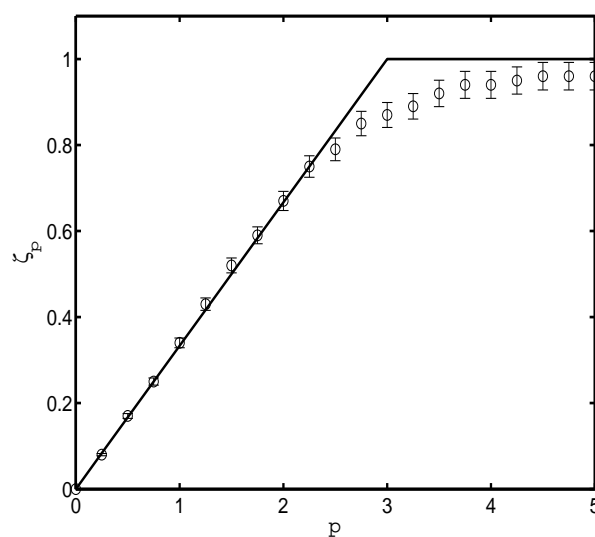
Figure 1.14: A representative plot of the exponents ζ_p, with error-bars, for the equal-time velocity structure functions of the stochastically forced Burgers equation; bifractal scaling is shown by the black solid line; the deviations from this are believed to arise from artefacts (see text).

one, in which usual Laplacian dissipation operator is replaced by its αth power; this is known as hyperviscosity for $\alpha > 1$. In Chapters 4 and 5 we will examine this problem in detail; in Chapter 6 we will return to the Burgers equation once more to show how we can understand the success of Extended Self-Similarity.

We end this Chapter with a short discussion on one of the important mathematical questions in turbulence. For over two centuries now, the well-posedeness of the solution to the three-dimensional incompressible fluid equations with sufficienty smooth initial data is still an open question [10, 128, 129, 130] (also many papers in [131] and references therein). Even for the viscous Navier-Stokes equations, which is of more interest to physicists, the issue of finite-time blow up is far from settled, either through rigorous theory or from reliable numerical data [7, 8, 132, 133, 134]. The situation is slightly different if we relax the constraint on the choice of initial conditions. In fact for analytic and spatially periodic initial data both the Euler and the Navier-Stokes equation in three dimensions have complex space singularities. Numerically, it was shown in [135] that a pseudo-spectral method for solving such equations lead to exponential decrease of the Fourier modes of the velocity at high wavenumbers. Such a Fourier space behaviour is a signature of complex singularities [135] as was conjectured by von Neumann [136]. As we have seen before, for some PDEs in lower space dimensions such as the Burgers equation it is possible to obtain exact results for the type and position of such singularities. Another example is the complex singularities which are related to poles of elliptic functions in the reaction diffusion equation [137] and the 2D incompressible Euler equations in Lagrangian coordinates [138].

In the three-dimensional Navier-Stokes, with real analytic data, finite-time blow up in the real domain can be eliminated by using hyperviscosity, i.e., replacing the dissipative term $\nu|k|^2$ by a higher power

of the Laplacian with symbol $\nu|k|^{2\alpha}$ ($\alpha > 5/4$) as shown by [132, 141]. There is numerical evidence though that complex singularities cannot be avoided by this procedure [142]. In Chapter 7 of this Thesis we show the first example of a nonlinear PDE, with the property that the Cauchy problem is well posed in the complex space domain, and which does not have any complex-space singularities at a finite distance from the real domain. In other words, we prove that solutions to a large class of pseudo-differential nonlinear equations, which include variants of the 3D NSE where the dissipation grows exponentially as $e^{|k|/k_d}$, where k_d is a reference wavenumber k_d, stays or becomes entire at all finite times.

Bibliography

[1] R. Ecke, *Los Alamos Science*, **29**, 124 (2005).

[2] G. Falkovich and K.R. Sreenivasan, Physics Today **59**, 43 (2006).

[3] I. Procaccia and K.R. Sreenivasan, Physica D **237**, 2167 (2008) and references therein.

[4] A.J. Reynolds *Turbulent flows in engineering* (John Wiley, New York, 1974).

[5] S.B. Pope, *Turbulent Flows* (Cambridge University, Cambridge, UK, 2000).

[6] C. Doering, Annu. Rev. Fluid Mech., **41**, 109 (2009).

[7] C. Fefferman, *Existence and smoothness of the Navier-Stokes equation. Clay Millenium Prize Problem Description* (2000); http://www.claymath.org/millennium/Navier-Stokes_Equations/Official_Problem_D escription.pdf.

[8] P. Constantin and C. Foias, *Navier-Stokes Equations* (University of Chicago Press, Chicago, 1988).

[9] C. Doering and J. Gibbon, *Applied Analysis of the Navier-Stokes Equations* (Cambridge University Press, Cambridge, UK, 1995).

[10] A.J. Majda and A.L. Bertozzi, *Vorticity and Incompressible Flow* (Cambridge University Press, Cambridge, UK, 2001).

[11] H. Tennekes and J. L. Lumley, *A First Course in Turbulence* (MIT Press, Cambridge, Massachusetts, 1972).

[12] M. Lesieur, *Turbulence in Fluids* (Springer, The Netherlands, 2008).

[13] P.A. Davidson, *Turbulence: An Introduction for Scientists and Engineers* (Oxford University Press, Oxford, 2007).

[14] V.M. Canuto and J. Christensen-Dalsgaard, Annu. Rev. Fluid Mech. **30**, 167 (1998); *Turbulence and Magnetic Fields in Astrophysics*, eds. E. Falgarone and T. Passot, (Springer, New York, 2003); M.S. Miesch and J. Toomre Annu. Rev. Fluid Mech. **41**, 317 (2009).

[15] A. Rai Choudhuri, *The Physics of Fluids and Plasmas: An Introduction for Astrophysicists* (Cambridge University Press, Cambridge, UK, 1998).

[16] V. Krishan, *Astrophysical Plasmas and Fluids* (Kluwer, Dordrecht, (1999).

[17] H. Goedbloed and S. Poedts, *Principles of Magnetohydrodynamics With Applications to Laboratory and Astrophysical Plasmas* (Cambridge University Press, Cambridge, UK, 2004).

[18] A S Monin, Russ. Math. Surv. **38** 127 (1983); P. Bradshaw and J. D. Woods, in *Turbulence*, ed. P. Bradshaw, (Springer, New York, 1978); A.J. Majda and X. Wang, *Nonlinear Dynamics and Statistical Theories of Basic Geophysical Flows* (Cambridge University Press, Cambridge, UK, 2006).

[19] G. Boer and T. Shepherd, J. Atmos. Sci. **40**, 164 (1983).

[20] R.A. Shaw, Annu. Rev. Fluid Mech., **35**, 183 (2003).

[21] D. Biskamp, *Magnetohydrodynamic Turbulence* (Cambridge University Press, Cambridge, UK, 2003).

[22] M.K. Verma, Phys. Rep. **401**, 229 (2004).

[23] S. Orszag, in *Fluid Dynamics, Les Houches*, eds. R. Balian and J. Peube (Gordon and Breach, New York, 1977) pp. 237-374.

[24] H. Rose and P. Sulem, J. Phys. France **39**, 441 (1978).

[25] C.D. Dominicis and P. Martin, Phys. Rev. A **19**, 419 (1979).

[26] V. Yakhot and S. Orszag, Phys. Rev. Lett **57**, 1722 (1986).

[27] W.D. McComb, *The Physics of Fluid Turbulence*, (Oxford University Press, Oxford, 1991).

[28] G.L. Eyink, Phys. Fluids A. **6** 3063 (1994); G.L. Eyink and N. Goldenfeld, Phys. Rev. E **50** 4679 (1994).

[29] T. Bohr, M.H. Jensen, G. Paladin, and A. Vulpiani, *Dynamical Systems Approach to Turbulence* (Cambridge University, Cambridge, UK, 1998).

[30] L. Ts. Adzhemyan, N.V. Antonov, and A.N. Vasiliev, *The Field Theoretic Renormalization Group in Fully Developed Turbulence* (Gordon and Breach, 1999).

[31] J.K. Bhattacharjee and S. Bhattacharyya, *Nonlinear Dynamics Near and Far From Equilibrium* (Hindustan Book Agency, New Delhi, 2007), Ch. 8, pp 231-274.

[32] *Non-equilibrium Statistical Mechanics and Turbulence*, eds. S. Nazarenko and O.V. Zaboronski (Cambridge University Press, Cambridge, UK, 2008).

[33] U. Frisch, *Turbulence: The Legacy of A.N. Kolmogorov* (Cambridge University, Cambridge, UK, 1996).

[34] G. Falkovich, K. Gawedzki and M. Vergassola, Rev. Mod. Phys. **73**, 913 (2001).

[35] P. Tabeling, Phys. Rep. **362**, 1 (2002).

[36] H. Kellay and W. Goldburg, Rep. Prog. Phys. **65** 845 (2002).

[37] J.M. Burgers, *The Nonlinear Diffusion Equation*, (D. Reidel, Dordrecht, 1974).

[38] U. Frisch and J. Bec, *Les Houches 2000: New Trends in Turbulence*, ed. M. Lesieur, (Springer EDP-Sciences 2000)

[39] J. Bec and K. Khanin, Phys. Rep., **447**, 1 (2007).

[40] R. Pandit, P. Perlekar, and S. S. Ray, *Statistical Properties of Turbulence: An Overview*, Pramana – Journal of Physics, **73**, 157 (2009).

[41] G.K. Batchelor *The Theory of Homogeneous Turbulence* (Cambridge University, Cambridge, UK, 1953).

[42] A.S. Monin and A.M. Yaglom, *Statistical Fluid Mechanics*, Vols. 1 and 2 (Dover, New York, 2007).

[43] R. Pandit, S.S. Ray, and D. Mitra, Eur. Phys. J. B **64**, 463 (2008).

[44] S.S. Ray, D. Mitra, and R. Pandit, New J. Phys. **10**, 033003 (2008).

[45] L.F. Richardson *Weather Prediction by Numerical Process* (Cambridge Univ. Press, 1922).

[46] A.N. Kolmogorov, Dokl. Akad. Nauk SSSR **30**, 301 (1941); A.N. Kolmogorov, Dokl. Akad. Nauk SSSR **31**, 538 (1941).

[47] T. Kurian and J.H.M. Fransson, Fluid Dyn. Res. **41**, 021403 (2007).

[48] N. Mordant, P. Metz, O. Michel, and J-F Pinton Phys. Rev. Lett. **87**, 214501 (2001); N. Mordant, E. Lévêque, and J-F Pinton, New J. Phys. **6**, 116 (2004).

[49] A. La Porta, G.A. Voth, A.M. Crawford, J. Alexander, E. Bodenschatz Nature **409**, 1017 (2001); G.A. Voth, A. La Porta, A.M. Crawford, J. Alexander, and E. Bodenschatz J. Fluid Mech. **469**, 121 (2002); A.M. Reynolds, N. Mordant, A.M. Crawford and E Bodenschatz, New J. of Phys. **7**, 58 (2005); F. Toschi and E. Bodenschatz, Annu. Rev. Fluid Mech., **41**, 375 (2009).

[50] A. Arneòdo, *et al.*, Phys. Rev. Lett. **100**, 254504 (2008).

[51] G.J. Kunkel and I. Marusic, J. Fluid Mech. **548**, 375 (2006).

[52] E.L. Andreas, K.J. Claffey, R.E. Jordan, C.W. Fairall, P.S. Guest, P.O.G. Persson, and A.A. Grachev, J. Fluid Mech. **559**, 117 (2006).

[53] G. Gulitski, M. Kholmyansky, W. Kinzelbach, B. Lüthi, A. Tsinober and S. Yorish, J. Fluid Mech., **589**, 57 (2007); *ibid*, 83 (2007); *ibid* 103 (2007).

[54] A. Talamelli, F. Persiani, J.H.M. Fransson, P.H. Alfredsson, A.V. Johansson, H.M. Nagib, J-D Rüedi, K.R. Sreenivasan, and P.A. Monkewitz, Fluid Dyn. Res. **41**, 021407 (2009).

[55] H.L. Grant, R.W. Stewart, and A. Moilliet, J. Fluid Mech. **12**, 241 (1968); *Marine turbulence: theories, observations, and models* H.Z. Baumert, J.H. Simpson, and J. Sündermann (Cambridge University Press, Cambridge, UK 2005).

[56] S. Tavoularis, *Measurement in Fluid Mechanics* (Cambridge University Press, Cambridge, UK, 2005).

[57] See, e.g., B.J. Mckeon, G. Comte-Bellot, J.F. Foss, J. Westereeel, F. Scarano, C. Tropea, J.F. Meyers, J.W. Lee, A.A. Cavone, R. Schodl,

M.M. Kochesfahani, D.G. Nocera, Y. Andreopoulos, W.J.A. Dahm, J.A. Mullin, J.M. Wallace, P.V. Vukoslavcevic, S.C. Morris, E.R. Pardyjak, and A. Cuerva, in *Springer Handbook of Experimental Fluid Mechanics*, eds. C. Tropea, A.L. Yarin, and J.F. Foss (Springer, Berlin 2007) pp 215-471.

[58] See, e.g., P.V. Vukoslavcević, N. Beratlis, E. Balaras, J.M. Wallace, and O. Sun, Exp. Fluids, **46**, 109 (2009).

[59] See, e.g., G.E. Elsinga, F. Scarano, B. Wieneke, and B.W. van Oudheusden, Exp. Fluids, **41**, 933 (2006).

[60] See, e.g., B. Tao, J. Katz, and C. Meneveau, Phys. Fluids, **12**, 941 (2000).

[61] See, e.g., J. Sheng, E. Malkiel, and J. Katz, Exp. Fluids, **45**, 1023 (2008).

[62] M. Van Dyke, *An Album of Fluid Motion* (The Parabolic Press, Stanford, California, 1988); see also the *Gallery of Fluid Motion* http://pof.aip.org/pof/gallery/index1.jsp.

[63] G.L. Brown, A. Roshko, J. Fluid Mech. **64**, 775 (1974).

[64] R.H. Kraichnan and D. Montgomery, Rep. Prog. Phys. **43**, 547 (1980).

[65] R. Kraichnan, Phys. Fluids **10**, 1417 (1967); C. Leith, Phys. Fluids, **11**, 671 (1968); G. Batchelor, Phys. Fluids Suppl. II **12**, 233 (1969).

[66] S. Douady, Y. Couder, and M.E. Brachet, Phys. Rev. Lett. **67**, 983 (1991).

[67] H. Mouri and A. Hori, Fluid Dyn. Res. **41**, 021402 (2009).

[68] C. Meneveau and K.R. Sreenivasan, J. Fluid Mech. **224**, 429 (1991).

[69] T. Isihara, T. Gotoh, and Y. Kaneda, Annu. Rev. Fluid Mech., **41**, 165 (2009).

[70] F. Anselmet, Y. Gagne, E. Hopfinnger, and R. Antonia, J. Fluid Mech. **140**, 63 (1984).

[71] Z-S. She and E. Leveque Phys. Rev. Lett. **72**, 336 (1994).

[72] K.R. Sreenivasan and R.A. Antonia, Annu. Rev. Fluid Mech. **29**, 435 (1997).

[73] A. Praskovsky and S. Oncley, Phys. Rev. Lett. **73**, 3399 (1994).

[74] J. Sommeria, J. Fluid Mech. **170**, 139 (1986).

[75] Y. Couder, J. Physique Lett. **45**, 353 (1984).

[76] M. Rivera and X.L. Wu, Phy. Rev. Lett. **85**, 976 (2000); M. Rivera, X.L. Wu, and C. Yeung, Phys. Rev. Lett. **87**, 044501 (2001); W.B. Daniel and M.A. Rutgers, Phys. Rev. Lett. **89**, 134502 (2002); M. Rivera and R. Ecke, arXiv:0710.5888v1 (2007).

[77] J. Chomaz, J. Fluid Mech. **442**, 387 (2001).

[78] P. Perlekar and R. Pandit, to be published (see http://arxiv.org/abs/0811.1324).

[79] A. Groisman and V. Steinberg, New J. Phys. **6**, 29 (2004).

[80] S. Berti, A. Bistagnino, G. Boffetta, A. Celani, and S. Musacchio Phys. Rev. E **77**, 055306(R) (2008).

[81] B.A. Toms, in *Proc. Intl. Rheological Congress Holland, 1948*, p. 135 (1949).

[82] J.W. Hoyt, Trans. ASME:J. Basic Engng **94**, 258 (1972).

[83] P.S. Virk, AIChE J. **21**, 625 (1975).

[84] K.R. Sreenivasan and C.M. White, J. Fluid Mech., **409**, 149 (2000).

[85] N.T. Ouellette, H. Xu, and E. Bodenschatz, to be published (2009); see arXiv:0708.3945.

[86] R. Kraichnan, Phys. Fluids **11**, 945 (1968); R. Kraichnan, Phys. Rev. Lett. **72**, 1016 (1994); R. Kraichnan, Phys. Rev. Lett. **78**, 4922 (1997).

[87] T. Vaithianathan and L. Collins, J. Comput. Phys. **187**, 1 (2003).

[88] E. Gledzer, Sov. Phys. Dokl. **18**, 216 (1973); K. Ohkitani and M. Yamada, Prog. Theor. Phys. **81**, 329 (1989).

[89] A. Wirth and L. Biferale, Phys. Rev. E **54**, 4982 (1996); M.H. Jensen, G. Paladin, and A. Vulpiani, Phys. Rev. A **45**, 7214 (1992).

[90] C. Kalelkar, R. Govindarajan, and R. Pandit, Phys. Rev. E **72**, 017301 (2005).

[91] V.I. Belinicher and V.S. L'vov, Sov. Phys. JETP **66**, 303(1987).

[92] V.S. L'vov, E. Podivilov, and I. Procaccia, Phys. Rev. E **55**, 7030 (1997).

[93] A. M. Obukhov, Izv. Akad. SSSR, Serv. Geogr. Geofiz. **13**, 58 (1949).

[94] S. Corrsin, J. Appl. Phys. **22**, 469 (1951).

[95] D. Stauffer, M. Ferer, and M. Wortis **29**, 345 (1972); A. Aharony, Phys. Rev. B, **9**, 2107 (1974).

[96] G. Parisi and U. Frisch in *Turbulence and Predictability of Geophysical Fluid Dynamics*, eds. M. Ghil, R. Benzi, and G. Parisi (North-Holland, Amsterdam, 1985) p 84.

[97] G. Boffetta, A. Mazzino, and A. Vulpiani, J. Phys. A: Math. Gen. **41**, 363001 (2008).

[98] D. Mitra and R. Pandit, Phys. Rev. Lett. **93**, 024501 (2004).

[99] D. Mitra and R. Pandit, Phys. Rev. Lett. **95**, 144501 (2005).

[100] A. Vincent and M. Meneguzzi, J. Fluid Mech. **225**, 1 (1991).

[101] C. Canuto, M. Hussaini, A. Quarteroni, and T. Zang, *Spectral Methods in Fluid Dynamics* (Spinger-Verlag, Berlin, 1988).

[102] W. Press, B. Flannery, S. Teukolsky, and W. Vetterling, pp. 848-852, *Numerical Recipes in Fortran* (Cambridge University Press, Cambridge, 1992).

[103] V. Eswaran and S. Pope, Comput. Fluids, **16**, 257 (1988); the forcing is stochastic and is generated by an Ornstein-Uhlenbeck process (i.e., the noise is coloured).

[104] B. J. Cantwell, Phys Fluids A **4**, 782 (1992).

[105] Y. Kaneda *et al.*, Phys. Fluids **15**, L21 (2003).

[106] R. Benzi *et al.*, Phys. Rev. E **48**, R29 (1993); S. Dhar, A. Sain, and R. Pandit, Phys. Rev. Lett. **78**, 2964 (1997).

[107] C. Y. Mou and P. B. Weichman, Phys. Rev. Lett. **70**, 1101 (1993).

[108] A. Sain, Manu, and R. Pandit, Phys. Rev. Lett. **81**, 4377 (1998).

[109] L Biferale, M Cencini, A S Lanotte, M Sbragaglia and F Toschi, New J. Phy. **6**37 (2004).

[110] L. Biferale, Annu. Rev. Fluid Mech., **35**, 441 (2003).

[111] P.K. Yeung, Annu. Rev. Fluid Mech., **34**, 115 (2002).

[112] G. Boffetta, J. Fluid Mech. **589**, 253 (2007).

[113] D. Bernard, G. Boffetta, A. Celani, and G. Falkovich, Nature Physics **2** 124 (2006); D. Bernard, G. Boffetta, A. Celani, and G. Falkovich, Phys. Rev. Lett. **98** 024501 (2007).

[114] M. Rivera and X.L. Wu, Phy. Rev. Lett. **85**, 976 (2000).

[115] M. Rivera, X.L. Wu, and C. Yeung, Phys. Rev. Lett. **87**, 044501 (2001).

[116] W.B. Daniel and M.A. Rutgers, Phys. Rev. Lett. **89**, 134502 (2002).

[117] M. Rivera and R. Ecke, arXiv:0710.5888v1 (2007).

[118] L. Biferale and I. Procaccia, Phys. Rep., **414**, 43 (2005).

[119] Y.-K. Tsang, E. Ott, T.M. Antonsen, and P.N. Guzdar, Phys. Rev. E **71**, 066313 (2005).

[120] D. Mitra, J. Bec, R. Pandit and U. Frisch, Phys. Rev. Lett. **94**, 194501 (2005).

[121] Z.S. She, G. Doolen, R.H. Kraichnan, and S.A. Orszag, Phys. Rev. Lett. **70**, 3251 (1993); Y. Kaneda, T. Ishihara, M. Yokokawa, K. Itakura, and A. Uno, Phys. Fluids, **15**, L21 (2003); S. Kurien, M.A. Taylor, and T. Matsumoto, Phys. Rev. E **69**, 066313 (2004); J. Schumacher, Europhys. Lett. **80**, 54001 (2007); P.D. Mininni, A. Alexakis, and A. Pouquet, Phys. Rev. E **77**, 036306 (2008).

[122] S.G. Saddoughi and S.V. Veeravalli, J. Fluid Mech. **268**, 333 (1994). As shown by W. Dobler, N.E.L. Haugen, T.A. Yousef and A. Brandenburg, Phys. Rev. E **68**, 026304 (2003).

[123] U. Frisch, S. Kurien, R. Pandit, W. Pauls, S. S. Ray, A. Wirth, and J-Z Zhu, Phys. Rev. Lett. **101**, 144501 (2008).

[124] T. D. Lee, Quart. J. Appl. Math. **10** 69 (1952) .

[125] R. H. Kraichnan, Phys. Fluids **10**, 2080 (1967).

[126] C. Cichowlas, P. Bonaïti, F. Debbasch, and M. Brachet, Phys. Rev. Lett. **95**, 264502 (2005).

[127] P. Perlekar, D. Mitra and R. Pandit, Phys. Rev. Lett. **97**, 264501 (2006); and to be published.

[128] Frisch, U.; Matsumoto, T.; Bec, J. Singularities of Euler flow? Not out of the blue! *J. Stat. Phys.* **113** (2003), 761–781.

[129] Bardos, C.; Titi, E.S. Euler equations of incompressible ideal fluids. *Uspekhi Mat. Nauk* **62**(2007), 5–46. English version *Russian Math. Surv.* **62** (2007), 409–451.

[130] Constantin, P. On the Euler equations of incompressible fluids. *Bull. Amer. Math. Soc.* **44** (2007), 603–621.

[131] Eyink, G.; Frisch, U.; Moreau, R.; Sobolevskii, A. Proceedings of *Euler Equations: 250 Years On*, Aussois, June 18–23, 2007. *Physica D* **237** (2008), no. 14–17.

[132] Lions, J.L. *Quelques Méthodes de Résolution des Problèmes aux Limites non Linéaires*, Gauthier-Villars, Paris, 1969.

[133] Temam, R. *Navier-Stokes equations. Theory and numerical analysis*. Revised edition. With an appendix by F. Thomasset. Published by AMS Bookstore, 2001.

[134] Sohr, H. *The Navier-Stokes equations*. Birkhäuser, Basel, 2001.

[135] Brachet, M.-E.; Meiron, D.I.; Orszag, S.A.; Nickel, B.G.; Morf, R.H.; Frisch, U. Small-scale structure of the Taylor-Green vortex, *J. Fluid Mech.* **130** (1983), 411–452.

[136] Neumann, J. von. Recent theories of turbulence (1949). In *Collected works (1949–1963)* **6**, 37–472, ed. A.H. Taub. Pergamon Press, New York, 1963.

[137] Oliver, M; Titi, E.S. On the domain of analyticity for solutions of second order analytic nonlinear differential equations. *J. Differ. Equations* **174** (2001), 55–74.

[138] Pauls, W.; Matsumoto, T. Lagrangian singularities of steady two-dimensional flow. *Geophys. Astrophys. Fluid. Dyn.* **99**, (2005), pp. 61–75,

[139] Senouf, D.; Caflisch, R.; Ercolani, N. Pole dynamics and oscillation for the complex Burgers equation in the small-dispersion limit. *Nonlinearity* **9** (1996), 1671–1702.

[140] Polá*vc*ik, P.; *vS*verák, V. Zeros of complex caloric functions and singularities of complex viscous Burgers equation. Preprint. 2008. arXiv:math/0612506v1 [math.AP].

[141] Ladyzhenskaya, O.A. *The Mathematical Theory of Viscous Incompressible Flow* (1st ed.) Gordon and Breach, New York, 1963.

[142] Holloway, G. Representing topographic stress for large-scale ocean models. *J. Phys. Oceanogr.* **22** (1992), 1033–1046.

Chapter 2

The Universality of Dynamic Multiscaling in Homogeneous, Isotropic Turbulence

2.1 Introduction

In this Chapter we discuss the universality of dynamic multiscaling in shell models for fluid and passive-scalar turbulence. The rest of the Chapter follows closely Refs. [1] and [2] The elucidation of the universal scaling properties of equal-time and time-dependent correlation functions in the vicinity of a critical point was one of the most important achievements of statistical mechanics over the past forty years. The analogous systematization of the power laws and associated exponents that govern the behaviours of structure functions in a turbulent fluid, or in a passive-scalar advected by such a fluid, is a major challenge in the areas of nonequilibrium statistical mechanics, fluid mechanics, and nonlinear dynamics. The power-law behaviours of *equal-time* structure functions have been studied in detail over the past few decades [3]; and, especially in the case of passive-scalar turbulence [4], significant progress has been made in understanding the *multiscaling* of *equal-time* structure functions. The nature of multiscaling of *time-dependent* structure functions has been examined recently

53

[5, 6, 7, 8, 9] but only for the case of *statistically steady* turbulence. We develop here the systematics of the multiscaling of time-dependent structure functions for the case of *decaying* fluid and passive-scalar turbulence [10].

To set the stage for our discussion of time-dependent structure functions in turbulence, it is useful to begin by recalling some well-known results from critical phenomena [12, 13]: At a critical point for a spin system in d dimensions, the equal-time, two-spin correlation function g and its spatial Fourier transform $\tilde{g}$ assume the following power-law scaling forms:

$$
\begin{aligned}
g(\mathbf{r}; \bar{t}, h) &\approx \frac{G(r\bar{t}^{\nu}, h/\bar{t}^{\Delta})}{r^{d-2+\eta}}; \\
\tilde{g}(\mathbf{k}; \bar{t}, h) &\approx \frac{\tilde{G}(k/\bar{t}^{\nu}, h/\bar{t}^{\Delta})}{k^{2-\eta}}.
\end{aligned}
\tag{2.1}
$$

Here $\bar{t} \equiv (|T - T_c|)/T_c$, T and T_c are the temperature and the critical temperature, respectively, $h \equiv H/k_B T_c$, H is the external field, k_B is the Boltzmann constant, the spins are separated by the vector $\mathbf{r}$ [$r = |\mathbf{r}|$], $\mathbf{k}$ is the wavevector, $k = |\mathbf{k}|$, ν, Δ, η are critical exponents, and G and $\tilde{G}$ are scaling functions. Away from the critical point such correlation functions decay exponentially; the associated correlation length ξ_c diverges in the vicinity of the critical point; e.g., as $\xi_c \sim \bar{t}^{-\nu}$, if $h = 0$. Time-dependent correlation functions also assume scaling forms in the vicinity of the critical point and the characteristic relaxation time τ diverges as suggested by the *dynamic-scaling Ansatz* [12]

$$
\tau \sim \xi_c^z,
\tag{2.2}
$$

which introduces the *dynamic-scaling exponent z*.

The generalisation of such a dynamic-scaling *Ansatz* to the case of homogeneous, isotropic turbulence is our prime concern here. The power-law behaviours of equal-time structure functions, in the inertial range (to be defined later), in turbulence are reminiscent of the

algebraic dependence on r of critical-point correlation functions. However, there are important differences between the two that must be appreciated before we embark on a systematization of time-dependent structure functions in turbulence. We begin with the increments of the longitudinal component of the velocity $\delta u_{\parallel}(\mathbf{x}, \mathbf{r}, t) \equiv [\mathbf{u}(\mathbf{x} + \mathbf{r}, t) - \mathbf{u}(\mathbf{x}, t)] \cdot (\mathbf{r}/r)$ and passive-scalar $\delta\theta(\mathbf{x}, \mathbf{r}, t) \equiv [\theta(\mathbf{x} + \mathbf{r}, t) - \theta(\mathbf{x}, t)]$, respectively; here $\mathbf{u}(\mathbf{x}, t)$ and $\theta(\mathbf{x}, t)$ denote, respectively, the velocity of the fluid and the passive-scalar density at the point $\mathbf{x}$ and time t, and the subscript $\parallel$ the longitudinal component. The order-p, equal-time structure functions, for the fluid (superscript u) and passive-scalar (superscript θ) fields, are defined as follows:

$$
\begin{aligned}
\mathcal{S}_p^u(r) &\equiv \langle [\delta u_{\parallel}(\mathbf{x}, \mathbf{r}, t)]^p \rangle \sim r^{\zeta_p^u}; \\
\mathcal{S}_p^\theta(r) &\equiv \langle [\delta\theta(\mathbf{x}, \mathbf{r}, t)]^p \rangle \sim r^{\zeta_p^\theta};
\end{aligned}
\tag{2.3}
$$

the angular brackets indicate averages over the steady state for statistically steady turbulence or over statistically independent initial configurations for decaying turbulence; for stochastic differential equations, like the Kraichnan Model (see Sec. 2.2.1), the angular brackets denote an average over the statistics of the noise; and the power laws, characterised by the equal-time exponents ζ_p^u and ζ_p^θ, hold for separations r in the inertial range $\eta_d \ll r \ll L$, where η_d is the Kolmogorov dissipation scale and L the large length scale at which energy is injected into the system.

Kolmogorov's phenomenological theory [3, 14, 15] of 1941 (K41) suggests simple scaling, with $\zeta_p^{u,K41} = p/3$, but experimental and numerical evidence favours equal-time multiscaling with ζ_p^u and ζ_p^θ non-linear, convex, monotone-increasing functions of p. For the simplified Kraichnan model [4, 16, 17, 18] of passive-scalar turbulence (see Sec. 2.2.1) multiscaling of equal-time structure functions can be demonstrated analytically in certain limits. The analogue of the K41 theory for passive-scalar turbulence is due to Obukhov and Corrsin [19, 20];

if the Schmidt number $Sc \equiv \nu/\kappa \simeq 1$, then their theory yields K41 exponents for the passive-scalar case; here ν is the kinematic viscosity of the fluid and κ is the diffusivity of the passive scalar.

A straightforward extension of simple, K41 scaling to time-dependent structure functions implies that the dynamic exponents $z_p^{K41} = 2/3$ for all p. This naïve extension fails for two reasons: (a) it does not distinguish between the temporal behaviours of structure functions of Eulerian, Lagrangian, and quasi-Lagrangian (see Sec. 2.2) velocities or passive-scalar densities; and (b) it does not account for the multiscaling of structure functions. These difficulties have been overcome to a large extent for statistically steady turbulence [5, 6, 7, 8, 9, 21] as we summarise below. There is consensus now that Eulerian structure functions display simple scaling with only one dynamic-scaling exponent $z^{\mathcal{E}} = 1$ because of the *sweeping effect*: the mean flow, or the flow caused by the largest eddy, advects small eddies, so spatial separations r in (2.3) are related *linearly* to temporal separations τ via the mean-flow velocity [21]. By contrast, it is expected that Lagrangian [21] or quasi-Lagrangian [5, 6, 7, 8, 9, 22] time-dependent structure functions should show nontrivial dynamic multiscaling. The task of extracting well-averaged time-dependent Lagrangian or quasi-Lagrangian structure functions from a direct numerical simulation (DNS) of the Navier-Stokes equation is a daunting one [23]: a dynamic exponent has been extracted from a full Lagrangian study [21] only for order $p = 2$. Thus the elucidation of dynamic multiscaling has relied on predictions based on generalisations of the multifractal formalism [5, 6, 7, 8, 9] and on numerical studies of shell models [6, 7, 8, 9]. These studies show that, if dynamic multiscaling exists, time-dependent structure functions must be characterised by an infinity of time scales and associated dynamic multiscaling exponents [8]. Furthermore, the dynamic exponents depend on how we extract time scales from time-dependent structure functions; e.g., for fluid turbu-

lence, time scales obtained from integrals (superscript I and subscript 1) and second derivatives (superscript D and subscript 2) of order-p time-dependent structure functions yield the *different* dynamic exponents $z_{p,1}^{I,u}$ and $z_{p,2}^{D,u}$. Finally, the different dynamic multiscaling exponents are related by *different classes of linear bridge relations* to the equal-time multiscaling exponents. For a careful discussion of these issues we must of course define time-dependent structure functions. The details are given in Sec. 2.2 and Sec. 2.4.

The dynamic multiscaling of time-dependent structure functions described briefly above applies to statistically steady turbulence. Does it have an analogue in the case of decaying turbulence, since time-dependent structure functions must, in this case, depend on the origin of time t_0 at which we start our measurements? This question has not been addressed hitherto. We show here how to answer it in decaying fluid and passive-scalar turbulence [10]. In particular, we propose suitable normalisations of time-dependent structure functions that eliminate their dependence on t_0; we demonstrate this *analytically* for the Kraichnan version of the passive-scalar problem and its shell-model analogue and *numerically* for the GOY shell model [3, 24, 25] for fluids and a shell-model version of the advection-diffusion equation. In these models we then analyse the normalised time-dependent structure functions for the case of decaying turbulence like their statistically steady counterparts [8, 9]. This requires a generalisation of the multifractal formalism [3] that finally yields the same bridge relations between dynamic and equal-time multiscaling exponents as for statistically steady turbulence [8, 9]. For the Kraichnan version of the passive-scalar problem we show analytically that simple dynamic scaling is obtained. This is because (see Sec. 2.3) the advecting velocity is random and white in time. In addition, we find numerically for shell models of fluid and passive-scalar turbulence that dynamic-multiscaling exponents have the same values for both sta-

tistically steady and decaying turbulence; so, in this sense, we have *universality* of the multiscaling of time-dependent structure functions in turbulence. The equal-time analogue of this universality has been discussed in Ref.[26].

The remaining part of this Chapter is organized as follows. In Sec. 2.2 we introduce the models we use and give the details of our numerical simulations. Section 2.3 presents our analytical studies of decaying turbulence in the Kraichnan model and its shell-model analogue. Section 2.4 shows how to generalise the multifractal formalism to allow for time-dependent structure functions in decaying turbulence and how to obtain bridge relations between dynamic and equal-time multiscaling exponents in this case. In Sec. 2.5 we present the results of our numerical studies of dynamic multiscaling in the GOY shell model for fluid turbulence and for shell models of a passive-scalar field advected by a turbulent velocity field. Section 2.6 is devoted to a discussion of our results in the context of earlier studies; we also suggest possible experimental tests of our predictions.

2.2 Models and Numerical Simulations

We have used several models to study time-dependent structure functions in fluid and passive-scalar turbulence. These range from the Navier-Stokes and advection-diffusion equations to simple shell models; the latter are well-suited for our extensive numerical studies. It is useful to begin with a systematic description of these models.

Fluid flows are governed by the Navier-Stokes (NS) equation (2.4) for the velocity field $\mathbf{u}(\mathbf{x}, t)$ at point $\mathbf{x}$ and time t, augmented by the incompressibility constraint (2.5), since we restrict ourselves to low Mach numbers:

$$\partial_t \mathbf{u} + \mathbf{u}.\nabla \mathbf{u} = -\nabla P + \nu_0 \nabla^2 \mathbf{u} + \mathbf{f}; \qquad (2.4)$$

$$\nabla.\mathbf{u} = 0. \qquad (2.5)$$

Here v_0 is the kinematic viscosity, P the pressure, the density ρ is taken to be 1, and $\mathbf{f}$ the external force, which is absent when we consider decaying turbulence. If ℓ and v are, respectively, characteristic length and velocity scales of the flow, the Reynolds number $Re \equiv \frac{\ell v}{v_0}$ provides a dimensionless measure of the strength of the nonlinear term in (2.4) relative to the viscous term; for the case of decaying turbulence it is convenient to use the Reynolds number for the initial state, i.e., Re with v the root-mean-square (rms) velocity of the initial condition and ℓ the system size [the linear size of the simulation box in a direct numerical simulation (DNS)]. Given the incompressibility condition (2.5), the pressure can be eliminated from (2.4) and related to the velocity by a Poisson equation. The equation for the velocity alone is most easily written in terms of the spatial Fourier transform $\tilde{\mathbf{u}}(\mathbf{k}, t)$ of $\mathbf{u}(\mathbf{x}, t)$; and it can be shown easily that $\tilde{\mathbf{u}}(\mathbf{k}, t)$ is affected *directly* by all other Fourier modes. This is the mathematical representation of the sweeping effect in which the largest eddies (i.e., modes with small $k \equiv |\mathbf{k}|$) *directly* advect the smallest eddies (i.e., large-k modes); such direct sweeping lies at the heart of the Taylor hypothesis [27] and leads eventually to trivial dynamic scaling for time-dependent structure functions of Eulerian fields with a dynamic exponent $z^{\mathcal{E}} = 1$ for fluid turbulence.

As we have mentioned above, nontrivial dynamic multiscaling is expected if we use Lagrangian or quasi-Lagrangian velocities. The Lagrangian formulation is well known [28]; the quasi-Lagrangian [5, 22] one uses the following transformation for any Eulerian field $\psi(\mathbf{x}, t)$:

$$\hat{\psi}(\mathbf{x}, t) \equiv \psi[\mathbf{x} + \mathbf{R}(t; \mathbf{r_0}, 0), t], \tag{2.6}$$

where $\hat{\psi}$ is the quasi-Lagrangian field and $\mathbf{R}(t; \mathbf{r_0}, 0)$ is the position at time t of a Lagrangian particle that was at point $\mathbf{r_0}$ at time $t = 0$.

The advection-diffusion (AD) equation for the Eulerian passive-scalar field $\theta(\mathbf{x}, t)$ is

$$\frac{\partial \theta}{\partial t} + \mathbf{u}.\nabla\theta = \kappa\nabla^2\theta + f_\theta, \tag{2.7}$$

where κ is the passive-scalar diffusivity and, if we consider decaying passive-scalar turbulence, the external force f_θ is set to zero. The advecting velocity field $\mathbf{u}$ should be obtained, in principle, by solving equations (2.4) and (2.5). By using equation (2.6) we get the quasi-Lagrangian version of the advection-diffusion equation (2.7):

$$\frac{\partial\hat{\theta}(\mathbf{x}, t)}{\partial t} + [\hat{\mathbf{u}}(\mathbf{x}, t) - \hat{\mathbf{u}}(\mathbf{x}, 0)].\nabla\hat{\theta}(\mathbf{x}, t) = \kappa\nabla^2\hat{\theta}(\mathbf{x}, t) + \hat{f}_\theta(\mathbf{x}, t). \tag{2.8}$$

Direct numerical simulations of equations (2.4) and (2.5) or equation (2.7), though feasible, have not yet provided data that are averaged well enough to yield reliable *time-dependent* structure functions of quasi-Lagrangian velocity [23] or passive-scalar fields. Time-dependent Lagrangian structure functions have been obtained [21] only for order $p = 2$. Thus a first-principles DNS study of dynamic multiscaling in fluid or passive-scalar turbulence is not possible at the moment. However, significant progress has been made in statistically steady turbulence by studying dynamic multiscaling in simplified models like the Kraichnan model for passive-scalar turbulence and shell models for fluid and passive-scalar turbulence. We discuss these models below since our studies of decaying turbulence will be based on them.

2.2.1 The Kraichnan Model (Model A)

The Kraichnan model for passive-scalar turbulence [4, 16, 17, 18] begins with the advection-diffusion equation (2.7) but replaces the Navier-Stokes velocity field by one in which each component $u_i(\mathbf{x}, t)$ of the velocity is a zero-mean, delta-correlated, Gaussian random vari-

able with the covariance

$$\left\langle u_i(\mathbf{x}, t)u_j(\mathbf{x} + \mathbf{r}, t')\right\rangle = 2D_{ij}(\mathbf{r})\delta(t - t'). \tag{2.9}$$

The Fourier transform of $D_{ij}(\mathbf{r})$ has the form

$$\tilde{D}_{ij}(\mathbf{q}) \propto \left(q^2 + \frac{1}{L^2}\right)^{-(d+\xi)/2} e^{-\eta q^2}\left[\delta_{ij} - \frac{q_i q_j}{q^2}\right], \tag{2.10}$$

where $\mathbf{q}$ is the wave vector, L the characteristic large length scale, η_d the dissipation scale, and ξ a tunable parameter. In the limits $L \to \infty$ and $\eta_d \to 0$, of relevance to turbulence, we have, in real space,

$$D_{ij}(\mathbf{r}) = D^0\delta_{ij} - \frac{1}{2}d_{ij}(\mathbf{r}), \tag{2.11}$$

with

$$d_{ij} = D_1 r^\xi\left[(d - 1 + \xi)\delta_{ij} - \xi\frac{r_i r_j}{r^2}\right], \tag{2.12}$$

where $D^0 \sim C_1 L^\xi$; C_1 and D_1 are dimensional constants. We refer to (2.7-2.12) as Model A to distinguish it from other models that we use. For $0 < \xi < 2$, this model shows multiscaling of order-p, equal-time passive-scalar structure functions, as can be shown analytically, in certain limits [4]. However, for the case of statistically steady turbulence, this model exhibits simple dynamic scaling [8].

2.2.2 Shell Models

We will also use some shell models for fluid and passive-scalar turbulence. These models are highly simplified representations of the Navier-Stokes or the advection-diffusion equations (2.4-2.7) and are, therefore, far more tractable numerically than (2.4-2.7). Nevertheless, shell models retain enough properties of their parent equations to make them useful testing grounds for the multiscaling of structure functions in turbulence. Shell models are defined on a logarithmically discretised Fourier space in which complex scalar variables (e.g., the

velocity u_n or passive scalar θ_n) are associated with the shells n and scalar wave vectors $k_n = k_0 \lambda^n$; typically $\lambda = 2$, $k_0 = 1/16$; and the boundary conditions are that the shell variables vanish if $n < 1$ or $n > N$ (we use $N = 22$). These models consist of coupled, nonlinear, ordinary differential equations (ODEs) that specify the temporal evolution of the shell variables u_n and θ_n. Shell-model ODEs are similar to the Fourier-space versions of their parent partial differential equations: (a) their dissipative terms are linear in one of the shell variables and quadratic in k_n; (b) their analogues of advection terms are linear in k_n and bilinear in the shell variables; e.g., for fluid turbulence a representative term is of the form $i k_n u_n u_{n'}$, with $n \neq n'$; and (c) they conserve the shell-model analogues of the energy, helicity, etc., in the absence of dissipation and forcing. However, variables in a given shell are influenced directly only by their nearest- and next-nearest-neighbour shell variables; by contrast, Fourier transformations of the NS and the AD equations couple every Fourier mode to every other Fourier mode, leading to the sweeping effect mentioned above. Thus direct sweeping is absent in shell models, so they are often thought of as an approximate, quasi-Lagrangian representation of their parent equations.

For studies of decaying turbulence one can envisage several initial conditions. We have used initial conditions of two types: (a) in the first (Type-I) we drive the system to a statistically steady turbulent state by forcing the first shell ($n = 1$); we then turn off the force and allow the turbulent state and the associated energy spectrum to decay freely; our measurements are made in this decaying state; and (b) for the case of fluid turbulence we use a second initial condition (Type-II) in which all the energy is concentrated in the first few shells with small k_n, i.e., large length scales; we then allow the system to evolve without any force; the energy cascades to large values of k_n till the energy spectrum becomes similar to that in forced turbulence; this

spectrum then decays slowly in time and the measurements we report are made during this stage of evolution.

2.2.3 Model B

We use the shell-model analogue of the Kraichnan model introduced in [29] in which the equation for the passive-scalar variable θ_n is

$$\left[\frac{d}{dt} + \kappa k_n^2\right]\theta_n = \iota\left[a_n(\theta_{n+1}^* u_{n-1}^* - \theta_{n-1}^* u_{n+1}^*) + b_n(\theta_{n-1}^* u_{n-2}^* + \theta_{n-2}^* u_{n-1})\right.$$
$$\left. + c_n(\theta_{n+2}^* u_{n+1} + \theta_{n+1}^* u_{n+2}^*)\right] + f_n, \tag{2.13}$$

where the asterisks denote complex conjugation, $a_n = k_n/2$, $b_n = -k_{n-1}/2$, and $c_n = k_{n+1}/2$; f_n is an additive force that is used to drive the system to a steady state; the boundary conditions are $u_{-1} = u_0 = \theta_{-1} = \theta_0 = 0$; $u_{N+1} = u_{N+2} = \theta_{N+1} = \theta_{N+2} = 0$. The advecting velocity variables are taken to be zero-mean, white-in-time, Gaussian random complex variables with covariance

$$\langle u_n(t)u_m^*(t')\rangle = C_2 k_n^{-\xi}\delta_{mn}\delta(t - t'), \tag{2.14}$$

where C_2 is a dimensional constant. We refer to equations (2.13-2.14) as Model B.

In our numerical simulations of this model we first obtain a statistically steady turbulent state by forcing the first shell with a random, Gaussian, white-in-time force. The force is then switched off and measurements are made as the turbulence decays. We use a weak, order-one, Euler scheme to integrate the resulting Ito form [29] of (2.13) with an integration time step $\delta t = 2^{-24}$, diffusivity $\kappa = 2^{-14}$, and $\xi = 0.6$.

For such a passive-scalar shell model the order-p, equal-time, structure function and its exponent are defined via

$$S_p^\theta(k_n) \equiv \left\langle[\theta_n(t)\theta_n^*(t)]^{p/2}\right\rangle \sim k_n^{-\zeta_p^\theta}; \tag{2.15}$$

it is natural, therefore, to define the time-dependent version of $S_p^\theta(k_n)$ as follows:

$$F_p^\theta(k_n, t_0, t) \equiv \left\langle [\theta_n(t_0)\theta_n^*(t_0 + t)]^{p/2} \right\rangle. \tag{2.16}$$

The power-law dependence on the right-hand-side of (2.15) is obtained for k_n in the inertial range. In our numerical calculations we use extended self-similarity (ESS) to extract the exponent ratios $\zeta_p^\theta/\zeta_2^\theta$.

2.2.4 Model C

The most commonly used shell-model analogue of the NS equation is the GOY model [3, 24, 25]:

$$\left[\frac{d}{dt} + \nu k_n^2\right]u_n = \iota\left[a_n u_{n+1}u_{n+2} + b_n u_{n-1}u_{n+1} + c_n u_{n-1}u_{n-2}\right]^* + f_n. \tag{2.17}$$

The coefficients $a_n = k_n$, $b_n = -\delta k_{n-1}$, $c_n = -(1-\delta)k_{n-2}$ are chosen in a manner that conserves the shell-model analogues of energy and helicity in the inviscid, unforced limit; an external force f_n drives the system to a steady state. We use the standard value $\delta = 1/2$; the boundary conditions are $u_{-1} = u_0 = 0; u_{N+1} = u_{N+2} = 0$. We will refer to this as Model C.

We use two different kinds of initial conditions in our study of decaying fluid turbulence in this model. For Type-I initial conditions we first drive the system to a statistically steady turbulent state with an external force $f_n = (1 + \iota) \times 5 \times 10^{-3}\delta_{n,1}$. The force is then switched off and the shell velocities at this instant are taken as the initial condition. The turbulence then decays. Our structure-function measurements are made during this period of decay. To obtain the second type of initial condition, the energy is initially concentrated in the first few shells by choosing the following initial (superscript 0) velocities: $u_n^0 = k_n^{1/2}e^{\iota\vartheta_n}$, for $n = 1, 2$, and $u_n^0 = k_n^{1/2}e^{-k_n^2}e^{\iota\vartheta_n}$, for $3 \le n \le N$, with ϑ_n a random phase angle distributed uniformly between 0 and

2π. This energy then cascades down the inertial-range scales without significant dissipation until it reaches dissipation-range scales at cascade completion. The energy dissipation-rate per unit mass shows a peak, as a function of time, roughly at cascade completion [11, 30], and the energy spectrum $E(k)$ and the structure function (2.18) show well-developed inertial ranges. These decay very slowly in time, so at each instant exponents can be determined from plots of $E(k)$ and the structure functions. Therefore, for initial conditions of this type, we wait for cascade completion before making measurements of structure functions.

We employ the slaved, Adams-Bashforth scheme [31, 32] to integrate the GOY-model equations with a time step $\delta t = 10^{-4}$. In our numerical simulations the viscosity $\nu = 10^{-7}$ and the total number of shells $N = 22$; this provides us with a large inertial range from which exponents can be obtained reliably.

For this model, the order-p, equal-time structure function and its exponent are defined as follows:

$$S_p^u(k_n) \equiv \left\langle [u_n(t)u_n^*(t)]^{p/2} \right\rangle \sim k_n^{-\zeta_p^u}; \qquad (2.18)$$

the associated time-dependent structure function is

$$F_p^u(k_n, t_0, t) \equiv \left\langle [u_n(t_0)u_n^*(t_0 + t)]^{p/2} \right\rangle, \qquad (2.19)$$

where the power-law dependence on the right-hand-side of (2.18) holds for k_n in the inertial range. (For statistically steady turbulence, the time-dependent structure function has no dependence on t_0, so, without loss of generality, t_0 can be taken to be 0.) A direct determination of ζ_p^u from (2.18) is not very accurate because of an underlying 3-cycle in the static version of the GOY shell model [33]. The effects of this 3-cycle can be filtered out to a large extent by using the modified structure function

$$\Sigma_p^u(n) \equiv \left\langle |\Im[u_{n+2}u_{n+1}u_n - (1/4)u_{n-1}u_nu_{n+1}]|^{p/3} \right\rangle \sim k_n^{-\zeta_p^u}; \qquad (2.20)$$

we use $\Sigma_p^u(n)$ in our numerical calculation of ζ_p^u. We measure time in terms of the initial large eddy-turnover time $t_L \equiv 1/(u_{rms}k_1)$; the root-mean-square velocity $u_{rms} \equiv [\langle \sum_n |u_n^0|^2 \rangle]^{1/2}$.

2.2.5 Model D

A turbulent velocity field does not have the simple statistical properties assumed in Models A and B. To overcome this we study the shell model of Ref.[34], hereafter referred to as Model D, in which the advecting velocity u_n is a solution of the GOY shell model(2.71). The passive-scalar shell variables θ_n obey

$$\left[\frac{d}{dt} + \kappa k_n^2\right]\theta_n = \iota\left[a_n(\theta_{n+1}u_{n-1} - \theta_{n-1}u_{n+1}) + b_n(\theta_{n-1}u_{n-2} + \theta_{n-2}u_{n-1})\right.$$
$$\left. + c_n(\theta_{n+2}u_{n+1} + \theta_{n+1}u_{n+2})\right]^* + f_n, \tag{2.21}$$

where $a_n = k_n$, $b_n = -k_{n-1}/2$, and $c_n = -k_{n+1}/2$; $f_n = (1+\iota)\times 5\times 10^{-3}\delta_{n,1}$ is an additive force that drives the system to a steady state; the boundary conditions are $u_{-1} = u_0 = \theta_{-1} = \theta_0 = 0$; $u_{N+1} = u_{N+2} = \theta_{N+1} = \theta_{N+2} = 0$.

For this model we start with Type-I initial conditions, i.e., we force both the coupled equations (2.71) and (2.21) till a statistically steady turbulent state is obtained and then switch off the force. The shell variables at this instant of time are taken as the initial condition; and then the turbulence is allowed to decay.

We employ a second-order Adams-Bashforth scheme to integrate Model D with a time step $\delta t = 10^{-4}$ and set the diffusivity $\kappa = 5 \times 10^{-7}$ so the Schmidt number $\nu/\kappa = 1/5$; and $N = 22$ as in Model C. The definitions of structure functions for Model D are the same as those for Model B, i.e., equations (2.15) and (2.16). We limit the effects of the 3-cycle (mentioned above for Model C) in our numerical evaluations of ζ_p^θ by using the modified structure function

$$\Sigma_p^\theta(n) \equiv \left\langle |\Im[\theta_{n+2}\theta_{n+1}\theta_n - (1/4)\theta_{n-1}\theta_n\theta_{n+1}]|^{p/3} \right\rangle \sim k_n^{-\zeta_p^\theta}. \tag{2.22}$$

2.3   Analytical Results for Models A and B

In this *Section* we present our analytical results for time-dependent, passive-scalar structure functions for the Kraichnan model (Model A) and its shell-model analogue Model B. For Model A we obtain results for both Eulerian and quasi-Lagrangian structure functions. We find, in particular, that time-dependent structure functions for these models can be factorised into a part that depends on the time origin t_0 and a part that depends on t but is independent of t_0. This important result motivates a similar factorisation hypothesis that we propose, and verify numerically, for Models C and D in subsequent *Sections*.

2.3.1   Model A

Consider first the Eulerian version of the AD equation (2.7). We assume that a turbulent statistical steady state has been established because of an external force f_θ. We turn off this force at time 0. A spatial Fourier transform of (2.7) now yields

$$\frac{\partial \tilde{\theta}(\mathbf{k}, t)}{\partial t} = \iota \int k_j \tilde{u}_j(\mathbf{q}, t) \tilde{\theta}(\mathbf{k} - \mathbf{q}, t) d^d q - \kappa k_j k_j \tilde{\theta}(\mathbf{k}, t), \qquad (2.23)$$

where the tildes denote spatial Fourier transforms, we sum over repeated indices, and the statistics of $\tilde{u}_j(\mathbf{q}, t)$ are specified by equations (2.9) and (2.10). The Fourier-space, second-order correlation function $\tilde{\mathcal{F}}_2^\theta(\mathbf{k}, t_0, t) \equiv \langle \tilde{\theta}(-\mathbf{k}, t_0) \tilde{\theta}(\mathbf{k}, t_0 + t) \rangle$ ($t_0 \geq 0$ is any time origin) satisfies the equation

$$\frac{\partial \tilde{\mathcal{F}}_2^\theta(\mathbf{k}, t_0, t)}{\partial t} = \langle \tilde{\theta}(-\mathbf{k}, t_0) \frac{\partial \tilde{\theta}(\mathbf{k}, t_0 + t)}{\partial t} \rangle, \qquad (2.24)$$

which can be combined with (2.23) to get

$$\begin{aligned} \frac{\partial \tilde{\mathcal{F}}_2^\theta(\mathbf{k}, t_0, t)}{\partial t} = & \ \iota k_j \int \langle \tilde{\theta}(-\mathbf{k}, t_0) \tilde{u}_j(\mathbf{q}, t_0 + t) \tilde{\theta}(\mathbf{k} - \mathbf{q}, t_0 + t) \rangle d^3 q \\ & - \kappa k_j k_j \langle \tilde{\theta}(-\mathbf{k}, t_0) \tilde{\theta}(\mathbf{k}, t_0 + t) \rangle. \end{aligned} \qquad (2.25)$$

We average over the statistics of the advecting velocity field (2.9) by using Novikov's theorem [35]: e.g., the first term in (2.25) reduces to

$$\langle \tilde{\theta}(-\mathbf{k}, t_0) \tilde{u}_j(\mathbf{q}, t_0 + t) \tilde{\theta}(\mathbf{k} - \mathbf{q}, t_0 + t) \rangle =$$

$$\int_0^\infty dt' \left[\langle \tilde{u}_j(\mathbf{q}, t_0 + t) \tilde{u}_i(-\mathbf{q}, t') \rangle \langle \tilde{\theta}(-\mathbf{k}, t_0) \frac{\delta}{\delta \tilde{u}_i(-\mathbf{q}, t_0 + t')} \tilde{\theta}(\mathbf{k} - \mathbf{q}, t_0 + t') \rangle \right]. \quad (2.26)$$

Finally equations (2.9) and (2.23)-(24) yield

$$\frac{\partial \tilde{\mathcal{F}}_2^\theta(\mathbf{k}, t_0, t)}{\partial t} = -2k_i k_j \tilde{\mathcal{F}}_2^\theta(\mathbf{k}, t_0, t) \int_0^\infty d^d q \tilde{D}_{ij}(q). \quad (2.27)$$

Since $2 \int_0^\infty \tilde{D}_{ij} d^d q = D^0 \delta_{ij} \sim C_1 L^\xi$, where C_1 is a dimensional constant, in the limits $\kappa \to 0$, $\eta_d \to 0$, and $L \to \infty$ of relevance to turbulence, we get

$$\frac{\partial \mathcal{F}_2^\theta(r, t_0, t)}{\partial t} \sim C_1 L^\xi \frac{\partial^2 \mathcal{F}_2^\theta(r, t_0, t)}{\partial r^2}. \quad (2.28)$$

A spatial Fourier transform allows us to integrate this equation to obtain

$$\tilde{\mathcal{F}}_2^\theta(\mathbf{k}, t_0, t) \sim \varphi_2^\theta(k, t_0) \exp\left[-C_1 L^\xi k^2 t \right]. \quad (2.29)$$

If we set $t = 0$, we see that $\tilde{\mathcal{F}}_2^\theta(\mathbf{k}, t_0, 0)$ is just the passive-scalar, equal-time structure function; $\varphi_2^\theta(k, t_0)$ is, therefore, proportional to the Fourier transform of the passive-scalar equal-time structure function $\mathcal{S}_2^\theta(r)$. Thus, for a fixed but large value of L, we get, in the Eulerian framework, simple dynamic scaling with an exponent $z_2^\mathcal{E} = 2$. We note that we get an exponent which is not equal to unity (see Sec. 6.1) in this case because of the white-in-time nature of the advecting field.

The analogue of equation (2.28) for the second-order, quasi-Lagrangian structure function follows from [9] the quasi-Lagrangian form of the advection-diffusion equation (2.8).

$$\frac{\partial \mathcal{F}_2^{\hat{\theta}}(r, t_0, t)}{\partial t} = (D^0 \delta_{ij} - D_{ij}) \frac{\partial \mathcal{F}_2^{\hat{\theta}}(r, t_0, t)}{\partial r_i \partial r_j}$$

$$\sim d_{ij} \frac{\partial \mathcal{F}_2^{\hat{\theta}}(r, t_0, t)}{\partial r_i \partial r_j}. \quad (2.30)$$

By substituting for d_{ij} from (2.12) we obtain, for the isotropic case,

$$\frac{\partial \mathcal{F}_2^{\hat{\theta}}(r, t_0, t)}{\partial t} \sim D_1 r^{\xi} \frac{\partial^2 \mathcal{F}_2^{\hat{\theta}}(r, t_0, t)}{\partial r^2}. \tag{2.31}$$

A spatial Fourier transformation allows us to integrate this equation to obtain, in the limits $\kappa \to 0$, $\eta \to 0$, and $L \to \infty$,

$$\tilde{\mathcal{F}}_2^{\hat{\theta}}(\mathbf{k}, t_0, t) \sim \varphi_2^{\hat{\theta}}(k, t_0) \exp\left[-D_1 k^{2-\xi} t\right]. \tag{2.32}$$

$\varphi_2^{\hat{\theta}}(k, t_0)$ is now proportional to the Fourier transform of the equal-time, quasi-Lagrangian, passive-scalar structure function (which is, of course, the same as the equal-time, Eulerian, passive-scalar structure function). Equation (2.32) shows that, in the quasi-Lagrangian framework, $\tilde{\mathcal{F}}_2^{\hat{\theta}}(\mathbf{k}, t_0, t)$ factorises into a part that depends on t_0 and another which depends only on t. From the second factor we get simple dynamic scaling with an exponent $z_2 = 2 - \xi$, which is different from the Eulerian exponent $z_2^{\mathcal{E}} = 2$ for Model A. Such a factorisation should also follow for higher-order, time-dependent, structure functions as we show in the next subsection for Model B.

2.3.2   Model B

We can use the methods of the previous subsection to obtain analytical expressions for time-dependent structure functions for Model B. Consider first the second-order structure function

$$F_2^{\theta}(n, t_0, t) = \langle \theta_n(t_0) \theta_n^*(t_0 + t) \rangle, \tag{2.33}$$

whence

$$\frac{\partial F_2^{\theta}(n, t_0, t)}{\partial t} = \langle \theta_n(t_0) \frac{\partial \theta_n^*(t_0 + t)}{\partial t} \rangle; \tag{2.34}$$

the angular brackets denote an average over the statistics of $u_n(t)$ that are specified by equation (2.14). By using the complex conjugate of

(2.13) in (2.34) and Novikov's theorem we get terms of the form

$$
\begin{aligned}
\langle \theta_n(t_0)\theta_{n+1}^*(t_0 + t)u_{n-1}^*(t_0 + t)\rangle &= \langle u_{n-1}^*(t_0 + t)u_{n-1}(t_0 + t)\rangle \times \\
&\left\langle \frac{\delta}{\delta u_{n-1}(t_0 + t)}\theta_n(t_0)\theta_{n+1}^*(t_0 + t)\right\rangle.
\end{aligned} \tag{2.35}
$$

Finally by using (2.14) we obtain

$$
\frac{\partial F_2^\theta(n, t_0, t)}{\partial t} = -\frac{1}{4}C_2 k_n^{2-\xi} A(\xi) F_2^\theta(n, t_0, t), \tag{2.36}
$$

where C_2 is a dimensional constant. Integration now yields

$$
F_2^\theta(n, t_0, t) = \phi_2^\theta(n, t_0) \exp\left[-\frac{1}{4}C_2 k_n^{2-\xi} A(\xi)t\right], \tag{2.37}
$$

with $A(\xi) = (2^{(2\xi-2)} + 2^{-(2\xi-2)}) + (2^\xi + 2^{-\xi}) + (2^{(\xi-2)} + 2^{-(\xi-2)})$. Similarly, we obtain the following exact expression for the fourth-order structure function:

$$
F_4^\theta(n, t_0, t) = \phi_4^\theta(n, t_0) \exp\left[-\frac{1}{2}C_2 k_n^{2-\xi} A(\xi)t\right]. \tag{2.38}
$$

$\phi_2^\theta(n, t_0)$ and $\phi_4^\theta(n, t_0)$ are, respectively, the second- and fourth-order, equal-time, quasi-Lagrangian, passive-scalar structure functions. Thus $z_2 = z_4 = 2-\xi$, as for the quasi-Lagrangian structure functions of Model A. (Recall that we expect quasi-Lagrangian behaviour for shell models since they do not have a direct sweeping effect.) The equality of z_2 and z_4 indicates that we have simple dynamic scaling in Model B. We expect all the quasi-Lagrangian exponents z_p to be $2 - \xi$ for this model, but the analytical demonstration of this result becomes more and more complex with increasing p.

Given a factorisation of the form shown in (2.37), it is possible to normalise the time-dependent, passive-scalar structure function $F_p^\theta(n, t_0, t)$ by its value at $t = 0$ and thus make it independent of t_0. We cannot prove that such a factorisation exists in Models C and D, but we present compelling numerical evidence for it in Sec. 2.5.

2.4   Multifractal Formalism for Models C and D

Equal-time Eulerian and quasi-Lagrangian structure functions are the same for homogeneous and isotropic turbulence [36]. Since quasi-Lagrangian structure functions are required for our study of dynamic multiscaling, we present the multifractal formalism in terms of quasi-Lagrangian variables. Multiscaling in statistically steady fluid turbulence can be rationalised by using the multifractal formalism, which assumes that a turbulent flow has a continuous set of scaling exponents h in the set $\mathcal{I} \equiv (h_{min}, h_{max})$, instead of a single exponent (e.g., $h = 1/3$ yields simple K41 scaling) [3]. The scaling exponents h characterise the behaviour of velocity differences $\delta\hat{u}_r(\mathbf{x})$: For each $h \in \mathcal{I}$ there exists a set $\Sigma_h \subset \mathbb{R}^3$ of fractal dimension $\mathcal{D}^{\hat{u}}(h)$ and $\delta\hat{u}_r(\mathbf{x})/\hat{u}_L \sim (r/L)^h$ for separations r in the inertial range if $\mathbf{x} \in \Sigma_h$ and with $\hat{u}_L$ the velocity at the forcing scale L. Given the measure $d\mu(h)$ for the weights of the different values of h, the order-p, equal-time velocity structure function is

$$\frac{\mathcal{S}_p^{\hat{u}}(r)}{\hat{u}_L^p} \equiv \frac{\left\langle \delta\hat{u}_r^p(\mathbf{x}) \right\rangle}{\hat{u}_L^p} \sim \int_{\mathcal{I}} d\mu(h)(\frac{r}{L})^{ph+3-\mathcal{D}^{\hat{u}}(h)}, \tag{2.39}$$

where the ph term comes from p factors of $(r/L)^h$ and the additional factor of $(r/L)^{3-\mathcal{D}^{\hat{u}}(h)}$ is the probability of being within a distance $\sim r$ of the set Σ_h, of dimension $\mathcal{D}^{\hat{u}}(h)$, which is embedded in three dimensions. $\mathcal{D}^{\hat{u}}(h)$, h_{min}, and h_{max} are assumed to be universal. In the limit $r/L \to 0$, of relevance to fully developed turbulence, we get the equal-time scaling exponent $\zeta_p^{\hat{u}} = \inf_h[ph + 3 - \mathcal{D}^{\hat{u}}(h)]$ by the method of steepest descents.

We now define the order-p, time-dependent, quasi-Lagrangian velocity structure function

$$\mathcal{F}_p^{\hat{u}}(r, \{t_1, \ldots, t_p\}) \equiv \left\langle [\delta\hat{u}_\parallel(\mathbf{x}, r, t_1) \ldots \delta\hat{u}_\parallel(\mathbf{x}, r, t_p)] \right\rangle. \tag{2.40}$$

For simplicity, we consider $t_1 = t$ and $t_2 = \ldots = t_p = 0$, denote the structure function by $\mathcal{F}_p^{\hat{u}}(r, t)$, and suppress the subscript $\parallel$, i.e., we use

$\delta \hat{u}_r(\mathbf{x}) \equiv \delta \hat{u}_{\parallel}(\mathbf{x}, r, t_1)$. The natural extension of the multifractal formalism to the case of time-dependent structure functions in statistically steady fluid turbulence follows from the *Ansatz* [8]

$$\frac{\mathcal{F}_p^{\hat{u}}(r, t)}{\hat{u}_L^p} \propto \int_I d\mu(h) \left(\frac{r}{L}\right)^{3+ph-\mathcal{D}^{\hat{u}}(h)} \mathcal{G}^{p,h}\left(\frac{t}{\tau_{p,h}}\right), \tag{2.41}$$

where the scaling function $\mathcal{G}^{p,h}\left(\frac{t}{\tau_{p,h}}\right)$ is assumed to have a characteristic decay time $\tau_{p,h} \sim r/\delta \hat{u}_r(\mathbf{x}) \sim r^{1-h}$ and $\mathcal{G}^{p,h}(0) = 1$.

For statistically steady passive-scalar turbulence the application of the multifractal formalism is more complicated than it is for fluid turbulence. This is because we must now deal with a joint multifractal distribution of both the velocity and passive-scalar variables. Therefore, the order-(p, p'), equal-time structure function for passive-scalar turbulence

$$S_{p,p'}^{\hat{\theta},\hat{u}}(r) \equiv \langle \delta \hat{\theta}_r^p(\mathbf{x}) \delta \hat{u}_r^{p'}(\mathbf{x}) \rangle \tag{2.42}$$

has the multifractal representation

$$\frac{S_{p,p'}^{\hat{\theta},\hat{u}}(r)}{\hat{\theta}_L^p \hat{u}_L^{p'}} \propto \int_{I,I'} d\mu(h, g) \left(\frac{r}{L}\right)^{3+pg+p'h-\mathcal{D}^{\hat{u},\hat{\theta}}(h,g)}, \tag{2.43}$$

where $\hat{u}$ and $\hat{\theta}$ are assumed to possess a range of universal scaling exponents $h \in \mathcal{I} \equiv (h_{min}, h_{max})$ and $g \in \mathcal{I}' \equiv (g_{min}, g_{max})$, respectively. For each pair of h and g in these ranges, there exists a set $\Sigma_{h,g} \subset \mathbb{R}^3$ of fractal dimension $\mathcal{D}^{\hat{u},\hat{\theta}}(h, g)$. The increments in the velocity $\delta \hat{u}_r(\mathbf{x})$ and the passive-scalar field $\delta \hat{\theta}_r(\mathbf{x})$ scale as $\delta \hat{u}_r(\mathbf{x})/\hat{u}_L \sim (r/L)^h$ and $\delta \hat{\theta}_r(\mathbf{x})/\hat{\theta}_L \sim (r/L)^g$ for separations r in the inertial range if $\mathbf{x} \in \Sigma_{h,g}$. $\hat{u}_L$ and $\hat{\theta}_L$ are, respectively, the velocity and the passive-scalar variables at the forcing scale L. For simplicity we will only consider passive-scalar structure functions with $p' = 0$ in equation (2.42), i.e.,

$$S_p^{\hat{\theta}}(r) \equiv \langle \delta \hat{\theta}_r^p(\mathbf{x}) \rangle, \tag{2.44}$$

which have the multifractal representation

$$\frac{\mathcal{S}_p^{\hat{\theta}}(r)}{\hat{\theta}_L^p} \propto \int_{\mathcal{I}\mathcal{I}'} d\mu(h,g) \left(\frac{r}{L}\right)^{3+pg-\mathcal{D}^{\hat{u},\hat{\theta}}(h,g)} ; \tag{2.45}$$

as before, the equal-time exponents $\zeta_p^{\hat{\theta}}$ can be related to $\mathcal{D}^{\hat{u},\hat{\theta}}(h,g)$ by the method of steepest descents. The corresponding order-p, time-dependent passive-scalar structure function is

$$\mathcal{F}_p^{\hat{\theta}}(r, \{t_1, \dots, t_p\}) \equiv \langle [\delta\hat{\theta}(\mathbf{x}, r, t_1) \dots \delta\hat{\theta}(\mathbf{x}, r, t_p)] \rangle. \tag{2.46}$$

As in (2.40), we consider $t_1 = t$ and $t_2 = \dots = t_p = 0$ for simplicity. Given the nature of multiscaling in passive scalars advected by a turbulent velocity field, it is possible to understand passive-scalar turbulence within the framework of the multifractal formalism. However, the analogous expression for time-dependent structure functions in passive-scalar turbulence has to take into account the multifractal nature of the advecting velocity field [9]. We generalise the multifractal representation of time-dependent structure functions in the following way:

$$\frac{\mathcal{F}_p^{\hat{\theta}}(r, t)}{\hat{\theta}_L^p} \propto \int_{\mathcal{I}, \mathcal{I}'} d\mu(h,g) \left(\frac{r}{L}\right)^{3+pg-\mathcal{D}^{\hat{u},\hat{\theta}}(h,g)} \mathcal{G}^{p,h,g}\left(\frac{t}{\tau_{phg}}\right); \tag{2.47}$$

and we assume that (a) the function $\mathcal{G}^{p,h,g}(\frac{t}{\tau_{phg}})$ has a characteristic decay time τ_{phg}, (b) $\mathcal{G}^{p,h,g}(0) = 1$, and (c) that the dominant contribution to τ_{phg}, in the limits $\kappa \to 0$, $\eta_d \to 0$ and $L \to \infty$, has the following scaling form

$$\tau_{phg} \sim r/\delta\hat{u}_r(\mathbf{x}) \sim r^{1-h}. \tag{2.48}$$

Given $\mathcal{F}_p^{\hat{u}}(r, t)$ and $\mathcal{F}_p^{\hat{\theta}}(r, t)$, we define the order-$p$, degree-$M$, integral-($I$) and derivative-($D$) times as follows [8, 9] (if the integrals and derivatives in equations (3.13) and (2.50) exist):

$$\mathcal{T}_{p,M}^{I,\hat{\phi}}(r) \equiv \left[\frac{1}{\mathcal{S}_p^{\hat{\phi}}(r)} \int_0^\infty \mathcal{F}_p^{\hat{\phi}}(r, t) t^{(M-1)} dt\right]^{(1/M)} \tag{2.49}$$

and

$$\mathcal{T}_{p,M}^{D,\hat{\phi}}(r) \equiv \left[\frac{1}{\mathcal{S}_p^{\hat{\phi}}(r)}\frac{\partial^M \mathcal{F}_p^{\hat{\phi}}(r,t)}{\partial t^M}\bigg|_{t=0}\right]^{(-1/M)}, \tag{2.50}$$

respectively, with $\hat{\phi}$ either $\hat{u}$ or $\hat{\theta}$. For statistically steady turbulence we can then use the dynamic-multiscaling *Ansatz* to define the integral- and derivative-time multiscaling exponents for fluid turbulence $z_{p,M}^{I,\hat{u}}$ and $z_{p,M}^{D,\hat{u}}$ via

$$\mathcal{T}_{p,M}^{I,\hat{u}}(r) \sim r^{z_{p,M}^{I,\hat{u}}} \tag{2.51}$$

and

$$\mathcal{T}_{p,M}^{D,\hat{u}}(r) \sim r^{z_{p,M}^{D,\hat{u}}}, \tag{2.52}$$

respectively, for r in the inertial range.

By substituting the multifractal form (2.41) in (2.51), evaluating the time integral first, and then performing the integration over the multifractal measure by the saddle-point method, we obtain the *integral* bridge relations

$$z_{p,M}^{I,\hat{u}} = 1 + \left[\zeta_{p-M}^{\hat{u}} - \zeta_p^{\hat{u}}\right]/M, \tag{2.53}$$

which were first obtained in [5]. Similarly we get the *derivative* bridge relations

$$z_{p,M}^{D,\hat{u}} = 1 + \left[\zeta_p^{\hat{u}} - \zeta_{p+M}^{\hat{u}}\right]/M, \tag{2.54}$$

which were first obtained in forced Burgers turbulence [37, 38] for the special cases (a) $p = 2$, $M = 1$ and (b) $p = 2$, $M = 2$, respectively, and for statistically steady fluid turbulence in [8]. We note that within the K41 phenomenology ($\zeta_p^{u,K41} = p/3$) the bridge relations yield the same dynamic exponent $z_p^{K41} = 2/3$ for both integral- and derivative-time scales.

For passive-scalars advected by a turbulent velocity field, the corresponding dynamic-multiscaling exponents are defined via

$$\mathcal{T}_{p,M}^{I,\hat{\theta}}(r) \sim r^{z_{p,M}^{I,\hat{\theta}}} \tag{2.55}$$

and

$$\mathcal{T}_{p,M}^{D,\hat{\theta}}(r) \sim r^{z_{p,M}^{D,\hat{\theta}}}. \tag{2.56}$$

To obtain bridge relations for dynamic-multiscaling exponents in statistically steady passive-scalar turbulence we define the degree-M, order-p *integral*-time for this case:

$$\mathcal{T}_{p,1}^{I,\hat{\theta}}(r) \equiv \left[\frac{1}{\mathcal{S}_p^{\hat{\theta}}(r)} \int_{I,I'} d\mu(h,g) \left(\frac{r}{L}\right)^Z \tau_{p,g,h}^M \int_0^\infty \mathcal{G}^{p,h,g} \left(\frac{t}{\tau_{pgh}}\right)^{M-1} d\left(\frac{t}{\tau_{pgh}}\right) \right]^{1/M}, \tag{2.57}$$

where $Z = 3 + pg - \mathcal{D}^{\hat{u},\hat{\theta}}(h,g)$ and the argument of the scaling function is suppressed for notational convenience. By using the scaling form of τ_{pgh} (2.48) and assuming, as in Ref.[34], that

$$\langle \delta\hat{\theta}^p \delta\hat{u}^{-q} \rangle \approx \langle \delta\hat{\theta}^p \rangle \langle \delta\hat{u}^{-q} \rangle, \tag{2.58}$$

we get

$$\mathcal{T}_{p,1}^{I,\hat{\theta}}(r) \sim \left[\frac{r^M}{\mathcal{S}_p^{\hat{\theta}}(r)} \langle \delta\hat{\theta}^p \rangle \langle \delta\hat{u}^{-M} \rangle \right]^{1/M}. \tag{2.59}$$

Thus the degree-M, order-p, integral-time, dynamic-multiscaling exponent $z_{p,1}^{I,\hat{\theta}} = 1 + \zeta_{-M}^{\hat{u}}/M$.

Similarly we obtain the degree-M, order-p *derivative* time scale for passive-scalars by substituting for $\mathcal{F}_p^{\hat{\theta}}$ from (2.47) in (2.50) and using (2.48) and (2.58):

$$
\begin{aligned}
\mathcal{T}_{p,M}^{D,\hat{\theta}}(r) &= \left[\frac{1}{\mathcal{S}_p^{\hat{\theta}}(r)} \int_{I,I'} d\mu(h,g) \left(\frac{r}{L}\right)^Z \left(\left.\frac{\partial^M}{\partial t^M}\mathcal{G}^{p,h,g}\right|_{t=0}\right) \frac{1}{\tau_{pgh}^M} \right]^{-1/M} \\
&\sim \left[\frac{1}{\mathcal{S}_p^{\hat{\theta}}(r)} \int_{I,I'} d\mu(h,g) \left(\frac{r}{L}\right)^Z \left(\left.\frac{\partial^M}{\partial t^M}\mathcal{G}^{p,h,g}\right|_{t=0}\right) \frac{[\delta\hat{u}(r)]^M}{r^M} \right]^{-1/M} \\
&\sim \left[\frac{1}{r^M \mathcal{S}_p^{\hat{\theta}}(r)} \left\langle \delta\hat{u}^M(r)\delta\hat{\theta}^p(r) \right\rangle \right]^{-1/M} \\
&\sim \left[\frac{1}{r^M \mathcal{S}_p^{\hat{\theta}}(r)} \left\langle \delta\hat{u}^M(r) \right\rangle \left\langle \delta\hat{\theta}^p(r) \right\rangle \right]^{-1/M} \\
&\sim r^{1-\zeta_M^{\hat{u}}/M},
\end{aligned} \tag{2.60}
$$

which, along with (2.56), yields the bridge relation $z_{p,M}^{D,\hat{\theta}} = 1 - \zeta_M^{\hat{u}}/M$.
To summarise, the bridge-relations for degree-M, order-p, derivative-
and integral-time dynamic-multiscaling exponents are, respectively:

$$z_{p,M}^{I,\hat{\theta}} = 1 + \frac{\zeta_{-M}^{\hat{u}}}{M}; \quad z_{p,M}^{D,\hat{\theta}} = 1 - \frac{\zeta_M^{\hat{u}}}{M}. \tag{2.61}$$

Note that, in contrast to the bridge relations (3.18) and (3.18), there is
no p-dependence on the right-hand sides of these relations. However
the M-dependence is the signature of nontrivial dynamic multiscaling
here. Furthermore, the integral scale bridge relation is meaningful
only for those values of M for which $\zeta_{-M}^{\hat{u}}$ is well defined [9]. We now
extend our discussion to the the case of decaying turbulence and de-
fine the order-p, time-dependent quasi-Lagrangian velocity structure
function (for fluid turbulence) and passive-scalar structure function
(for passive-scalar turbulence) as

$$\mathcal{F}_p^{\hat{u}}(r, \{t_1, \ldots, t_p\}) \equiv \left\langle [\delta\hat{u}_\parallel(\mathbf{x}, r, t_1) \ldots \delta\hat{u}_\parallel(\mathbf{x}, r, t_p)] \right\rangle \tag{2.62}$$

and

$$\mathcal{F}_p^{\hat{\theta}}(r, \{t_1, \ldots, t_p\}) \equiv \langle [\delta\hat{\theta}(\mathbf{x}, r, t_1) \ldots \delta\hat{\theta}(\mathbf{x}, r, t_p)] \rangle, \tag{2.63}$$

respectively. For simplicity, we consider the case $t_1 = t_0 + t$ and $t_2 =
\ldots = t_p = t_0$. The derivations of the bridge relations we have given
above go through if we *assume* the following multifractal forms for
time-dependent velocity and passive-scalar structure functions, re-
spectively, in decaying turbulence:

$$\frac{\mathcal{F}_p^{\hat{u}}(r, t_0, t)}{\hat{u}_L^p} \propto A^{\hat{u}}(r, t_0) \int_{\mathcal{I}} d\mu(h) \left(\frac{r}{L}\right)^{3+ph-\mathcal{D}^{\hat{u}}(h)} \mathcal{G}^{p,h}\left(\frac{t}{\tau_{p,h}}\right); \tag{2.64}$$

and

$$\frac{\mathcal{F}_p^{\hat{\theta}}(r, t_0, t)}{\hat{\theta}_L^p} \propto A^{\hat{\theta}}(r, t_0) \int_{\mathcal{I}, \mathcal{I}'} d\mu(h, g) \left(\frac{r}{L}\right)^{3+pg-\mathcal{D}^{\hat{u},\hat{\theta}}(h,g)} \mathcal{G}^{p,h,g}\left(\frac{t}{\tau_{pgh}}\right); \tag{2.65}$$

i.e., we assume that the multifractal form factorises into a part $A^{\hat{u}}(r, t_0)$
[or $A^{\hat{\theta}}(r, t_0)$ in the case of passive scalars], which depends on the origin

of time t_0, and an integral that is independent of t_0. This assumption is motivated by the factorisation we have seen in Sec. 2.3 above in (2.32), (2.37), and (2.38) for time-dependent passive-scalar structure functions in Models A and B. [The analogous expressions for equal-time structure functions in decaying turbulence are obtained by setting $t = 0$ in (2.64) and (2.65).] Given (2.64) and (2.65), the integral-and derivative-time scales for decaying turbulence become *independent* of t_0 and assume forms identical to (3.13) and (2.50); consequently the bridge relations (3.18), (3.18) and (2.61) remain unaltered in decaying turbulence.

In the next *Section* we give compelling numerical evidence in support of our assumptions (2.64) and (2.65).

2.5 Numerical Results

We now present our numerical results for dynamic multiscaling in decaying, homogeneous, isotropic turbulence in Models B,C, and D in Secs. 2.5.1, 2.5.2, and 2.5.3, respectively. We show *en passant* that, for Models B and D, equal-time multiscaling exponents are universal in the sense that the exponents obtained from decaying-turbulence runs are equal (within error bars) to the exponents for statistically steady turbulence in these models [8, 29, 34]. The underlying reason for this universality for passive-scalar turbulence has been discussed earlier [39, 40], but we believe that ours is the first numerical demonstration of such universality in these models. Since we use shell models in this *Section*, we replace $\hat{u}$ and $\hat{\theta}$ by u and θ, respectively.

2.5.1 Model B

Let us begin with the equal-time exponents ζ_p^θ for the case of decaying turbulence in Model B. As in Ref. [29], we use the extended-self-similarity (ESS) procedure to obtain exponent ratios from log-log plots

[Fig. (2.1)] of the equal-time structure functions $S_p^\theta(k_n)$ versus $S_2^\theta(k_n)$. In particular, the slopes of the linear regions of the plots in Fig. (2.1), with $4 \leq n \leq 12$, yield the inertial-range exponent ratios $\zeta_p^\theta / \zeta_2^\theta$. From 50 such statistically independent runs (each run, in turn, is averaged over 5000 independent initial conditions) we calculate the means of the equal-time multiscaling exponent ratios $\zeta_p^\theta / \zeta_2^\theta$; these are plotted in Fig. (2.2) as functions of the order p for $1 \leq p \leq 8$. The standard deviations of these exponent ratios (calculated from our 50 runs) provide us with error bars; these are smaller than the symbol sizes used in Fig. (2.2). Our exponents ratios are in agreement (within the error bars) with earlier results for equal-time exponents for statistically steady passive-scalar turbulence in Model B [9, 29]. We have also determined the exponent ζ_2^θ directly from log-log plots of $\Sigma_2^\theta(k_n)$ versus k_n [equation (2.22)]. We find $\zeta_2^\theta = 1.403 \pm 0.003$; this agrees well with the analytical prediction [29, 41] $\zeta_2^\theta = 2 - \xi$, since we use $\xi = 0.6$ in our simulations.

We begin the discussion of our numerical results for time-dependent, passive-scalar structure functions in decaying turbulence by comparing our analytical result (2.37) with data from our simulations of Model B. In Fig. (2.3) we show the agreement between the two. The error bars have been calculated as in the the case of equal-time multiscaling exponents: The data we present are the means of the values obtained from 50 different statistically independent runs; and the standard deviations of these values yield the error bars. Here and henceforth time is scaled by the large-eddy-turnover time t_L. Given the exponential decays of time-dependent passive-scalar structure functions in Models A and B [equations (2.32) and (2.37)], we can extract a *unique* time scale from plots like the one in Fig. (2.4). Thus we do not expect time-dependent structure functions to exhibit dynamic multiscaling in Models A and B. In particular, equation (2.37) implies $T_2^\theta(k_n) = [1/4k_n^{2-\xi}A(\xi)]^{-1}$ whence $z_2 = 2 - \xi$. For our choice of $\xi = 0.6$
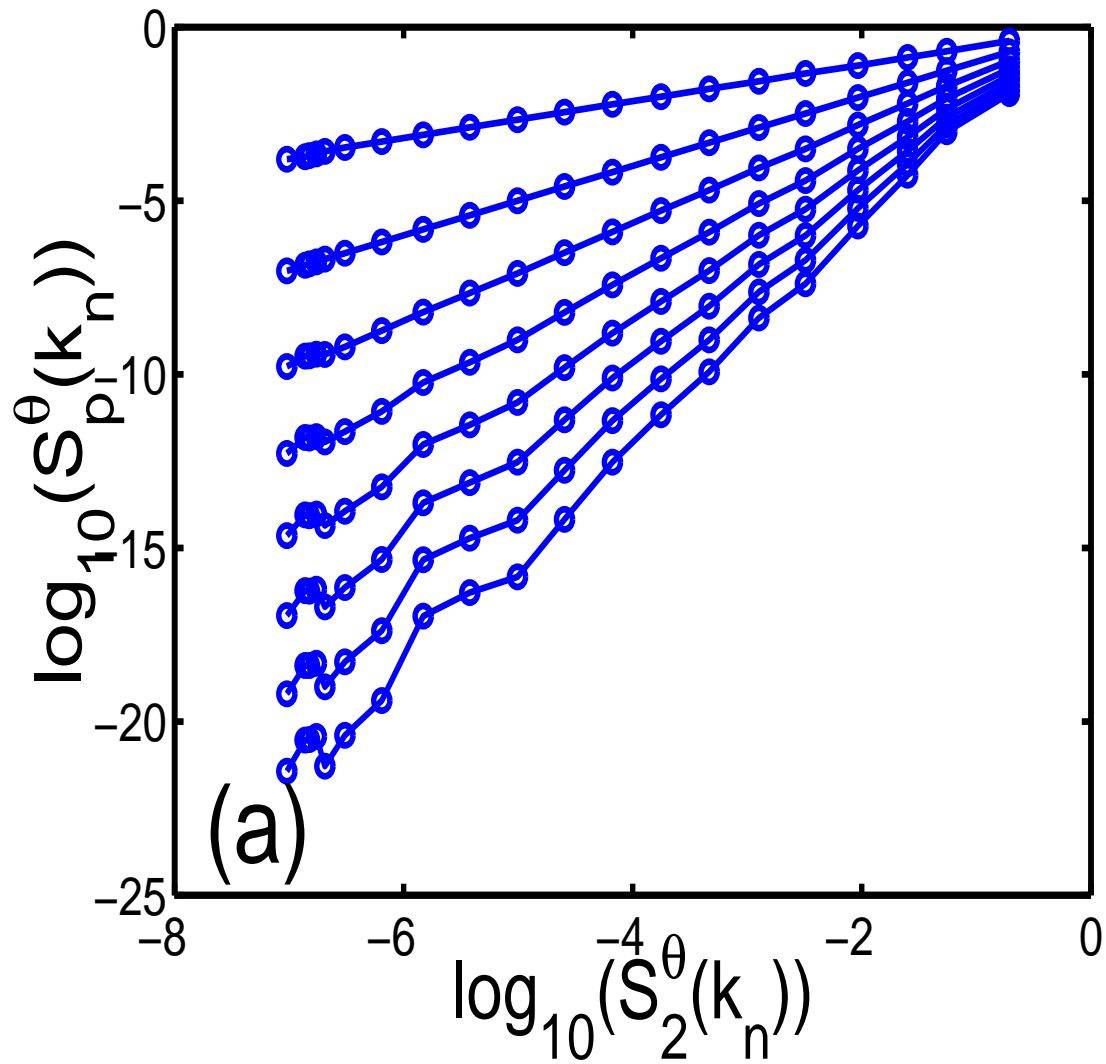
Figure 2.1: Log-log plots of the order-p structure functions $S_p^\theta(k_n)$ versus the second-order structure function $S_2^\theta(k_n)$ from our numerical simulations of Model B for $p = 1$ (uppermost curve) to $p = 8$ (lowermost curve).
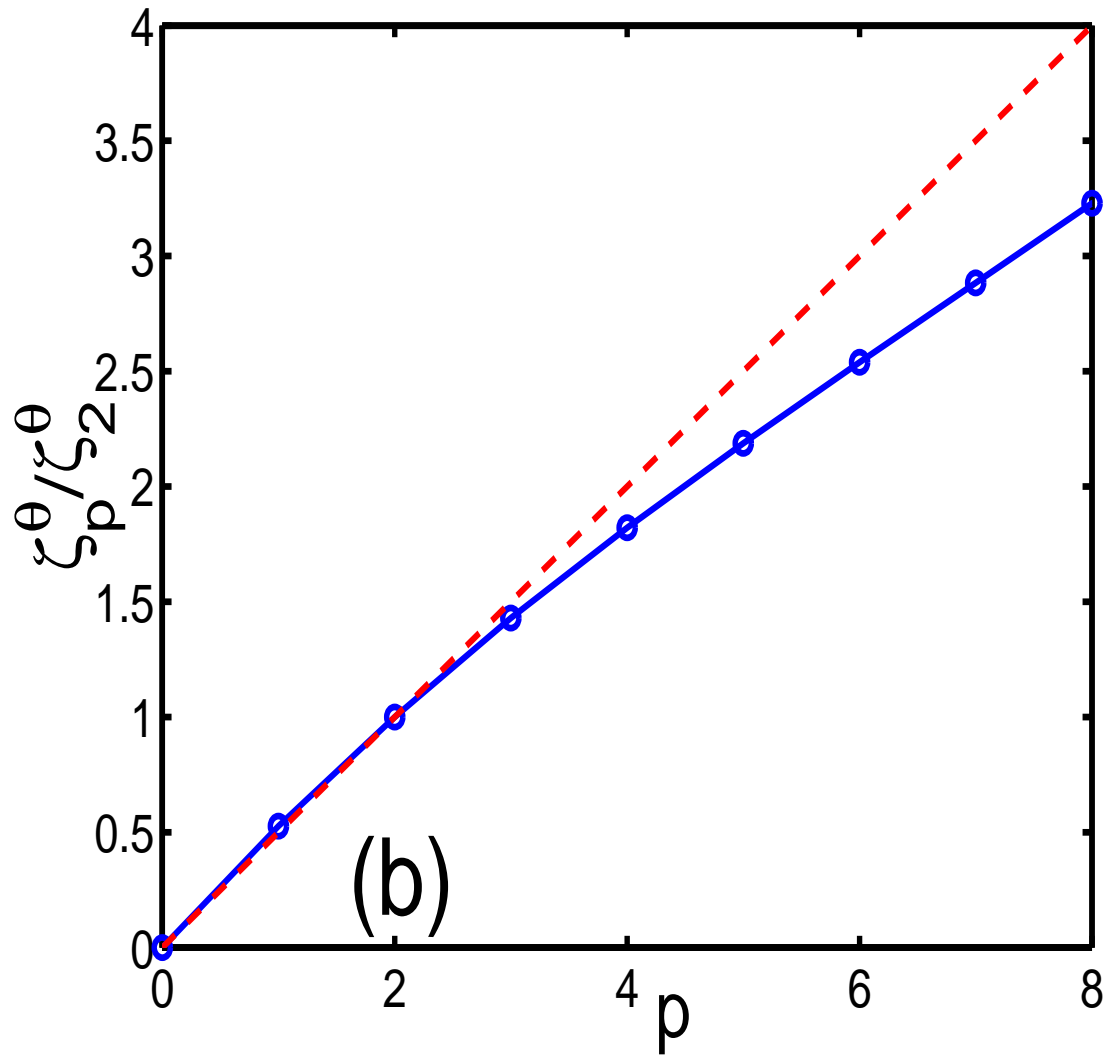
Figure 2.2: Plot of the exponent ratios $\zeta_p^\theta/\zeta_2^\theta$, obtained from the slopes of the linear, inertial region in (a), versus p. Our data points ($\circ$) are connected by a line to guide the eye; the error bars are smaller than the sizes of our symbols; the dashed straight line corresponds to the analogue of the K41 scaling prediction for this case.

we should, therefore, obtain $z_2 = 1.4$, and indeed our numerical simulations yield $z_2 = 1.398 \pm 0.003$ [Fig. (2.4)]. To demonstrate numerically that higher-order time-dependent structure functions also have a dynamic scaling exponent equal to z_2, as shown in Sec. 2.3.2 for the fourth-order time-dependent structure function, we show in Figs. (2.5) and (2.6) our numerical results for the third- and fourth-order time-dependent structure functions versus t/t_L for $6 \leq n \leq 13$ from which we extract $T_3^\theta(k_n)$ and $T_4^\theta(k_n)$, respectively. The insets show log-log plots of these times versus k_n; the slopes of these plots yield the dynamic-scaling exponents $z_3 = 1.398 \pm 0.003$ and $z_4 = 1.402 \pm 0.005$ in agreement with our expectation $z_p = 2 - \xi$, for all p, since $\xi = 0.6$ in our calculations.

2.5.2 Model C

The equality of equal-time exponents for decaying and statistically steady fluid turbulence was demonstrated numerically for the Sabra shell model in Ref. [26]. We have carried out a similar exercise for the GOY shell model of fluid turbulence and found, unsurprisingly, that the universality of equal-time multiscaling exponents holds for the GOY model as well. Furthermore, we have also checked that a replacement of the viscous term $\nu_0 k_n^2$ in equation (2.71) by the hyperviscous term $\nu_\alpha k_n^2 (k_n/k_d)^\alpha$ does not affect these exponents [2].

We investigate now whether time-dependent velocity structure functions in decaying fluid turbulence show a factorisation similar to (2.32) and (2.37) for Models A and B. Let us normalise the order-p, time-dependent structure function by its value at $t = 0$:

$$Q_p^u(n, t) \equiv \frac{F_p^u(k_n, t_0, t)}{F_p^u(k_n, t_0, 0)}; \tag{2.66}$$

to examine the dependence of $Q_p^u(n, t)$ on t_0. We give, in Figure (2.7), representative plots of $Q_2^u(n = 9, t)$ and $Q_4^u(n = 5, t)$ versus t/t_L for 6
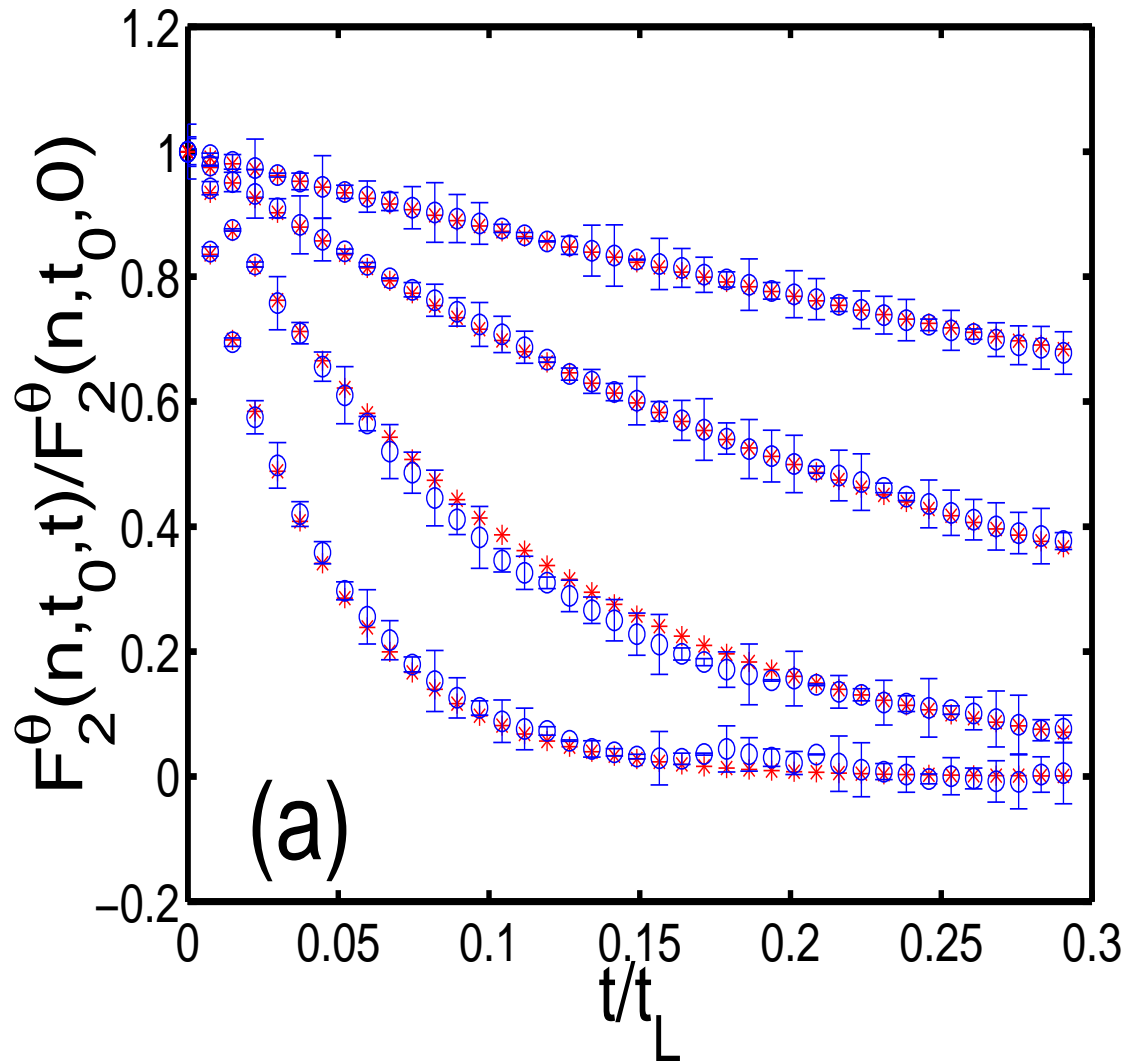
Figure 2.3: Plots comparing the normalised, second-order, time-dependent structure function versus the dimensionless time t/t_L from our numerical simulations (o) of Model B with our analytical expression (2.37) (*). For clarity we show data for four shells, from $n = 6$ (uppermost) to $n = 9$ (lowermost). The error bars on our numerical simulations are shown as vertical lines on the data points.
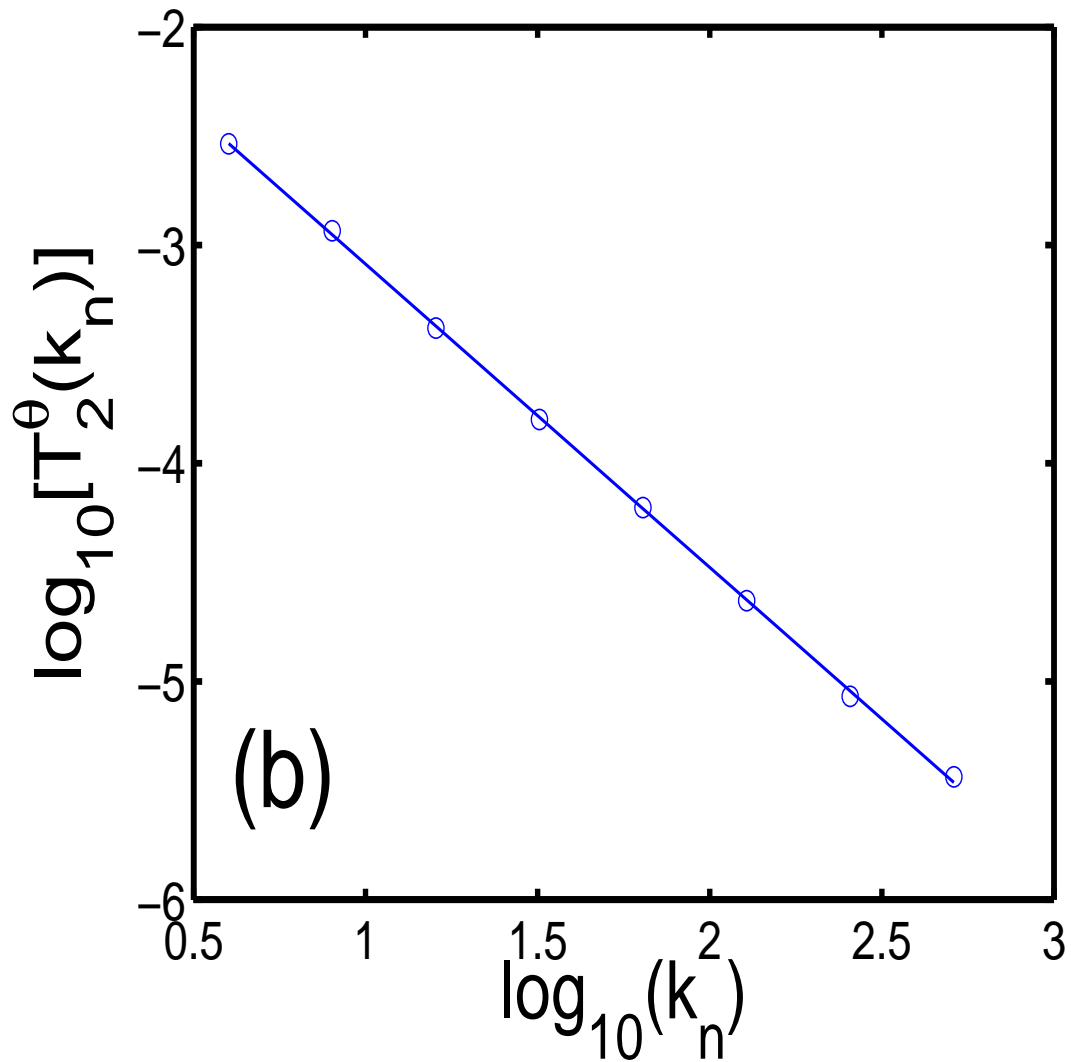
Figure 2.4: A log-log plot of $T_2^\theta(k_n)$ versus k_n. The slope of this plot gives the dynamic scaling exponent $z_2 = 1.398 \pm 0.003$. Our result from numerical simulations agree well with the analytical result $z_2 = 2 - \xi$, since we have chosen $\xi = 0.6$.
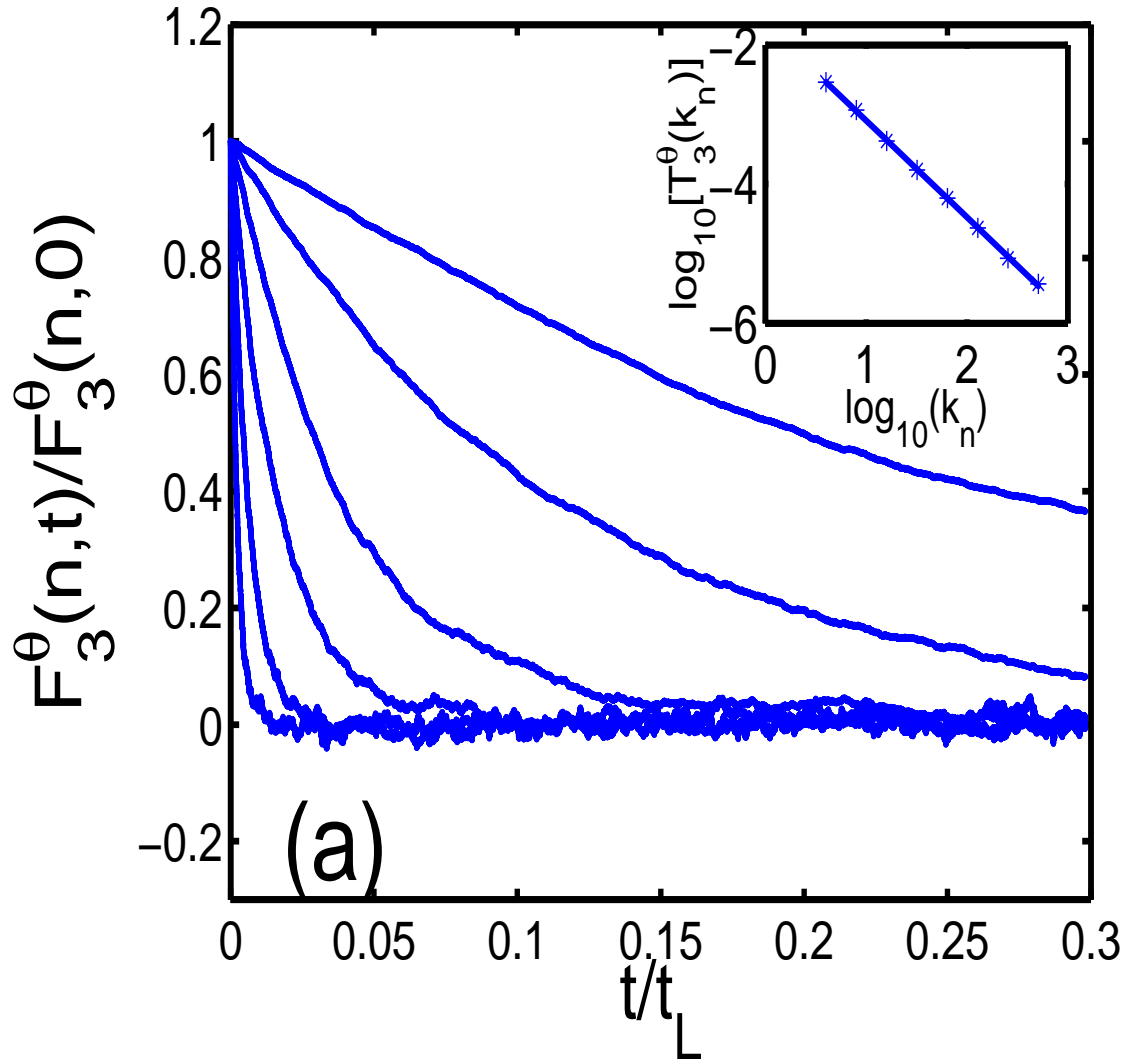
Figure 2.5: Representative plots of the normalised, third-order time-dependent structure function versus the dimensionless time t/t_L from our numerical simulations of Model B for shell numbers $n = 6$ (uppermost) to $n = 11$ (lowermost). The inset shows a log-log plot of $T_3^\theta(k_n)$ versus k_n. The slope of this plot gives the dynamic scaling exponent $z_3 = 1.398 \pm 0.003$.
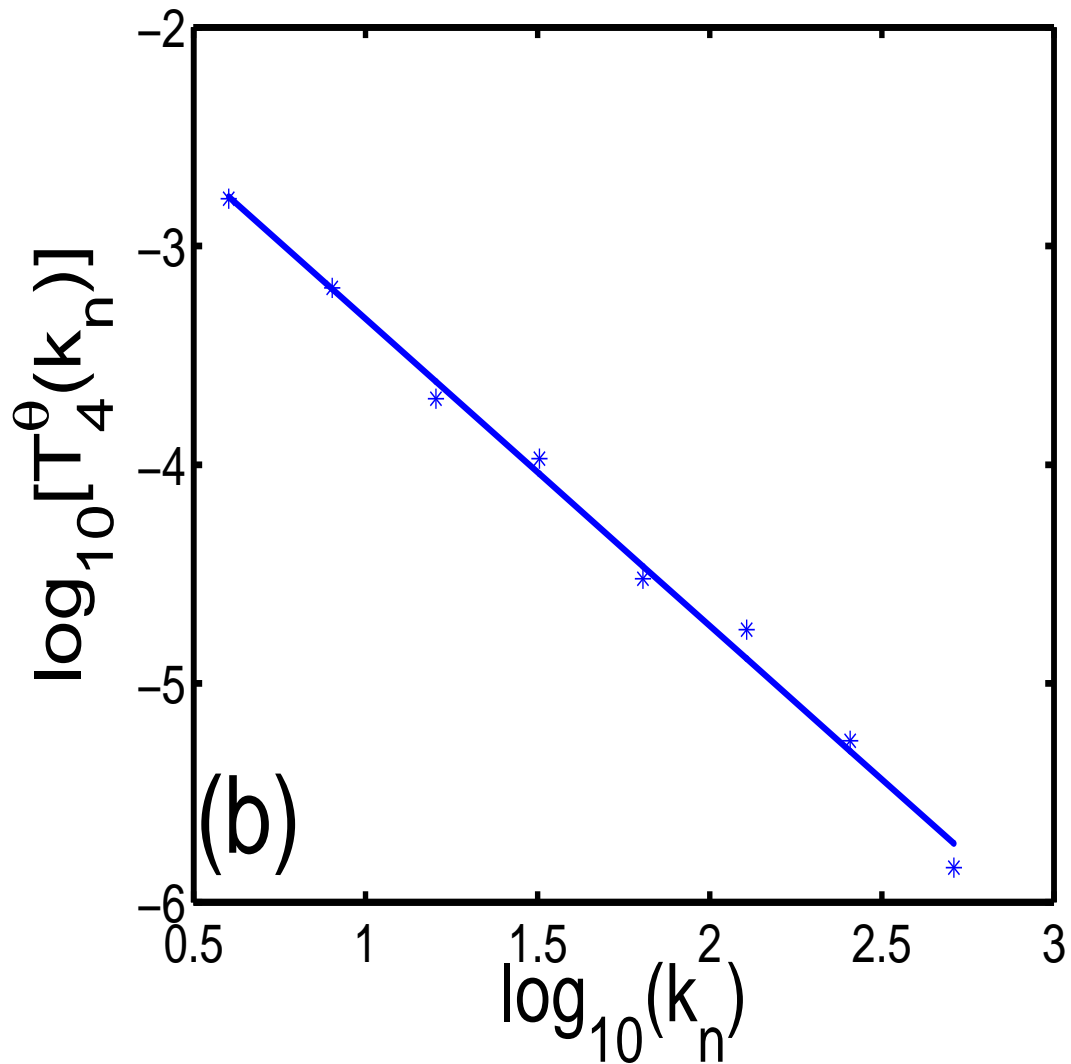
Figure 2.6: A log-log plot of $T_4^\theta(k_n)$ versus k_n. The slope of this plot gives the time-dependent scaling exponent $z_4 = 1.402 \pm 0.005$. Our result from numerical simulations agree well with the analytical result $z_2 = z_4 = 2 - \xi$, since we have chosen $\xi = 0.6$.

different time origins t_0; succesive values of t_0 are separated from each other by $0.5t_L$. To the extent that the symbols for different values of t_0 overlap, our results show that $Q_p^u(n, t)$ is independent of t_0 (so we have not included t_0 as an argument of Q_p^u), i.e., $F_p^u(k_n, t_0, t)$ factorises into a part that depends on t_0 and another that does not [cf., (2.32) and (2.37) for the simple, linear Models A and B]. Clearly the dynamic-multiscaling exponents extracted from $Q_p^u(n, t)$ cannot depend on t_0.

Furthermore, these exponents are the same as their counterparts for statistically steady, forced turbulence. We illustrate this in Fig. (2.8) by comparing our numerical results for the normalised, time-dependent structure function $F_4^f(k_n, t)/S_4^u(k_n)$, for statistically steady, forced (superscript f) turbulence, and $Q_4^u(n, t)$. [To obtain a statistical steady state for the GOY shell model we use the external force $f_n = (1 + \iota) \times 5 \times 10^{-3} \delta_{n,1}$.] We have checked explicitly, for $1 \leq p \leq 6$, that $Q_p^u(n, t)$ and $F_p^f(k_n, t)/S_p^u(k_n)$ agree within our error bars. Hence we propose the following factorisation that relates the time-dependent structure functions for decaying and statistically steady (superscript f) turbulence,

$$F_p^u(k_n, t_0, t) = A_p(k_n, t_0)F_p^f(k_n, t), \qquad (2.67)$$

with all the t_0 dependence on the right-hand side in the coefficient function A_p. If we now use the multifractal form for F_p^f suggested in [8], we obtain the shell-model analogue of equation (2.64).

We calculate the integral- and the derivative-time scales and their associated exponents $z_{p,1}^{I,u}$ and $z_{p,2}^{D,u}$. The counterparts of equations (3.13), for $M = 1$, and (2.50), for $M = 2$, for the GOY model are :

$$T_{p,1}^{I,u}(n) = \int_0^{t_\mu} Q_p^u(n, t)dt; \qquad (2.68)$$

$$T_{p,2}^{D,u}(n) = \left[\frac{d^2 Q_p^u(n, t)}{dt^2} \bigg|_{t=0} \right]^{-1/2}; \qquad (2.69)$$

here t_μ is the time at which $Q_p^u(n, t) = \mu$, with $0 \leq \mu \leq 1$. In principle we should use $\mu = 0$, i.e., $t_\mu = \infty$, but this is not possible in any numerical
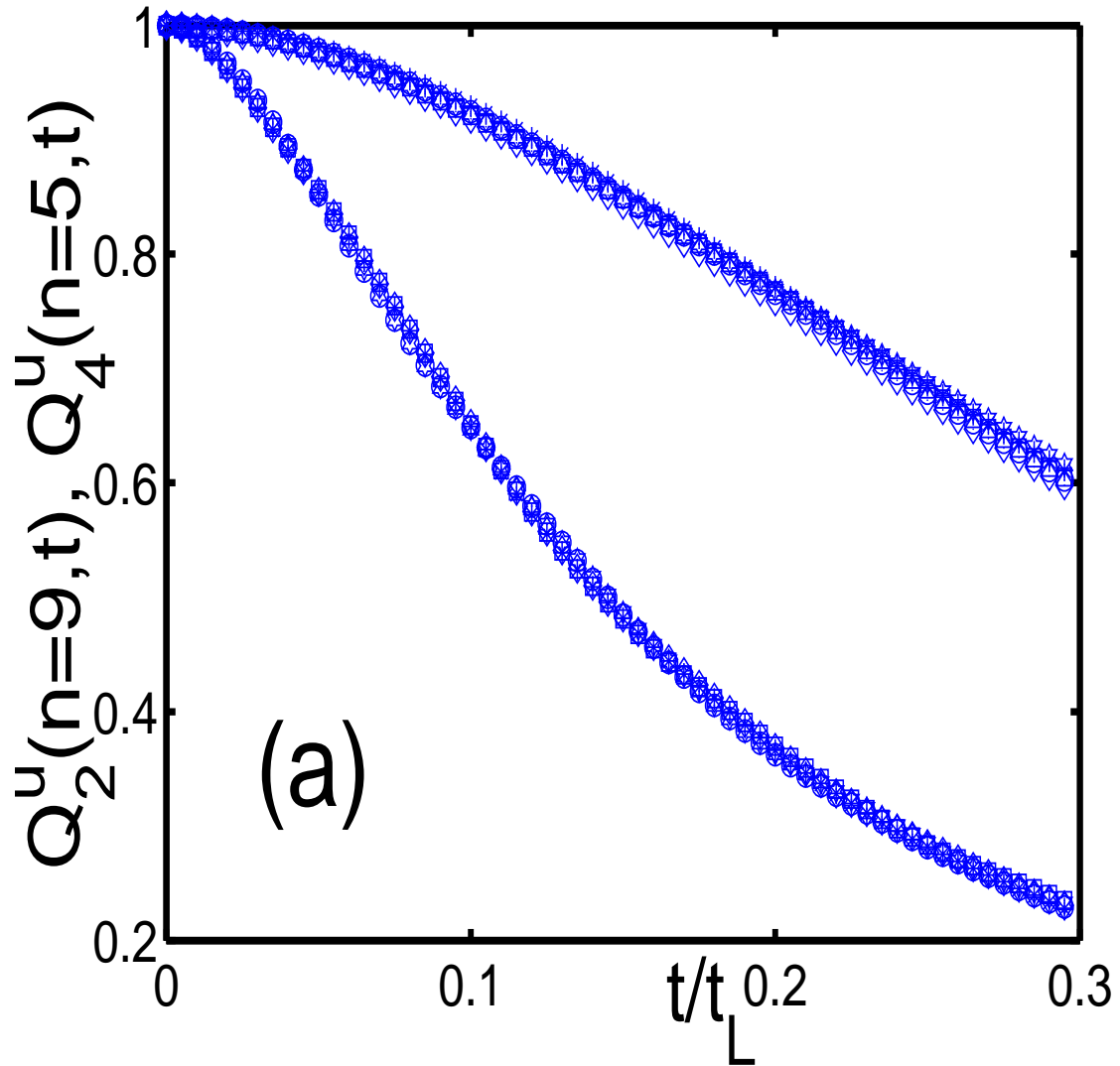
Figure 2.7: Representative plots of $Q_p^u(n,t)$ versus the dimensionless time t/t_L, for $p=2$, $n=9$ (lower curve) and $p=4$, $n=5$ (upper curve), and 6 different time-origins t_0 in decaying fluid turbulence for Model C. Successive time origins are separated by $0.5t_L$. The different symbols for the different sets of data for the different time-origins are indistinguishable; this is compelling numerical evidence for our proposed factorised form of the time-dependent structure functions.
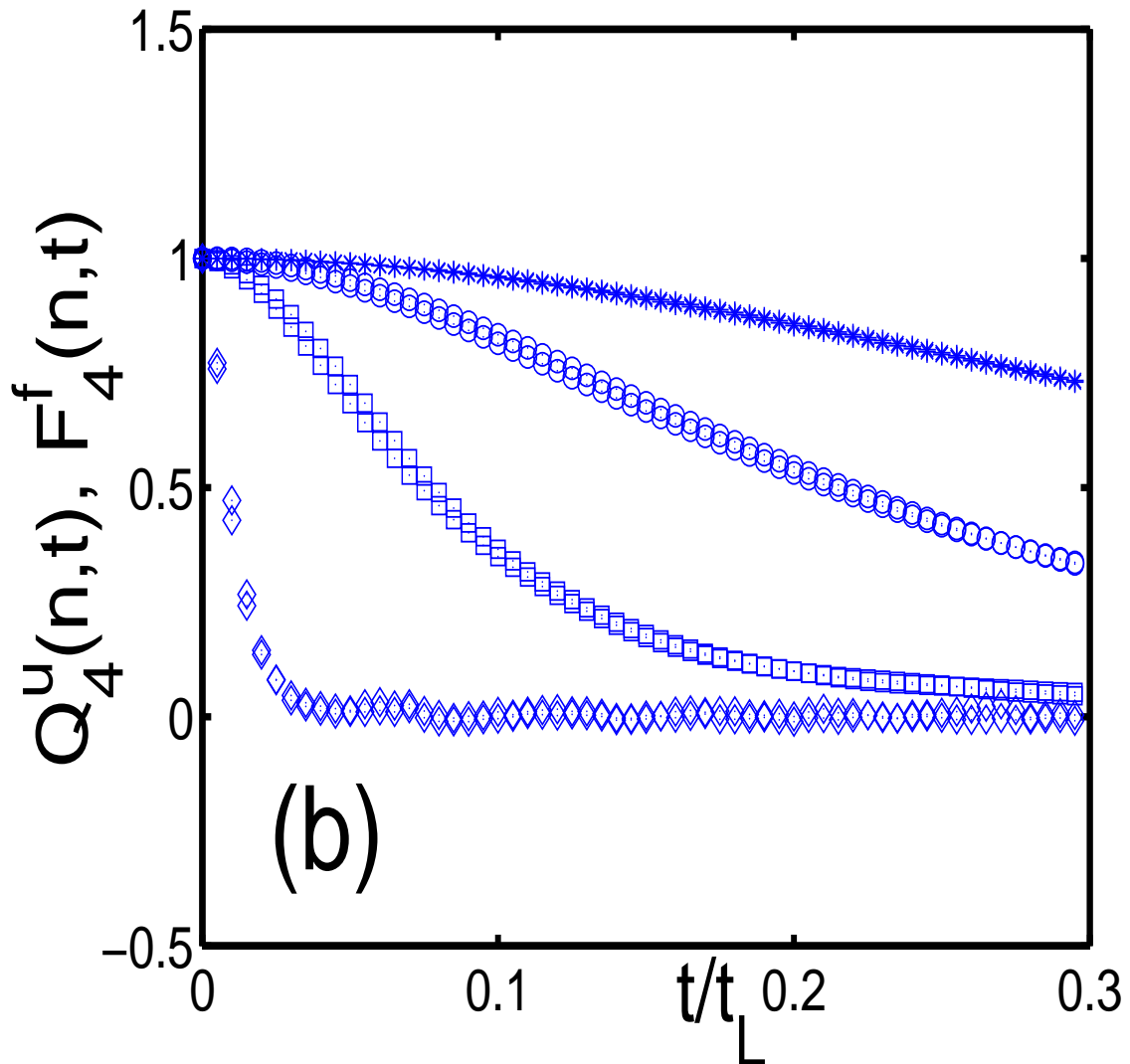
Figure 2.8: Plots of $Q_4^u(k_n, t)$ and $F_4^f(k_n, t)$ as a function of t/t_L to numerically test our proposed *Ansatz* (2.67) decaying turbulence in Model C. Results are shown only for shells $n = 4$ (uppermost curve), 6, 8, and 12 (lowermost curve) for clarity.

calculation since Q_p^u cannot be obtained accurately for large t. We use $\mu = 0.6$; and we have checked in representative cases that our results do not change for $0.3 < \mu < 0.7$. To compute $T_{p,2}^{D,u}(n)$ we use a centred, finite-difference, sixth-order scheme. Slopes of log-log plots of $T_{p,1}^{I,u}(n)$ and $T_{p,2}^{D,u}(n)$ versus k_n ($4 \leq n \leq 14$) give us $z_{p,1}^{I,u}$ (Fig 2.13) and $z_{p,2}^{D,u}$ (Fig 2.14), respectively.

Our results for equal-time and dynamic-multiscaling exponents for the GOY model (for both types of initial conditions) are given in Tables 1 and 2, respectively. We compute the multiscaling exponents for equal-time and time-dependent structure functions for 50 different cases. Tables 1 and 2 list the means of these values and their standard deviations yield the error bars. By comparing columns 2 of Tables 1 and 2 with column 2 of Table II in Ref. [8] we confirm, for the GOY model, the *weak* version of universality [26], i.e., the equal-time exponents ζ_p^u are the same for both decaying and statistically steady turbulence. Furthermore, our exponents for the GOY shell model agree with those presented in Ref. [26] for the Sabra shell model.

A comparison of the remaining columns of Tables 1 and 2 with their counterparts in Table II of Ref. [8] shows that this weak universality also applies to dynamic multiscaling exponents. Moreover, our direct numerical results for $z_{p,1}^{I,u}$ and $z_{p,2}^{D,u}$ (columns 4 and 6 in Tables 1 and 2) agree with the bridge-relation values of these exponents (columns 3 and 5 in Tables 1 and 2) that follow from equations (3.18) and (3.18) and ζ_p^u (columns 2 of Tables 1 and 2). Note that the agreement between corresponding entries in Tables 1 and 2 shows that our results are insensitive to the type of initial conditions we use. Finally, if we compare these Tables with Table II in Ref. [8], we find that our dynamic-multiscaling exponents for *decaying*, homogeneous, isotropic turbulence agree with their counterparts for the *statistically steady* case. Pictorial comparisons of the data in Tables 1 and 2 and the results of Ref. [8] are shown in Figs. (2.15) and (2.16) for integral-time
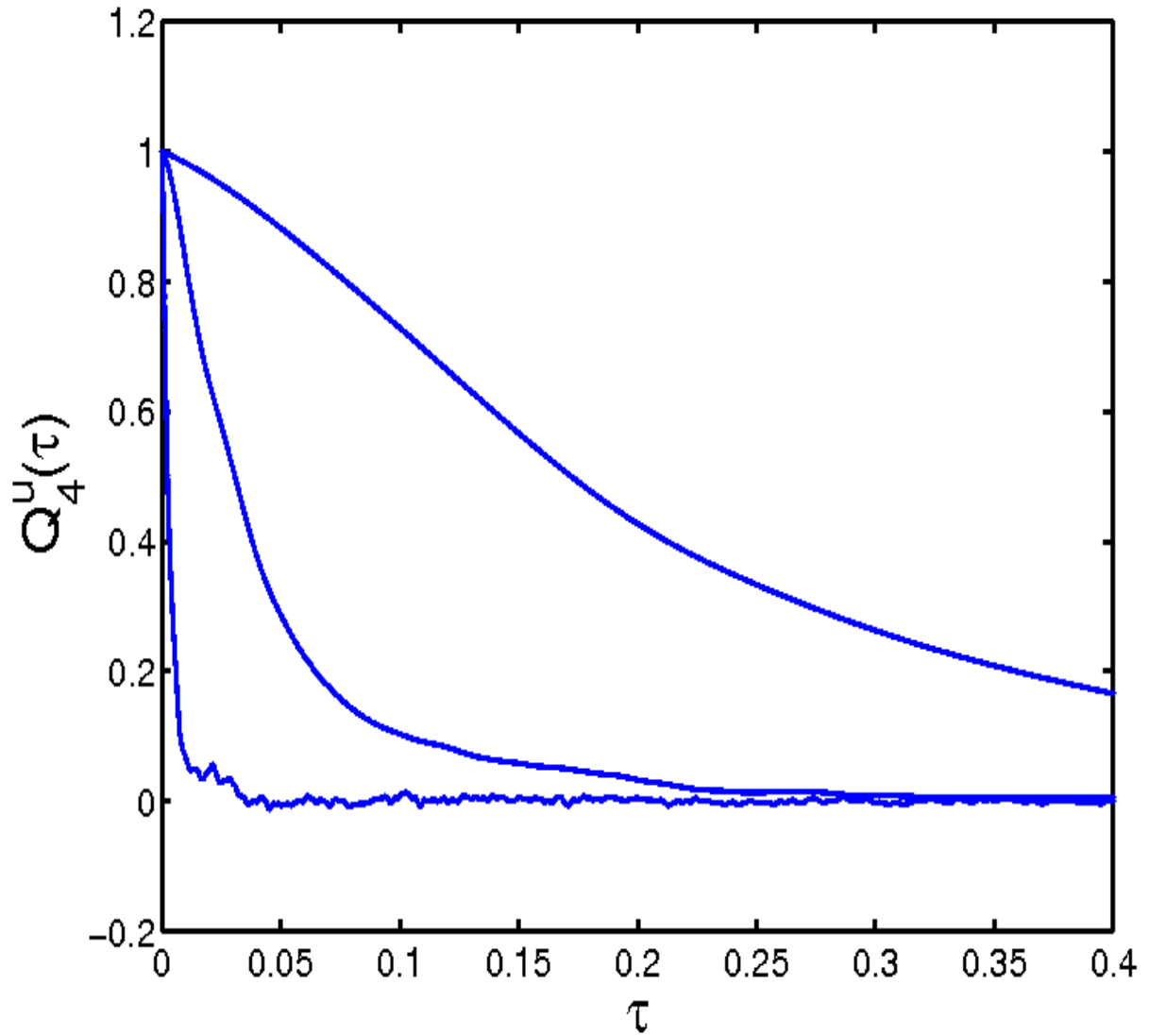
Figure 2.9: A representative plot of the normalised fourth order time-dependent structure function versus the dimensionless time τ obtained from the GOY shell model. The plots are for shells 4, 6, and 8 (from top to bottom).
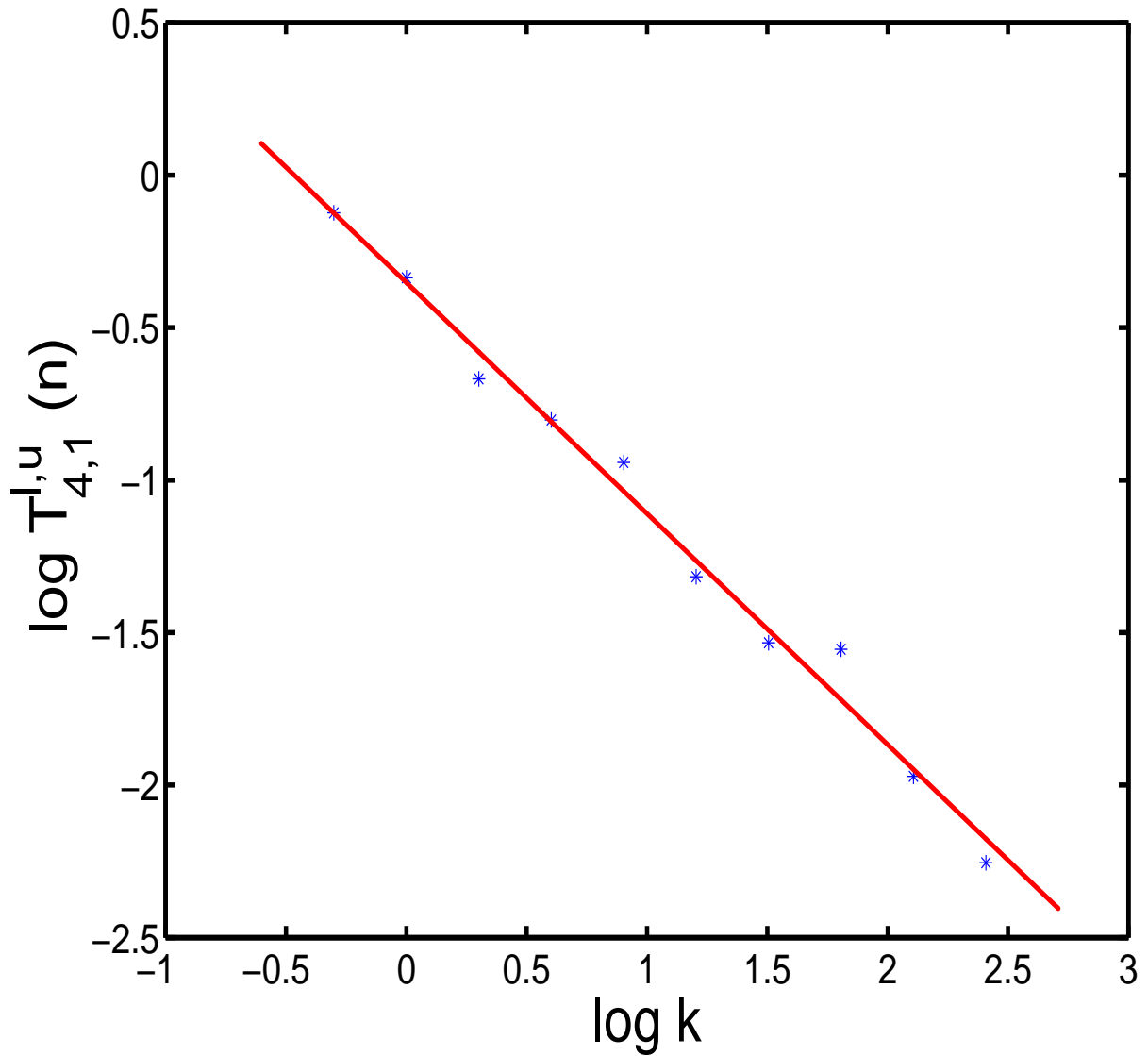
Figure 2.10: A log-log plot of $T_{4,1}^{I,u}(n)$ versus k (for convenience, we have dropped the subscript n in the label of the x-axis in the figure); a linear fit gives the dynamic mulstiscaling exponent $z_{4,1}^{I,u}$.
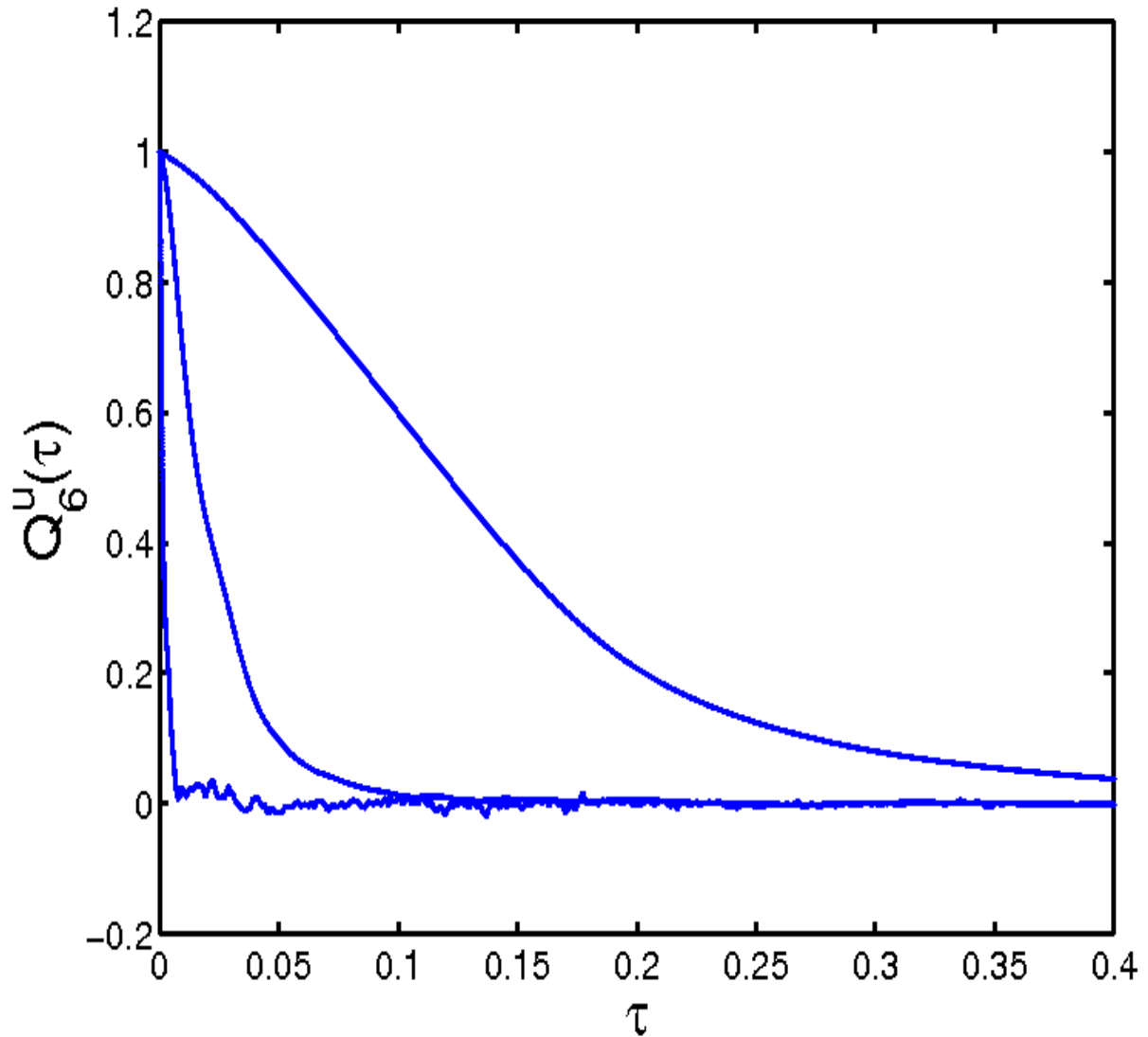
Figure 2.11: A representative plot of the normalised sixth order time-dependent structure function versus the dimensionless time τ obtained from the GOY shell model. The plots are for shells 4, 6, and 8 (from top to bottom).
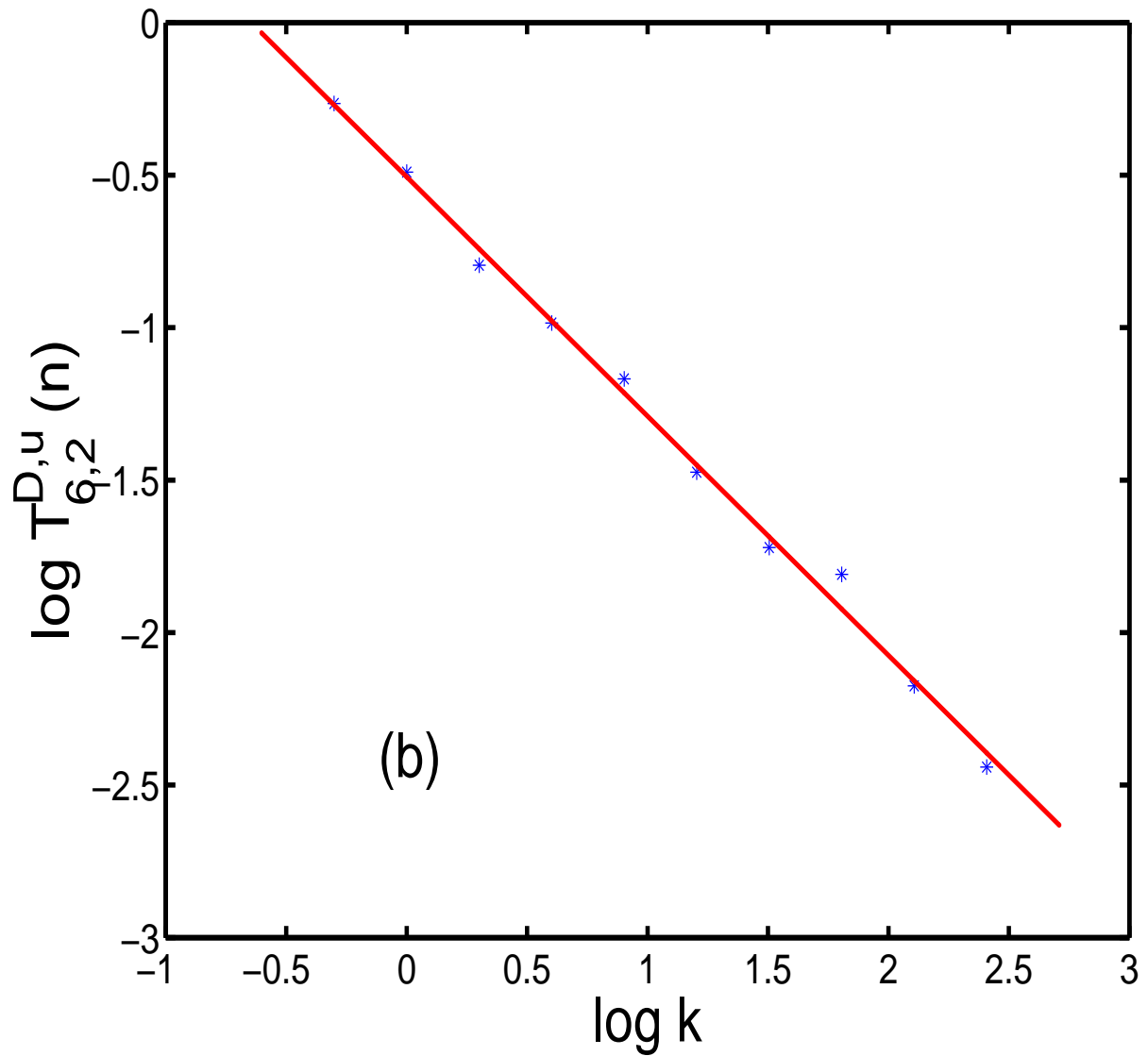
Figure 2.12: A log-log plot of $T_{6,2}^{D,u}(n)$ versus k (for convenience, we have dropped the subscript n in the label of the x-axis in the figure); a linear fit gives the dynamic multiscaling exponent $z_{6,2}^{D,u}$.
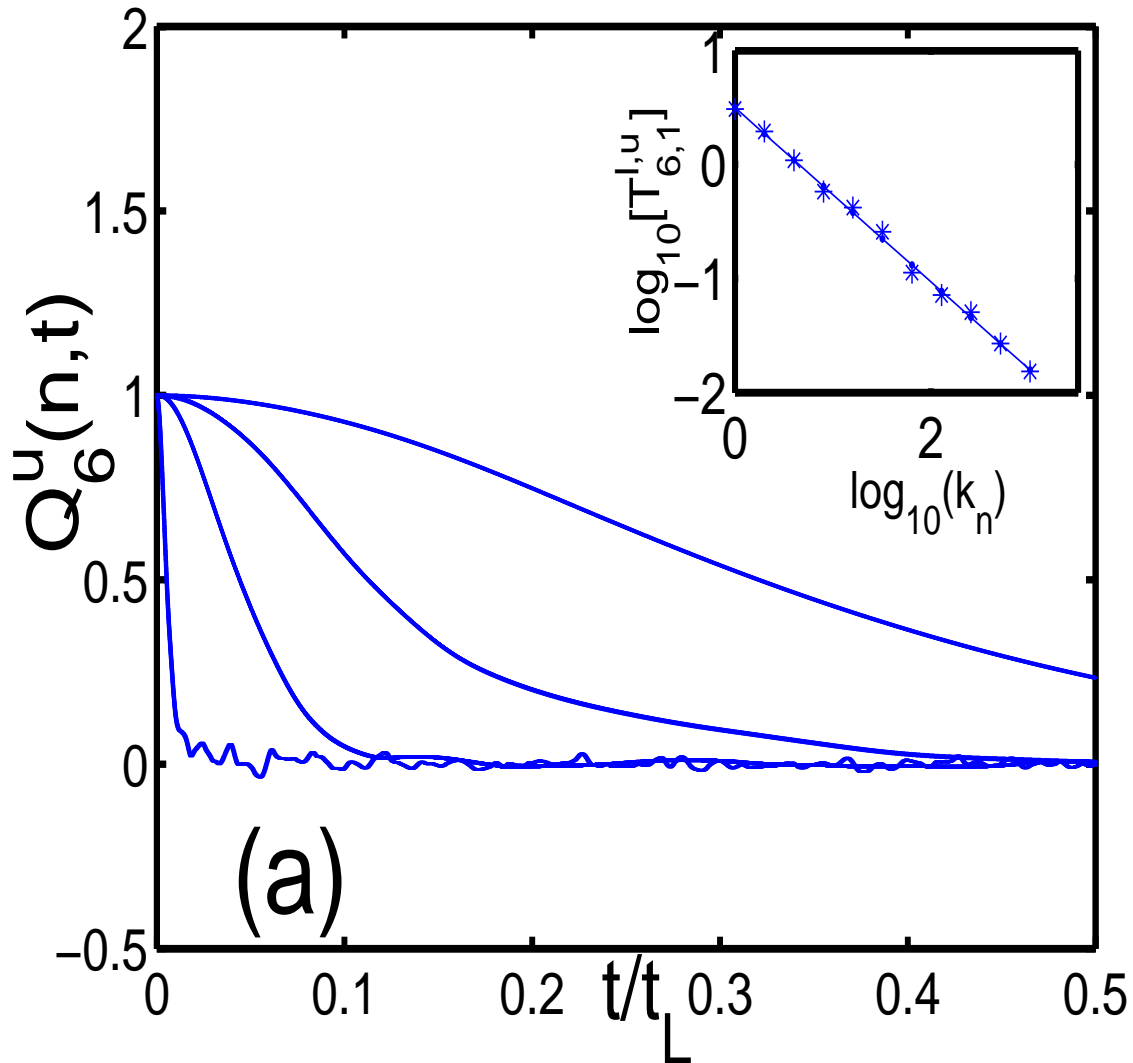
Figure 2.13: Representative plots of $Q_6^u(n,t)$ versus t/t_L for Model C; for clarity we show shell numbers $n = 4$ (uppermost), 6, 8 and 12 (lowermost). The inset shows $T_{6,1}^{I,u}(n)$ versus k_n on a log-log scale. A linear fit yields the dynamic-multiscaling exponent $z_{6,1}^{I,u} = 0.76 \pm 0.02$.
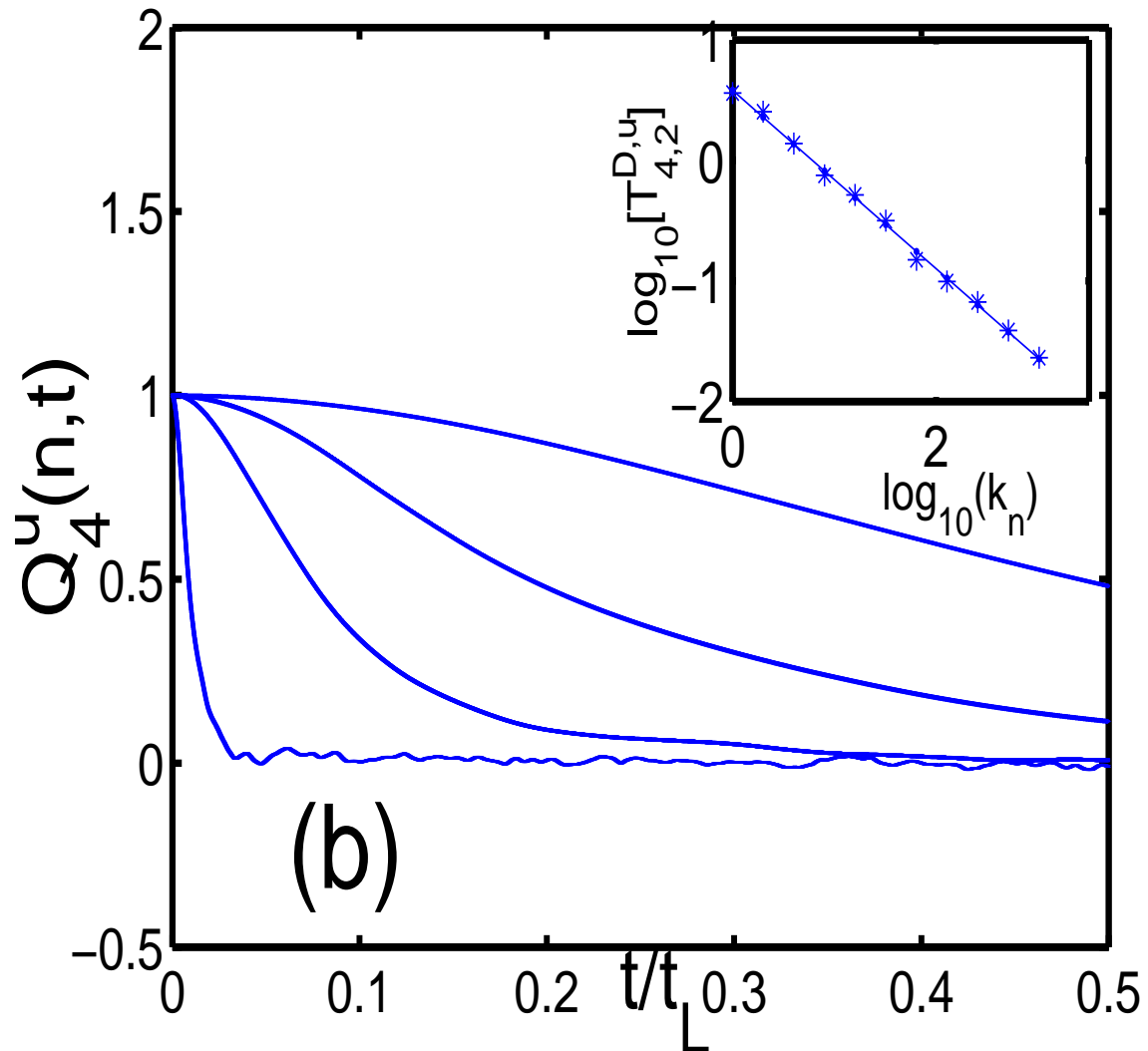
Figure 2.14: Representative plots of $Q_4^u(n,t)$ versus t/t_L for the same shell numbers as in the previous figure. The inset shows $T_{4,2}^{D,u}(n)$ versus k_n on a log-log scale. A linear fit yields $z_{4,2}^{D,u} = 0.76 \pm 0.01$.

order(p)	ζ_p^u	$z_{p,1}^{I,u}$[Eq.(3.18)]	$z_{p,1}^{I,u}$	$z_{p,2}^{D,u}$[$Eq.$(3.18)]	$z_{p,2}^{D,u}$
1	0.379 ± 0.008	0.621 ± 0.008	0.61 ± 0.03	0.68 ± 0.01	0.699 ± 0.008
2	0.711 ± 0.002	0.66 ± 0.01	0.68 ± 0.01	0.716 ± 0.008	0.723 ± 0.006
3	1.007 ± 0.003	0.704 ± 0.005	0.711 ± 0.001	0.74 ± 0.01	0.752 ± 0.005
4	1.279 ± 0.006	0.728 ± 0.009	0.734 ± 0.002	0.76 ± 0.02	0.76 ± 0.01
5	1.525 ± 0.009	0.75 ± 0.02	0.755 ± 0.002	0.77 ± 0.02	0.77 ± 0.02
6	1.74 ± 0.01	0.78 ± 0.02	0.78 ± 0.03	0.77 ± 0.03	0.78 ± 0.02

Table 2.1: Our simulation results for Model C with Type I initial conditions. Order-p (column 1); equal-time exponents ζ_p^u (column 2); integral-scale dynamic-multiscaling exponent $z_{p,1}^{I,u}$ (column 3) from the bridge relation (3.18) and the values of ζ_p^u in column 2; $z_{p,1}^{I,u}$ from our calculation using time-dependent structure functions (column 4); the derivative-time exponents $z_{p,2}^{D,u}$ (column 6) from the bridge relation (3.18) and the values of ζ_p^u in column 2; $z_{p,2}^{D,u}$ from our calculation using time-dependent structure function (column 7). The error estimates are obtained as described in the text.

(columns 4 in Tables 1 and 2) and derivative-time (columns 6 in Tables 1 and 2) exponents. Similarly Figs. (2.17) and (2.18) compare the dynamic-multiscaling exponents from our direct numerical simulations with the values predicted for them by the bridge relations (3.18) and (3.18) and the equal-time exponents ζ_p^u given in Tables 1 and 2.

2.5.3 Model D

From a numerical study of a passive-scalar shell model, with advecting velocities from the Sabra shell model, it was shown [39, 40] that the equal-time scaling exponents ζ_p^θ are universal: they are the same for decaying and statistically steady turbulence; and, in the latter case, they do not depend on the type of forcing. We find, not surprisingly, that this universality holds even when the advecting velocity field is a solution of the GOY model, i.e., for Model D: Table 3 column 2 shows the values of ζ_p^θ for $1 \leq p \leq 6$, which we have obtained for decaying turbulence; these agree with the results of Refs. [9, 34] for
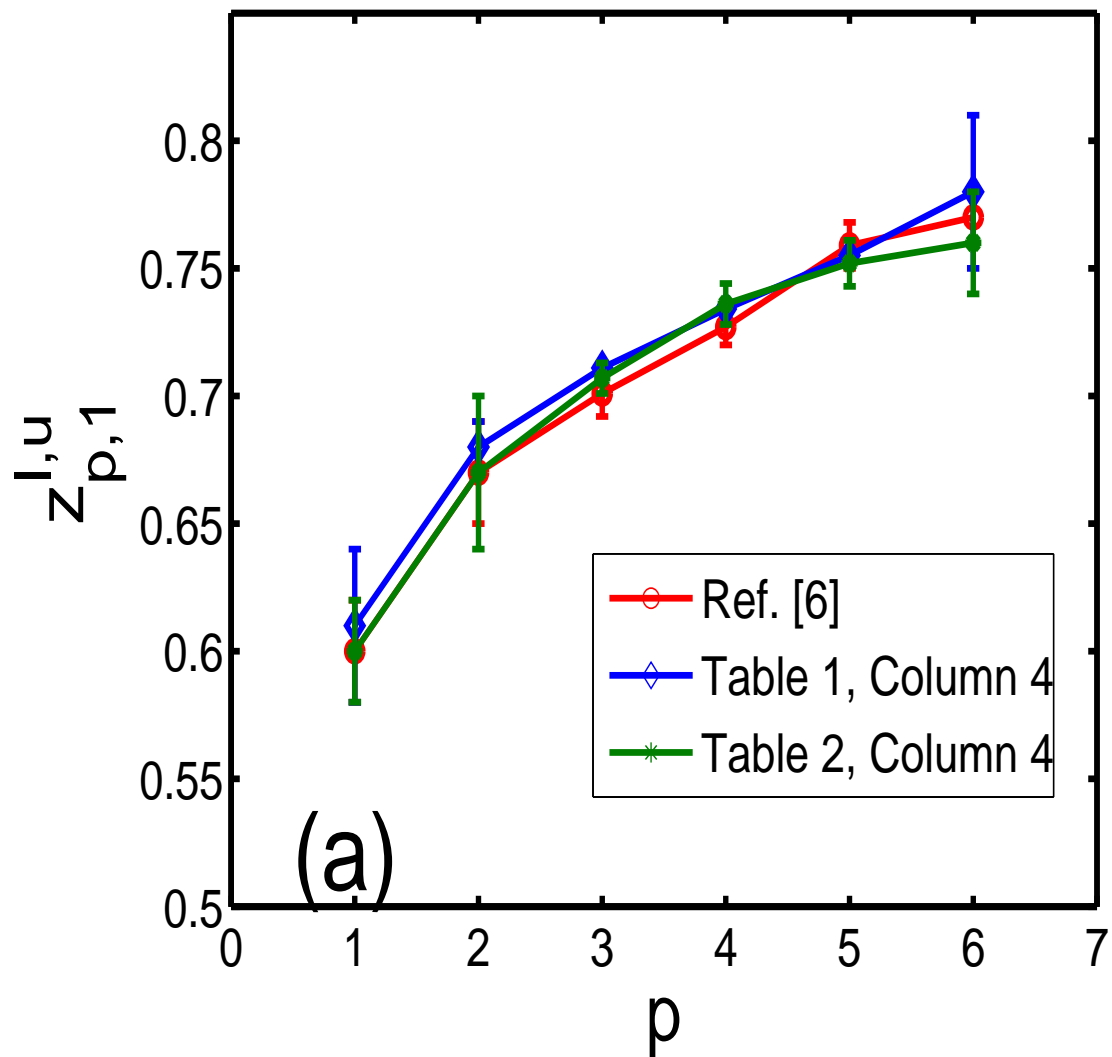
Figure 2.15: Plots of $z_{p,1}^{I,u}$, with error bars, versus p for Model C with data from [8], for statistically steady turbulence, and columns 4 of Tables 1 and 2, for decaying turbulence; these plots illustrate the agreement between the three sets of exponents.
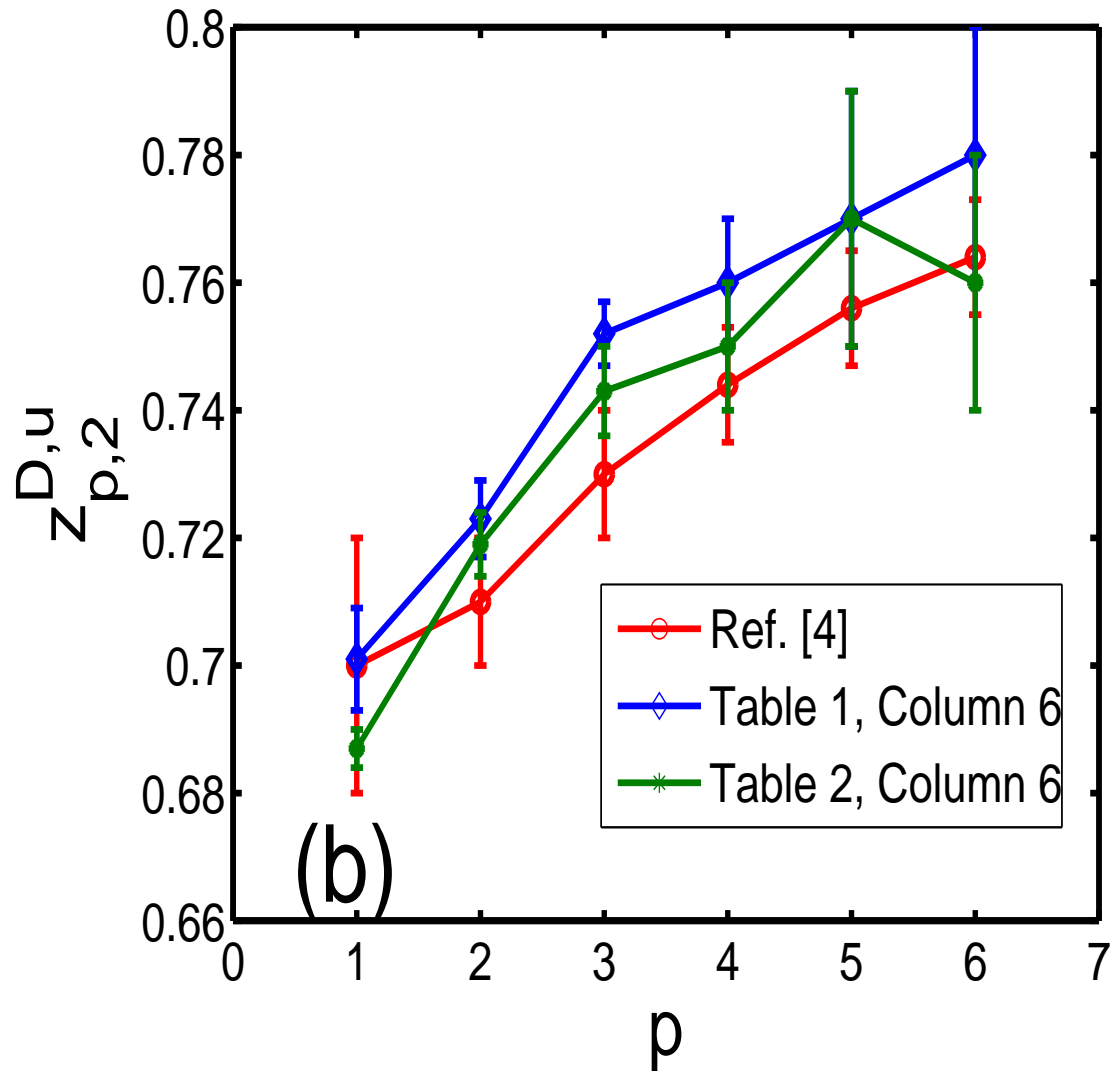
Figure 2.16: We compare the derivative-time exponents $z_{p,2}^{D,u}$ from [8] and columns 6 of Tables 1 and 2. As in (a), we find that the three sets of exponents agree, within error bars, with each other.
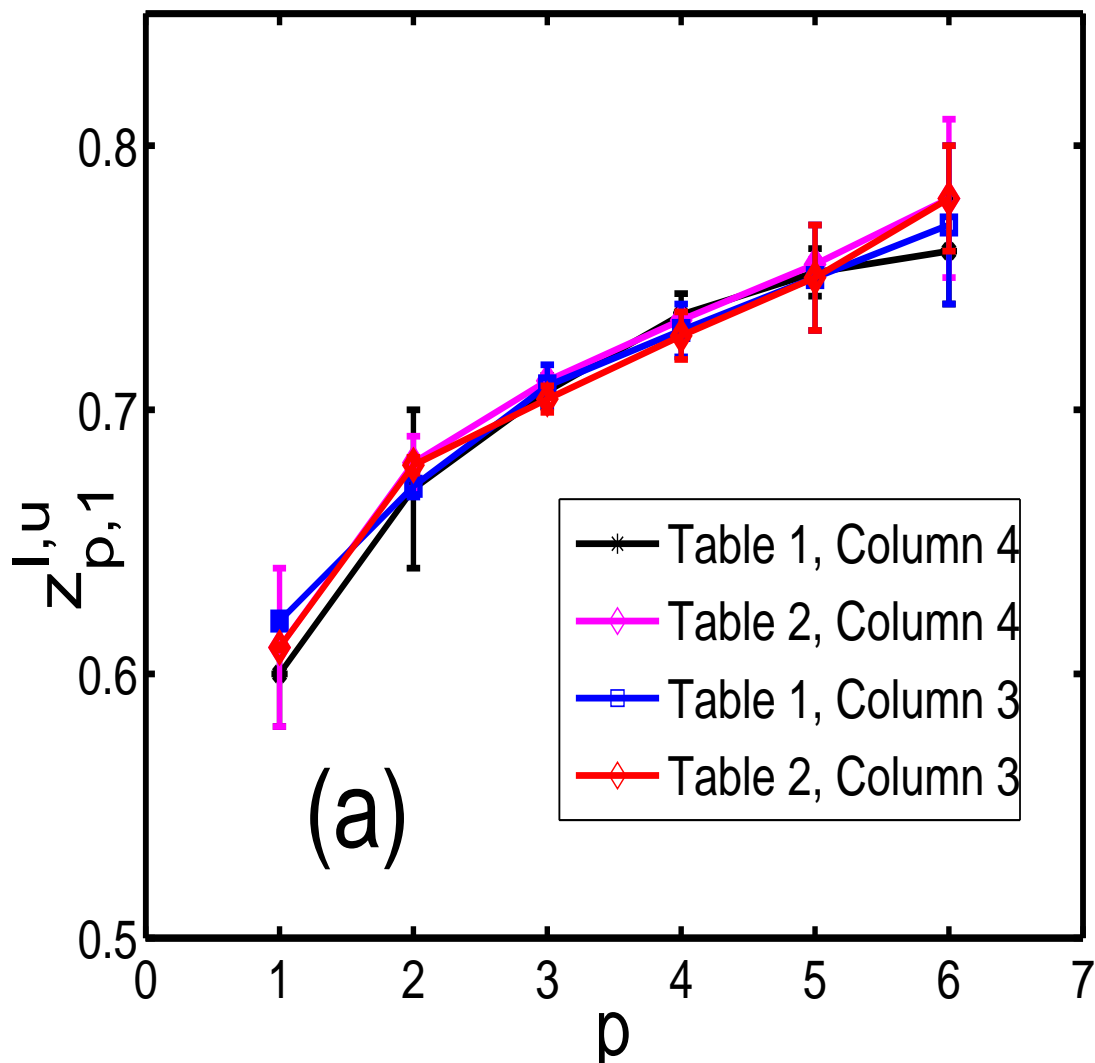
Figure 2.17: Plots of $z_{p,1}^{I,u}$, with error bars, versus p for Model C with values obtained via the bridge relations (columns 3, Tables 1 and 2) and those obtained from our numerical simulations (columns 4, Tables 1 and 2).
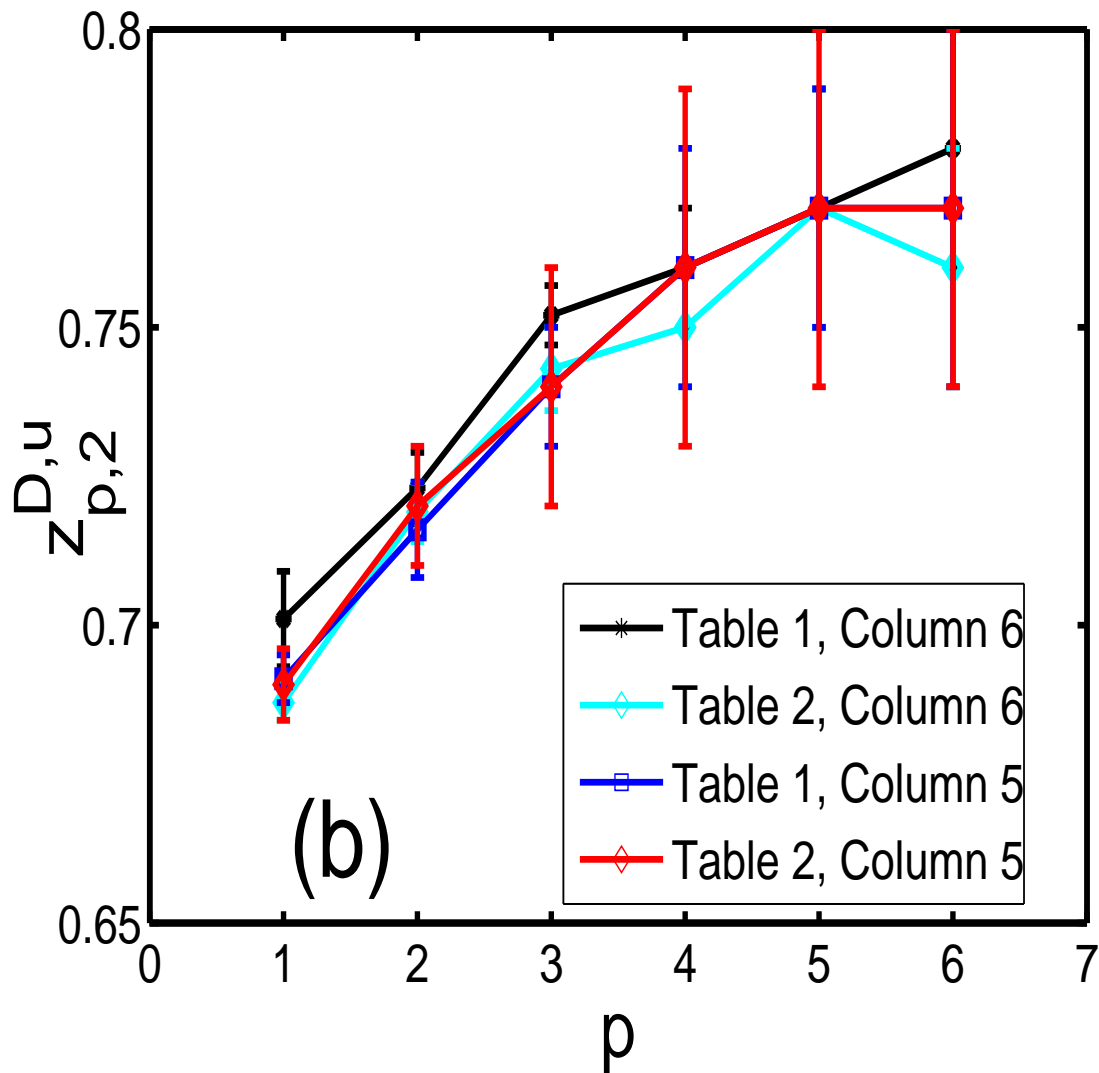
Figure 2.18: Plots of $z_{p,2}^{D,u}$, with error bars, versus p for Model C with values obtained via the bridge relations (columns 5, Tables 1 and 2) and those obtained from our numerical simulations (columns 6, Tables 1 and 2).

order(p)	ζ_p^u	$z_{p,1}^{I,u}$[Eq.(3.18)]	$z_{p,1}^{I,u}$	$z_{p,2}^{D,u}$[$Eq.$(3.18)]	$z_{p,2}^{D,u}$
1	0.380 ± 0.004	0.620 ± 0.004	0.60 ± 0.02	0.690 ± 0.009	0.687 ± 0.003
2	0.709 ± 0.003	0.671 ± 0.007	0.67 ± 0.03	0.72 ± 0.01	0.719 ± 0.005
3	1.000 ± 0.005	0.709 ± 0.008	0.707 ± 0.006	0.74 ± 0.02	0.743 ± 0.007
4	1.266 ± 0.008	0.73 ± 0.01	0.736 ± 0.008	0.76 ± 0.03	0.75 ± 0.01
5	1.51 ± 0.01	0.75 ± 0.02	0.752 ± 0.009	0.77 ± 0.03	0.77 ± 0.02
6	1.74 ± 0.02	0.77 ± 0.03	0.76 ± 0.02	0.77 ± 0.03	0.76 ± 0.02

Table 2.2: Our simulation results for Model C with Type II initial conditions. Order-p (column 1); equal-time exponents ζ_p^u (column 2); integral-scale dynamic-multiscaling exponent $z_{p,1}^{I,u}$ (column 3) from the bridge relation (3.18) and the values of ζ_p^u in column 2; $z_{p,1}^{I,u}$ from our calculation using time-dependent structure functions (column 4); the derivative-time exponents $z_{p,2}^{D,u}$ (column 6) from the bridge relation (3.18) and the values of ζ_p^u in column 2; $z_{p,2}^{D,u}$ from our calculation using time-dependent structure function (column 7). The error estimates are obtained as described in the text.

statistically steady turbulence in Model D. Our equal-time exponents are also within error bars of their counterparts for the passive-scalar shell model of Refs. [39, 40]. We obtain ζ_p^θ from log-log plots such as Fig. (2.19) for the modified, equal-time structure function (2.22) Σ_p^θ versus k_n; the slope of the linear region $4 \leq n \leq 12$ yields ζ_p^θ that is plotted versus p in Fig. (2.20).

To analyse the time-dependent, passive-scalar structure functions we follow Sec. 2.5.2 for Model C: We obtain integral- and derivative-time scales from equations (3.13) and (2.50), for $M = 1$ and $M = 2$, respectively. In the integral in (3.13) we set the upper limit to t_μ, the time at which the normalised, time-dependent structure function

$$Q_p^\theta(n, t) \equiv \frac{F_p^\theta(k_n, t_0, t)}{F_p^\theta(k_n, t_0, 0)} \tag{2.70}$$

is equal to μ, with $0 \leq \mu \leq 1$. We use $\mu = 0.6$, but we have checked in representative cases that our results remain unchanged if we use the range of values $0.3 \leq \mu \leq 0.8$. Slopes of log-log plots of $T_{p,1}^{I,\theta}(n)$ versus k_n yield $z_{p,1}^{I,\theta}$. To extract the derivative-time scale, we use a centred,
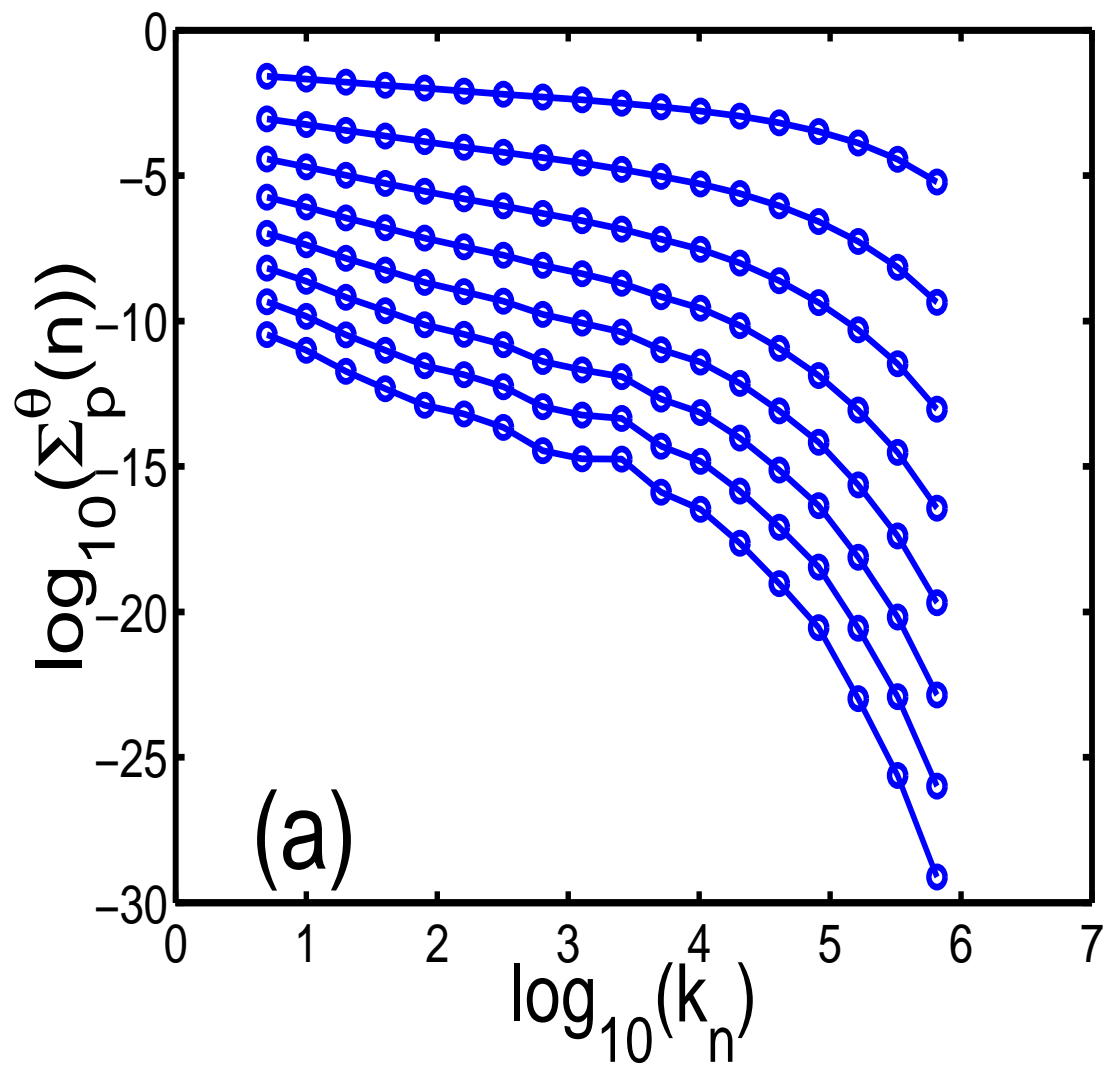
Figure 2.19: Representative plots of $\Sigma_p^\theta(n)$ versus k_n on a logarithmic scale for $p = 1$ (uppermost curve) to 8 (lowermost curve) for Model D.
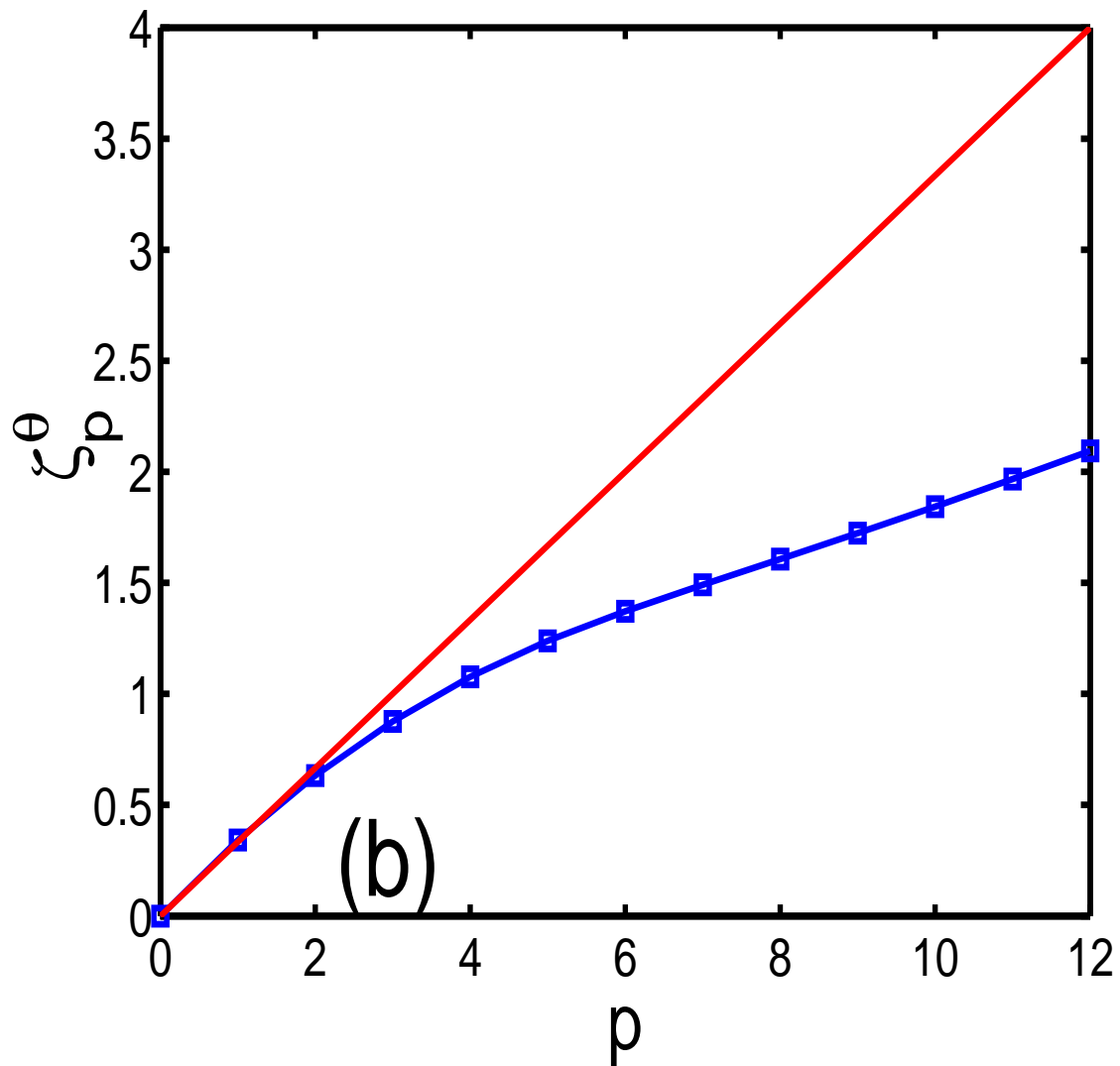
Figure 2.20: Plot of ζ_p^θ, obtained from the linear, inertial region in (a), versus p. Our data points, shown as squares, are connected by a line; the error bars are smaller than the size of the symbol. The straight line corresponds to the Kolmogorov prediction of $p/3$.

finite-difference, sixth-order scheme to obtain $T^{D,\theta}_{p,2}(n)$ from which we get $z^{D,\theta}_{p,2}$. Integral- and derivative-time multiscaling exponents are extracted from linear fits in the inertial range $4 \leq n \leq 10$ as shown in the insets of the representative plots in Figs. (2.21) and (2.22) for, respectively, $Q^{\theta}_5(n,t)$ and $Q^{\theta}_3(n,t)$ versus t/t_L. Finally, from the bridge relations (2.61) and our GOY-model, equal-time exponents $\zeta^u_{-1} = -0.44 \pm 0.04$ and $\zeta^u_2 = 0.709 \pm 0.003$ we obtain $z^{I,\theta}_{p,1} = 0.56 \pm 0.04$ and $z^{D,\theta}_{p,2} = 0.645 \pm 0.003$ in agreement with the values from our simulations listed in columns 3 and 4 of Table 3. By comparing these columns with their counterparts in Table II of Ref. [9], we find agreement, within our error bars, between the dynamic-multiscaling exponents for Model D for both statistically steady and decaying turbulence.

We end this Section by investigating the effect of hyperviscosity, i.e., by using different powers α of the Laplacian instead of the Laplacian in the dissipation term, on the GOY shell model for fluid turbulence [2]. We thus rewrite our GOY shell model evolution equation as

$$\left[\frac{d}{dt} + \nu_0 \left(\frac{k_n}{k_d} \right)^{\alpha} k_n^2 \right] u_n = \imath \left[a_n u_{n+1} u_{n+2} + b_n u_{n-1} u_{n+1} + c_n u_{n-1} u_{n-2} \right]^*, \qquad (2.71)$$

where the second term allows for hyperviscous dissipation with degree α (the case $\alpha = 0$ corresponds to conventional viscous dissipation); k_d is a large wavenumber whose inverse is comparable to the dissipation length scale; we choose $k_d = 2^{18}$ and $\alpha = 2$. Since we concentrate on decaying turbulence here, the forcing term, required to drive the system into a statistically steady state, is absent.

We begin by looking at the mean energy dissipation rate ϵ as a function of time. A representative plot, averaged over 2000 initial conditions, is shown for $\alpha = 2$ in Figure 2.23. Though this plot is noisy, it shows a clear peak. This peak, at $t/t_L \simeq 1.2$ ($t_L \simeq 5$) in Figure 2.23, signals the completion of the cascade that transfers energy from the scale at which it is injected to the small scales where viscous dissi-
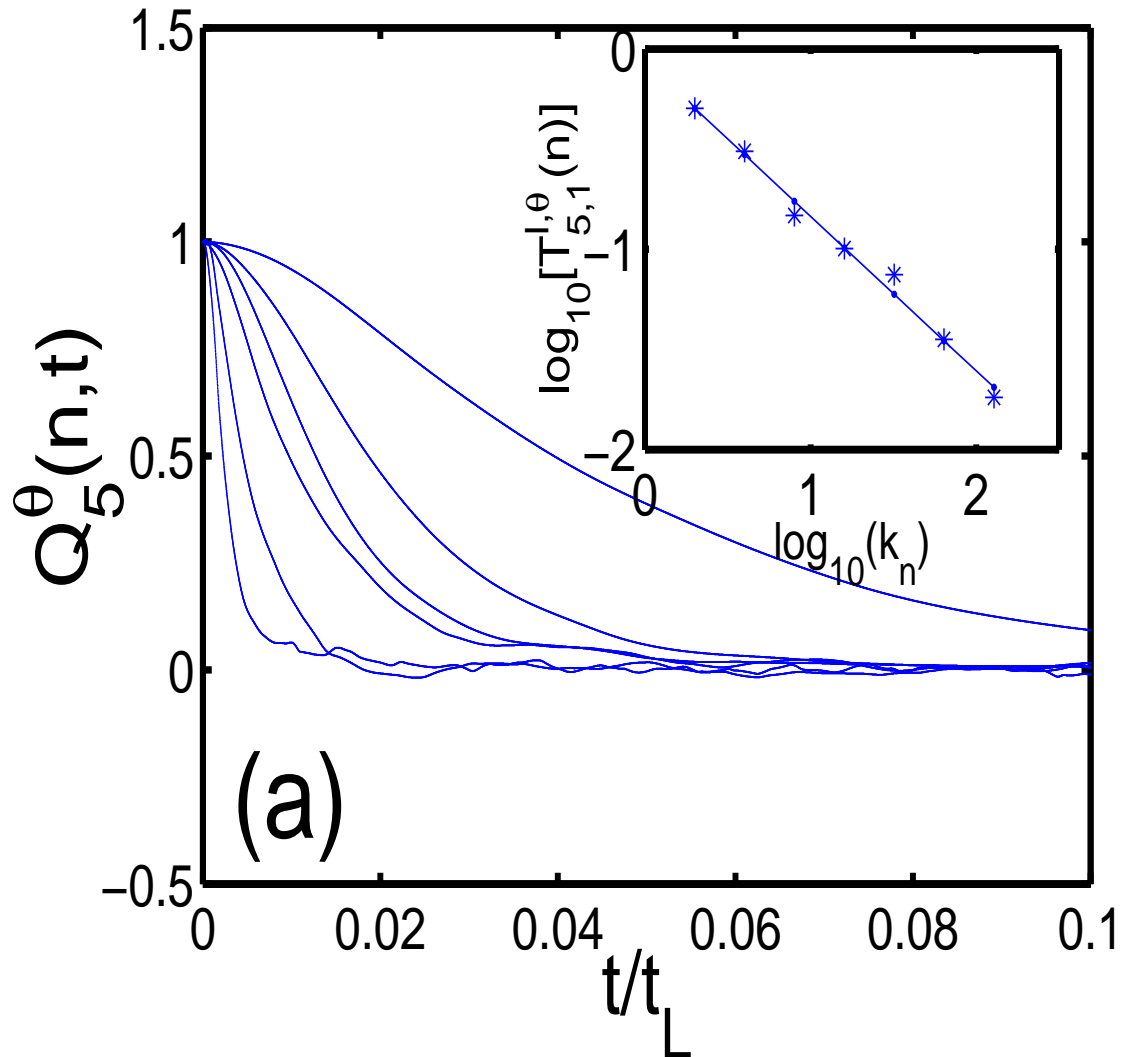
Figure 2.21: Representative plots of $Q_5^\theta(n,t)$ versus t/t_L, for shell numbers 6 (uppermost) to 11 (lowermost) for Model D. The inset shows a log-log plot of $T_{5,2}^{I,\theta}(n)$ versus k_n. A linear fit yields $z_{5,1}^{I,\theta} = 0.562 \pm 0.006$.
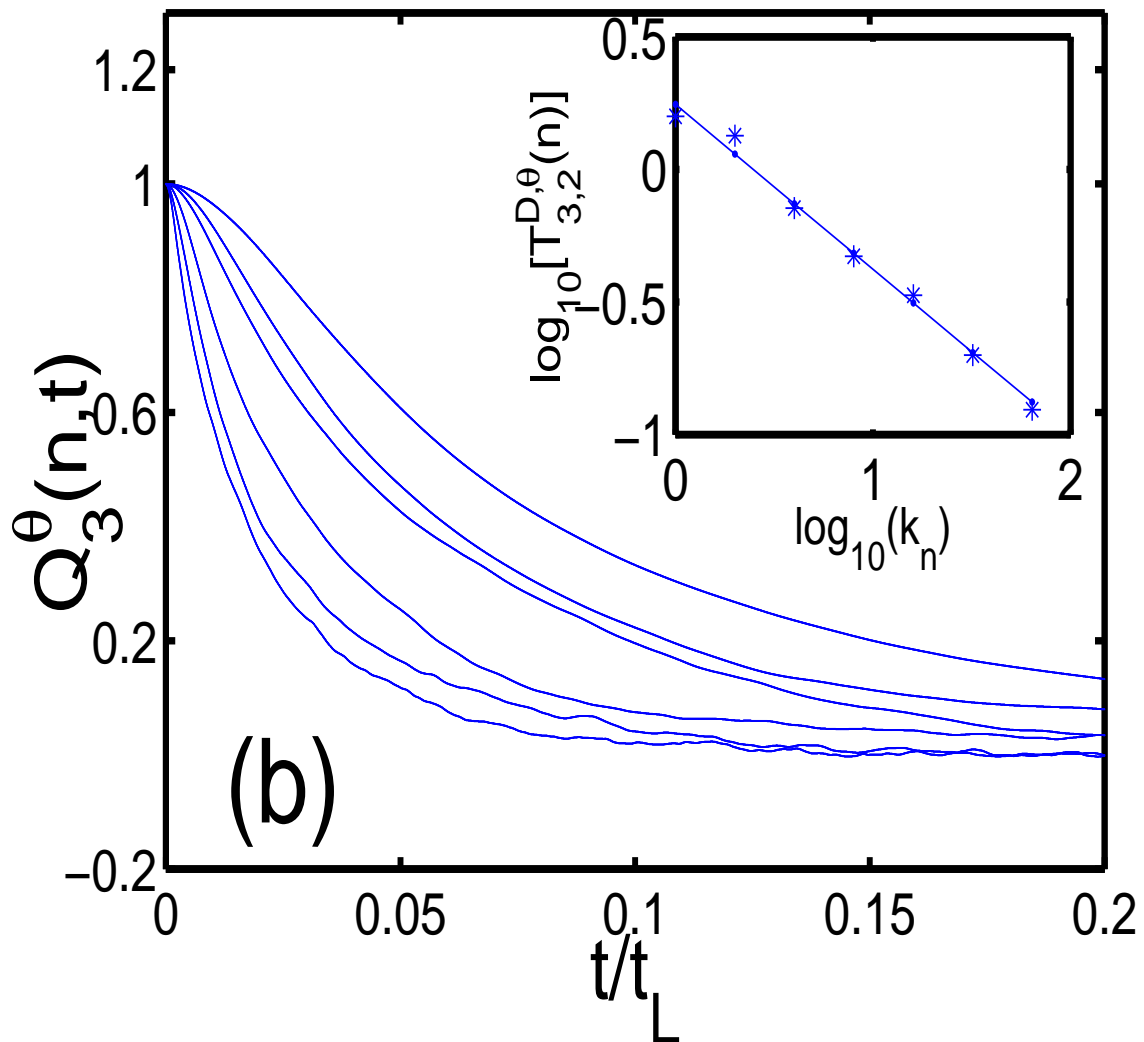
Figure 2.22: Representative plots of $Q_3^\theta(n,t)$ versus t/t_L for the same shell numbers as in (a). The inset shows $T_{3,2}^{D,\theta}(n)$ versus k_n on a log-log scale. A linear fit yields $z_{3,2}^{D,\theta} = 0.646 \pm 0.003$.

pation becomes significant. Representative energy spectra at cascade completion are shown in Figure 5.2; after this point in time the energy spectrum decays very slowly without an *appreciable* change in the slope of the scaling regime, which appears as a nearly straight-line segment in the log-log plots of Figure 5.2. Straight-line segments also show up in plots of the structure function Σ_p at (or after) cascade completion as shown in the representative plots, for $\alpha = 2$, of Figure 2.26; each curve in this Figure has been averaged over 5000 independent initial conditions. From the slopes of the straight-line segments in these plots (see Table 1) we obtain the equal-time multiscaling exponents ζ_p whose dependence on p is shown in Figure 2.27. The values we quote for these (and other) exponents are the means of the slopes of 50 different plots like Figure 2.26, which are obtained from 50 statistically independent runs; the corresponding standard deviations yield the error bars shown in Table 1.

Our results for the equal-time exponents ζ_p for $\alpha = 0$ and $\alpha = 2$ are presented in Table 4. By comparing Columns 2 and 3 in this Table we see that the exponents for both values of α agree with each other and with the exponents reported earlier for statistically steady turbulence [8]. Thus we reconfirm the universality of equal-time exponents: they neither depend on the precise dissipation mechanism nor on whether we consider statistically steady or decaying turbulence.

We next calculate the integral-time scale $T^I_{p,1}$. In Figure 2.28 we show representative plots of Q_4 versus time t/t_L for shells $n = 3, 4, 7,$ and 9 and $\alpha = 2$; from this we obtain $T^I_{4,1}$ as described above. The slopes of log-log plots of $T^I_{p,1}$ versus k_n now yield $z^I_{p,1}$ as shown in Figure 2.29 for $p = 4$. The derivative-time scale $T^D_{p,2}$ is calculated by using a sixth-order, centred difference scheme. The derivative-time exponent $z^D_{p,2}$ is then obtained from slopes of log-log plots of $T^D_{p,2}$ versus k_n.

Table 5 summarise our results for the dynamic-multiscaling exponents. All these exponents have been calculated for k_n in the iner-
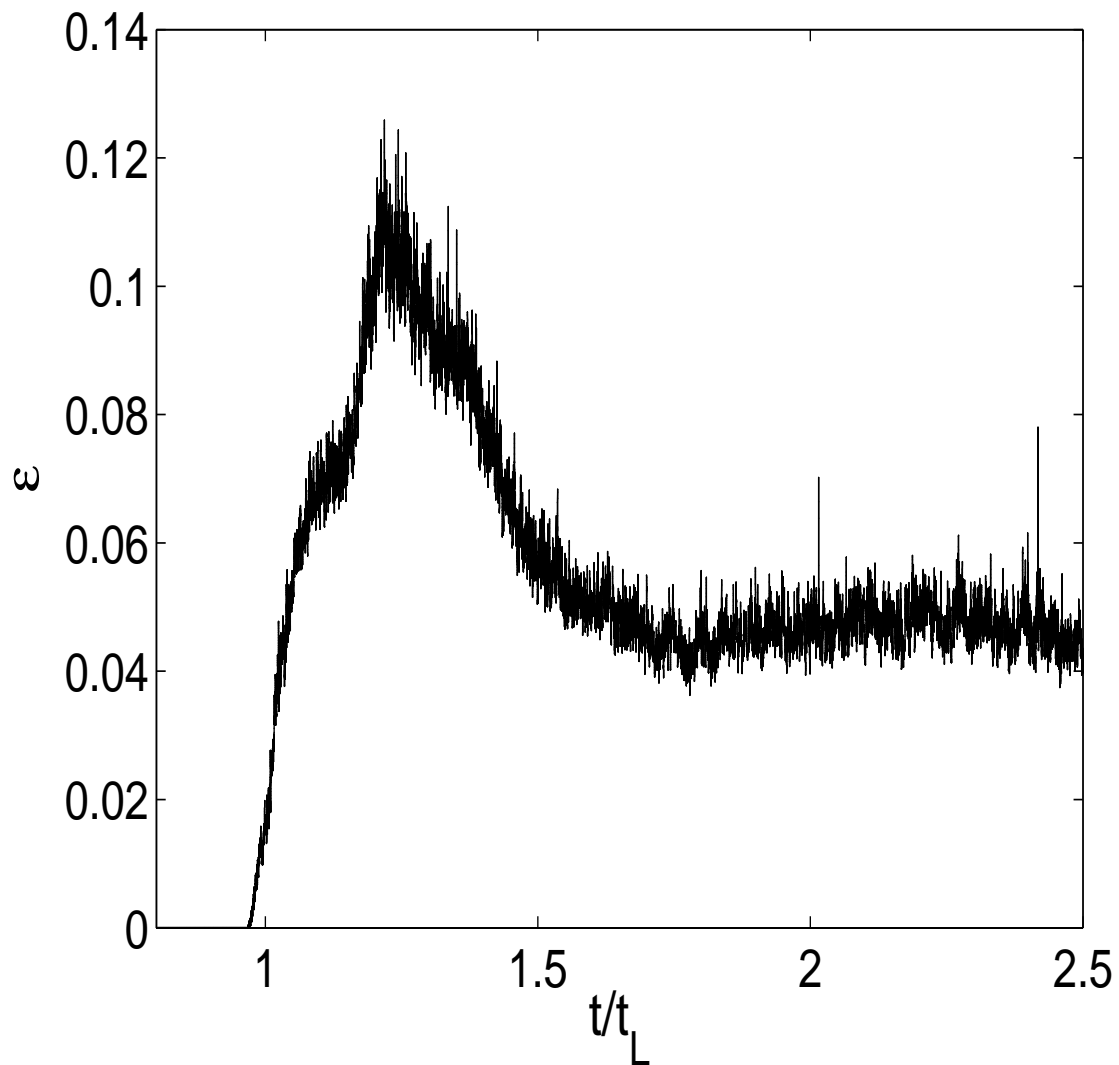
Figure 2.23: The mean energy dissipation rate ϵ versus time for $\alpha = 2$ (for clarity we show data for $0.8 \leq t/t_L \leq 2.5$); these data have been averaged over 2000 initial conditions. The main peak at $t/t_L \simeq 1.2$ is a signature of cascade completion. For $\alpha = 0$ ϵ displays a similar peak.
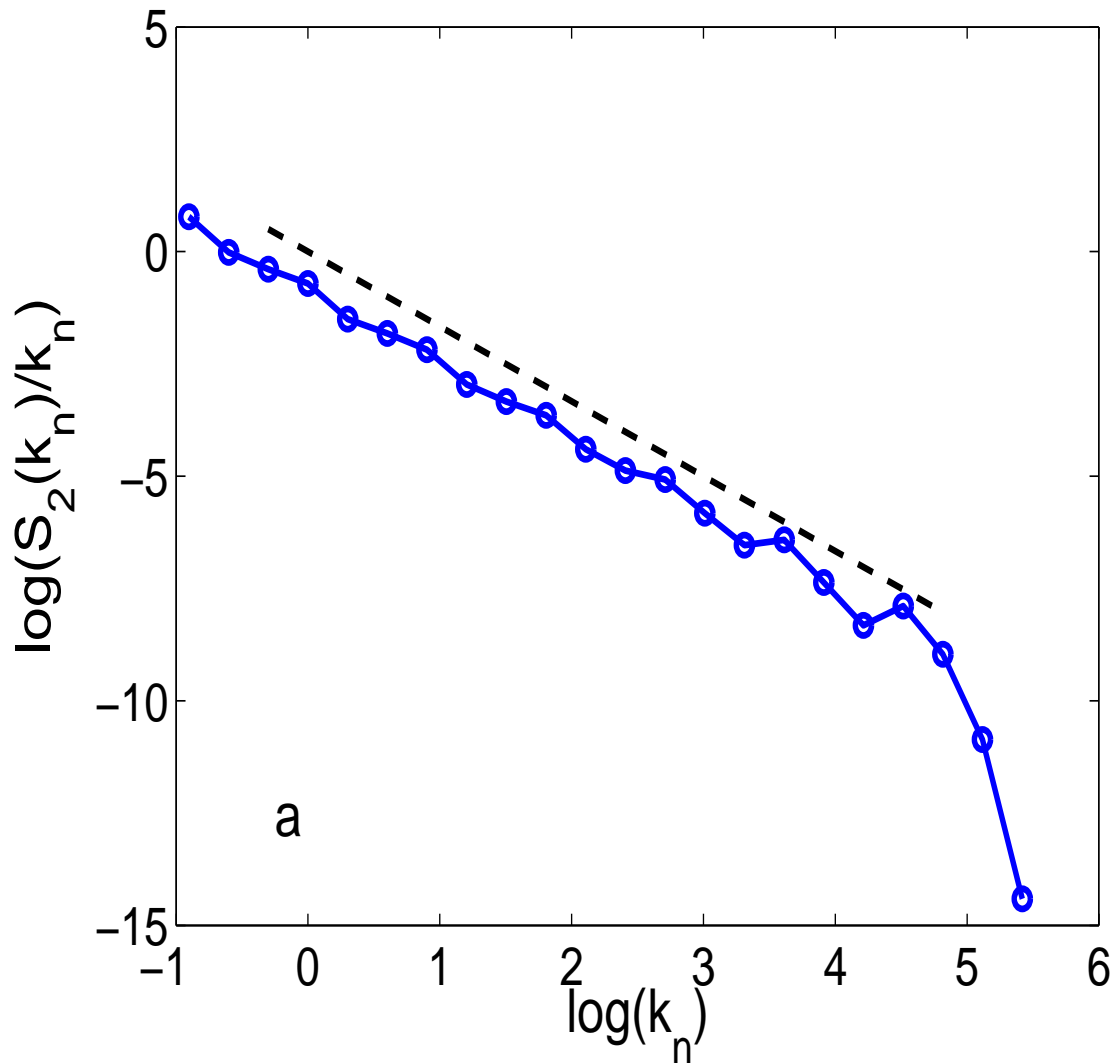
Figure 2.24: Log-log plot of the kinetic energy spectrum $E(k_n) = S_2(k_n)/k_n$ versus k_n with the period-three oscillations (see text). The black dashed line corresponds to the K41 scaling prediction $E(k_n) \sim k^{-5/3}$.
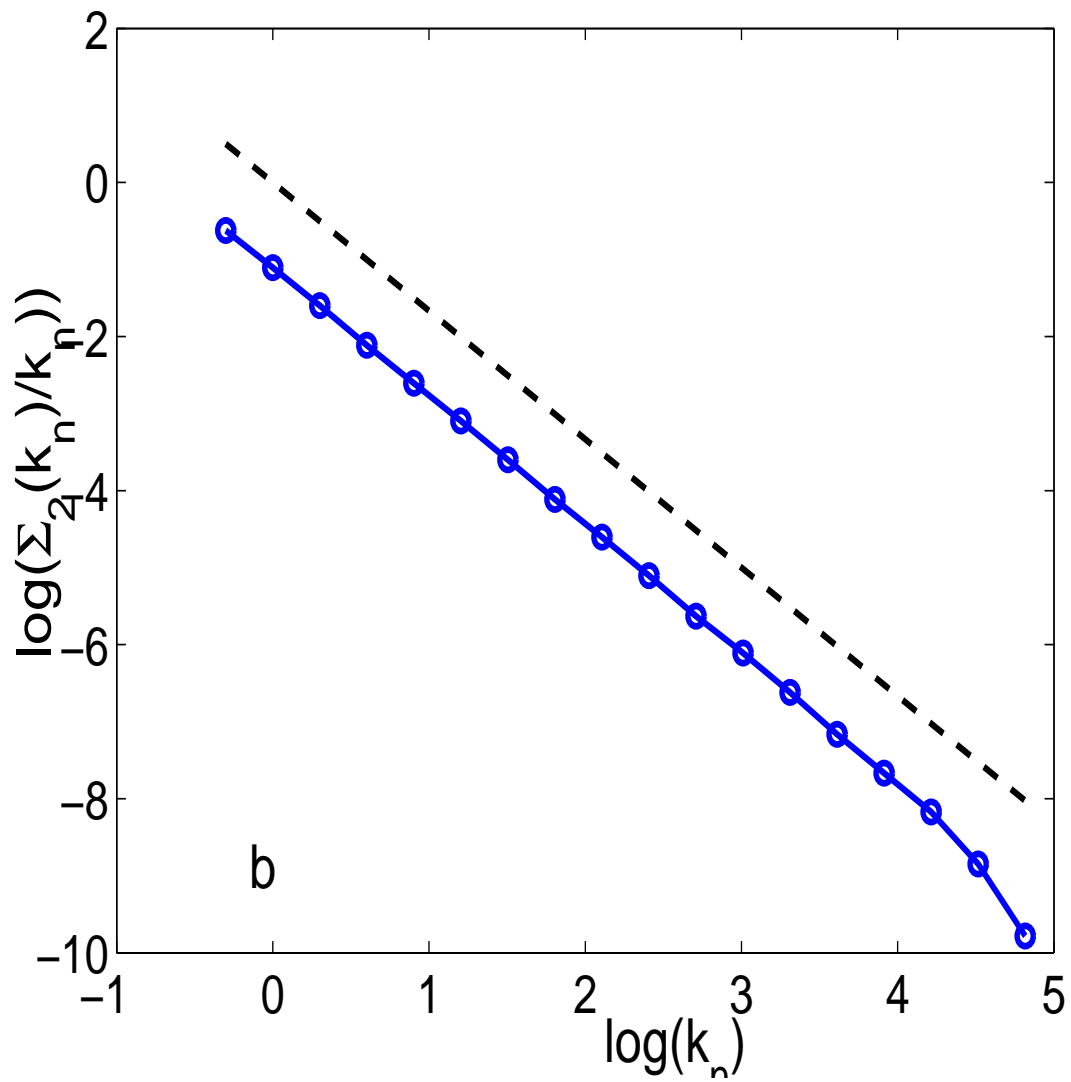
Figure 2.25: Log-log plot of $\Sigma_2(k_n)/k_n$ versus k_n; note that the period-three oscillations are suppressed here; the black dashed line indicates the K41 scaling prediction.
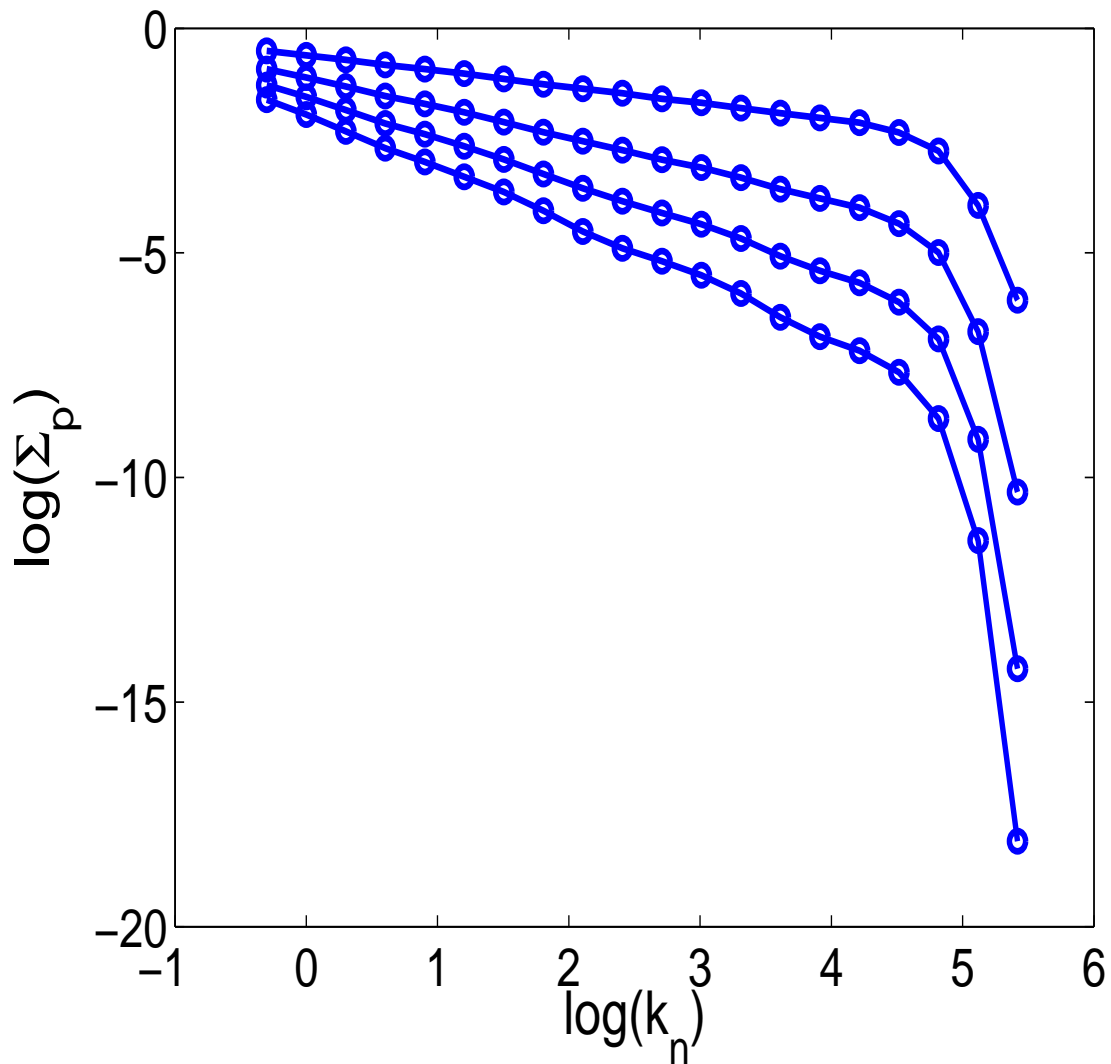
Figure 2.26: (a) Log-log plot of the modified structure function Σ_p, for $p = 1$ to 4 (top to bottom), versus k_n for $\alpha = 2$ and number of shells $N = 35$ (we show data only for the first 22 shells).
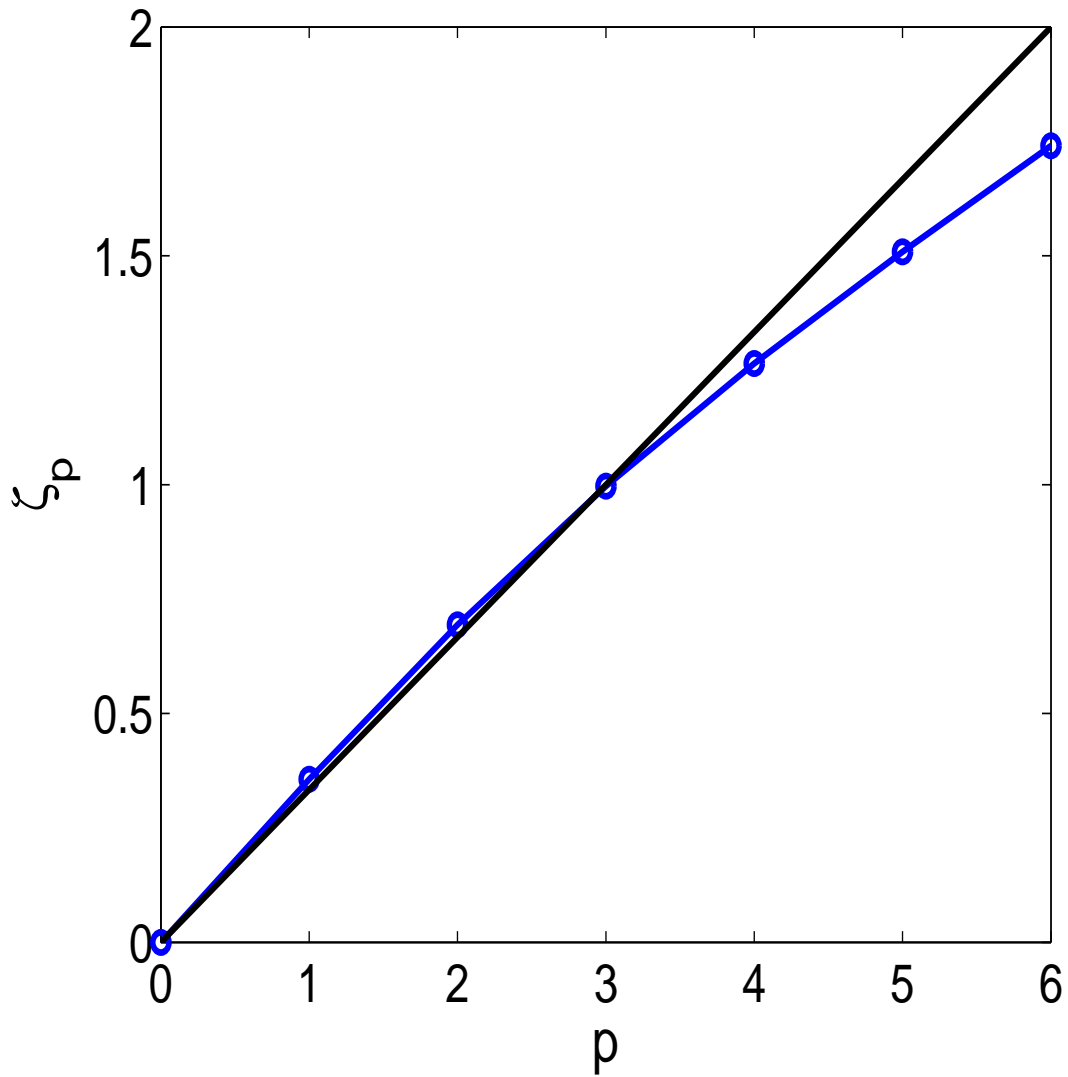
Figure 2.27: Plot of the equal-time multiscaling exponents ζ_p (obtained from (a) and listed in Table 1) versus the order p. The open circles (o), connected by a curve to guide the eye, indicate data from our numerical simulations; the thick black line is the K41 prediction $\zeta_p^{K41} = p/3$.

Table 2.3: Our results for the equal-time multiscaling exponents ζ_p at cascade completion for $\alpha = 0$ (Column 2) and $\alpha = 2$ (Column 3). We indicate, in parentheses, the ranges of shell numbers n over which we fit our data for equal-time structure functions to obtain these exponents. Note that the exponents in Columns 2 and 3 agree very well with each other.

order-p	ζ_p (4-14)	ζ_p (4-16)
1	0.380 ± 0.001	0.37 ± 0.01
2	0.709 ± 0.003	0.699 ± 0.008
3	1.000 ± 0.005	1.003 ± 0.008
4	1.266 ± 0.008	1.29 ± 0.02
5	1.51 ± 0.01	1.55 ± 0.03
6	1.74 ± 0.02	1.79 ± 0.05

tial range $4 \leq n \leq 14$. The exponents $z_{p,1}^I$ for $\alpha = 2$, which we obtain for decaying turbulence, are equal (within error bars) to their counterparts (see Ref. [8]) for statistically steady turbulence. Thus the dynamic-multiscaling exponents for the GOY model are universal even in the presence of hyperviscosity. Plots of these exponents versus p are shown in Figures **??** and **??**.

2.6   Conclusions

We have systematised the study of the dynamic multiscaling of time-dependent structure functions in four Models (A-D) for passive-scalar (A,B, and D) and fluid (C) turbulence. By a suitable normalisation of these structure functions, we eliminate their dependence on the origin of time t_0 at which we initiate our measurements. We have shown analytically that for the Kraichnan model of passive-scalar turbulence (Models A and B) the two-point time-dependent structure function can be factorised into two parts, one depending on the origin of time t_0 and another that does not. This suggests a suitable normalisation of the
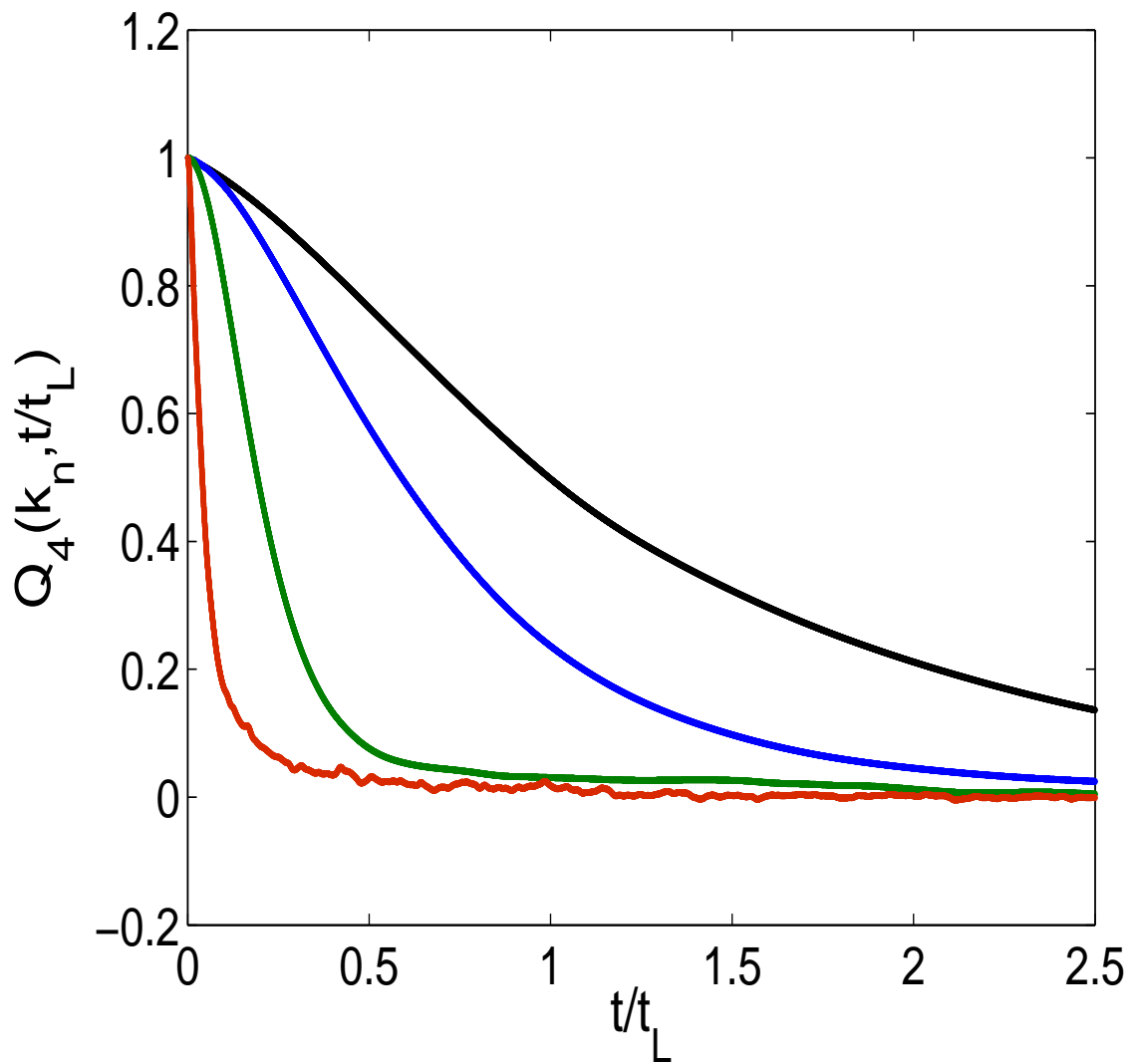
Figure 2.28: Illustrative plots of the normalised, fourth-order, time-dependent structure function $Q_4(k_n, t)$ versus time t/t_L for shells $n = 3, 4, 7$ and 9 (from top to bottom).
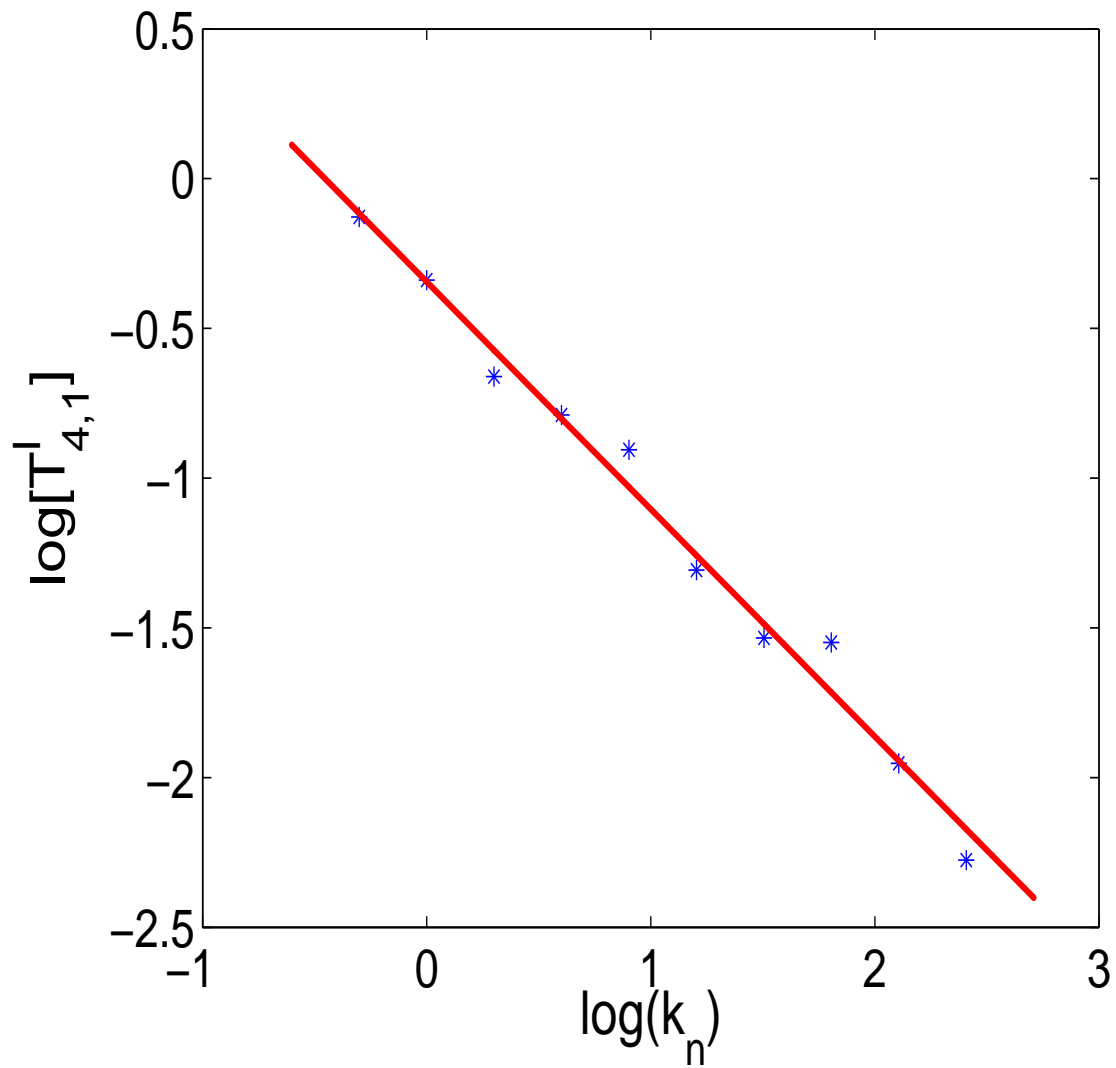
Figure 2.29: A log-log plot of the integral-time scale $T^I_{4,1}$ versus k_n; the integral-time exponent $z^I_{4,1} = 0.728\pm0.006$ follows from the slope of the line (in the range $4 \leq n \leq 12$).

Table 2.4: Column 2: The dynamic multiscaling exponents $z^I_{p,1}$ from the bridge relation (3.18) and our numerical results for ζ_p (Table 1). Column 3: The same exponents as in Column 2 but now obtained from our numerical simulations of decaying turbulence in the GOY shell model for the case $\alpha = 2$. Note the agreement between the exponents in Columns 2 and 3.

order-p	$z^I_{p,1}$[Eq.(3.18)]	$z^I_{p,1}$
1	0.630 ± 0.001	0.62 ± 0.01
2	0.675 ± 0.009	0.683 ± 0.003
3	0.69 ± 0.01	0.712 ± 0.004
4	0.71 ± 0.02	0.728 ± 0.006
5	0.74 ± 0.05	0.750 ± 0.009
6	0.76 ± 0.08	0.76 ± 0.01

structure functions by which we can eliminate their dependence on t_0. Surprisingly the same normalisation works for other models of fluid turbulence (Model C) and passive-scalar turbulence (Model D) as we have shown by extensive numerical simulations. Once this dependence on t_0 has been factored out, the methods developed earlier [8, 9] for statistically steady turbulence yield linear bridge relations that connect dynamic-multiscaling and equal-time exponents. We show analytically, for Models A and B, and numerically, for Models B, C, and D, that these exponents and bridge relations are the same for statistically steady and decaying turbulence. Thus we have generalised the universality of equal-time exponents [26] and provided strong evidence for dynamic universality, i.e., dynamic-multiscaling exponents do not depend on whether the turbulence decays or is statistically steady for each of the Models A-D.

It is useful to distinguish our results from other studies of temporal dependences of quantities in turbulence. Two such results are described below.

The first example is the result $E_{tot}(t) \sim t^{-2}$, which holds for the total energy E_{tot} at large times t in decaying turbulence [3]. This result holds for times that are longer than the time at which the integral length scale becomes comparable to the size of the system. [In decaying turbulence, the integral scale $L_{int}(t) \equiv (\int dk E(k,t)/k)/(\int dk E(k,t))$ increases with time since the large-k part of the energy spectrum $E(k,t)$, at time t, gets depleted as t increases.] In all the results we report here, our shell-model analogue of L_{int} is well below the linear size of the system, i.e., $L_{int} \ll k_0^{-1}$. Thus our results are not modified significantly by finite-size corrections, nor does the trivial decay of E_{tot}, mentioned above, set in and mask the dynamic multiscaling we have elucidated.

The second example is the intermittency of velocity time increments studied in Ref. [42]. These studies calculate structure functions along a single Lagrangian trajectory. Spatial separations, of the sort used in defining equal-time Eulerian structure functions, are replaced by temporal separations along a Lagrangian trajectory. This is distinct from the spatiotemporal structure functions we consider and which are required for a full elucidation of dynamic multiscaling here (and analogous dynamic scaling in critical phenomena).

We have described the way in which we have obtained error bars for the equal-time and dynamic-multiscaling exponents. These error bars only account for statistical errors but not the systematic errors associated with the values of n over which we fit inertial-range exponents. One can try to estimate such systematic errors by obtaining local slopes of log-log plots that yield these exponents. However, local slopes can be deceptive in shell models since the values of k_n are separated by factors of 2. Instead, we can try to estimate these systematic errors by comparing the exponents we obtain by fitting over the ranges $3 \le n \le 15$, $4 \le n \le 14$, and $5 \le n \le 13$. We have carried out such checks in representative cases for the dynamic-multiscaling

order(p)	ζ_p^θ	$z_{p,1}^{I,\theta}$	$z_{p,2}^{D,\theta}$
1	0.342 ± 0.002	0.522 ± 0.002	0.632 ± 0.003
2	0.634 ± 0.003	0.531 ± 0.004	0.647 ± 0.003
3	0.873 ± 0.003	0.553 ± 0.006	0.646 ± 0.003
4	1.072 ± 0.004	0.563 ± 0.003	0.642 ± 0.005
5	1.245 ± 0.004	0.562 ± 0.006	0.643 ± 0.006
6	1.370 ± 0.006	0.576 ± 0.006	0.640 ± 0.005

Table 2.5: Our simulation results for Model D. Order-p (column 1); equal-time exponents ζ_p^θ (column 2); integral-scale dynamic-multiscaling exponent $z_{p,1}^{I,\theta}$ (column 3); the derivative-time exponents $z_{p,2}^{D,\theta}$ (column 4). The error estimates are obtained as described in the text.

exponents we report. The error bars we then obtain are about a factor of 4 larger than those shown in Tables 1-3.

We hope our work will stimulate experimental studies of dynamic multiscaling in turbulence. Recent advances in the experimental techniques of particle tracking in turbulent flows [43, 44] have made it possible to obtain accurate measurements of Lagrangian properties. To obtain the types of structure functions that we have described it will be necessary at least to track two Lagrangian trajectories of particles that are separated initially by a distance r. At the level of second-order structure functions this has been attempted in the direct numerical simulations of Ref. [21].

Appendix A

The Adams-Bashforth method

In this Appendix we outline the numerical scheme used for time integration of the shell-model equations studied in this Chapter. For clarity let us consider the following ordinary differential equation (ODE):

$$\frac{dq}{dt} = -\alpha q + f(t).$$ (A.1)

For an ODE of the form above, we have the identity :

$$e^{\alpha(t+\delta t)}q(t + \delta t) - e^{\alpha t} = \int_t^{t+\delta t} e^{\alpha s} f(s)ds.$$ (A.2)

The slaved scheme is obtained by first writing down the equation for $q(t)$ and $q(t - \delta t)$; we then add the two to obtain :

$$q(t + \delta t) = e^{-2\alpha\delta t}q(t - \delta t) + \int_{t-\delta t}^{t+\delta t} e^{-\alpha(t+\delta t-s)} f(s)ds.$$ (A.3)

It is now reasonable to approximate $f(s)$ by either replacing $f(s)$ by $f(t)$ (the slaved-frog scheme) or by making the substitution $f(s) = (3/2)f(t) - (1/2)f(t - \delta t)$. The former yields the solution

$$q(t + \delta t) = e^{-2\alpha\delta t}q(t - \delta t) + \frac{1 - e^{-2\alpha\delta t}}{\alpha}f(t);$$ (A.4)

the latter yields the slaved Adams-Bashforth scheme

$$q(t + \delta t) = e^{-2\alpha\delta t}q(t - \delta t) + \frac{1 - e^{-2\alpha\delta t}}{\alpha}\left[\frac{3}{2}f(t) - \frac{1}{2}f(t - \delta t)\right].$$ (A.5)

In this Chapter we use the slaved Adams-Bashforth scheme to integrate the shell model evolution equations.

Bibliography

[1] S. S. Ray, D. Mitra, and R. Pandit, New J. of Phys., **10**, 033003 (2008).

[2] R. Pandit, S. S. Ray, and D. Mitra, Eur. Phys. J. B **64**, 463 (2008).

[3] U. Frisch, *Turbulence: The Legacy of A.N. Kolmogorov* (Cambridge University, Cambridge, England, 1996).

[4] G. Falkovich, K. Gawedzki and M. Vergassola, Rev. Mod. Phys. **73**, 913 (2001).

[5] V.S. L'vov, E. Podivilov, and I. Procaccia, Phys. Rev. E **55**,7030 (1997).

[6] L. Biferale, G. Bofetta, A. Celani, and F. Toschi, Physica (Amsterdam) **127D**, 187 (1999).

[7] D. Mitra and R. Pandit, Physica (Amsterdam) **318A**, 179 (2003).

[8] D. Mitra and R. Pandit, Phys. Rev. Lett. **93**, 2 (2004).

[9] D. Mitra and R. Pandit, Phys. Rev. Lett. **95**, 144501 (2005).

[10] In our studies of decaying turbulence, we restrict ourselves to initial conditions that lead to a cascade of energy from large to small length scales, where viscous dissipation becomes significant. Certain types of power-law initial conditions[11] do not lead to such a cascade and lead to trivial scaling.

[11] C. Kalelkar and R. Pandit, Phys. Rev. E, **69**, 046304 (2004) and references therein.

[12] P.C. Hohenberg and B.I. Halperin, Rev. Mod. Phys. **49**, 435 (2004) and references therein.

[13] P.M. Chaikin and T.C. Lubensky, *Principles of Condensed Matter Physics* (Cambridge University, Cambridge, England, 2004).

[14] A.N. Kolmogorov, Dokl. Akad. Nauk SSSR **30**, 301 (1941).

[15] A.N. Kolmogorov, Dokl. Akad. Nauk SSSR **31**, 538 (1941).

[16] R. Kraichnan, Phys. Fluids **11**, 945 (1968).

[17] R. Kraichnan, Phys. Rev. Lett. **72**, 1016 (1994).

[18] R. Kraichnan, Phys. Rev. Lett. **78**, 4922 (1997).

[19] A. M. Obukhov, Izv. Akad. SSSR, Serv. Geogr. Geofiz. **13**, 58 (1949).

[20] S. Corrsin, J. Appl. Phys. **22**, 469 (1951).

[21] Y. Kaneda, T. Ishihara, and K. Gotoh, Phys. Fluids **11**, 2154 (1999).

[22] V.I. Belinicher and V.S. L'vov, Sov. Phys. JETP **66**, 303(1987).

[23] D. Mitra, *Studies of Static and Dynamic Multiscaling in Turbulence*, PhD Thesis, Indian Institute of Science, Bangalore (2005), unpublished.

[24] E. Gledzer, Sov. Phys. Dokl. **18**, 216 (1973).

[25] K. Ohkitani and M. Yamada, Prog. Theor. Phys. **81**, 329 (1989).

[26] V.S. L'vov, R.A. Pasmanter, A. Pomyalov, and I. Procaccia, Phys. Rev. E **67**, 066310 (2003).

[27] G.I. Taylor, Proc. R. Soc. London, Ser A **151**, 421(1935).

[28] S.B. Pope, *Turbulent Flows* (Cambridge University, Cambridge, England, 2000).

[29] A. Wirth and L. Biferale, Phys. Rev. E **54**, 4982 (1996).

[30] P. Perlekar, D. Mitra, and R. Pandit, Phys. Rev. Lett. **97**, 264501 (2006).

[31] S. Dhar, A. Sain, and R. Pandit, Phys. Rev. Lett. **78**, 2964 (1997).

[32] D. Pisarenko, L. Biferale, D. Courvoisier, U. Frisch, and M. Vergassola, Phys. Fluids A **5**, 2533 (1993).

[33] L.P. Kadanoff, D. Lohse, J. Wang, and R. Benzi, Phys. Fluids. **7**, 617 (1995).

[34] M.H. Jensen, G. Paladin, and A. Vulpiani, Phys. Rev. A **45**, 7214 (1992).

[35] J. Zinn-Justin, *Quantum Field Theory and Critical Phenomena*(Oxford University Press, Oxford, 1999) p.59; this relation is also known as Novikov's theorem.

[36] V. S. L'vov and V. L. Lebedev, Phys. Rev. E **47**, 1794 (1993).

[37] F. Hayot and C. Jayaprakash, Phys. Rev. E **57**, R4867 (1998).

[38] F. Hayot and C. Jayaprakash, Int. J. Mod. Phys. B **14**, 1781 (2000).

[39] I. Arad, L. Biferale, A. Celani, I. Procaccia, and M. Vergassola, Phys. Rev. Lett. **87**, 164502 (2001).

[40] Y. Cohen, T. Gilbert, and I. Procaccia Phys. Rev. E **65**, 026314 (2002).

[41] R. H. Kraichnan, V. Yakhot, and S. Chen, Phys. Rev. Lett. **75**, 240 (1995).

[42] L. Chevillard, S. G. Roux, E. Leveque, N. Mordant, J. -F. Pinton, and A. Arneodo, Phys. Rev. Lett, **95**, 064501.

[43] A. La Porta, G.A. Voth, A.M. Crawford, J. Alexander, and E. Bodenschatz Nature **409**, 1017 (2001).

[44] N. Mordant, J. Delour, E. Leveque, A. Arneodo, and J. -F. Pinton, Phys. Rev. Lett, **89**, 254502.

Chapter 3

Dynamic Multiscaling in Two-dimensional Fluid Turbulence

In the previous Chapter we had discussed the universality of dynamic multiscaling for turbulence in fluids and passive-scalars in a variety of shell models for the three-dimensional Navier-Stokes and the advection-diffusion equations. As we had pointed out, such studies have not been carried out via Direct Numerical Simulations (DNS) of the Navier-Stokes equation or in experiments so far. In two dimensions there have been no such studies to the best of our knowledge. In this Chapter we address the issue of dynamic multiscaling in two-dimensional fluid flows. In particular we show that just like in three-dimensional flows there exists different ways of extracting time scales from time-dependent vorticity structure functions in two-dimensional turbulence. These lead to different dynamic-multiscaling exponents which are related to equal-time multiscaling exponents by different classes of bridge relations. We also find, surprisingly, that sweeping effects in two dimensions are eliminated because of the presence of air-drag induced Ekman friction. Thus the non-trivial dynamic exponents that we obtain by using quasi-Lagrangian vorticity structure functions are the same as those we obtain by using their Eulerian counterparts. [In contrast, in three-dimensions, because of the sweeping effect discussed in Chapter 2, it is believed that time-dependent

velocity structure functions yield trivial dynamic exponents.] We check this explicitly by detailed numerical simulations of statistically steady, forced, two-dimensional turbulence with Ekman friction.

We recall that, in critical phenomena, the scaling properties of both time-dependent and equal-time structure functions close to a critical point have been well understood for nearly four decades [1]. However, so far, we do not have an analogous understanding of structure functions in turbulent flows. Since the pioneering work of Kolmogorov [2] for three-dimensional turbulence which, based on dimensional grounds, predicts a simple scaling form for the equal-time velocity structure functions, various experiments and numerical simulations have shown that, unlike in critical phenomenon, the deviation from simple scaling is marked. Indeed the consensus is that there is multiscaling in equal-time velocity structure functions in three-dimensional homogeneous, isotropic turbulence [3]. Studies of time-dependent structure functions, in contrast to their equal-time counterparts, have been even rarer [4, 5, 6, 7, 8, 9, 10]. The reason for this partly stems from the sweeping effect which relates spatial and temporal scales linearly and thus give rise to trivial dynamic scaling of Eulerian structure functions (see Chapter 2). Moreover, as we shall show below, even when we eliminate such sweeping, by going to a Lagrangian or quasi-Lagrangian description, time-dependent structure functions give rise to an infinity of multiscaling exponents. The elucidation of dynamic multiscaling exponents have so far been limited to shell models for three-dimensional, homogeneous, isotropic turbulence [6, 7, 8, 9, 10] as we have discussed in Chapter 2. These studies have not yet been extended to DNS of three-dimensional flows.

The study of time-dependent structure functions has not been attempted for two-dimensional turbulence. Ever since the work of Kraichnan, we know that fluid turbulence in two dimensions is markedly different from that of three dimensions primarily because of its dual

cascade : the kinetic energy cascades from small to large length scales (this is the inverse cascade) and the enstrophy cascade in the opposite direction (this is the direct cascade) [11]. The scaling properties of various quantities in this direct cascade regime have been the subject of many studies. For statistically steady, two-dimensional turbulence, in the presence of an air-drag induced friction term, there is consensus that scaling exponents of equal-time, order-p structure functions of the velocity field depend linearly on p, whereas those of the vorticity field multiscale [12]. However, there is little consensus on the universality of these multiscaling exponents; in particular, they seem to depend on α, the coefficient of Ekman friction. Furthermore, there have been no studies of the statistical properties of time-dependent structure functions in two-dimensional turbulence. Given the rich equal-time multiscaling nature of the vorticity field, it behooves us to investigate dynamic multiscaling of vorticity structure functions in two-dimensional turbulence. Therefore we have initiated a systematic DNS of homogeneous, isotropic turbulence in thin fluid films with air-drag induced Ekman friction. Before giving the details of our study, we outline our principal results. We show, for the first time via a DNS of homogeneous, isotropic turbulence in two dimensions, how to obtain time-dependent quasi-Lagrangian structure functions for the vorticity field. From these and their Eulerian counterparts we extract integral and derivative time scales, and thence dynamic exponents, as we did for shell-model structure functions in Chapter 2. Here too we find that our data are consistent with linear bridge relations between dynamic exponents and equal-time exponents. We find, in accord with earlier studies of equal-time structure functions for two-dimensional turbulence, that velocity structure functions show simple scaling whereas the vorticity structure functions display multiscaling in the forward cascade regime if Ekman friction is present. The implications of this for dynamic exponents is elucidated here. We also find that Ekman

friction terms suppresses small-wave-vector modes and hence also the sweeping effect.

Our formulation for the forced, two-dimensional Navier-Stokes equation, with periodic boundary conditions, and the Ekman friction term uses the stream-function ψ and vorticity ω. The velocity $\mathbf{u}$ is a function of the x and y coordinates only and the vorticity, which is a pseudo-scalar, is defined as

$$\omega \equiv \nabla \times \mathbf{u}. \tag{3.1}$$

The incompressibility constraint,

$$\partial_x u_x + \partial_y u_y = 0 \tag{3.2}$$

ensures that the velocity is uniquely determined by the stream-function, ψ, as

$$\mathbf{u} \equiv (-\partial_y \psi, \partial_x \psi). \tag{3.3}$$

The Navier-Stokes equation, in the $\omega - \psi$ formulation, can thus be written as

$$\partial_t \omega - J(\psi, \omega) = \nu \nabla^2 \omega - \mu \omega + f, \tag{3.4}$$

where

$$\nabla^2 \psi \;\; = \;\; \omega, \tag{3.5}$$

$$J(\psi, \omega) \;\; \equiv \;\; (\partial_x \psi)(\partial_y \omega) - (\partial_x \omega)(\partial_y \psi), \tag{3.6}$$

f is the forcing term, and μ is the coefficient of the Ekman friction. To study dynamic multiscaling in time-dependent vorticity structure functions, we work with both Eulerian and quasi-Lagrangian fields. The quasi-Lagrangian velocity field, defined with respect to a Lagrangian particle which was at the point $\vec{r}_0$ at time t_0, is defined by

$$u^{\mathrm{ql}}(\vec{x}, t | \vec{r}_0, t_0) = \vec{u}(\vec{x} + \vec{r}(t | \vec{r}_0, t_0), t), \tag{3.7}$$

where $\vec{u}$ denotes the Eulerian velocity and $\vec{r}(t | \vec{r}_0, t_0)$ is the position of the Lagrangian particle at time t. Likewise, we can define the quasi-Lagrangian vorticity field ω^{ql}. The superscript ql is used to denote

quasi-Lagrangian. In short, the quasi-Lagrangian field is the field associated with a single Lagrangian particle which moves with the Eulerian flow.

The equal-time, order-p, vorticity structure functions, in homogeneous, isotropic turbulence

$$S_p(r) \equiv \langle [\delta\omega(r, t)]^p \rangle \sim r^{\zeta_p}, \tag{3.8}$$

for $\eta_d \ll r \ll L_{\mathrm{inj}}$, where

$$\delta\omega(\vec{r}, t) = [\omega(\vec{x} + \vec{r}, t) - \omega(\vec{x}, t)], \tag{3.9}$$

$\omega(\vec{x}, t)$ is the vorticity at point x and time t, L_{inj} is the large spatial scale at which energy is injected into the system, η_d is the small length scale at which enstrophy dissipation becomes significant and r lies in the forward-cascade range of length scales over which power-law scaling holds. ζ_p is the order-p, equal-time multiscaling exponent, and the angular brackets denote an average over the statistical steady state of the turbulent fluid. We will often be interested in the equal-time structure functions for the quasi-Lagrangian fields; in such cases we will use the superscript ql to make a distinction between the Eulerian quantities. Thus, for instance we will denote the equal-time structure function as $S_p^{\mathrm{ql}}(r)$ and the equal-time exponents ζ_p^{ql}.

As in Chapter 2 we now define the time-dependent, order-p structure function [13] associated with the Eulerian field ω is given by

$$\mathcal{F}_p(r, \{t_1, \dots, t_p\}) \equiv \langle [\delta\omega(r, t_1) \dots \delta\omega(r, t_p)] \rangle; \tag{3.10}$$

for the quasi-Lagrangian field ω^{ql} the time-dependent structure function $\mathcal{F}_p^{\mathrm{ql}}(r, \{t_1, \dots, t_p\})$ is defined in an analogous way by making use of the quasi-Lagrangian instead of the Eulerian field. We also observe that, by definition,

$$\mathcal{F}_p(r, \{t_1 = \dots = t_p = 0\}) = S_p(r) \tag{3.11}$$

and

$$\mathcal{F}_p^{\mathrm{ql}}(r, \{t_1 = \ldots = t_p = 0\}) = \mathcal{S}_p^{\mathrm{ql}}(r). \tag{3.12}$$

In this Chapter, we take the simplest case $t_1 = t_2 = \ldots = t_q \equiv t$ and $t_{q+1} = t_{q+2} = \ldots = t_p = 0$ and for simplicity write $\mathcal{F}_p(r, t)$ and $\mathcal{F}_p^{\mathrm{ql}}(r, t)$. The q-dependence does not affect dynamic-multiscaling exponents and hence is suppressed Given $\mathcal{F}_p(r, t)$, it is possible to extract a characteristic time scale $\tau_p(r)$ in many different ways. These time scales can, in turn, be used to extract the order-p *dynamic-multiscaling exponents* z_p via the dynamic-multiscaling Ansatz $\tau_p(r) \sim r^{z_p}$. In particular we concentrate on the order-p, degree-M, *integral* time scale

$$\mathcal{T}_{p,M}^I(r) \equiv \left[\frac{1}{\mathcal{S}_p(r)} \int_0^\infty \mathcal{F}_p(r, t) t^{(M-1)} dt \right]^{(1/M)}, \tag{3.13}$$

whence it is possible to extract the *integral* dynamic-multiscaling exponents $z_{p,M}^I$ by using the relation $\mathcal{T}_{p,M}^I \sim r^{z_{p,M}^I}$. We also look at the order-p, degree-M, *derivative* time scale, defined as,

$$\mathcal{T}_{p,M}^D(r) \equiv \left[\frac{1}{\mathcal{S}_p(r)} \frac{\partial^M}{\partial t^M} \mathcal{F}_p(r, t) \Big|_{t=0} \right]^{(-1/M)}; \tag{3.14}$$

the associated *derivative* dynamic-multiscaling exponents $z_{p,M}^D$ can be extracted via $\mathcal{T}_{p,M}^D \sim r^{z_{p,M}^D}$. Similarly, we obtain the time-scales $\mathcal{T}_{p,M}^{I,\mathrm{ql}}$ and $\mathcal{T}_{p,M}^{D,\mathrm{ql}}$ and their related exponents $z_{p,M}^{I,\mathrm{ql}}$ and $z_{p,M}^{D,\mathrm{ql}}$.

Given the clear evidence of multiscaling of equal-time vorticity structure functions in two-dimensional flows with Ekman friction (Fig. 3.3), we adapt the multifractal model [3] for 2D turbulent flows. It was shown earlier that for three-dimensional, homogeneous, isotropic turbulence the dynamic multiscaling exponents are related to the equal-time exponents ζ_p through bridge relations [6, 7, 8, 9, 10]. By analogy, the corresponding bridge relations for the vorticity exponents in two-dimensional turbulence should be

$$z_{p,M}^I = 1 + [\zeta_{p-M} - \zeta_p]/M, \tag{3.15}$$

$$z_{p,M}^D = 1 + [\zeta_p - \zeta_{p+M}]/M; \tag{3.16}$$

and

$$z_{p,M}^{I,\mathrm{ql}} = 1 + [\zeta_{p-M}^{\mathrm{ql}} - \zeta_p^{\mathrm{ql}}]/M, \tag{3.17}$$

$$z_{p,M}^{D,\mathrm{ql}} = 1 + [\zeta_p^{\mathrm{ql}} - \zeta_{p+M}^{\mathrm{ql}}]/M. \tag{3.18}$$

For homogeneous, isotropic three-dimensional turbulence a detailed derivation of the bridge relations is given in Refs [6, 7, 8, 9, 10] and Chapter 2.

To obtain evidence for dynamic multiscaling and to verify our bridge relations we integrate the two-dimensional Navier-Stokes equations by using a pseudospectral method and a second-order Runge-Kutta scheme for time marching (see Appendix B). The fluid is forced deterministically on the second shell ($k = 2$) and we use an Ekman coefficient of friction $\mu = 0.1$, kinematic viscosity $\nu = 10^{-4}$ and $N = 2048^2$ collocation points. In our simulations, a single Lagrangian particle is tracked by the method of bilinear interpolation (see Appendix C). The quasi-Lagrangian field is then calculated by using Eq. (3.2).

The vorticity field $\omega = \langle\omega\rangle + \omega'$, is composed of the mean flow $\langle\omega\rangle$, where the angular brackets imply time averages, and fluctuations ω' about the mean. We make a similar decomposition for the quasi-Lagrangian field, namely, $\omega^{\mathrm{ql}} = \langle\omega^{\mathrm{ql}}\rangle + \omega'^{\mathrm{ql}}$. In Fig. (3.1), we show a snapshot of the quasi-Lagrangian vorticity field in a statistically steady state.

To obtain good statistics, it is important to eliminate any anisotropy in the flow. This is most conveniently done by subtracting out the mean flow from the field and then using only the fluctuations to calculate statistical quantities. Hence we use ω' (or ω'^{ql}) to calculate the order-p, equal-time and time-dependent, structure functions. The equal-time exponents are extracted as follows: We first redefine the order-p structure function

$$S_p\omega(\mathbf{r_c}, \mathbf{R}) \equiv \langle|\omega'(\mathbf{r_c} + \mathbf{R}) - \omega'(\mathbf{r})|^p\rangle, \tag{3.19}$$
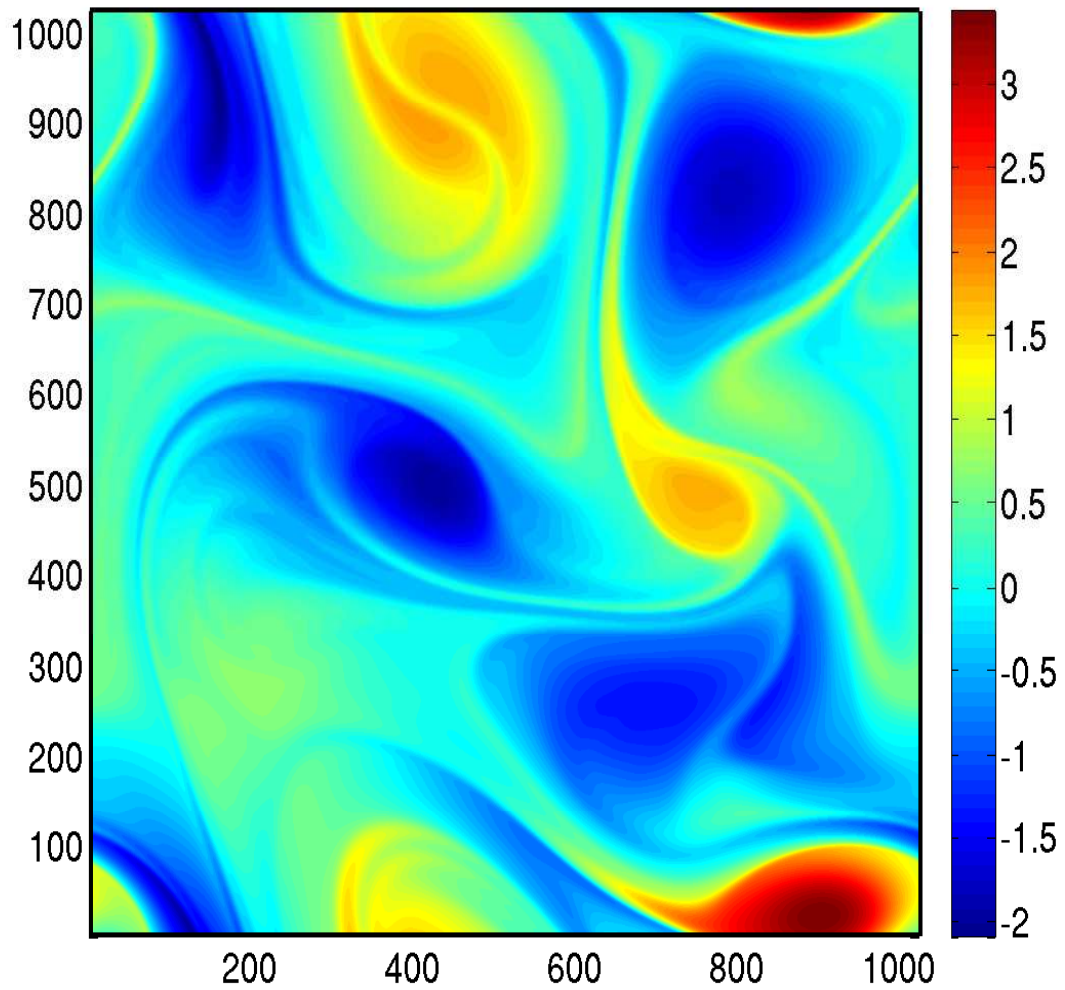
Figure 3.1: A snapshot of the quasi-Lagrangian vorticity field in the statistically steady state.

where **R** has magnitude R and $\mathbf{r_c}$ is an origin. We next use

$$S_2(\mathbf{R}) \equiv \langle S_2^\omega(\mathbf{r_c}, \mathbf{R})\rangle_{\mathbf{r_c}}, \tag{3.20}$$

where the subscript $\mathbf{r_c}$ denotes an average over the origin (we use $\mathbf{r_c} = (i, j), 2 \leq i, j \leq 5$). These averaged structure functions are isotropic; the same method is applied for the quasi-Lagrangian case. In Figs. (3.2) and (3.3) we show representative pseudocolor plots for third-order, equal-time, vorticity Eulerian and quasi-Lagrangian structure functions, respectively. The isotropic parts of such structure functions are obtained, by using an $SO(2)$ decomposition [14], via an integration over the angle θ that **R** makes with the x axis. We thus get $S_p(R) \equiv \int_0^{2\pi} S_p(\mathbf{R}) d\theta$ and $S_p^{\text{ql}}(R)$.

Having obtained the order-p, equal-time structure functions, we extract the scaling exponents ζ_p and ζ_p^{ql} through linear fits in scaling ranges of log-log plots of $S_p(r)$ and $S_p^{\text{ql}}(r)$, respectively, versus r. To calculate these exponents and their error bars, in a given plot we fit in 30 different regions of the scaling range and obtain a set of 30 different exponents. The mean of these yield ζ_p and ζ_p^{ql} and we quote their standard deviations as error bars. The equal-time multiscaling exponents for $1 \leq p \leq 6$ versus p for both the Eulerian vorticity fields (Column 2, Table 1) and the quasi-Lagrangian (Column 2, Table 2) and are shown in Fig. (3.4). We see that the two sets of exponents are equal within error bars. We also find that not only do the two sets of exponents agree, the Eulerian and quasi-Lagrangian structure functions themselves are in agreement with each other. We show an illustrative plot of this for the third-order structure function in Fig. (3.5).

Next, we look at the dynamic scaling exponents. We obtain the time-dependent structure function in a manner similar to the one detailed above for equal-time structure functions : We calculate the vorticity differences, in the isotropic sector, at different times and use such a time series to calculate $\mathcal{F}_p(r, t)$ and $\mathcal{F}_p^{\text{ql}}(r, t)$. Having obtained the order-p, time-dependent structure function of the quasi-Lagrangian
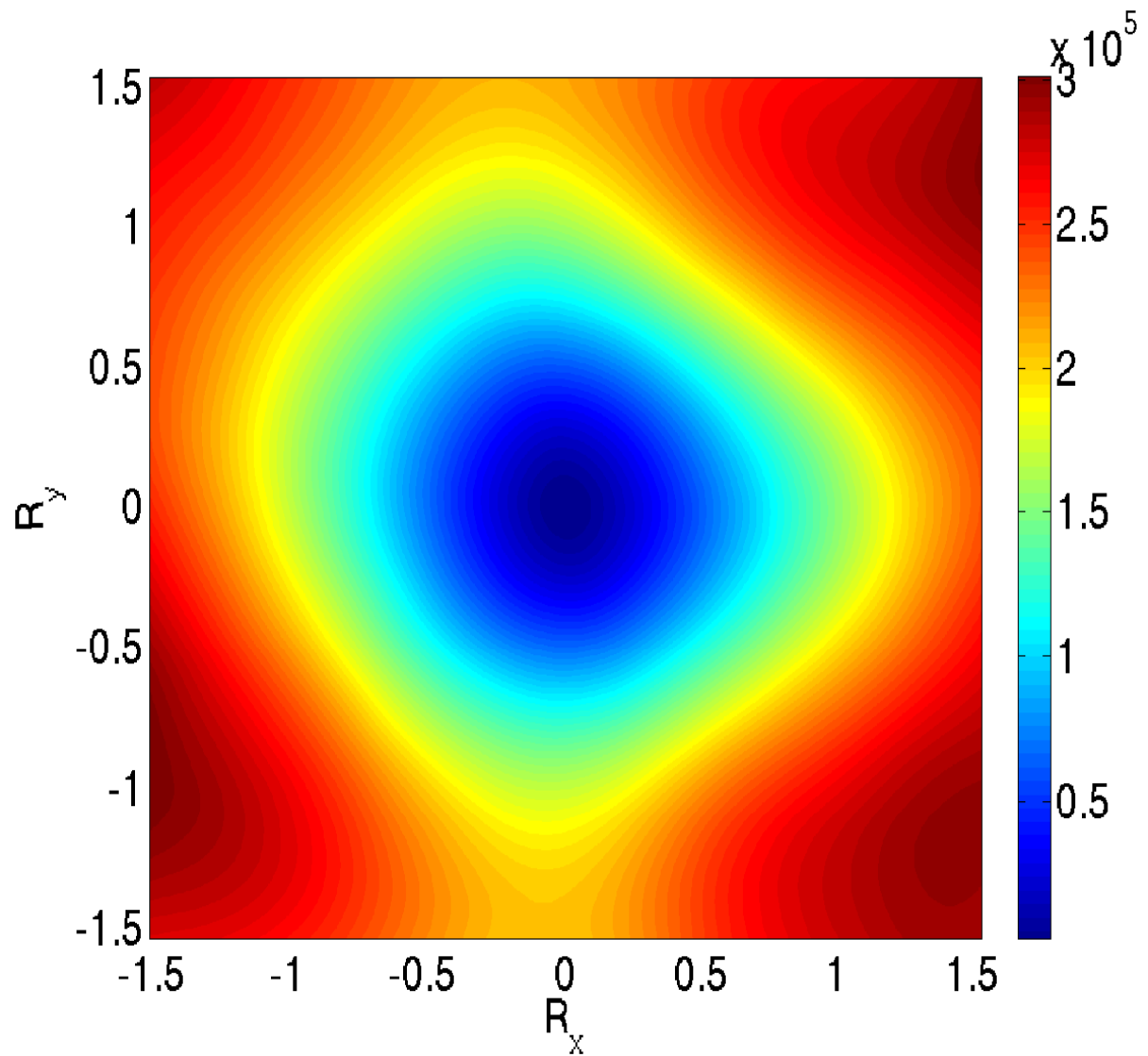
Figure 3.2: Pseudocolor plot of the equal-time, third-order vorticity Eulerian structure function averaged over different centers.
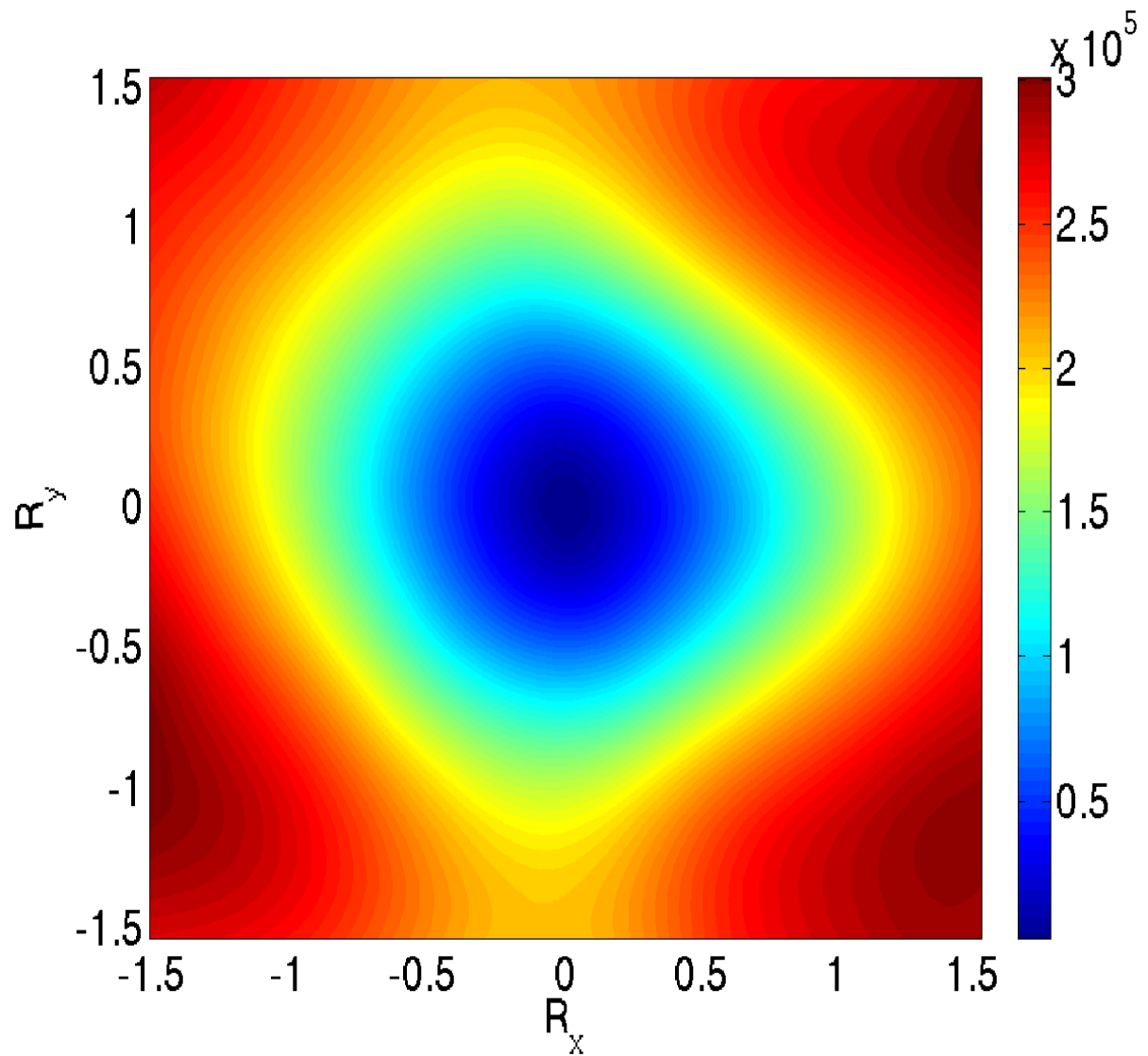
Figure 3.3: Pseudocolor plot of the equal-time, third-order vorticity quasi-Lagrangian structure function averaged over different centers.
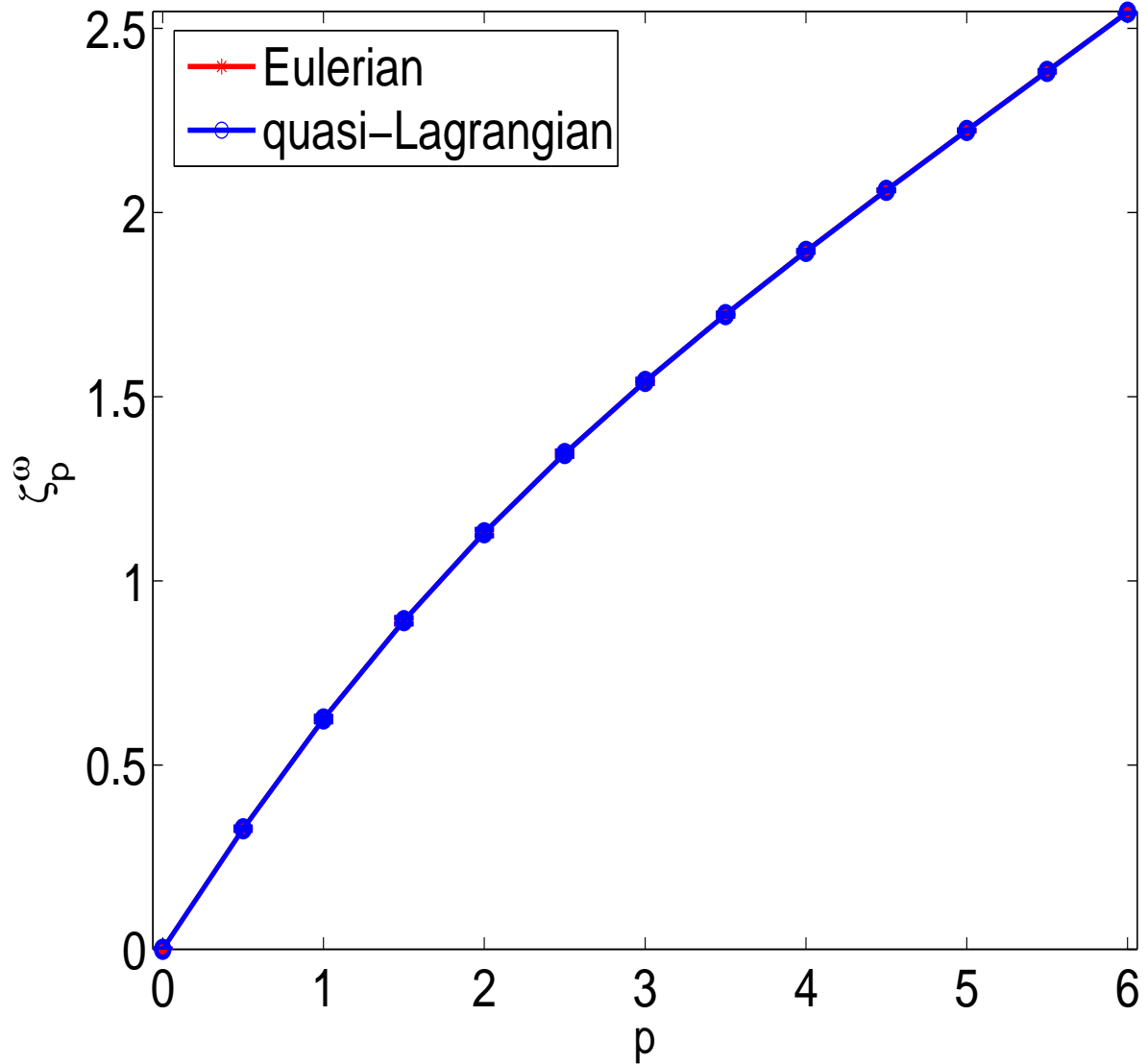
Figure 3.4: The equal-time exponents ζ_p, for the vorticity field, versus p for both the Eulerian (in red) and quasi-Lagrangian (in blue) fields. The two sets of exponents are equal to each other within error bars. The error bars are seen to be comparable to the symbol size.
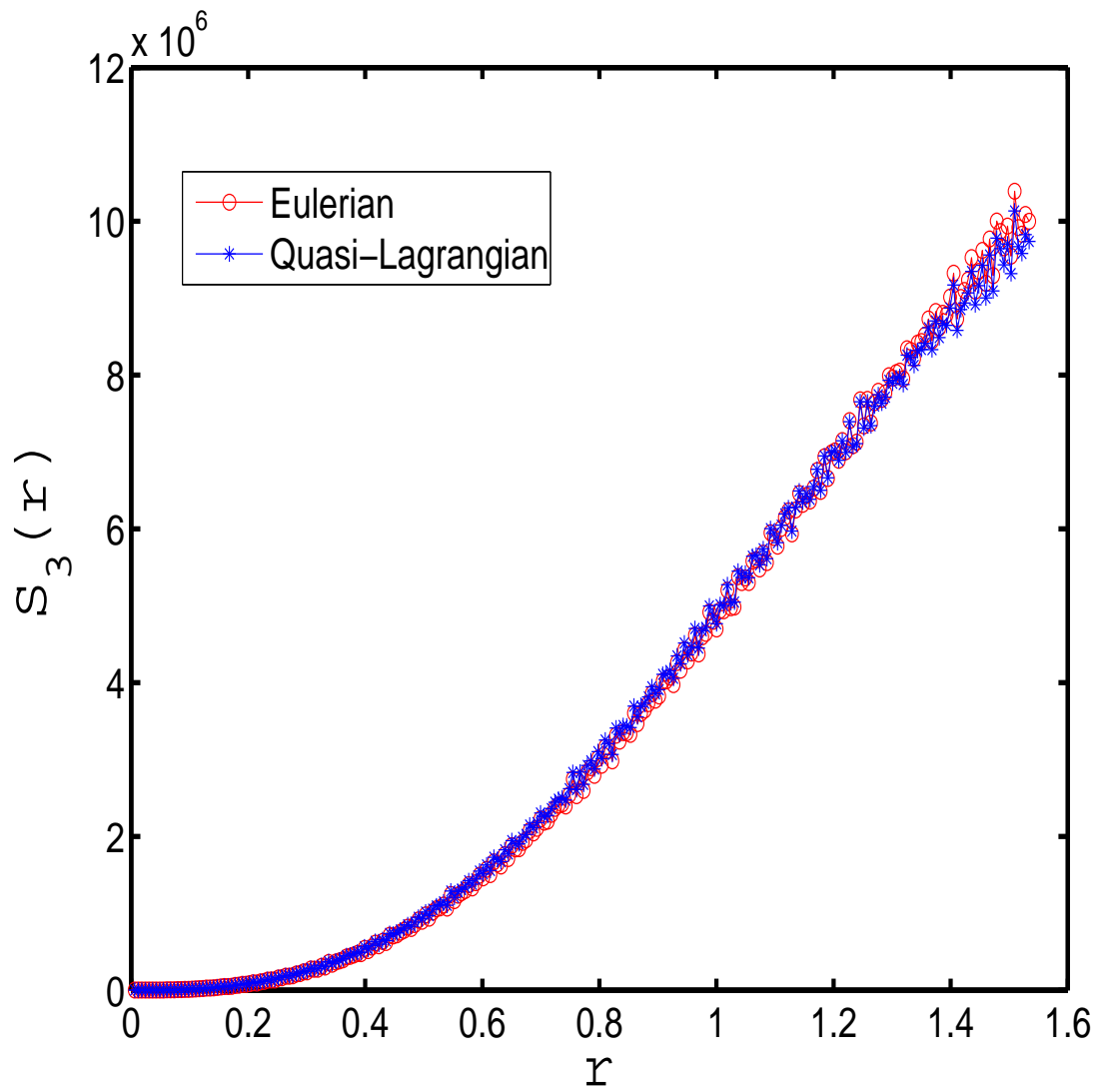
Figure 3.5: A comparison of the third-order equal-time structure function for the Eulerian (in red) and quasi-Lagrangian fields (in blue) versus the separation r.

field it is possible to calculate the degree-1, order-p integral-time scale. Although in principle, we should integrate over time from $t = 0$ to $t = \infty$, in practice, because of poor statistics at long times, we integrate $\mathcal{F}_p^{\mathrm{ql}}(r, t)$ from $t = 0$ to $t = t_*$, where t_* is the time at which $\mathcal{F}_p^{\mathrm{ql}}(r, t) = \epsilon$; we choose $\epsilon = 0.6$ but have checked that the results do not change, within error bars for $0.5 \leq \epsilon \leq 0.75$. From a log-log plot of $\mathcal{T}_{p,1}^{I,\mathrm{ql}}$ versus r, we extract the dynamic multiscaling exponent $z_{p,1}^{I,\mathrm{ql}}$. In Fig. (3.9) we show a representative plot, on a log log scale, of $\mathcal{T}_{2,1}^{I,\mathrm{ql}}$ versus r; a linear fit yields the dynamic multiscaling exponent $z_{2,1}^{I,\mathrm{ql}}$. We show the same for the Eulerian field in Fig. (3.7). Similarly, we calculate the degree-2, order-p derivative time exponents by using a sixth-order finite difference scheme to obtain $\mathcal{T}_{p,2}^{D,\mathrm{ql}}$ from which we calculate $z_{p,2}^{D,\mathrm{ql}}$. In Fig. (3.8) we show a representative plot of the $\mathcal{T}_{6,2}^{D,\mathrm{ql}}$ versus r. We use a linear fit to obtain the dynamic multiscaling exponent $z_{6,2}^{D,\mathrm{ql}}$.

Our different dynamic multiscaling exponents and their errorbars are calculated from loglog plots of the different time-scales versus the separation in the same way as has been detailed for the case of the equal-time exponents. In Table 1, we compare the dynamic multiscaling exponents obtained from our numerical simulation with those obtained from the linear bridge relations (by using equal-time exponents which are obtained from our DNS). We see that the dynamic multiscaling exponents, obtained through these two different ways, are in agreement with each other within errorbars (see Table 1).

We have shown systematically how different ways of extracting time scales from time-dependent vorticity structure functions lead to different sets of dynamic-multiscaling exponents, which are related in turn to the equal-time multiscaling exponents by different classes of bridge relations. Our extensive numerical study, the first of its kind in fluid turbulence, of two-dimensional flows verifies explicitly that such bridge relations hold. Importantly our work shows that in two-dimensional turbulence the Ekman friction controls the size of the
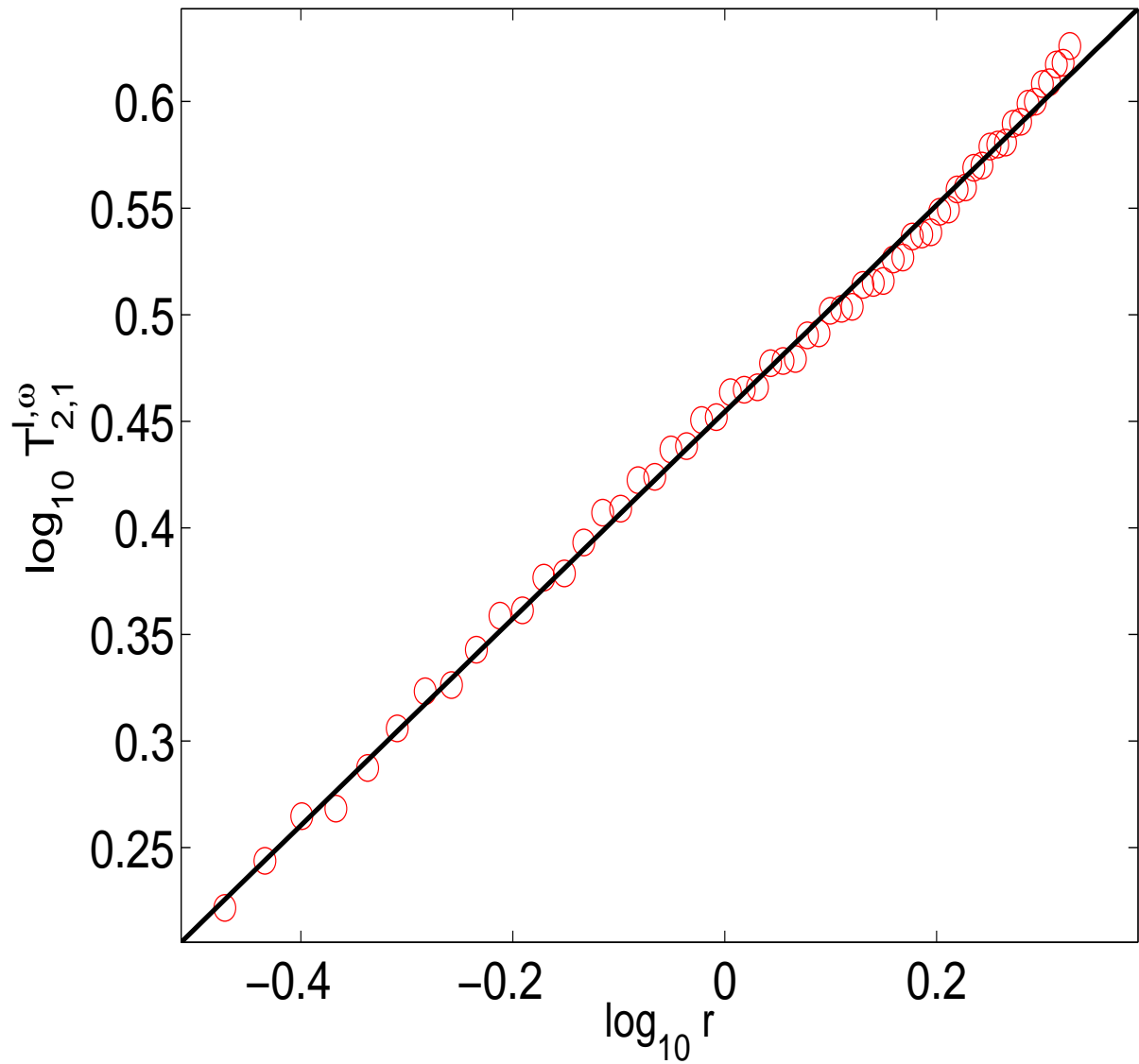
Figure 3.6: A loglog plot of $T_{2,1}^{I,ql}$ versus the separation r; the data points are shown by open red circles and the straight black line shows the line of best fit in the inertial range.
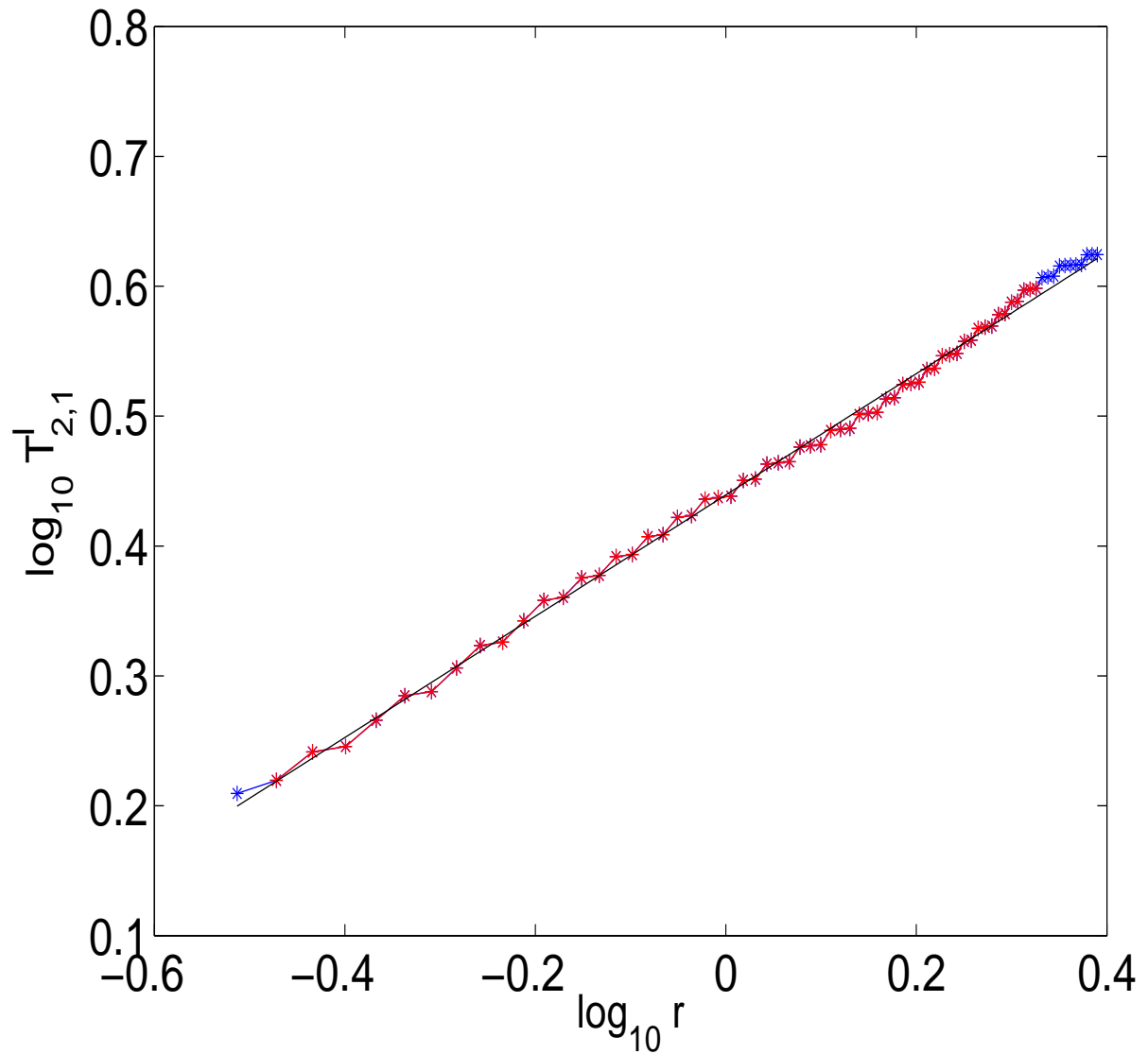
Figure 3.7: A loglog plot of $T_{2,1}^I$ versus the separation r; the data points are shown by blue circles, the range over which we fit is shown by red circles and the straight black line shows the line of best fit in the inertial range.
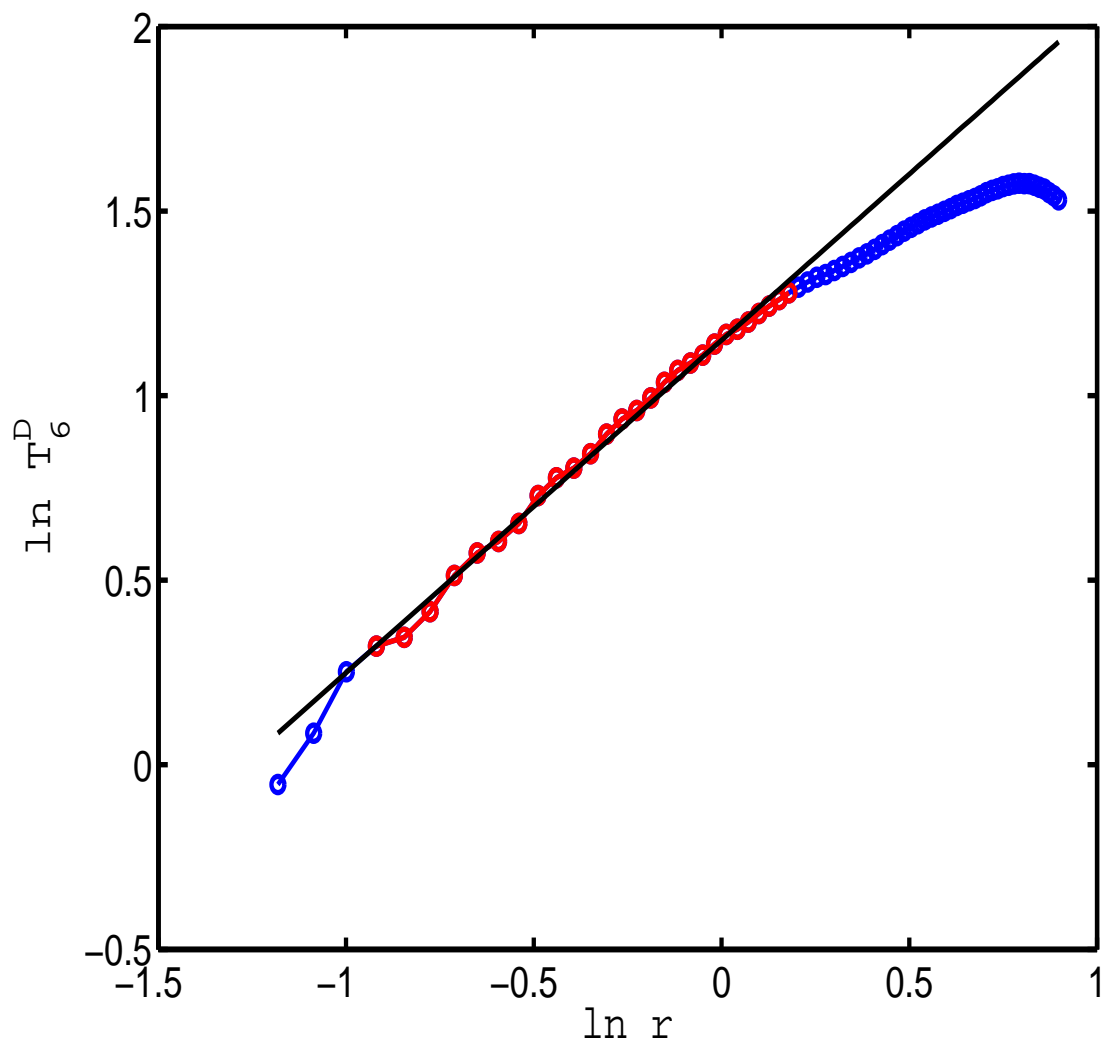
Figure 3.8: A loglog plot of $T_{6,2}^{D,\mathrm{ql}}$ versus the separation r; the data points are shown by open red circles and the straight black line shows the line of best fit in the inertial range.

order(p)	ζ_p	$z^I_{p,1}$[Eq.(3.18)]	$z^I_{p,1}$	$z^D_{p,2}$[Eq.(3.18)]	$z^D_{p,2}$
1	0.625 ± 0.003	0.375 ± 0.007	0.37 ± 0.02	0.541 ± 0.008	0.53 ± 0.02
2	1.131 ± 0.005	0.49 ± 0.02	0.48 ± 0.01	0.618 ± 0.009	0.62 ± 0.02
3	1.541 ± 0.005	0.58 ± 0.01	0.57 ± 0.01	0.66 ± 0.01	0.67 ± 0.01
4	1.895 ± 0.004	0.65 ± 0.01	0.65 ± 0.01	0.675 ± 0.008	0.66 ± 0.03
5	2.222 ± 0.008	0.67 ± 0.01	0.65 ± 0.02	0.70 ± 0.01	0.70 ± 0.02
6	2.544 ± 0.004	0.68 ± 0.01	0.66 ± 0.02	0.71 ± 0.02	0.71 ± 0.03

Table 3.1: Order-p (column 1); equal-time Eulerian exponents ζ^{ql}_p (column 2); integral-scale dynamic-multiscaling exponent $z^I_{p,1}$ (column 3) from the bridge relation and the values of ζ^{ql}_p in column 2; $z^I_{p,1}$ from our calculation using time-dependent structure functions (column 4); the derivative-time exponents $z^D_{p,2}$ (column 6) from the bridge relation and the values of ζ^{ql}_p in column 2; $z^{D,u}_{p,2}$ from our calculation using time-dependent structure function (column 7). The error estimates are obtained as described in the text.

order(p)	ζ^{ql}_p	$z^{I,\mathrm{ql}}_{p,1}$[Eq.(3.18)]	$z^{I,\mathrm{ql}}_{p,1}$	$z^{D,\mathrm{ql}}_{p,2}$[Eq.(3.18)]	$z^{D,\mathrm{ql}}_{p,2}$
1	0.625 ± 0.005	0.375 ± 0.005	0.37 ± 0.03	0.54 ± 0.01	0.53 ± 0.01
2	1.131 ± 0.005	0.49 ± 0.01	0.48 ± 0.01	0.62 ± 0.01	0.62 ± 0.01
3	1.540 ± 0.007	0.58 ± 0.01	0.57 ± 0.01	0.66 ± 0.02	0.67 ± 0.01
4	1.896 ± 0.006	0.65 ± 0.01	0.65 ± 0.01	0.67 ± 0.01	0.67 ± 0.03
5	2.221 ± 0.009	0.67 ± 0.02	0.65 ± 0.02	0.70 ± 0.01	0.70 ± 0.02
6	2.554 ± 0.007	0.68 ± 0.02	0.66 ± 0.02	0.71 ± 0.02	0.71 ± 0.02

Table 3.2: Order-p (column 1); equal-time quasi-Lagrangian exponents ζ^{ql}_p (column 2); integral-scale dynamic-multiscaling exponent $z^I_{p,1}$ (column 3) from the bridge relation and the values of ζ^{ql}_p in column 2; $z^I_{p,1}$ from our calculation using time-dependent structure functions (column 4); the derivative-time exponents $z^D_{p,2}$ (column 6) from the bridge relation and the values of ζ^{ql}_p in column 2; $z^{D,u}_{p,2}$ from our calculation using time-dependent structure function (column 7). The error estimates are obtained as described in the text.

largest vortices and thus provides a cut-off scale. To see this more clearly we performed a simulation with 1024^2 collocation points and a forcing at wave-vector 80 with different values of μ. Such a simulation resolves the inverse cascade regime in the statistically steady state. In Fig. (**??**) we see that clearly with increasing values of μ a cut-off in the inverse cascade occurs at larger and larger values of k. Or in other words, Ekman friction produces a regularisation of the flow which inhibits infrared divergences. Thus the numerical evidence seems to suggest that for such flows sweeping is eliminated and, hence, Eulerian and quasi-Lagrangian statistics lead to the same dynamic exponents.

In conclusion, we find that our results are in close agreement with those found in shell models for three-dimensional turbulence. Analogous studies in a DNS of three-dimensional, homogeneous, isotropic turbulence still remains a challenge. Experimental studies of Lagrangian quantities in three-dimensional turbulence have been increasing over the past few years [17]. We hope our work will encourage studies of dynamic multiscaling in such experiments.
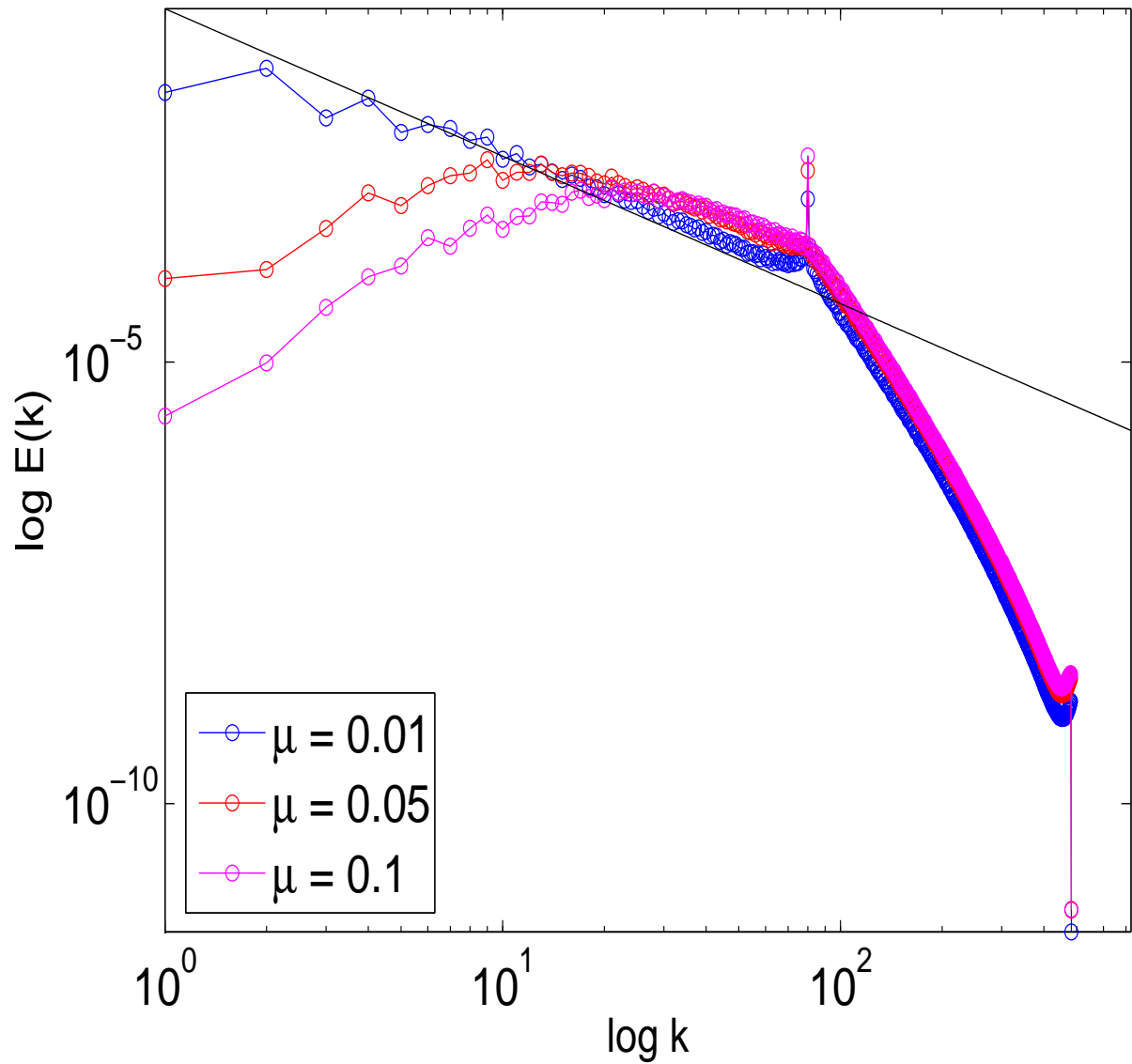
Figure 3.9: A log log plot of the energy spectrum versus the wavevector k for various values of μ. The injection scale is at $k = 80$, as shown by the little peak there, and the thick black line shows the K41 scaling.

Appendix B

Algorithm for the Eulerian code

We consider the Navier-Stokes equation in 2D with periodic boundary conditions. Our formulation uses the stream-function ψ and vorticity ω. The velocity $\mathbf{u}$ is a function of the x and y coordinates only. The vorticity, which is a pseudo-scalar, is defined as

$$\omega \equiv \nabla \times \mathbf{u}. \tag{B.1}$$

The incompressibility constraint

$$\partial_x u_x + \partial_y u_y = 0 \tag{B.2}$$

ensures that the velocity is uniquely determined by the stream-function via

$$\mathbf{u} \equiv (-\partial_y \psi, \partial_x \psi). \tag{B.3}$$

The Navier-Stokes equation, in the $\omega - \psi$ formulation, can be written as follows :

$$\partial_t \omega - J(\psi, \omega) = \nu \nabla^2 \omega + f; \tag{B.4}$$

$$\nabla^2 \psi = \omega; \tag{B.5}$$

here

$$J(\psi, \omega) \equiv (\partial_x \psi)(\partial_y \omega) - (\partial_x \omega)(\partial_y \psi). \tag{B.6}$$

Our pseudospectral DNS proceeds along the following lines :

145

We first write the Navier-Stokes equation in the following equivalent form :

$$\hat{\psi} = -\frac{1}{k^2}\hat{\omega};\tag{B.7}$$

$$\partial_t\omega + \partial_x(u_x\omega) + \partial_y(u_y\omega) = \nu\nabla^2\omega + f,\tag{B.8}$$

where u_x and u_y are, respectively, the x and y component of the velocity vector **u**. f is the source function or the forcing. The spatial Fourier transform of this equation is

$$\partial_t\hat{\omega} = \imath(k_x\widehat{u_x\omega} + k_y\widehat{u_y\omega}) - \nu k^2\hat{\omega},\tag{B.9}$$

where carets denote Fourier transformation. Our algorithm proceeds via the following steps:

1. Start with $\hat{\omega}$ in Fourier space.

2. Evaluate the stream function $\hat{\psi}$ and from it the velocities in Fourier space $\hat{u}_x$ and $\hat{u}_y$:

$$\hat{\psi} = -\frac{1}{k^2}\hat{\omega};\tag{B.10}$$
$$\hat{u}_x = \imath k_y\hat{\psi};\tag{B.11}$$
$$\hat{u}_y = -\imath k_x\hat{\psi}.\tag{B.12}$$
$$\tag{B.13}$$

3. Inverse Fourier Transform (IFT) $\hat{\omega}$ to real space ω. IFT $\hat{u}_x \rightarrow u_x$ and $\hat{u}_y \rightarrow u_y$.

4. Evaluate ωu_x and ωu_y in real space.

5. Fourier Transform (FT) $\omega u_x \rightarrow \widehat{\omega u_x}$ and $\omega u_y \rightarrow \widehat{\omega u_y}$. Let us define

$$\hat{N} = \imath(k_x\widehat{u_x\omega} + k_y\widehat{u_y\omega}).\tag{B.14}$$

Then the evolution equation (B.9) becomes:

$$\partial_t\hat{\omega} = \hat{N} - \nu k^2\hat{\omega}.\tag{B.15}$$

6. We now solve this equation by using the second-order Runge–Kutta scheme. Equation (B.15) can be written as

$$\partial_t(e^{\nu k^2 t}\hat{\omega}) = e^{\nu k^2 t}\hat{\mathcal{N}}. \tag{B.16}$$

This suggests the following scheme

$$\hat{\omega}_* = e^{-\nu k^2 \delta t/2}\left\{\hat{\omega}_n + \frac{\delta t}{2}\hat{\mathcal{N}}[\hat{\omega}_n]\right\}; \tag{B.17}$$

$$\hat{\omega}_{**} = e^{-\nu k^2 \delta t}\hat{\omega}_n + \delta t e^{-\nu k^2 \delta t/2}\hat{\mathcal{N}}[\hat{\omega}_*]; \tag{B.18}$$

$$\hat{\omega}_{n+1} = \hat{\omega}_{**}. \tag{B.19}$$

Appendix C

Lagrangian particle tracking

In this Appendix we describe how a Lagrangian particle is tracked in a 2D flow. Let us assume that the tracer particle is at a point (x, y) where (x, y) does not correspond to any point on the Eulerian grid. Let us assume therefore that this particle is somewhere inside a square whose vertices are the Eulerian grid points (x_i, y_j), (x_{i+1}, y_j), (x_i, y_{j+1}), and (x_{i+1}, y_{j+1}). To know the position of the particle at the next time step, we need first to know the velocity of the particle at its present position; then we use Newton's laws to update the particle position at the next time step. Thus, if (u_x, u_y) is the Eulerian velocity at the point (x, y), then, after a time step δt, the particle will be in the new position (x', y'), where

$$x' = x + u_x \delta t;$$
$$y' = y + u_y \delta t. \tag{C.1}$$

Therefore, to track a particle efficiently it is important to interpolate the velocity field at an off-grid position from the known velocities at the neighbouring grid points. The bilinear-interpolation method gives the following interpolation formula for each component of $u(x, y)$:

$$u(x, y) = \quad u(x_i, y_j) \quad \frac{(x_{i+1} - x)(y_{j+1} - y)}{(x_{i+1} - x_i)(y_{j+1} - y_j)} +$$
$$u(x_{i+1}, y_j) \quad \frac{(x - xi)(y_{i+1} - y)}{(x_{i+1} - x_i)(yj + 1 - y_j)} +$$

148

$$u(x_i, y_{j+1}) \ \frac{(x_{i+1} - x)(y - y_j)}{(x_{i+1} - x_i)(y_{j+1} - y_j)} +$$

$$u(x_i, y_{j+1}) \ \frac{(x - x_i)(y - y_j)}{(x_{i+1} - x_i)(y_{j+1} - y_j)}. \tag{C.2}$$

Bibliography

[1] P. C. Hohenberg and B. I. Halperin, *Rev. Mod. Phys.* **49** 435 (1977) and references therein.

[2] A.N. Kolmogorov, *Dokl. Acad. Nauk USSR* **30** 9 (1941).

[3] U. Frisch, *Turbulence: The Legacy of A.N. Kolmogorov* (Cambridge University Press, Cambridge, 1996).

[4] V.S. L'vov, E. Podivilov, and I. Procaccia, Phys. Rev. E **55**,7030 (1997).

[5] L. Biferale, G. Bofetta, A. Celani, and F. Toschi, Physica (Amsterdam) **127D**, 187 (1999).

[6] D. Mitra and R. Pandit, Physica (Amsterdam) **318A**, 179 (2003).

[7] D. Mitra and R. Pandit, Phys. Rev. Lett. **93**, 2 (2004).

[8] D. Mitra and R. Pandit, Phys. Rev. Lett. **95**, 144501 (2005).

[9] R. Pandit, S.S. Ray, and D. Mitra, Eur. Phys. J. B **64**, 463 (2008).

[10] S.S. Ray, D. Mitra, and R. Pandit, New J. Phys. **10**, 033003 (2008).

[11] R. Kraichnan, Phys. Fluids **10**, 1417 (1967); C. Leith, Phys. Fluids, **11**, 671 (1968); G. Batchelor, Phys. Fluids Suppl. II **12**, 233 (1969).

[12] G. Boffetta, J. Fluid Mech. **589**, 253 (2007); Y.-K. Tsang, E. Ott, T.M. Antonsen, and P.N. Guzdar, Phys. Rev. E **71**, 066313 (2005);

P. Perlekar and R. Pandit, New Journal of Physics, 11, 073003 (2009).

[13] V.S. L'vov, E. Podivilov, and I. Procaccia, *Phys. Rev. E* **55** 7030 (1997).

[14] E. Bouchbinder, I. Procaccia, and S. Sela, Phys. Rev. Lett. **95**, 255503 (2005).

[15] F. Hayot and C. Jayaprakash, *Phys. Rev. E* **57** R4867 (1998).

[16] F. Hayot and C. Jayaprakash, *Int. J. Mod. Phys. B*, **14**, 1781 (2000).

[17] See, e.g., S. Ott and J. Mann, J. Fluid Mech. **422** 207 (2000); A. La Porta, G.A. Voth, A.M. Crawford, J. Alexander, and E. Bodenschatz, Nature(London) **409** (2002); N. Mordant, P. Metz, O. Michel, and J.-F. Pinton, Phys. Rev. Lett. **87** 214501 (2001).

Chapter 4

Hyperviscosity, Galerkin Truncation and Bottlenecks in Turbulence

In this Chapter we study the bottleneck in the energy spectrum of turbulent flows in three dimensions as well as the hyperviscous Burgers equation. We interpret the bottleneck as stemming from incomplete thermalization. The EQDNM calculations were done by S. Kurien and J-Z. Zhu in Los Alomos and the work was done in collaboration with U. Frisch. W. Pauls and R. Pandit. A. Wirth was the first person, to our knowledge, to observe this phenomenon in the hyperviscous Burgers equation in the 1990s. We follow Ref. [1] closely for most of this Chapter.

A single Maxwell daemon embedded in a turbulent flow would hardly notice that the fluid is not exactly in thermal equilibrium because incompressible turbulence, even at very high Reynolds numbers, constitutes a tiny perturbation on thermal molecular motion. Dissipation in real fluids is just the transfer of macroscopically organized (hydrodynamic) energy to molecular thermal energy. Artificial microscopic systems can act just like the real one as far as the emergence of hydrodynamics is concerned; for instance, in lattice gases the "molecules" are discrete Boolean entities [2] and thermalization

152

is easily observed at high wavenumbers [3]. Another example has been found recently by Cichowlas *et al.* [4] wherein the Euler equations of ideal non-dissipative flow are (Galerkin) truncated by keeping only a finite – but large – number of spatial Fourier harmonics. The modes with the highest wavenumbers k then rapidly thermalize through a mechanism discovered by T.D. Lee [5] and studied further by R.H. Kraichnan [6], leading in three dimensions (3D) to an equipartition energy spectrum $\propto k^2$. The thermalized modes act as a fictitious microworld on modes with smaller wavenumbers in such a way that the usual dissipative Navier–Stokes dynamics is recovered at large scales [1].

All the known systems presenting thermalization are *conservative*. As we shall show themalization may be present in *dissipative* hydrodynamic systems when the dissipation rate increases so fast with the wavenumber that it mimics ideal hydrodynamics with a Galerkin truncation. This is best understood by considering hydrodynamics with *hyperviscosity*: the usual momentum diffusion operator (a Laplacian) is replaced by the αth power of the Laplacian, where $\alpha > 1$ is the dissipativity. Hyperviscosity is frequently used in turbulence modeling to avoid wasting numerical resolution by reducing the range of scales over which dissipation is effective [7].

The unforced hyperviscous 1D Burgers and multi-dimensional incompressible Navier–Stokes (NS) equations are:

$$\partial_t v + v \partial_x v = -\mu k_{\mathrm{G}}^{-2\alpha}(-\partial_x^2)^\alpha v; \tag{4.1}$$

$$\partial_t \boldsymbol{v} + \boldsymbol{v} \cdot \nabla \boldsymbol{v} = -\nabla p - \mu k_{\mathrm{G}}^{-2\alpha}(-\nabla^2)^\alpha \boldsymbol{v}; \quad \nabla \cdot \boldsymbol{v} = 0 \,. \tag{4.2}$$

The equations must be supplemented with suitable initial and boundary conditions. We employ 2π-periodic boundary conditions in space, so that we can use Fourier decompositions such as $\boldsymbol{v}(\boldsymbol{x}) = \sum_k \hat{\boldsymbol{v}}_k \, \mathrm{e}^{\mathrm{i}\,k\cdot x}$.

---

[1]A similar mechanism, involving sound waves, explains why superfluid and ordinary turbulence can be similar; see C. Nore, M. Abid, and M.E. Brachet, Phys. Rev. Lett. **78**, 3896 (1997).

Note that minus the Laplacian is a positive operator, with Fourier transform k^2, which can be raised to an arbitrary power α. The coefficient μ is taken positive to make the hyperviscous operator dissipative. The *Galerkin wavenumber* $k_G > 0$ is chosen *off-lattice* so that no wavenumber is exactly equal to k_G. In Fourier space the hyperdissipation rate is $\mu(k/k_G)^{2\alpha}$, where $k \equiv |\boldsymbol{k}|$.

If we now hold μ and k_G fixed and let $\alpha \to \infty$ we see that the hyperdissipation rate tends to zero, for $k < k_G$, and to infinity, for $k > k_G$. This implies that *in the limit of infinite dissipativity, the solution of a hyperviscous hydrodynamical equation converges to that of the corresponding inviscid equations Galerkin-truncated at wavenumber k_G.*

To define inviscid Galerkin truncation precisely, we rewrite Eqs. (4.1) and (4.2) in the abstract form $\partial_t v = B(v, v) + L_\alpha v$, where B is a quadratic form representing the nonlinear term (including the pressure p in the NS case). The truncation projector P_{k_G} is the linear, low-pass filtering operator that, when applied to v, sets all Fourier harmonics with $k > k_G$ to zero. The inviscid, Galerkin-truncated equation, with initial condition v_0, is

$$\partial_t u = P_{k_G} B(u, u), \qquad u_0 = P_{k_G} v_0 \ . \tag{4.3}$$

Since u can be written in terms of a finite number of modes with $k < k_G$, Eq. (4.3) is a dynamical system of finite dimension. In addition to momentum, it conserves the energy and other quadratic invariants for the inviscid equations [6]. There is good numerical evidence – but no rigorous proof – that the solutions of the Galerkin-truncated inviscid Burgers and 3D Euler equations tend, at large times, to statistical equilibria defined by their respective invariants.

A rigorous proof of the convergence, as $\alpha \to \infty$, of solutions of the hyperviscous Burgers equation (4.1) and of the hyperviscous NS equation (4.2) in any dimension to those of the associated Galerkin-truncated, inviscid equation will be given elsewhere. It uses standard tools of functional analysis; note that the formidable mathematical

difficulties that beset the ordinary ($\alpha = 1$) 3D NS equation disappear for $\alpha \geq 5/4$ [8].

From a physicist's point of view the convergence result looks rather obvious, though it has hardly been noted before (see, however, Refs. [9, 10, 11]): as $\alpha \to \infty$ all the modes with $k > k_{\mathrm{G}}$ are immediately suppressed by an infinite dissipation, whereas those with $k < k_{\mathrm{G}}$ obey inviscid truncated dynamics. Not surprisingly, the fate of couplings between triads of modes whose wavenumbers straddle k_{G} is a delicate point. In a Galerkin truncation any such triad should be left out. It may be shown that for $\alpha \to \infty$ such straddling couplings are suppressed, not only for the Burgers and NS equation but also for the hyperviscous magnetohydrodynamical equations and for some turbulence closures, specifically, the Direct Interaction Approximation (DIA) [9] and the Eddy-Damped-Quasi-Normal-Markovian (EDQNM) approximation [12]. Hence the convergence to the corresponding Galerkin-truncated equations holds for all the aforementioned equations in any dimension of space.

There are, however, interesting exceptions among hydrodynamical equations for which the result does not hold. They include the kinetic theory of resonant wave interactions [13] and the Markovian Random Coupling Model [14]. Indeed, the resonant wave interaction theory arises in the limit when the period of the waves goes to zero and this limit does not commute with the limit of a vanishing damping time for modes having $k > k_{\mathrm{G}}$; a similar remark can be made about the MRCM equation.

Let us stress that systems with a *finite* dissipativity – however large – are quite different from Galerkin-truncated systems. For example, consider the 3D NS equation with a random force, delta-correlated in time, for which we know the mean energy input ε per unit volume. It is still true that, for $\alpha \to \infty$, the solution of this equation converges to that of the Galerkin-truncated equation, but this time with a ran-

dom force. If E_0 is the initial energy, this solution has a mean energy $E(t) = E_0 + \varepsilon t$, which grows indefinitely in time. But, as soon as α is given a finite value, however large, a statistical steady state, in which energy input and hyperviscous energy dissipation balance, is achieved at large times. Such a steady state presents an interesting interplay of thermalization and dissipation, when α is large, as we show below.

The direct numerical simulation (DNS) of the Galerkin-truncated 3D Euler equations in Ref. [4] used 1600^3 Fourier modes. Large-α simulations of Eq. (4.2) would require significantly higher resolution to identify the various spectral ranges that we can expect, namely, inertial, thermalized, and far-dissipation ranges and transition regimes between these. Fortunately, Bos and Bertoglio [15] have shown that key features of the Galerkin-truncated Euler equations, such as the presence of inertial and thermalized ranges, can be reproduced by the two-point EDQNM closure [12] for the energy spectrum. For Eq. (4.2), with stochastic, white-in-time, homogeneous and isotropic forcing with spectrum $F(k)$, the hyperviscous EDQNM equations are

$$
\left.\begin{aligned}
&\left(\partial_t + 2\mu\left(\frac{k}{k_{\mathrm{G}}}\right)^{2\alpha}\right)E(k,t) = \iint_{\triangle_k} dp\,dq\,\theta_{kpq} \times \\
&b(k,p,q)\frac{k}{pq}E(q,t)\left[k^2 E(p,t) - p^2 E(k,t)\right] + F(k)\,, \\
&\theta_{kpq} = \frac{1}{\mu_k + \mu_p + \mu_q}\,, \quad b(k,p,q) = \frac{p}{k}(xy + z^3)\,, \\
&\mu_k = \mu\left(\frac{k}{k_{\mathrm{G}}}\right)^{2\alpha} + \lambda\left[\int_0^k p^2 E(p,t)dp\right]^{\frac{1}{2}}\,.
\end{aligned}\right\}
\tag{4.4}
$$

Here $E(k,t)$ is the energy spectrum, $\triangle_k$ defines the set of $p \geq 0$ and $q \geq 0$ such that k, p, q can form a triangle, x, y, z are the cosines of its angles and the eddy-damping parameter λ is expressed in terms of the Kolmogorov constant. The EDQNM equations have been studied numerically for more than three decades [16], but their hyperviscous versions Eq. (4.4) present new difficulties that we overcome as follows. Since

we are interested in the steady state we use an iterative method: the emission term, $E(p,t)E(q,t)$ in Eq. (4.4), is considered as a renormalization of the force $F(k)$; the absorption term, $E(q,t)E(k,t)$, is treated as a renormalization of the hyperviscous damping [17]. We then construct a sequence of energy spectra that, at stage $n+1$, is just the renormalized force divided by the renormalized damping, both based on stage n. This gives rapid convergence to the steady state at low wavenumbers; but, beyond a certain (α-dependent) wavenumber, convergence slows down dramatically and it is better to use time marching to obtain the steady state. At large values of k and α the problem becomes very stiff, so we use a slaved fourth-order Runge–Kutta scheme [18]. We discretize k logarithmically, with N_c collocation points per octave. Triad interactions involving wavenumber ratios significantly larger than N_c are poorly represented [19]; so, since wavenumber ratios of up to 50 play an important role for large α, we have used $N_c \lesssim 90$; this is computationally demanding because the complexity of the code is $O(N_c^3)$. We force at the lowest wavenumber ($k = 1$) in our numerical study of Eq. (4.4) with $k_{\mathrm{G}} = 10^5$, $\lambda = 0.36$, and $1 \le \alpha \le 729$. The resulting compensated, steady-state energy spectra $k^{+5/3}E(k)$ are shown in Fig. 4.1; flat regions, extending over two to five decades of k (depending on α), are close to the Kolmogorov inertial range; for large α there is a distinct thermalized range with $E(k) \sim k^2$ (also found in the transition between classical and quantum superfluid turbulence [20]), as we expect from our discussion of the Galerkin-truncated Euler equations [2]. In the far-dissipation range $k > k_{\mathrm{G}}$ the spectra fall off very rapidly [3]. For all values of α the far-dissipation range is preceded by a bump or *bottleneck*. It is also observed, in some experiments [21] and DNS of Navier–Stokes, with a shape that is quite independent of the

---

[2]A scaling argument suggests that the width of the thermalized range grows as $\alpha^{1/4}$ (up to logarithms); checking this numerically at high α is difficult because there is a boundary layer near k_{G}, of width $O(k_{\mathrm{G}}/\alpha)$, in which a transition occurs from very small to very large dissipation.

[3]Dominant balance gives for the leading term a decreasing exponential with a $k^{2\alpha+1}$ prefactor for the 3D EDQNM case and a $k^{2\alpha-2}$ prefactor for the 1D Burgers case.

Reynolds number [22]. The bottleneck for $\alpha = 1$ has previously been explained as the inhibition of the energy cascade from low to high wavenumbers because of viscous suppression of the cascade in the dissipation range [23]. Our work provides an alternative explanation: the usual bottleneck may be viewed as *incomplete thermalization*.

At large values of α the thermalized range gives rise to an eddy viscosity ν_{eddy}. This acts on modes with wavenumbers lower than those in the thermalized range; the corresponding damping rate is $\nu_{\mathrm{eddy}}k^2$. The eddy viscosity can be expressed as an integral over the thermalized range [15, 19]. As α grows, so does ν_{eddy} and, eventually, the renormalized viscous damping overwhelms the hyperviscous damping for modes at low wavenumbers (below those in the thermalized range). The dynamics of these modes is then governed by the usual $\alpha = 1$ equation. Not surprisingly, then, we find a pseudo-dissipation range around $k \simeq 10^4$ that is shown in an expanded scale in the inset of Fig. 4.1; a similar range for the Galerkin-truncated case is discussed in Ref. [15] and is already visible in the DNS of Ref. [4]. For large α the inset of Fig. 4.1 also shows a *secondary bottleneck* range for $10^3 < k < 10^4$; this may be viewed as the usual ($\alpha = 1$) EDQNM bottleneck stemming from ν_{eddy} [4].

Our results apply to compressible flows also. We have studied the simplest instance, that is the unforced hyperviscous 1D Burgers equation (4.1) [5]. Its solution converges to the *entropy* solution, i.e., the standard solution with shocks, obtained when $k_{\mathrm{G}} \to \infty$ for any $\alpha \geq 1$ [24]. Here we are interested in the large-α behavior at fixed k_{G}. We do not have to resort to closure now since we can solve the primitive equation (4.1) directly by a pseudospectral method. If we choose a single initial condition the resulting spectrum is noisy because, un-

---

[4]The secondary bottleneck overshoots by $\simeq 3 - 5\%$, compared to $\simeq 20\%$ for the usual bottleneck, perhaps because of higher-order terms in the renormalized damping, which are beyond the eddy-viscosity approximation.

[5]It is easily shown that the ordinary Burgers equation produces no bottleneck.
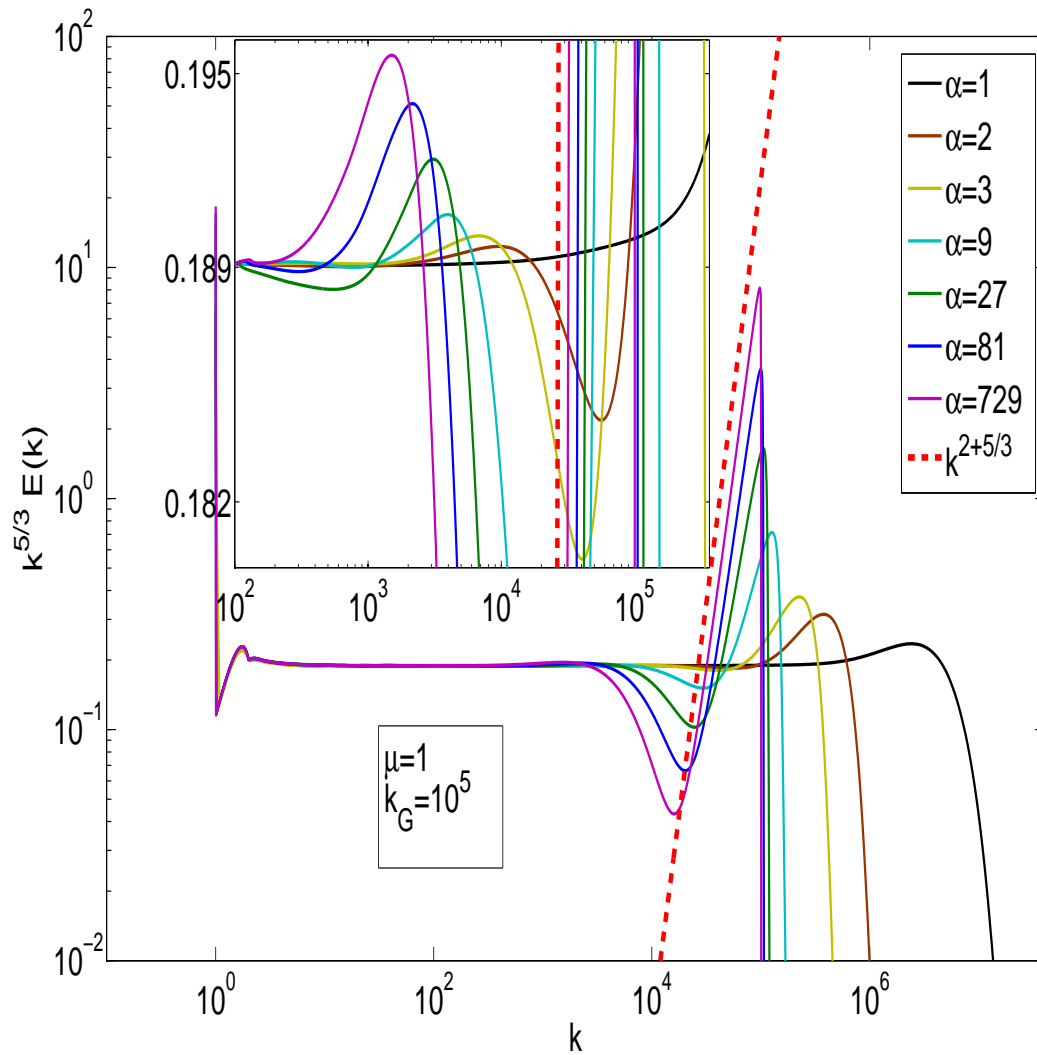
Figure 4.1: Log-log plots of the compensated spectrum $k^{5/3}E(k)$ versus k from a numerical integration of the hyperviscous EDQNM Eq. (4.4) for different values of α; inset: enlarged spectra showing a secondary bottleneck (see text).

like the ordinary Burgers equation, its Galerkin-truncated version and thus also the high-α versions are believed to be chaotic dynamical systems [25]. So we solve (4.1) with the two-mode random initial condition $v_0(x) = \sin x + \sin(2x + \phi)$, where ϕ is distributed uniformly in the interval $[-\pi, \pi]$. We use 2^{14} collocation points and set $\mu = 1$, $k_{\mathrm{G}} = 342.1$ and $\alpha = 1000$.

In Fig. 4.2 we show the Burgers energy spectrum $E(k) = \mid \tilde{v}(k) \mid^2$, averaged over 20 realizations of the phase ϕ at various times. At the latest output times the spectrum is almost completely flat, i.e., thermalized, with equipartition of the energy between all the Fourier modes. At earlier times $E(k)$ behaves approximately as k^{-2} in an inertial range that corresponds to shocks in physical space; there is a thermalized range at higher wavenumbers up to k_{G}; for $k > k_{\mathrm{G}}$ the spectrum falls very rapidly. In Figs. 4.3 and 4.4 we show some more representative plots showing the effects of thermalisation for different values of α. No pseudo-dissipation range is observed here between the inertial and thermalized ranges as seen in the 3D NS case (Fig. 4.1). Perhaps the data are too noisy, but a careful examination of $v(x)$ in physical space indicates that this phenomenon might arise from the compressible nature of the Burgers dynamics: thermalization begins over the whole physical range (as high-frequency noise with wavenumber $\approx k_{\mathrm{G}}$); noise generated close to shocks is absorbed by them and not enough is left to produce any appreciable eddy viscosity that could broaden the shocks.

We now summarize our main findings from the study of hyperviscous hydrodynamical equations with powers α of the Laplacian ranging from unity to very large values.

The simplest results are obtained for very large α. The solutions of the 1D Burgers equation or the Navier–Stokes equations in any space dimension d are then very close to the solutions of the corresponding Galerkin-truncated equations, displaying thermalization at
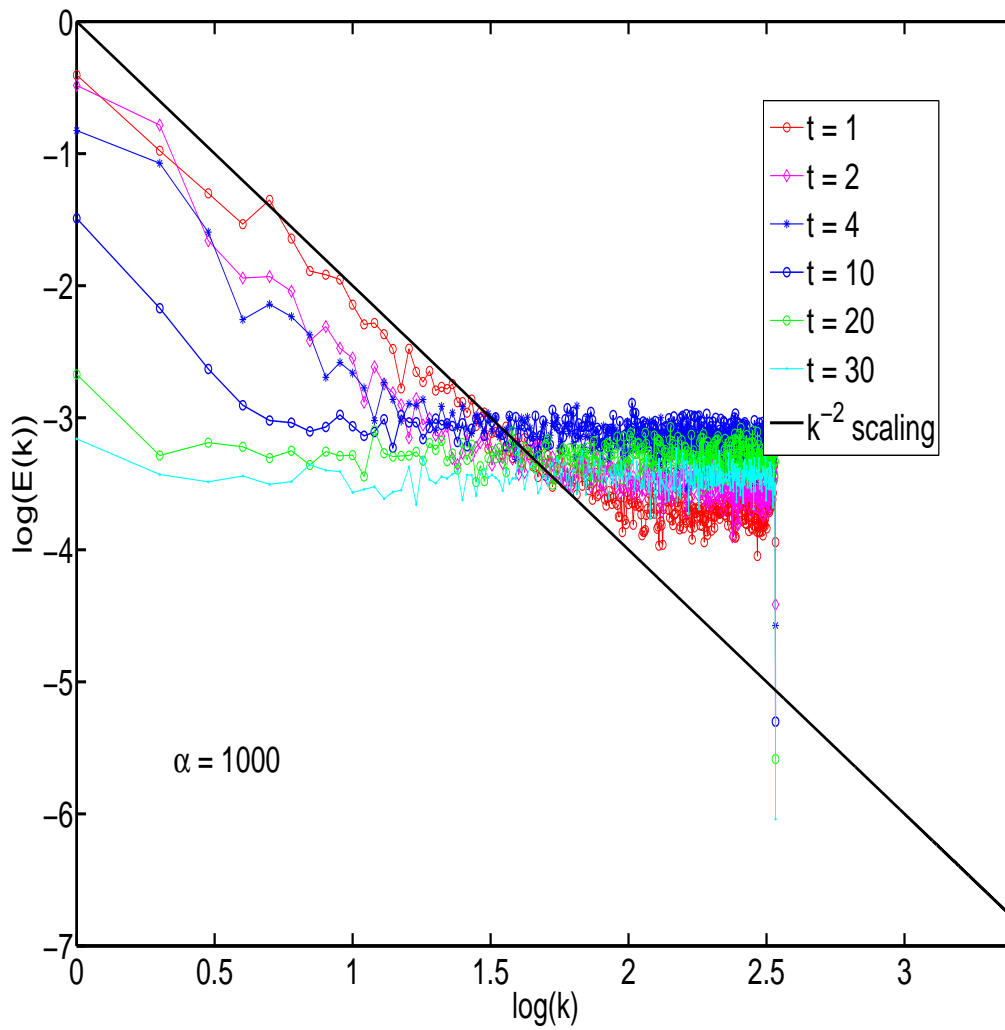
Figure 4.2: Log-log plots of averaged energy spectra (see text) versus wavenumber k for the hyperviscous Burgers equation (4.1) at various times.
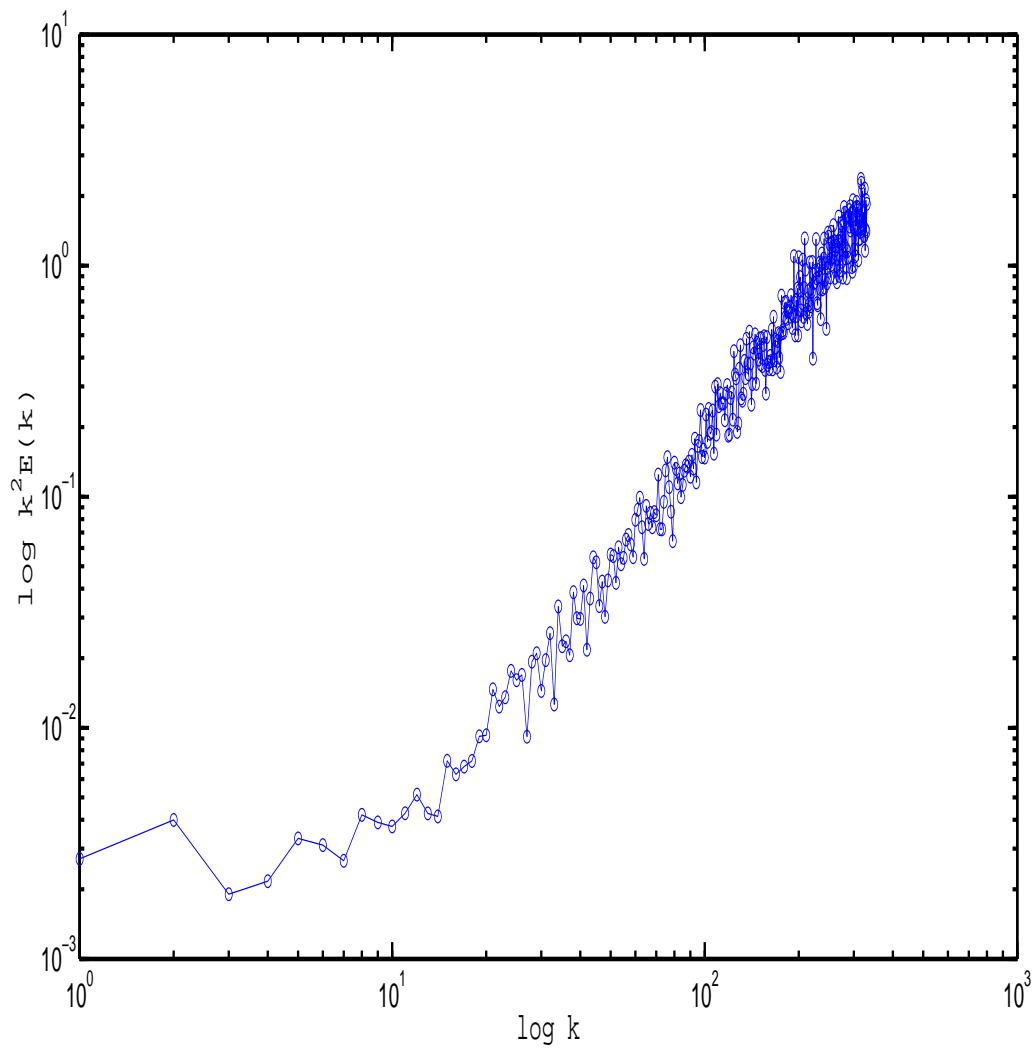
Figure 4.3: A representative log-log plot of $k^2E(k)$ versus k for $\alpha = 800$ at time $t = 30$. We see clear signatures of thermalization at large k (see text).
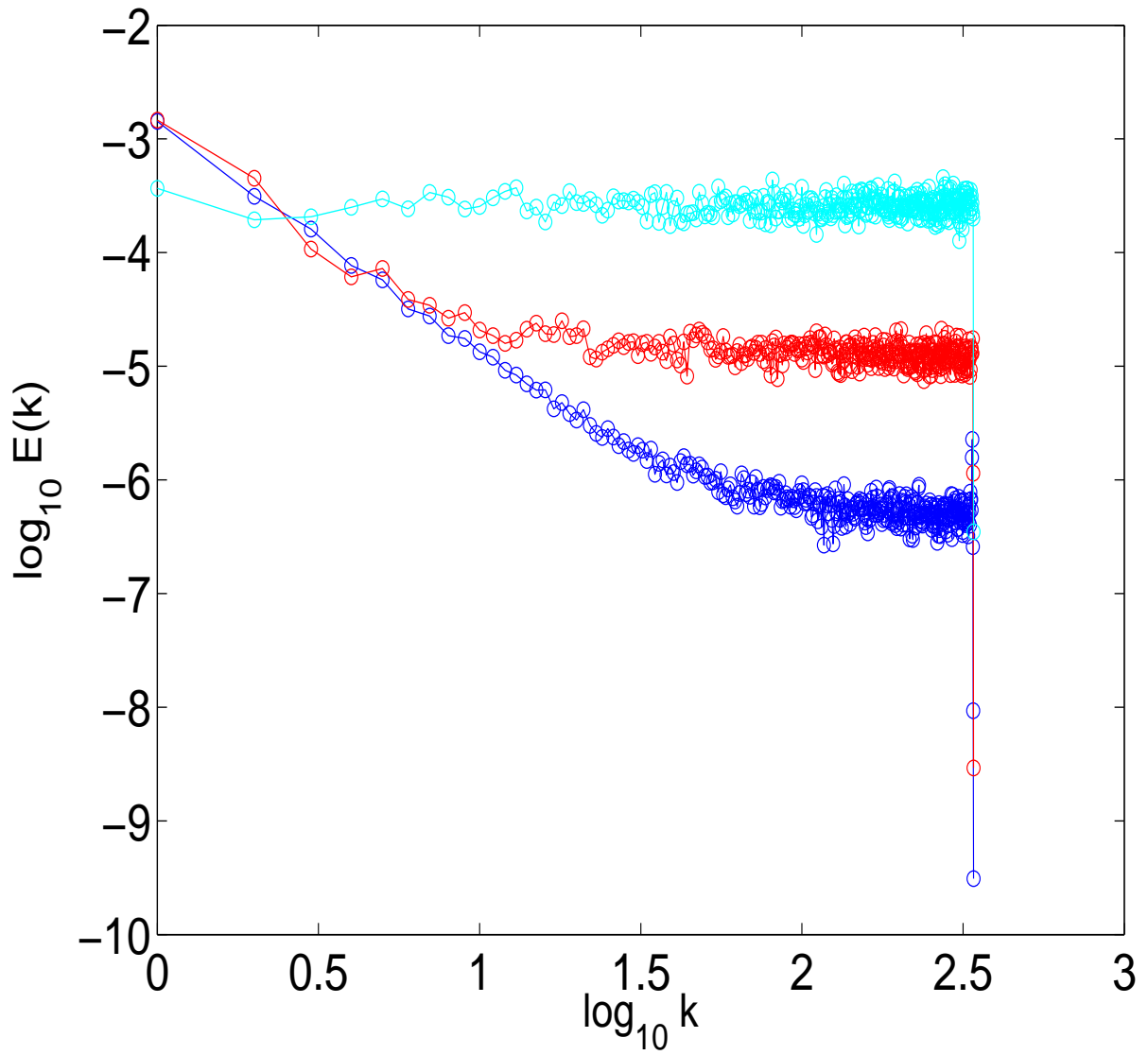
Figure 4.4: Representative log-log plots of $E(k)$ versus k for $\alpha = 250$ (in blue, lower-most curve), $\alpha = 500$ (in red, middle curve), and $\alpha = 1000$ (in cyan, uppermost curve) at time $t = 30$. We see clear signatures of thermalization at large k (see text).

wavenumbers below k_G. The detailed scenario will of course be affected by the dimension of space. In 3D, with enough resolution, we may be able to observe up to five ranges: an inertial range, a secondary bottleneck, a pseudo-dissipation range, a thermalized range, and a far dissipation range. Because of enstrophy conservation and of the predominance of Fourier-space nonlocal interactions, the 2D case is rather special and deserves a separate study[6].

The most relevant case is of course that of ordinary dissipation ($\alpha = 1$). The energy-spectrum bottleneck generally observed at high Reynolds numbers in 3D incompressible turbulence may be viewed as an incomplete thermalization: as we increase α larger and larger bottlenecks are present, eventually displaying thermalization on their rising side.

We finally deal with the case of moderately large α of the sort used in many simulations [7]. How safe is this procedure and what kind of artifacts can we expect?

Using large values of α in simulations to "avoid wasting resolution" is hardly advocated by anybody, but we now understand what goes wrong: a huge thermalized bottleneck will develop at high wavenumbers, whose action on smaller wavenumbers is an ordinary $\alpha = 1$ dissipation with an eddy viscosity much larger than what would be permissible in a normal $\alpha = 1$ simulation.

When α is chosen just a bit larger than unity (e.g. $\alpha = 2$ which is standard in oceanography [7]) the advantage of widening the inertial range may be offset by artifacts at bottleneck scales; indeed, even an incomplete thermalization will bring the statistical properties of such scales closer to Gaussian, thereby reducing the rather strong intermittency which would otherwise be expected [7]. For similar reasons spu-

---

[6]In the 2D case several aspects other than thermalization can be captured by the linear hyperviscous theory of Ref. [10].

[7]For $\alpha = 1$ a lull in the growth of intermittency at bottleneck scales may already be observed; cf. Fig. 2 Panel R4 of J.-Z. Zhu, Chin. Phys. Lett. **8**, 2139 (2006).

rious isotropization can be expected for problems with an anisotropic constraint, such as rapidly rotating or stratified flow or MHD with a strong uniform magnetic field.

Bibliography

[1] U. Frisch, S. Kurien, R. Pandit, W. Pauls, S. S. Ray, A. Wirth, and J-Z Zhu, Phys. Rev. Lett., **101**, 144501 (2008).

[2] U. Frisch, B. Hasslacher, and Y. Pomeau, Phys. Rev. Lett. **56**, 1905 (1986).

[3] S. Succi, P. Santangelo, and R. Benzi, Phys. Rev. Lett. **60**, 2738 (1988).

[4] C. Cichowlas, P. Bonaïti, F. Debbasch, and M. Brachet, Phys. Rev. Lett. **95**, 264502 (2005).

[5] T. D. Lee, Quart. J. Appl. Math. **10** 69 (1952) .

[6] R. H. Kraichnan, Phys. Fluids **10**, 2080 (1967).

[7] G. Holloway, J. Phys. Oceanogr. **22**, 1033 (1992); V. Borue and S.A. Orszag Europhys. Lett. **29**, 685 (1995); N.E.L. Haugen and A. Brandenburg, Phys. Rev. E **70**, 026405 (2004).

[8] J.L. Lions, *Quelques Méthodes de Résolution des Problèmes aux Limites non Linéaires*, Gauthier-Villars (1969).

[9] R.H. Kraichnan, Phys. Rev. **109**, 1407 (1958). While introducing the DIA here, Kraichnan wrote the following about Galerkin truncation: "We may regard this as the introduction of infinite damping (infinite resistance) for the degrees of freedom removed."

[10] J. Jiménez, J. Fluid Mech. **279**, 169 (1994), notes that "An interesting property of the hyperviscous solutions is the sharpness of their spectral cutoff, which goes from smooth Gaussian ..., to a step function in the ultraviscosity limit."

[11] J.P. Boyd, J. Sci. Comput. **9**, 81 (1994), obtained a truncation result for the *linear* hyper-diffusion equation.

[12] S.A. Orszag, *Statistical Theory of Turbulence*, in *Fluid Dynamics*, Les Houches 1973, 237, eds. R. Balian and J.L. Peube. Gordon and Breach (1977).

[13] V. E. Zakharov, V. S. L'vov, and G. Falkovich, *Kolmogorov Spectra of Turbulence* I, Springer (1992).

[14] U. Frisch, M. Lesieur, and A. Brissaud, J. Fluid Mech. **65**, 145 (1974).

[15] W. J. T. Bos and J.-P. Bertoglio, Phys. Fluids **18**, 071701, 2006.

[16] J.R. Herring and R.H. Kraichnan, J. Fluid Mech. **91**, 581 (1979).

[17] R. H. Kraichnan, Phys. Fluids **7**, 1163 (1964).

[18] Scheme ETD4RK of C.M. Cox and P.C. Matthews, J. Comput. Phys. **76**, 430 (2002).

[19] M. Lesieur and D. Schertzer, J. de Mécanique. **17**, 609 (1978).

[20] V. L'vov, S. Nazarenko, and O. Rudenko, Phys. Rev. B **76**, 024520 (2007).

[21] S.G. Saddoughi and S.V. Veeravalli, J. Fluid Mech. **268**, 333 (1994). As shown by W. Dobler, N.E.L. Haugen, T.A. Yousef and A. Brandenburg, Phys. Rev. E **68**, 026304 (2003), the 1D spectrum, generally measured in experiments, may not display a bottleneck even if the 3D spectrum does.

[22] Z.S. She, G. Doolen, R.H. Kraichnan, and S.A. Orszag, Phys. Rev. Lett. **70**, 3251 (1993); Y. Kaneda, T. Ishihara, M. Yokokawa, K. Itakura, and A. Uno, Phys. Fluids, **15**, L21 (2003); S. Kurien, M.A. Taylor, and T. Matsumoto, Phys. Rev. E **69**, 066313 (2004); J. Schumacher, Europhys. Lett. **80**, 54001 (2007); P.D. Mininni, A. Alexakis, and A. Pouquet, Phys. Rev. E **77**, 036306 (2008).

[23] G. Falkovich, Phys. Fluids **6**, 1411 (1994); D. Lohse and A. Müller-Groeling, Phys. Rev. Lett. **74**, 1747 (1995).

[24] E. Tadmor, Commun. Math. Sci. **2**, pp. 317-324 (2004).

[25] R. V. Abramov, G. Kovacic, and A. J. Majda, Commun Pure Appl. Math. **56**, 1 (2003).

Chapter 5

Bottlenecks in the Hyperviscous Burgers Equation and their Real-space Manifestations

A first step in the statistical characterization of fluid turbulence, in experiments and theory, is the measurement of the distribution of fluid kinetic energy amongst the Fourier modes k, i.e., the energy spectrum $E(k)$. In a statistically steady state and in the inertial range of length scales r, which lie between the large length scale L (small wavenumbers) and the dissipation length scale η_d (large wavenumbers), the energy spectrum typically shows a power law scaling $E(k) \equiv |\tilde{u}(k)|^2 \sim k^{-n}$, where $\tilde{u}(k)$ is the Fourier modes of the velocity field, before falling off exponentially in the dissipation range. The exponent n is close to 5/3 in 3D turbulence and 2 in the ordinary, deterministic Burgers equation [1]. In a variety of experiments [2] and numerical simulations [3] it has been seen that there is often a non-monotonic cross over from the power-law inertial range to the exponential dissipation range in the energy spectrum. This manifests itself as a bump, commonly called a *bottleneck*, between the inertial and dissipation scales. A key problem in fully developed turbulence is to understand the origins of this bottleneck. In this Chapter we elucidate how this bottleneck comes about in the one-dimensional, hyperviscous Burgers equation

and provide a theoretical framework for understanding our results from direct numerical simulations (DNS). Our work here builds on the work of Ref. [4]. We show, in particular, that, in real space, the bottleneck manifests itself as oscillations in the velocity field.

The one-dimensional hyper-viscous Burgers equation for the velocity field $u(x, t)$, at point x and time t, is

$$\frac{\partial u(x,t)}{\partial t} + u(x,t)\frac{\partial u(x,t)}{\partial x} = -\nu_\alpha \left(-\frac{\partial^2}{\partial x}\right)^\alpha u(x,t) + f(x), \qquad (5.1)$$

where the coefficient of viscosity is denoted by ν, the degree of dissipativity is determined by the exponent α, and $f(x)$ is an external force. To begin with we choose the initial condition $u(x, 0) = \sin x$ and the forcing $f(x) = \sin x$. We note in passing that the ordinary Burgers equation is recovered by setting $\alpha = 1$. For large $\alpha >> 1$ and with $f(x) = 0$, it was shown recently that the solution thermalises at long times and the thermalisation is the underlying reason for bottlenecks seen in such solutions. This phenomenon has been described in detail in Chapter 4 of this Thesis and in Ref. [5]. In this Chapter we concern ourselves with steady-state solutions of Eq. (5.1) and moderate values of α (= 2,4,8,16).

It is useful to recall that, in complex physical space, the hyperviscous Burgers equation can be shown to have simple pole singularities, which can be derived simply through the method of dominant balance as follows. In the steady state we can ignore the term which has a time-derivative. Next, by making the change of variable $X \equiv x/\nu_\alpha^\beta$, where $\beta = \frac{1}{2\alpha-1}$, in Eq. (5.1) we obtain the equation for the inner solution $u^i(X)$ of the hyperviscous Burgers equation :

$$\frac{d}{dX}\left(\frac{u^{i^2}}{2}\right) = (-1)^{\alpha+1}\frac{d^{2\alpha}}{dX^{2\alpha}}u^i + \nu_\alpha^{2\alpha\beta-1}\sin(\nu^\beta X). \qquad (5.2)$$

In the asymptotic case of small viscosity, by ignoring the term $\nu^{2\alpha\beta-1}\sin(\nu^\beta x)$ and solving the equation in complex z-space, we obtain the solution

$$u^i(z) \sim D_\alpha(z - z_*)^{\rho_\alpha}, \qquad (5.3)$$

where

$$\rho_\alpha = -2\alpha + 1 \tag{5.4}$$

and

$$D_\alpha = 2(-1)^{\alpha+1} \prod_{m=0}^{2\alpha-2} (-2\alpha - m) \tag{5.5}$$

We solve the hyperviscous Burgers equation by using a pseudo-spectral method with 2/3 de-aliasing scheme and a fourth-order Runga-Kutta method for integration in time [?]. For dimensional reasons, the dissipative term is normalised by a factor $k_d^{-(2\alpha-2)}$, where k_d is a reference wavenumber. We choose $N = 2^{14}$ collocation points, $\nu_2 = 5 \times 10^{-3}$, $\nu_4 = 5 \times 10^{-8}$, $\nu_8 = 5 \times 10^{-14}$, $\nu_{16} = 10^{-20}$, the time step $\delta t = 10^{-4}$, and $k_d = 100$. Our choice of parameters is dictated by the need to have a *sufficiently* large inertial range and the thinnest possible boundary layer straddling the shock. We also keep in mind that, for arbitrarily large k_d and an arbitrarily small ν_α, the hyperviscous Burgers equation reduces to the Galerkin-truncated equation and thermalisation sets in as discussed in Chapter 4.

We begin by looking at the evolution of the total kinetic energy $E(t) = \sum_k |\tilde{u}(k,t)|^2$ with time in Fig. (5.1) for the four different values of α, namely, $\alpha = 2, 4, 8$, and 16. In the steady state we find that for all values of α, the total energy is equal to 2 [shown as a thick black horizontal line in Fig. (5.1)]. We now show how to derive this analytically.

Once the steady state is reached we can drop the $\partial_t u(x,t)$ term from the Burgers equation to obtain

$$\frac{d}{dx}(u^2/2) = (-1)^{\alpha+1}\nu_\alpha \frac{d^{2\alpha}}{dx^{2\alpha}}u + \sin x. \tag{5.6}$$

To leading order, we can neglect the hyperviscous term to obtain the leading-order solution

$$u_0 = \text{sgn}(\pi - x)\sqrt{2(1 - \cos x)},$$

i.e.,

$$u_0 = \text{sgn}(\pi - x)2\sin(x/2). \tag{5.7}$$
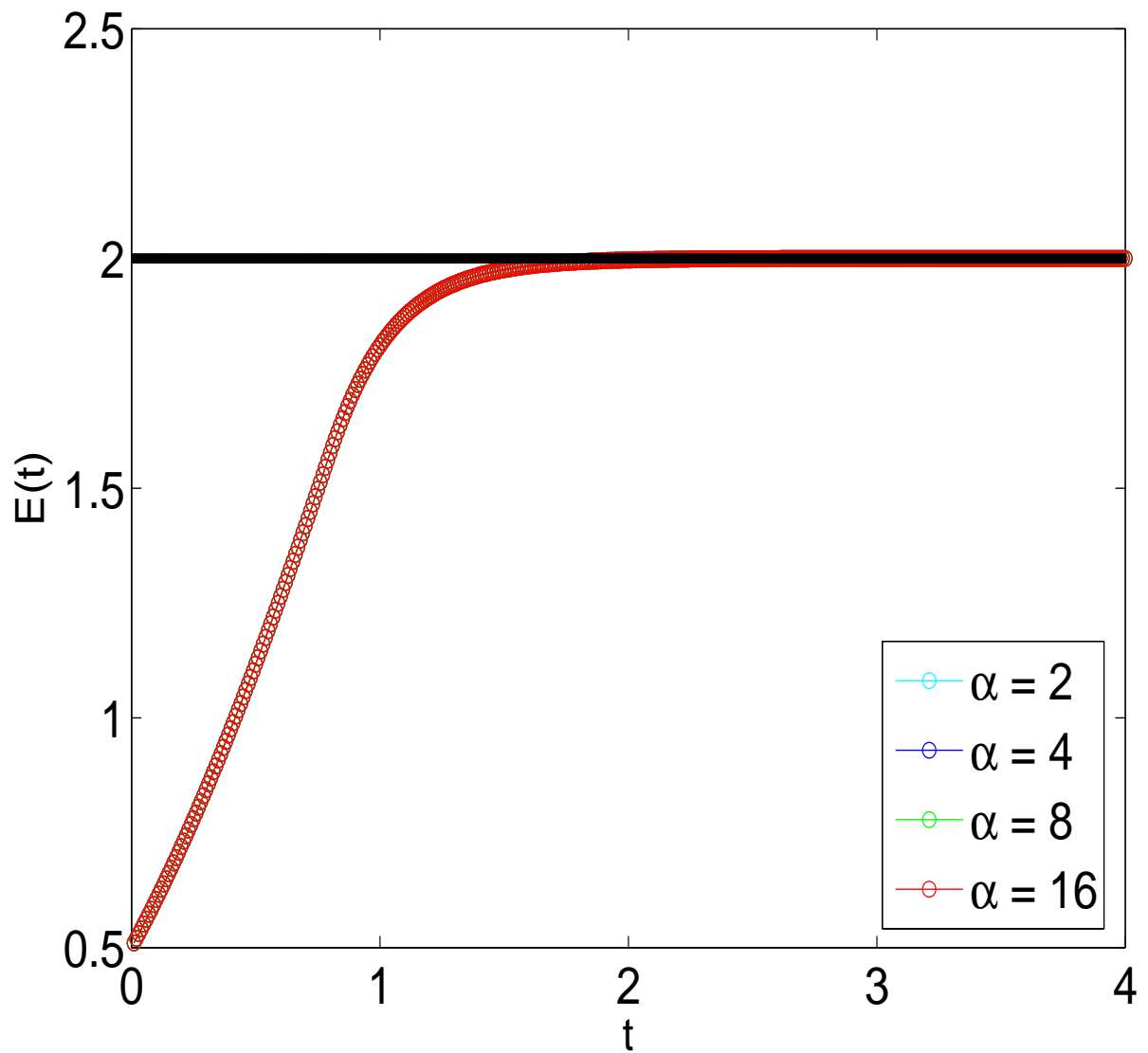
Figure 5.1: Plot of the total energy $E(t)$ versus time for $\alpha = 2, 4, 8, 16$. In the steady state the total energy saturates to $E(t) = 2$ as obtained via theoretical arguments (see text).

From Eq. 5.7, we can calculate the total kinetic energy $E_0 = \int u_0^2 dx = 2$, the steady state result from our DNS (see the thick black line in Fig. (5.1)).

We now calculate the energy spectra for the different values of α. These are shown in Fig. (5.2) in which the thick black line corresponds to the inertial-range scaling law k^{-2}. For the sake of clarity, in the Figure, we do not show $E(k)$, for $\alpha = 4, 8$ and 16, for values of k larger than the ones shown because the large dissipativity α makes $E(k)$ fall rapidly to values close to roundoff noise. To observe the bottleneck, it is best to look at the compensated energy spectra $E^c \equiv k^2 E(k)$; this is shown in Fig. (5.3) for $\alpha = 2, 4, 8$ and 16. The bottlenecks, which appear as bumps between the horizontal inertial ranges and the dissipation ranges, becomes more and more prominent as we increase α and they appear at wavenumbers K_b^α. An expanded view of the bottlenecks, given in Fig. (5.4), shows their structure of the bottleneck – a bump with a peak at K_b^α. The width of this bump decreases as α increases. We now seek to provide an explanation of such bottlenecks.

In Ref. [4], it was shown that the solution of the hyperviscous Burgers equation, in the vicinity of the shock, shows damped oscillations. These solutions were obtained numerically by using low resolution spectral methods. Our high-resolution pseudospectral DNS extends the study of Ref. [4] considerably. Furthermore it helps us to establish a link between these real-space oscillations and Fourier-space bottlenecks; this link has not been noticed in earlier studies.

Let us first look at the steady solution of the hyperviscous Burgers equation for various values of α in Fig. (5.5). As is clear from the figure, our numerical solution agrees with the asymptotic result $u^o(x)$ (Eq 5.7), shown in black, away from the shock. Around the region of the shock ($x = \pi$), there are oscillations, which are clearly visible when we zoom in to the region close to the shock as shown in Fig. (5.6). In order to characterise these oscillations, it is useful to look at the
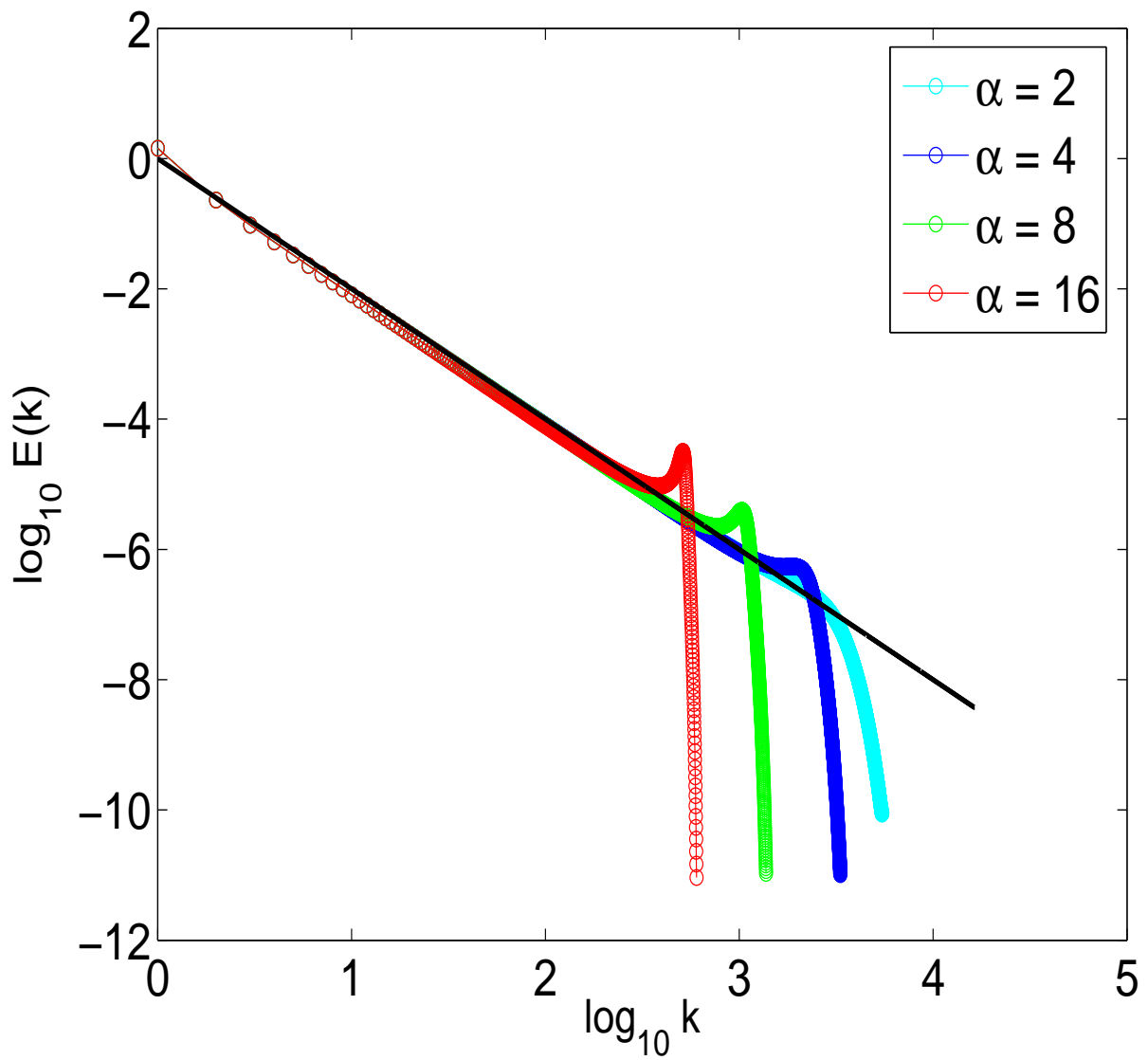
Figure 5.2: A loglog plot of the energy spectrum $E(k$ versus k for different values of α. The black line is a guide to the eye to show the inertial range scaling $E(k) \sim k^{-2}$.
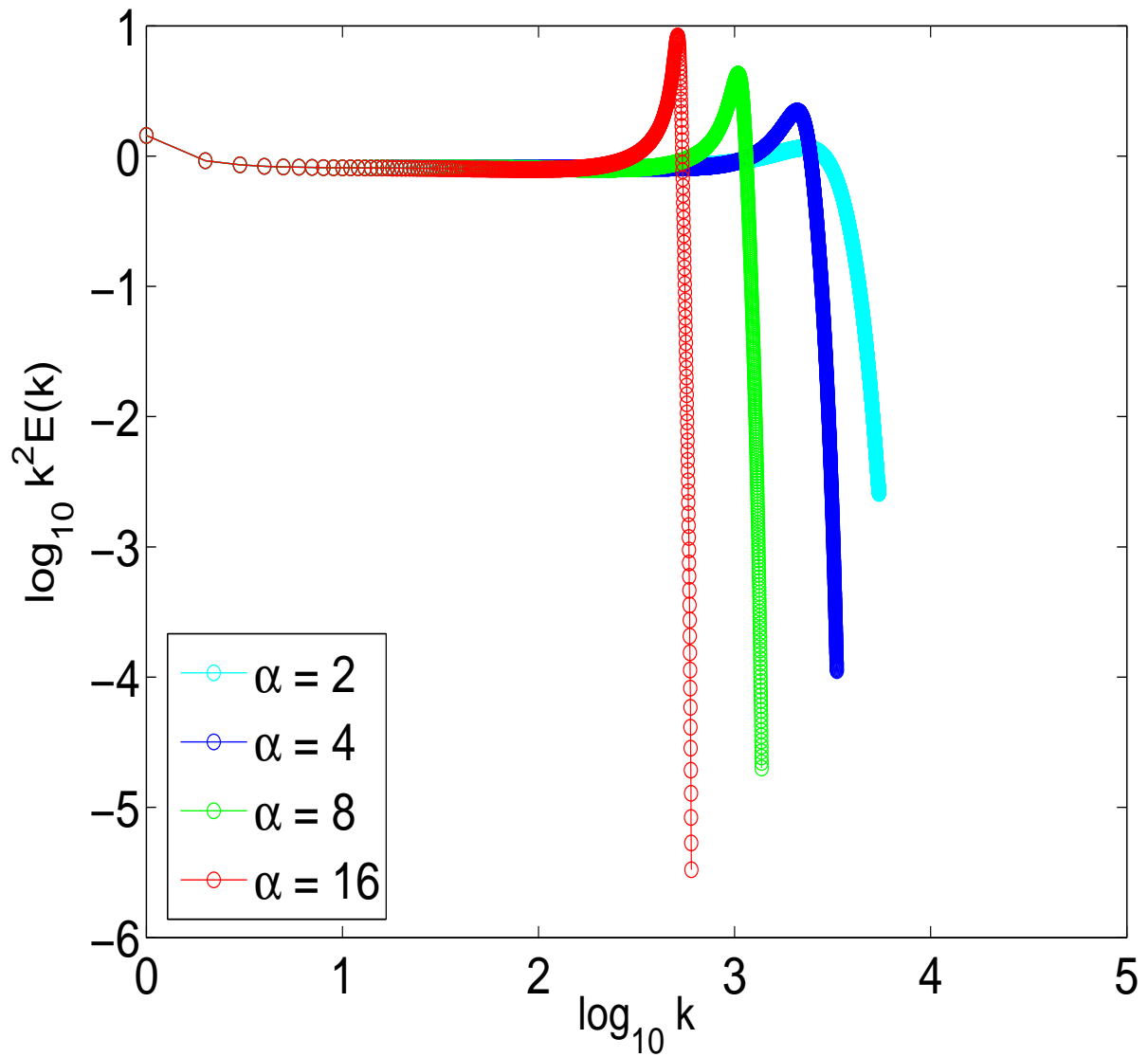
Figure 5.3: A loglog plot of the compensated energy spectrum $E^c(k)$ versus k. The horizontal region corresponds to the inertial range. With increasing α, we see progressively pronounced bottlenecks which appear as bumps at the end of the inertial range.
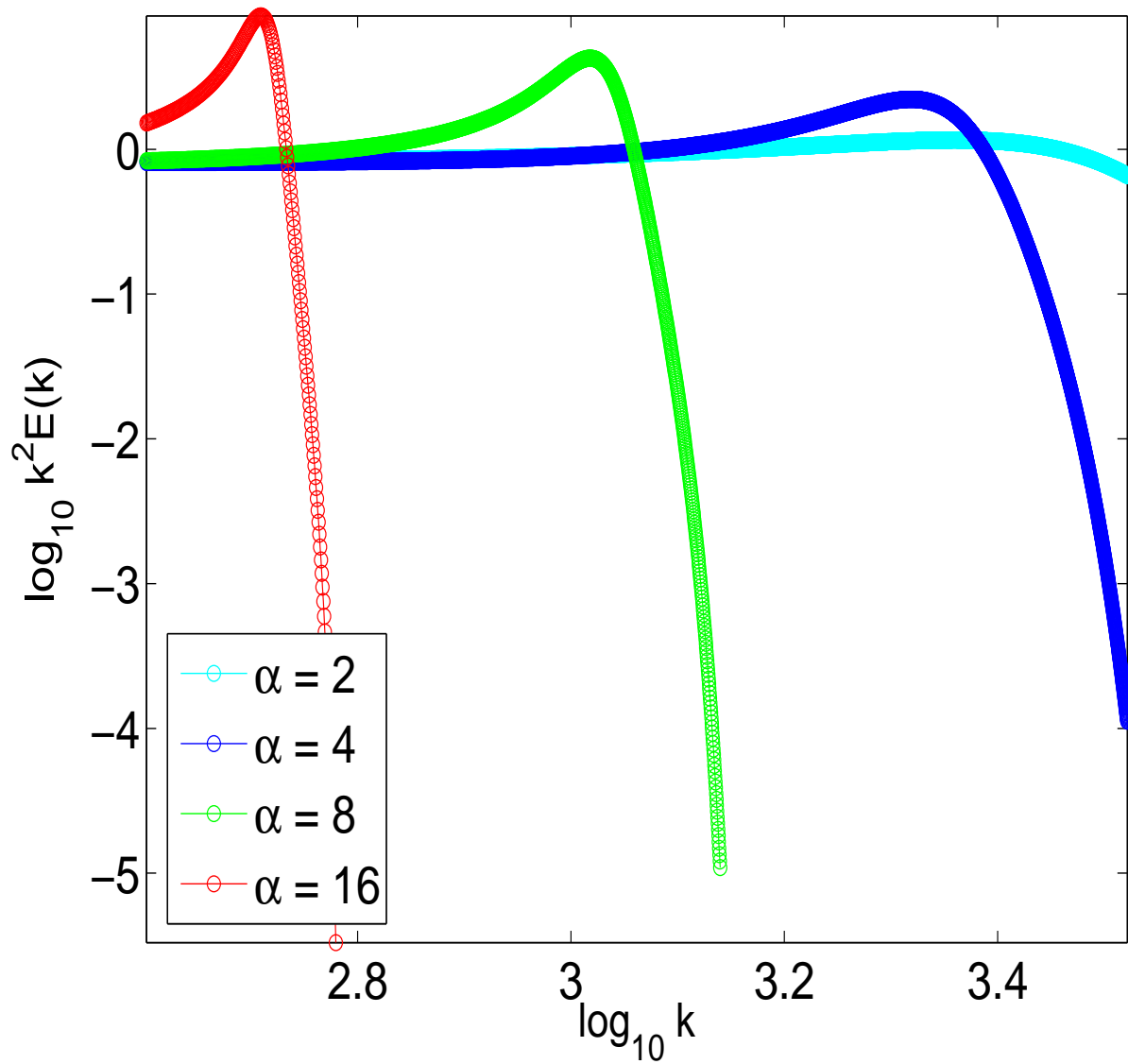
Figure 5.4: A loglog plot of the compensated energy spectrum $E^c(k)$ versus k, as shown in the previous figure, but zoomed in around the bottleneck region. It is clear, that with increasing α, we see progressively pronounced bottlenecks which appear as an asymetric bump at the end of the inertial range.
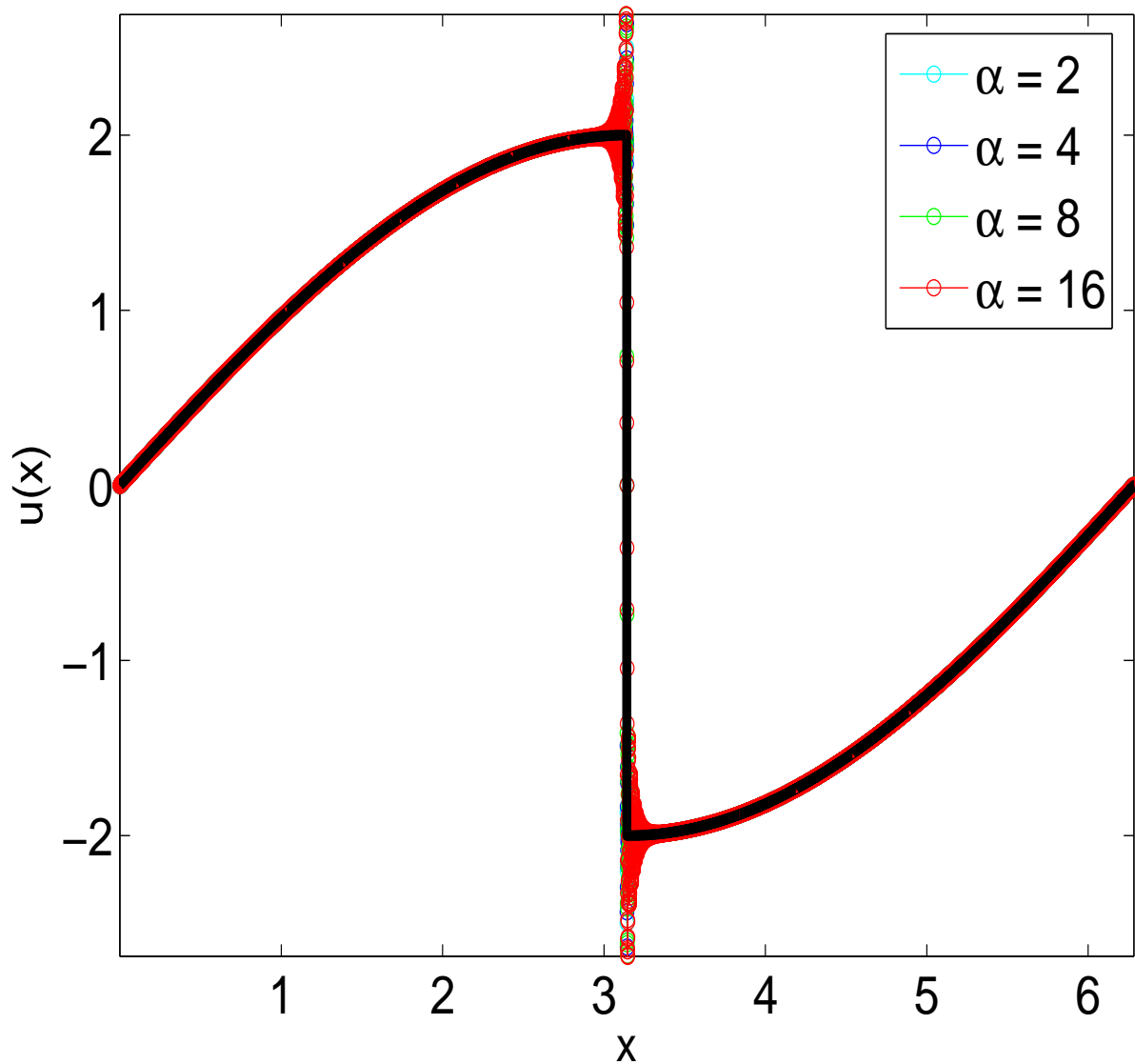
Figure 5.5: The steady state DNS solution $u(x)$ versus x for different values of α. At points away from a thin layer around the shock at $x = \pi$ the solution is in excellent agreement with the outer solution shown in black. Near $x = \pi$ we see strong oscillations and, hence, deviation from the outer solution.

deviation $u_d(x) = u(x) - u_0(x)$ as shown if Fig. (5.7). It is evident from the figures that the oscillations have a characteristic wavelength λ_α and the amplitude of the oscillations decays as we move away from the thin layer around the shock region. We have measured the wavelength of these oscillations carefully and have found that, for $\alpha = 8$ and $\alpha = 16$, the wavelengths are $\lambda_8 = 0.006$ and $\lambda_{16} = 0.012$, respectively. From the plots of compensated spectra in Figs. 6.3 and 6.4 we find $K_b^8 = 1042$ and $K_b^{16} = 512$ for $\alpha = 8$ and 16, respectively. These values are consistent with our results for λ_8 and λ_{16} because $2\pi/K_b^8 \approx 0.006$ and $2\pi/K_b^{16} \approx 0.012$. We thus provide strong numerical evidence that the real-space manifestation of the bottleneck in the energy spectrum of the hyperviscous Burgers equation is the oscillatory behaviour of the solution in a thin boundary layer around the shock : a Fourier transform of such oscillations gives a peak in k space at a wavenumber equal to the wavenumber of the oscillations. This is also consistent with what is known for the ordinary ($\alpha = 1$) Burgers equation: In Ref. [4] it is shown that the ordinary Burgers equation does not have any oscillatory behaviour around the shock region; and we also know from a variety of numerical simulations that no bottleneck in the energy spectrum exists for this equation.

The bottleneck in the energy spectrum of the hyperviscous Burgers equation is not a *sharp*, delta-function (Figs. 6.3 and 6.4). We show now that the width of the bottleneck peak is related to the decay of the envelope of the oscillations as we move away from the position of the shock. In the domain $0 \le x \le \pi$, let us denote the oscillatory part of the solution to be $u_d^\alpha = A_\alpha(\pi - x) \sin(K_b^\alpha(\pi - x))$, where $\pi - x$ is the distance from the shock. (The symmetry of the solution ensures that the region $\pi \le x \le 2\pi$ will have the same form.) We have measured $A_\alpha(\pi - x)$ as a function of $(\pi - x)$ for $\alpha = 8$ and $\alpha = 16$ as shown in Figs. (5.8) and Figs. (5.10); semilog plots of $A_\alpha(\pi - x)$ versus $(\pi - x)$ are shown Fig. (5.9) and Fig. (5.11). As is evident from the plots our data is consistent with the

exponential decay

$$A_\alpha = \exp[-x/\xi_\alpha].\tag{5.8}$$

For $\alpha = 8$, $\xi_8 = 0.008 \pm 0.003$ and $\alpha = 16$, $\xi_{16} = 0.038 \pm 0.001$. We also find that the full-width-at-half-maximum of the bottleneck bumps in Figs. (6.3) and (6.4) are comparable to ξ_α^{-1}.

In this Chapter we have shown conclusively that bottlenecks in the energy spectrum of the hyperviscous Burgers equations have clear real space manifestations. In particular, our work shows that such bottlenecks are inevitable in the presence of hyperviscosity. Furthermore, the bottleneck manifests itself as oscillations in $u(x)$ in the vicinity of the shock.
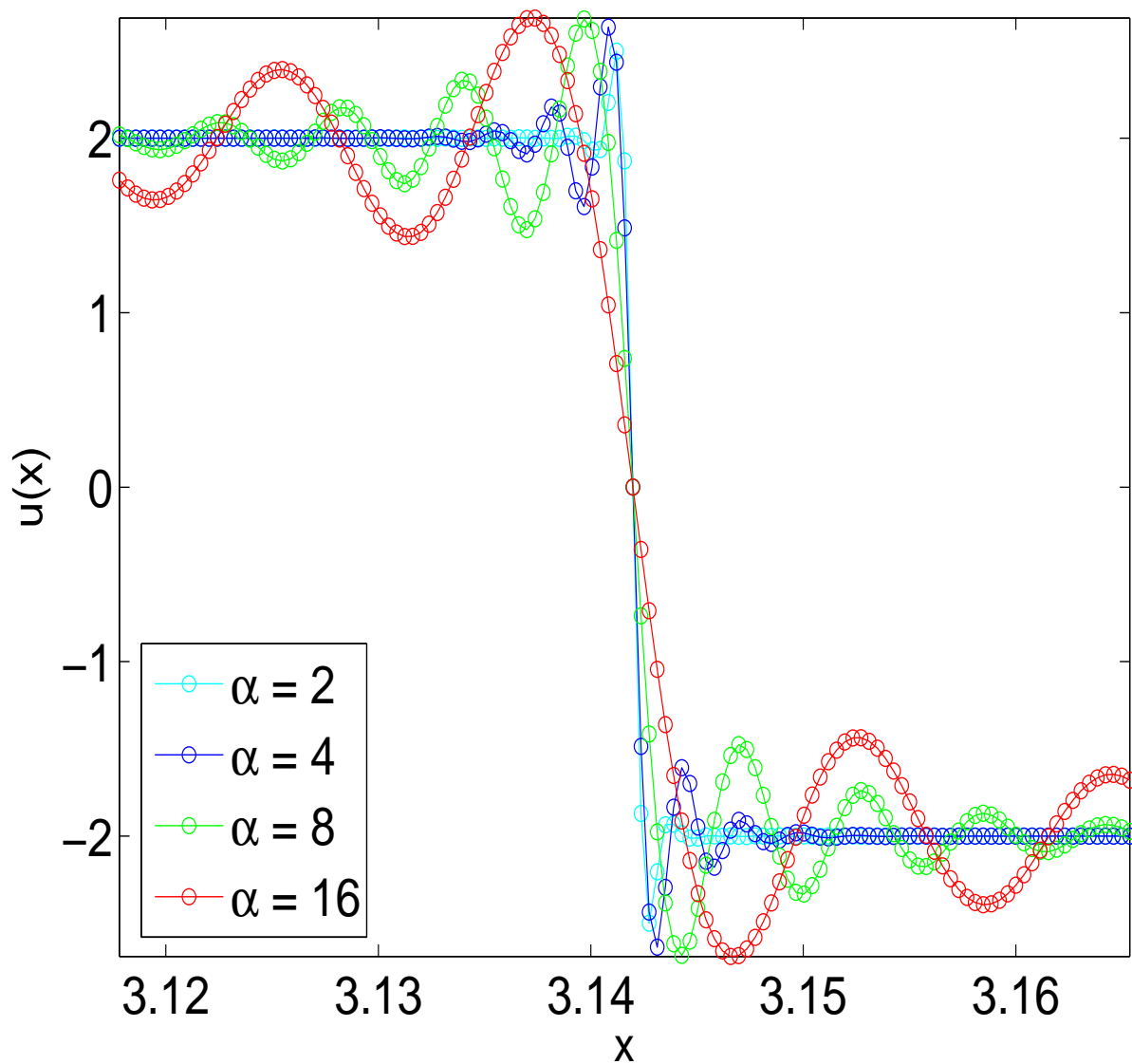
Figure 5.6: The steady state DNS solution $u(x)$ versus x for $\alpha = 2, 4, 8$ and 16 close to $x = \pi$. We see strong oscillations whose wavelength and amplitude depend strongly on α. The amplitude of these oscillations decays as we move away from the shock region.
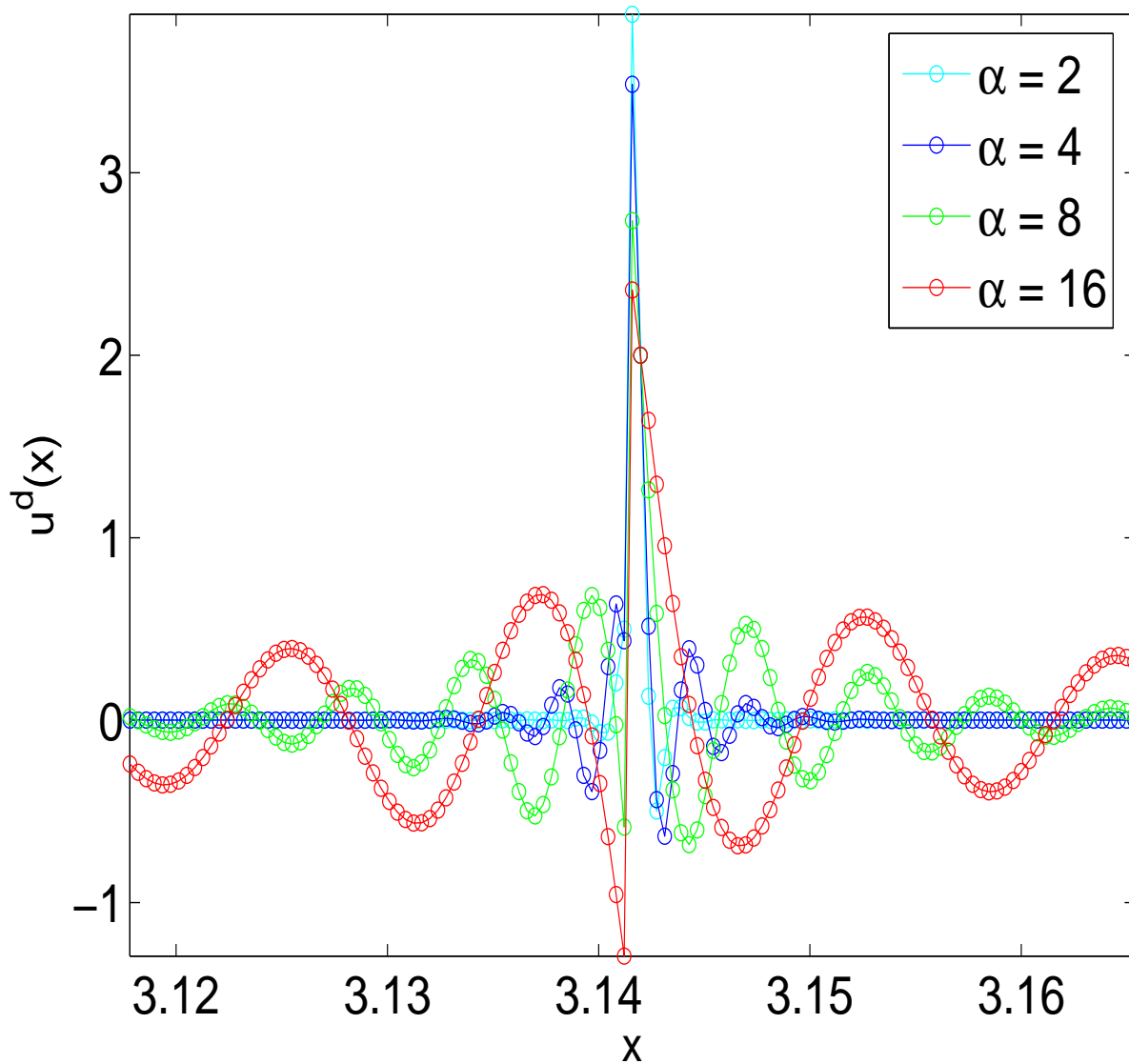
Figure 5.7: Plots of the deviation of the DNS steady solution from the outer solution, $u^d(x) = u(x) - u_0(x)$, versus x around $x = \pi$. These give clear evidence of oscillations in the vicinity of the shock at $x = \pi$; the wavelength of these oscillations increases with α as does the length ξ_α over which these oscillations get damped.
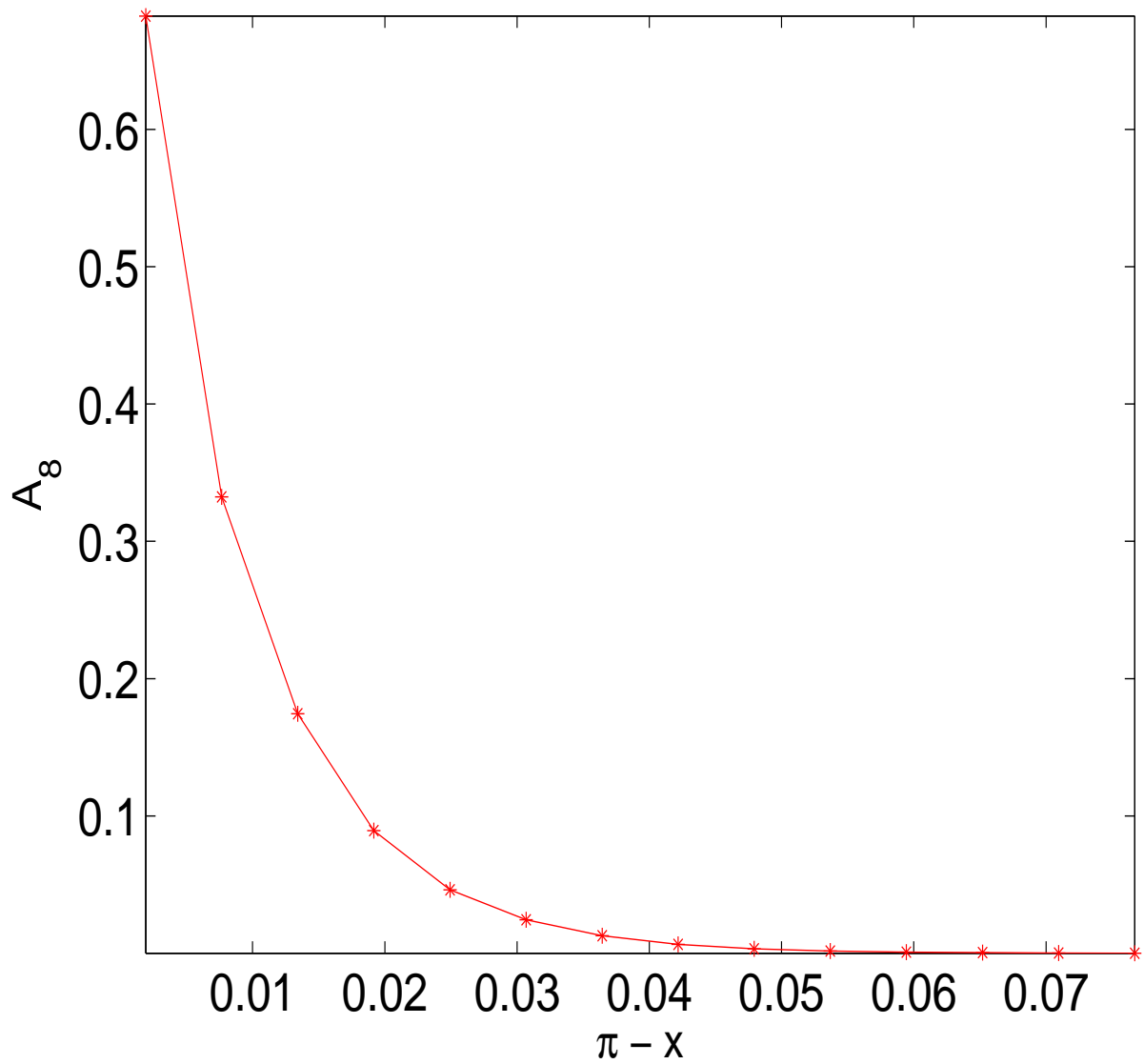
Figure 5.8: A plot of the amplitude $A_\alpha(\pi - x)$ versus the distance from the shock $\pi - x$ for $\alpha = 8$. The line connecting the data points, shown in red *, is a guide to the eye. As we move away from the shock at $x = \pi$ the amplitude of the oscillations decay exponentially.
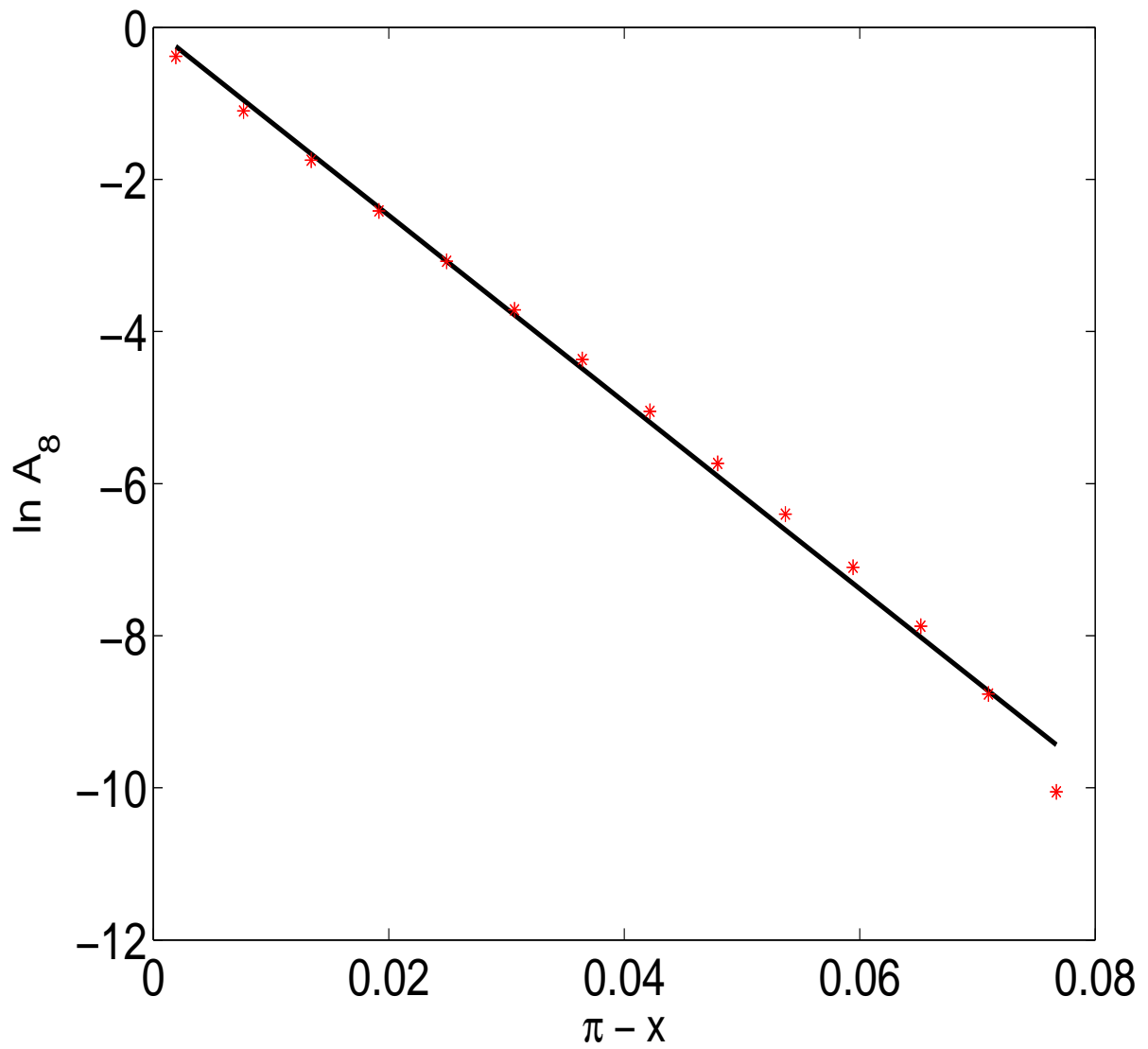
Figure 5.9: A semilog of $A_\alpha(\pi - x)$, shown as red *, versus the distance from the shock $\pi - x$ for $\alpha = 8$. The shock is at $x = \pi$. The black line is a linear fit; the plot is a clear signature that $A_8(\pi - x)$ decays exponentially with $(\pi - x)$.
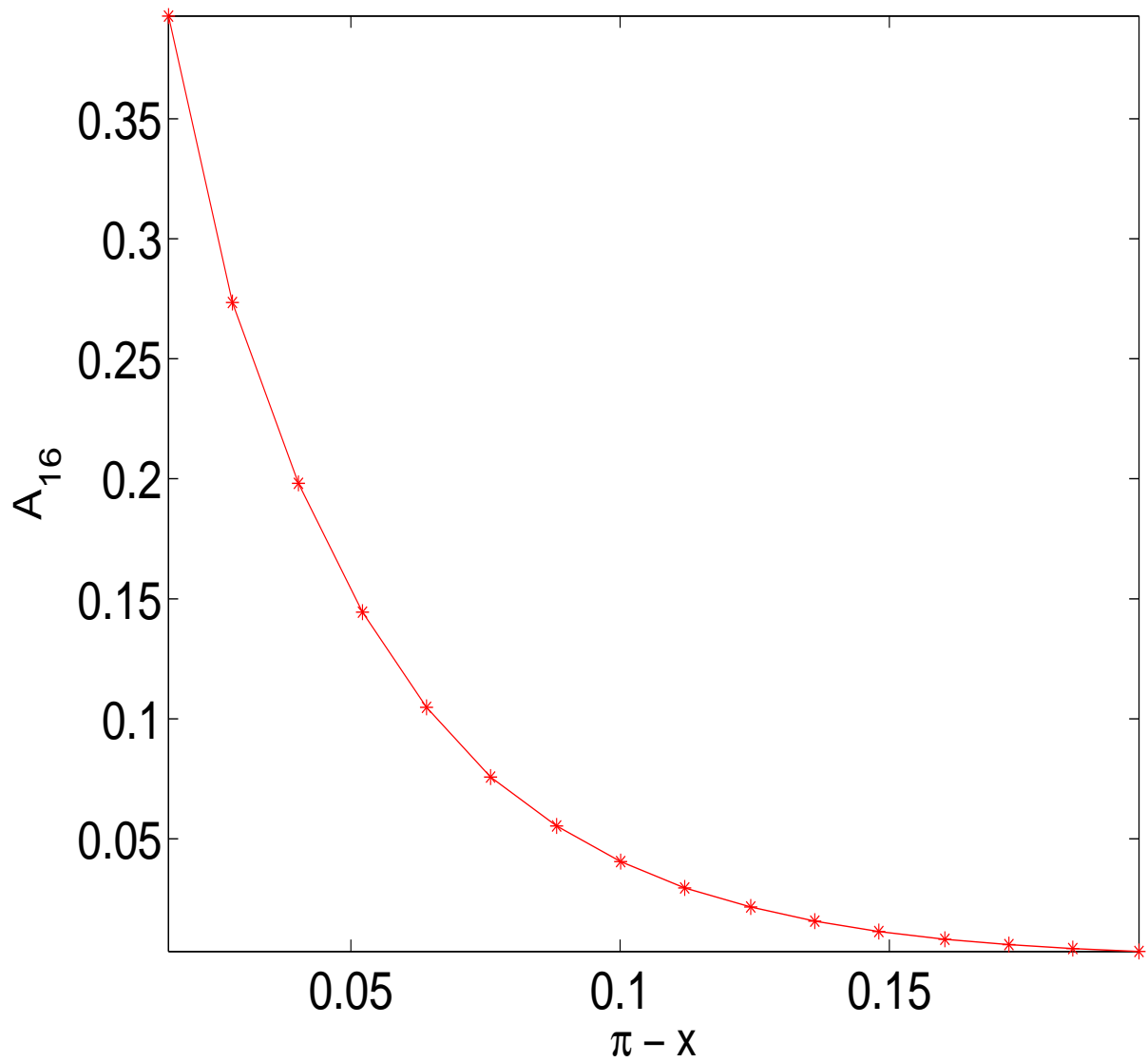
Figure 5.10: A plot of the amplitude $A_\alpha(\pi - x)$ versus the distance from the shock $\pi - x$ for $\alpha = 16$. The line connecting the data points, shown in red *, is a guide to the eye. As we move away from the shock at $x = \pi$ the amplitude of the oscillations decay exponentially.
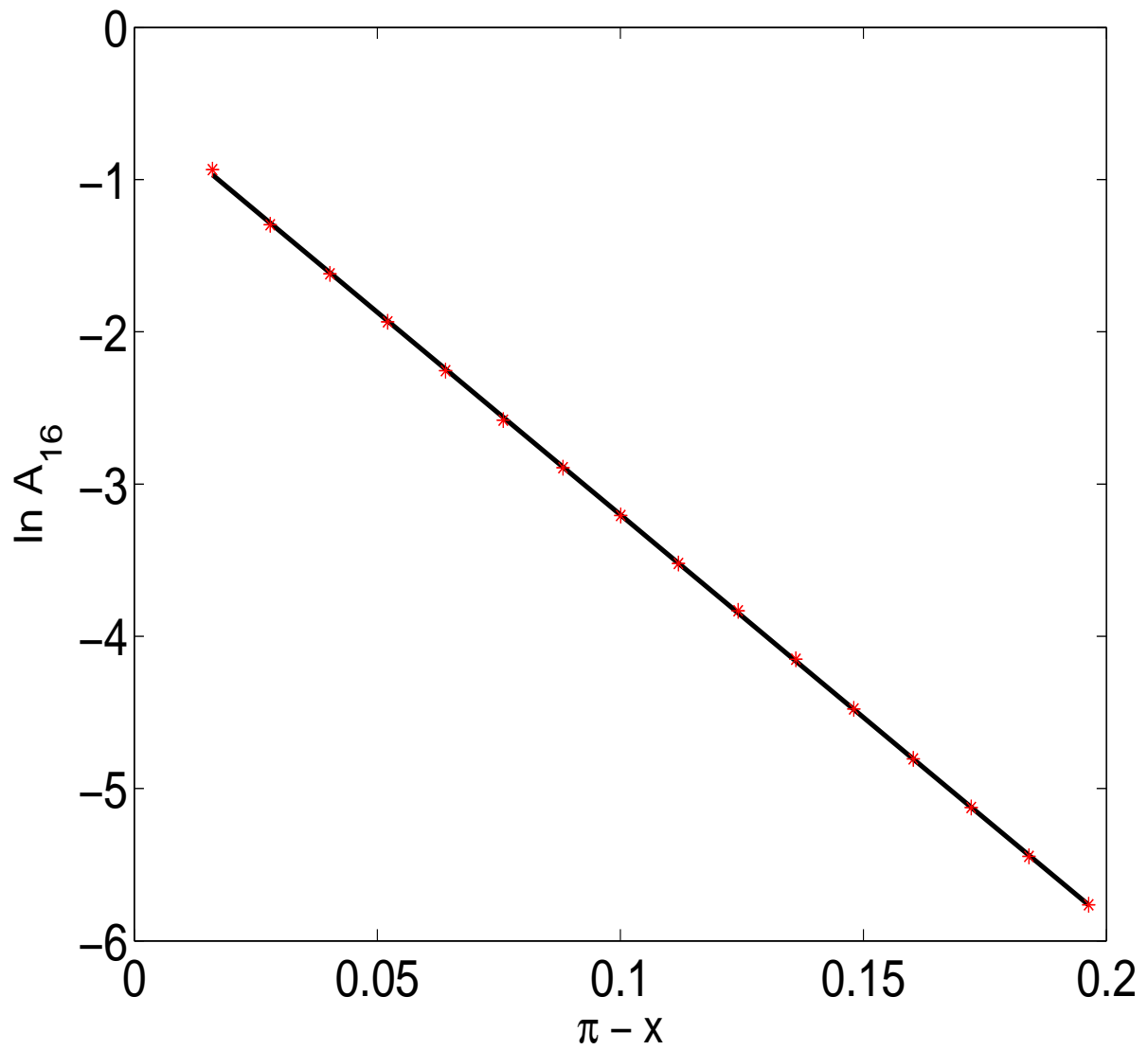
Figure 5.11: A semilog of $A_\alpha(\pi - x)$, shown as red *, versus the distance from the shock $\pi - x$ for $\alpha = 16$. The shock is at $x = \pi$. The black line is a linear fit; the plot is a clear signature that $A_{16}(\pi - x)$ decays exponentially with $(\pi - x)$.

Bibliography

[1] Frisch, U, *Turbulence: the Legacy of A.N. Kolmogorov*, Cambridge University Press, 1995.

[2] S.G. Saddoughi and S.V. Veeravalli, J. Fluid Mech. **268**, 333 (1994). As shown by W. Dobler, N.E.L. Haugen, T.A. Yousef and A. Brandenburg, Phys. Rev. E **68**, 026304 (2003), the 1D spectrum, generally measured in experiments, may not display a bottleneck even if the 3D spectrum does.

[3] Z.S. She, G. Doolen, R.H. Kraichnan, and S.A. Orszag, Phys. Rev. Lett. **70**, 3251 (1993); Y. Kaneda, T. Ishihara, M. Yokokawa, K. Itakura, and A. Uno, Phys. Fluids, **15**, L21 (2003); S. Kurien, M.A. Taylor, and T. Matsumoto, Phys. Rev. E **69**, 066313 (2004); J. Schumacher, Europhys. Lett. **80**, 54001 (2007); P.D. Mininni, A. Alexakis, and A. Pouquet, Phys. Rev. E **77**, 036306 (2008).

[4] J.P. Boyd, J. Sci. Comput. **9**, 81 (1994)

[5] Frisch, U., Kurien, S., Pandit, S., Pauls, W., Ray, S.S., Wirth, A. & Zhu, J-Z 2009 *Phys. Rev. Lett.* **101**, 144501.

[6] Ray, S.S., Frisch, U., Nazarenko, S., and Matsumoto, T. Unpublished.

Chapter 6

Extended Self Similarity for the Burgers Equation

6.1 Introduction

Extended Self-Similarity (ESS) was discovered in Ref. [1]. It is the empirical observation that, in fully developed turbulence, when plotting velocity structure functions of order p versus, say, the structure function of order three, rather than in the traditional way where they are plotted versus the separation, then the range over which clean, power-law scaling is observed can be substantially increased. This has improved the determination of the scaling exponents ζ_p of the structure functions of order p — or at least of ratios of such exponents — and has played a key role in confirming that three-dimensional, high-Reynolds-number, incompressible turbulence does not follow the [2] scaling law $\zeta_p = p/3$, but instead has *anomalous* scaling, with exponents that cannot be obtained solely through dimensional arguments. In this Chapter we revisit the problem of Extended Self-Similarity, principally for the Burgers equation, and also make predictions for the 3D Navier–Stokes equation. This work benefitted greatly from collaborations with U. Frisch and S. Chakraborty and the remaining part of this Chapter follows Ref. [3] closely.

In spite of several attempts to explain the success of ESS [4, 5, 6, 7, 8], the latter is still not fully understood and we do not know how much we can trust scaling exponents derived by ESS. It would be nice to have at least one instance for which ESS not only works, but does so for reasons we can rationally understand. A very natural candidate is the one-dimensional Burgers equation. Early attempts to test ESS on the Burgers equation did not show any appreciable increase in the quality of scaling through the use of ESS. As we show below, the conclusion that "ESS does not work for the Burgers equation" [9] was just a reflection of the computational limitations of the early 1990s.

In Section 6.2 we recall some basic facts and notations for ESS in three-dimensional Navier–Stokes turbulence. Then in Section 5.3 we turn to the Burgers equation and present new numerical evidence that ESS works for Burgers, provided high enough spatial resolution is used. In Section 6.4 we use asymptotic theory to explain in detail why ESS works for the Burgers case. Finally, in Section 6.5 we examine the possible lessons from our Burgers ESS study for three-dimensional Navier–Stokes turbulence.

6.2   ESS in a nutshell

Consider the three-dimensional Navier–Stokes (3DNS) equation

$$\partial_t \mathbf{v} + \mathbf{v} \cdot \nabla \mathbf{v} = -\nabla p + \nu \nabla^2 \mathbf{v}, \qquad \nabla \cdot \mathbf{v} = 0. \tag{6.1}$$

For the case of homogeneous, isotropic turbulence, (longitudinal) structure functions of integer order p are defined as

$$S_p(r) \equiv \left\langle (\delta v_{\parallel}(\mathbf{r}))^p \right\rangle, \tag{6.2}$$

in terms of the longitudinal velocity increments

$$\delta v_{\parallel}(\mathbf{r}) \equiv [\mathbf{v}(\mathbf{x} + \mathbf{r}) - \mathbf{v}(\mathbf{x})] \cdot \frac{\mathbf{r}}{r}, \tag{6.3}$$

where $r \equiv |\mathbf{r}|$. There is experimental and numerical evidence that, at high Reynolds numbers, structure functions follow scaling laws [10, 11]

$$S_p(r) \propto r^{\zeta_p} \qquad (6.4)$$

over some range of separations (the inertial range) $L \gg r \gg \eta_p$. Here L is the integral scale and η_p the dissipation scale. The latter may depend on the order p [12, 13].

Of course, the dominant-order behaviour given by (6.4) is accompanied by subdominant corrections involving the two small parameters characteristic of inertial-range intermediate asymptotics, namely r/L and η_p/r. The simplest would be to have

$$S_p(r) = C_p r^{\zeta_p} \left(1 + D_p^{\mathrm{IR}}(r/L)^{g_p^{\mathrm{IR}}} + D_p^{\mathrm{UV}}(\eta_p/r)^{g_p^{\mathrm{UV}}} \right) + \text{h.o.t.}, \qquad (6.5)$$

where h.o.t. stands for "higher-order terms" and where $g_p^{\mathrm{IR}} > 0$ and $g_p^{\mathrm{UV}} > 0$ are the infrared (IR) and ultraviolet (UV) gaps, respectively. For a given Reynolds number and thus a given ratio L/η_p, the smaller the gaps and the constants D_p^{IR} and D_p^{UV}, the larger the range of separations over which subdominant corrections remain small.

The ESS is an operational procedure that effectively enlarges the range of separations over which dominant-order scaling is a good approximation. In its simplest formulation, one considers two integer orders n and m and plots $|S_n(r)|$ vs $|S_m(r)|$ and finds empirically that the scaling relations

$$|S_n(r)| \approx |S_m(r)|^{\alpha(n,m)}, \qquad (6.6)$$

with suitable exponents $\alpha(n,m)$, hold much better than (6.4). One particularly interesting instance of this procedure is when $m = 3$. We then know from [2] that to dominant order we have the four-fifths law [11]

$$S_3(r) = -\frac{4}{5}\varepsilon r, \qquad (6.7)$$

where ε is the mean energy dissipation per unit mass. Thus, the third-order structure function (divided by $-(4/5)\varepsilon$) may be viewed as

a *deputy* of the separation r. A variant of the ESS, which frequently gives even better scaling, is to use alternative structure functions, defined with the absolute values of the longitudinal velocity increments, namely

$$F_p(r) \equiv \left\langle \left| \delta v_{\|}(\mathbf{r}) \right|^p \right\rangle . \tag{6.8}$$

It is then found empirically that

$$F_n(r) \approx F_m(r)^{\beta(n,m)} , \tag{6.9}$$

with suitable scaling exponents $\beta(n, m)$. Whatever its empirical merits, the variant procedure has the drawback that there is no equivalent to the four-fifths law for the third-order structure function with the absolute value of the longitudinal velocity increment. Thus we cannot safely use $F_3(r)$ as a deputy of r. We shall come back to this in Section 6.5.

6.3 ESS revisited for the Burgers equation

The one-dimensional Burgers equation

$$\partial_t u + u \partial_x u = \nu \partial_x^2 u; \quad u(x, 0) = u_0(x), \tag{6.10}$$

which was introduced originally as a poor man's Navier–Stokes equation [14], has some dramatic differences with three-dimensional Navier–Stokes (3DNS) turbulence. Foremost of these is that it is integrable [15, 16] and — as a consequence — does not display self-generated chaotic behaviour. Nevertheless it does display *anomalous scaling* in the following sense: superficially, the K41 theory [2] is applicable to the Burgers equation as much as it is to 3DNS. However, when starting with smooth initial data $u_0(x)$, the evolved solution displays shocks in the limit of vanishing viscosity ν. Thus $\zeta_p = 1$ for $p \geq 1$. When the Reynolds number is finite, structure functions will display scaling only over a limited range of separations r. Therefore, the Burgers

equation may be a good testing ground for ESS and also perhaps for understanding why and when it works. Such considerations did not escape the creators of the ESS technique. Unfortunately, no clean scaling for structure functions is observed with the Burgers equation, either in the standard representation or in ESS, as long as simulations are done with the spatial resolution easily available in the early nineties, namely, a few thousand collocation points. Scaling emerges only at much higher spatial resolutions with 128K (128×1024) Fourier modes and becomes fully manifest with 256K modes, which is now also the highest resolution achievable numerically within a time span of a few weeks.

Let us now explain our numerical strategy for studying ESS with the Burgers equation. Our goal in doing preliminary numerical experiments is to understand ESS in a rational way, starting from the basic equations. For this it is advisable to keep the formulation minimally complex. For example, there is no need at first to assume random initial conditions: we can just take an L-periodic initial condition and define the structure functions by integrating over the period:

$$S_p(r) \equiv (1/L) \int_0^L dx \, [u(x + r, t) - u(x, t)]^p. \tag{6.11}$$

We shall mostly work with a very simple *single-mode model* for which the initial condition is 2π-periodic, deterministic, and has a single Fourier mode, i.e.,

$$u_0 = \sin x. \tag{6.12}$$

As we shall see in Section 6.4, it is easy to extend the theory from the deterministic to the random case.

We integrated the Burgers equation (6.10) with the initial condition (6.12) by using a pseudo-spectral method with N collocation points and a two-thirds alias-removal rule. Time stepping was done in double precision by a fourth-order Runge–Kutta scheme with a constant time step δt. The viscous term was handled by the slaving technique
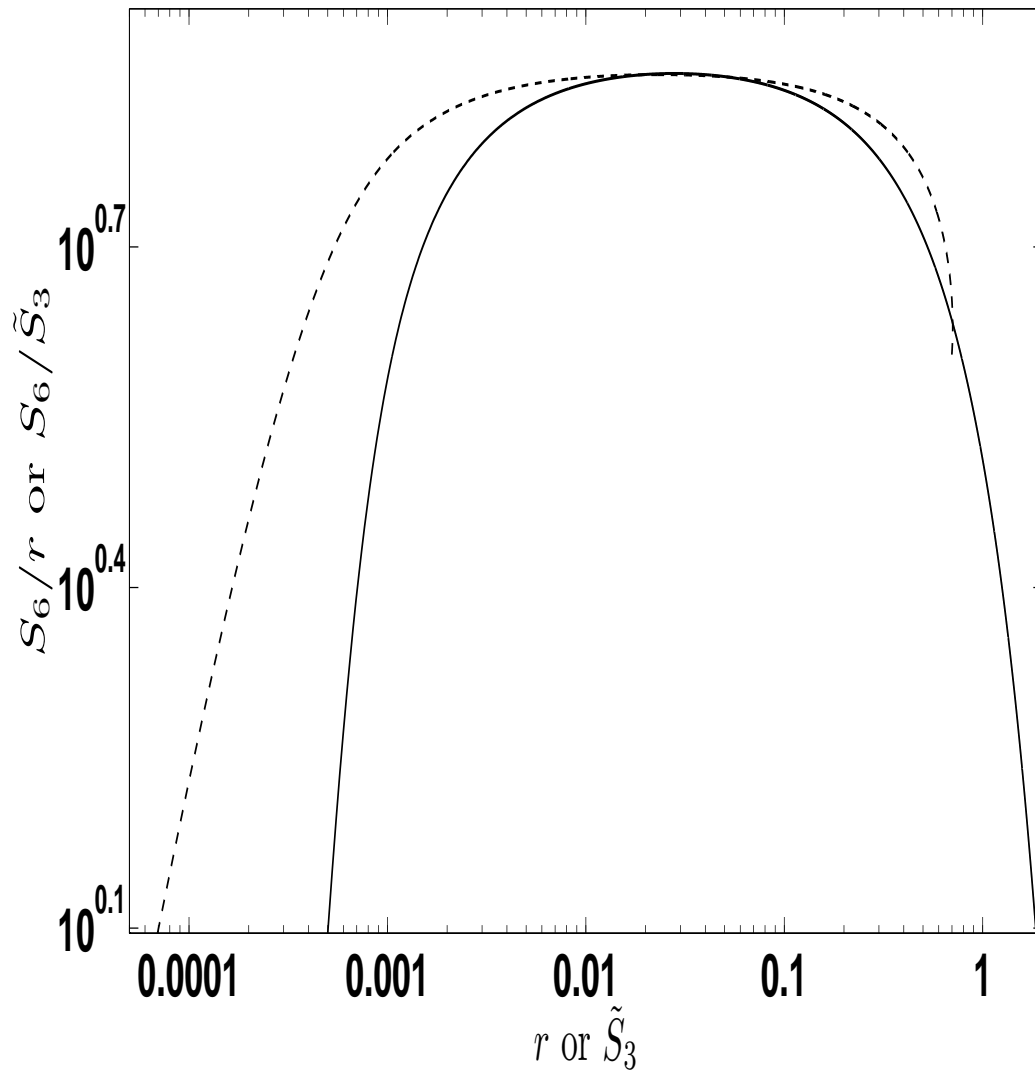
Figure 6.1: Compensated sixth-order structure function in standard (continuous line) and ESS (dashed line) representations.

known as ETDRK4 described in [17], which allows taking a time step about ten times larger than would be permitted with a direct handling of the viscous term. (It was pointed out by [18] that ETDRK4 can produce numerically ill-conditioned cancellations; following a suggestion of Zhu (private communication), we handled these by performing Taylor expansions to suitable order rather than by the complex-plane method proposed by [18].) This results not only in considerable speed-up but in much less accumulation of rounding noise.

The parameters of the run were $N = 256K$ and $\delta t = 10^{-5}$. Output was processed at $t = 2$, well beyond the time of appearance of the first shock at $t = t_\star = 1$.

Figure 6.1 shows the compensated structure function — that is divided by the theoretically predicted inertial-range dominant term — of order six in both the standard representation and in a variant of the ESS representation. Our variant uses

$$\tilde{S}_3(r) \equiv \frac{S_3(r)}{-12\varepsilon}, \tag{6.13}$$

where $\varepsilon \equiv -(1/L)(d/dt)\int_0^L dx\, u^2/2$ is the mean energy dissipation. It is easy to show that the Burgers counterpart of the four-fifth law for fluid turbulence is a "minus twelve" law [19], which makes $\tilde{S}_3$ the appropriate deputy of the separation r. In our opinion it is important to chose the constant in the definition of $\tilde{S}_3$ in such a way that it becomes r with a unit factor (to dominant order). Otherwise an ESS plot in log-log coordinates may show an overall improvement in quality of scaling, without our being able to disentangle the small-separation (UV) improvement from the large-separation (IR) improvement. As we shall see, both are present in general and have quite different origins.

A comparison of the two plots of compensated structure functions in Fig. 6.1 show that the ESS represents a substantial improvement in scaling both at the IR and UV ends. This is the first evidence that

ESS works for the Burgers equation. Next we shall understand why it works.

6.4 Asymptotic theory of ESS for the Burgers equation

We now give the theory for improved ESS scaling when $p \geq 3$, first for the single mode case and then for the case of random solutions.

To handle the infrared (IR) contributions to the structure functions we can work with an infinitely sharp shock by taking $\nu \to 0$. The dominant contribution to structure functions of integer order comes clearly from intervals $[x, x+r]$ which straddle the shock location $x_{\rm s}$ (in this Section the time variable is written explicitly only when needed). It is also easily shown that for $p \geq 3$ the first-order subdominant contributions comes from the small changes of the velocity, immediately to the left and the right of the shock, which are expressible by Taylor expanding the velocity to first order in these two regions [20]:

$$u(x) = u_- + (x - x_{\rm s})s_- + \text{h.o.t.}, \quad u(x) = u_+ + (x - x_{\rm s})s_+ + \text{h.o.t.}, \quad (6.14)$$

where u_- and u_+ are the velocities immediately to the left and to the right of the shock and s_- and s_+ their respective gradients. By starting from (6.11), limiting the integration domain to the interval $[x_{\rm s} - r, x_{\rm s}]$, which corresponds to the straddling condition, and using (6.14), we obtain

$$LS_p(r) = (-1)^p \left(\Delta^p r - \Delta^{p-1}(s_+ + s_-) \textit{f} p2r^2 \right) + \text{h.o.t.}, \quad (6.15)$$

where

$$\Delta \equiv u_- - u_+ > 0 \quad (6.16)$$

is the amplitude of the shock and $L = 2\pi$ is the spatial period. Specialising to the third-order structure function and to its rescaled version

the *separation deputy* $\tilde{S}_3(r) \equiv S_3(r)/(-12\varepsilon)$, we obtain

$$LS_3(r) = -\Delta^3 r + (f32)\,\Delta^2(s_- + s_+)r^2 + \text{h.o.t.} \qquad (6.17)$$

$$\tilde{S}_3(r) = r - (f32\Delta)\,(s_- + s_+)r^2 + \text{h.o.t.}, \qquad (6.18)$$

where we have used the relation

$$\varepsilon = \frac{\Delta^3}{12L} \qquad (6.19)$$

between the energy dissipation and the shock strength.

We now eliminate r between (6.18) and (6.15), so as to rewrite the structure function of order p as an expansion in the separation deputy as follows :

$$LS_p = (-1)^p \left(\Delta^p \tilde{S}_3 - \Delta^{p-1} (fp - 32)(s_- + s_+)\tilde{S}_3^2 \right) + \text{h.o.t.} \qquad (6.20)$$

Comparison of the standard expansion (6.15) of the structure function and its ESS expansion (6.20) shows that they have the same dominant terms and that their first subdominant corrections differ only by a numerical coefficient: $p/2$ for the standard case and $(p - 3)/2$ for ESS. Hence the subdominant correction has been decreased by a factor $p/(p - 3)$. For the case of the sixth-order structure function, considered in Fig. 6.1, this is a reduction by a factor two. Hence, the ESS inertial-range scaling extends by a factor 2 further into the IR direction before the same level of degradation is achieved as for the standard case. Note that for large ps the gain in scaling range becomes smaller.

Next we turn to the ultraviolet (UV) contributions which now require a finite viscosity ν that broadens the shock. Standard boundary-layer analysis for the shock, in the frame where the shock is at rest, (this basically amounts to dropping the time derivative term in the Burgers equation) gives the following, well-known result :

$$u(x) \approx -\frac{\Delta}{2} \tanh \frac{x\Delta}{4\nu}. \qquad (6.21)$$

Hence the UV structure functions are given by

$$LS_p(r) = \left(\frac{\Delta}{2}\right)^p \int_{-\infty}^{\infty} dx \left[\tanh\frac{x\Delta}{4\nu} - \tanh\frac{(x+r)\Delta}{4\nu}\right]^p. \qquad (6.22)$$

We are interested in the expansion of these structure functions for r much larger than the typical width $4\nu/\Delta$ of the shock. For this, we first establish the following expansion (for large $\tilde{r}$)

$$\int_{-\infty}^{\infty} d\tilde{x}\, [\tanh(\tilde{x}) - \tanh(\tilde{x} + \tilde{r})]^p = (-2)^p(\tilde{r} - H_{p-1}) + \text{t.s.t.} \qquad (6.23)$$

where t.s.t. stands for transcendentally small terms such as $\exp(-\tilde{r})$ and

$H_p \equiv 1 + 1/2 + 1/3 + \ldots + 1/p$ is the Harmonic function, which behaves as $\ln p$ for large p. By using (5.23) in (6.22), we obtain

$$LS_p(r) = (-1)^p \left(\Delta^p r - 4\nu H_{p-1}\Delta^{p-1}\right) + \text{t.s.t.}, \qquad (6.24)$$

and specialising to the case $p = 3$, we have

$$LS_3 = -\Delta^3 r + 6\nu\Delta^2 + \text{t.s.t.}, \quad \tilde{S}_3(r) = r - 6\frac{\nu}{\Delta} + \text{t.s.t.}. \qquad (6.25)$$

Proceeding as in the IR case, we re-expand S_p in terms of the deputy separation $\tilde{S}_3$:

$$LS_p(r) = (-1)^p \left(\tilde{S}_3\Delta^p - 4\nu\left(H_{p-1} - \frac{3}{2}\right)\Delta^{p-1}\right) + \text{t.s.t.} \qquad (6.26)$$

Thus, we see that with ESS the subdominant UV term for the structure function of order p is reduced by a factor $2H_{p-1}/(2H_{p-1} - 3)$ and, again, the range of scaling is extended by the same factor. For $p = 6$ the extension factor is $137/47 \approx 2.91$. Combining the UV and the IR gains, we see that the scaling for S_6 is extended by a factor 5.92, that is about three quarters of a decade.

Next we generalise these arguments to the case of the Burgers equation with smooth, random initial conditions and forcing, defined

on the whole real line. We assume that the forces and the initial conditions are statistically homogeneous and have rapidly decreasing spatial correlations (i.e., the system is mixing). We can then use ergodicity to obtain the following representation of structure functions:

$$S_p(r) \equiv \langle (u(x+r) - u(x))^p \rangle = \lim_{L \to \infty} \frac{1}{L} \int_0^L dx \, (u(x+r) - u(x))^p , \quad (6.27)$$

where the limit is in the almost sure sense and the angular brackets denote averaging over the statistically steady state. In the present context we have, typically, an infinite number of shocks on the whole line, but a finite number per unit length. The shock amplitudes Δ and the left and right velocity gradients s_- and s_+ become random variables. Revisiting the arguments given above for the deterministic, single-mode case, we find that, in both the IR and UV expansions, we now have to add the contributions stemming from the various shocks. By using ergodicity we obtain, in the UV domain,

$$S_p(r) = (-1)^p \left(\langle \Delta^p \rangle r - 4\nu H_{p-1} \langle \Delta^{p-1} \rangle \right) + \text{t.s.t.} \quad (6.28)$$

and, in the IR domain,

$$S_p(r) = (-1)^p \left(\langle \Delta^p \rangle r - \langle \Delta^{p-1}(s_+ + s_-) \rangle f p 2 r^2 \right) + \text{h.o.t.} \quad (6.29)$$

In the UV case we now make use of the inequality $\langle \Delta^p \rangle / \langle \Delta^{p-1} \rangle \geq \langle \Delta^3 \rangle / \langle \Delta^2 \rangle$, which follows, for $p \geq 3$, from the log-convexity of the moment function $q \mapsto \ln \langle \Delta^q \rangle$ for a positive random variable Δ. We can then finish the analysis of the depletion of subdominant contributions essentially as done above in the UV case and conclude that ESS extends the UV scaling by *at least* a factor $2H_{p-1}/(2H_{p-1} - 3)$. In the IR domain, the presence of the random quantity $s_+ + s_-$ prevents us from reaching similar conclusions and it is thus not clear that there is a general result regarding improved ESS scaling in the IR regime. This can, however, be circumvented, if we assume (i) that the Burgers turbulence is freely decaying (no forcing) and (ii) we limit ourselves to times large

compared to the typical turnover time of the initial condition. The solution degenerates then into a set of ramps of slope exactly $1/t$, separated by shocks. Hence $s_+ + s_- \approx 2/t$, which is the same as in the deterministic case. Thus, by using the same log-convexity inequality as above, we infer that ESS extends the IR scaling by *at least* a factor $p/(p-3)$.

6.5 Back to three-dimensional Navier–Stokes turbulence

We have explained the success of ESS by a depletion of subdominant IR and UV contributions. How does this relate to various explanations given over the past one-and-a-half decades for 3DNS turbulence? Let us mention a few. Sain and Bhattacharjee [4, 5] resorted to phenomenology in proposing cross-over functions from the dissipation- to the inertial-range for the structure functions defined in Fourier space. They inferred that, in the UV regime, the linear scaling in log-log plots of structure functions deteriorate at lower values of wavenumbers than in the corresponding ESS plots. Reference [6] introduced a scaling variable — again phenomenologically — to include crossovers between various subranges of scaling behaviour for the magnitude of longitudinal velocity differences and thereby showed that the scaling improves at the IR end when ESS is used. In the spirit of our formulation of a theory for ESS, the work of Ref. [7] comes closest. In this paper they have correctly identified the mechanism of increased scaling range at the UV end: a reduced coefficient in the subdominant diffusive correction. Their work on ESS was in the context of intermittency and anomalous scaling for passive-scalar dynamics. They used the model of Ref. [21, 22] and supplemented it by a closure relation suggested by Ref [22] which was later shown not to be fully inconsis-

tent with the original model by [23]. Benzi (private communication) also made a similar observation using a passive-scalar shell model.

How much of our findings for the Burgers equation carry over to 3DNS? It is important to realize that the improvement in scaling can arise both at the IR and the UV end of the scaling regime. In order to avoid mixing up these two types of improvements one should correctly *calibrate* the choice of the deputy for the separation r, by using the four-fifths law for 3DNS:

$$\tilde{S}_3(r) \equiv -\frac{S_3}{(4/5)\varepsilon}. \tag{6.30}$$

If a given turbulent flow shows a gain in scaling when using ESS, either in the IR or the UV domain or both, we can then use (6.5) to interpret the gain in terms of subdominant corrections. It is best to handle the IR and UV cases separately. By following the same procedure as in Section 6.4 it is easily shown that ESS gives just a modification of the coefficient of the first subdominant contribution provided the gap g_p, between the dominant and the first subdominant exponent, is independent of the order p. The fact that ESS works so nicely for 3DNS suggests that this independence may actually hold. If so, it is immediately seen that the reduction in the subdominant coefficient is equal to the gain in scaling raised to the gap value.

Thus we begin to see ESS as a way to obtain information on subdominant corrections. This is of interest for several reasons. For example, subdominant corrections can give rise to spurious multifractal scaling [24, 25]. Furthermore, consideration of subdominant corrections is needed to explain the absence of logarithms in the third-order structure function [26]. Also, the multifractal description of turbulence is quite heuristic and arbitrary and would be much more strongly constrained if we had information on subdominant terms and on gap values.

This may be the right place to discuss the issue of the best deputy of separation in the ESS procedure. Should one use $S_3(r)$ or the function

$F_3(r)$ which is defined with the third moment of the *absolute value* of the longitudinal velocity increment? It is not clear to what extent the two procedures are equivalent. For the case of the Burgers turbulence it is easy to show that $-S_3(r)$ and $F_3(r)$ have the same dominant and first-order subdominant terms: they differ only in sub-subdominant contributions. For 3DNS longitudinal velocity increments are somewhat more likely to be negative than positive but they have no reason to have exactly the same scaling behaviour. There has also been some amount of discussion regarding the scaling of longitudinal and transverse structure functions [27]. It may well be that they differ only by the relative strength of subdominant terms.

We finally address the issue of appropriate strategies to obtain systematically subdominant corrections from experimental or simulation data. The most straightforward method is to determine the dominant-order contribution by using ESS and then to subtract it from the data. The result can then be analysed either in the standard way or in the ESS fashion. However, it is known that, when subdominant terms are sizeable, it is best to determine them at the same time as the dominant ones. One instance of this is the simultaneous determination of dominant-order isotropic scaling and subdominant anisotropic corrections for weakly anisotropic turbulence [28, 29].

It might be possible to improve the determination of both dominant and subdominant terms by using the method of *asymptotic interpolation* [31, 32] which we will discuss in Chapter 7.

Bibliography

[1] Benzi, R., Ciliberto, S., Tripiccione, R., Baudet, C., Massaioli, F. & Succi, S, *Phys. Rev. E* **48**, R29, 1993.

[2] Kolmogorov, A.N, *Dokl. Akad. Nauk SSSR* **32**, 16, 1941.

[3] S. Chakraborty, U. Frisch, and S. S. Ray. J. Fluid Mech., *Fast Track*, in press. Available at http://arxiv.org/abs/0912.2406.

[4] Bhattacharjee, J.K. and Sain, A, *Physica A* **270**, 165, 1999.

[5] Sain, A. and Bhattacharjee, J.K, *Phys. Rev. E* **60**, 571, 1999.

[6] Fujisaka, H. and Grossman, S, *Phys. Rev. E* **63**, 026305, 2001.

[7] Segel, D., L'vov, V. & Procaccia, I, *Phys. Rev. Lett.* **76**, 1828, 1996.

[8] Yakhot, V, *Phys. Rev. Lett.* **87**, 234501, 2001.

[9] Benzi, R., Ciliberto, S., Baudet, C. & Chavarria, G.R, *Physica D* **80**, 385, 1995.

[10] Monin, A.S. and Yaglom, A.M, ed. J Lumley, MIT Press, Cambridge, MA, 1971.

[11] Frisch, U, *Turbulence: the Legacy of A.N. Kolmogorov*, Cambridge University Press, 1995.

[12] Paladin, G. and Vulpiani, A, *Phys.Rev. B* **35**, 2015, 1987.

[13] Frisch, U. and Vergassola, M, *Euro. Phys. Lett.* **14**, 439, 1991.

[14] Burgers, J.M., *The Nonlinear Diffusion Equation*, D. Reidel, Dordrecht, 1974.

[15] Hopf, E, *Comm. Pure Appl. Math.* **3**, 201, 1950.

[16] Cole, J.D, *Quart. Appl. Math.* **9**, 225, 1951.

[17] Cox, S.M. and Matthews, P.C, *J. Comp. Phys.* **176**, 430, 2002.

[18] Kassam, A.K. and Trefethen, L.N, *SIAM J. Sci. Comp.***26**, 1214, 2005.

[19] Gurbatov, S.N., Simdyankin, S.I., Aurell, E., Frisch, U. & Toth, G, *J. Fluid Mech.* **344**, 339, 1997.

[20] Bec, J., Frisch, U. & Khanin, K, *J. Fluid Mech.* **416**, 239–267, 2000.

[21] Kraichnan, R, *Phys. Fluids* **11**, 945, 1968.

[22] Kraichnan, R, *Phys. Rev. Lett.* **72**, 1016, 1994.

[23] Falkovich, G., Gawedzki, K. & Vergassola, M, *Rev. Mod. Phys.* **73**, 913, 2001.

[24] Aurell, E., Frisch, U., Lutsko, J. & Vergassola, M, 1992 *J. Fluid Mech.* **238**, 467, 1992.

[25] Mitra, D., Bec, J., Pandit, R. & Frisch, U, *Phys. Rev. Lett.* **94**, 194501, 2005.

[26] Frisch, U., Afonso, M.M., Mazzino, A.& Yakhot, V, *J. Fluid Mech.* **542**, 97. 2005.

[27] Benzi, R., Biferale, L., Fisher, R., Lamb, D.Q. & Toschi, F, *arXiv:0905.0082 [physics.flu-dyn]*, 2009.

[28] Biferale, L. and Procaccia, I, *Phys. Rep.* **414**, 43, 2005.

[29] Biferale, L., Lanotte, A.S. & Toschi, F, *Physica D* **237**, 1969, 2008.

[30] van der Hoeven, J, *J. Symb. Comput.* **44**, 1000, 2009.

[31] Pauls, W. and Frisch, U, *J. Stat. Phys.* **127**, 1095, 2007.

[32] Bardos, C., Frisch, U., Pauls, W., Ray, S.S. & Titi, E.S, *Commun. Math. Phys.* **293**, 519, 2010

Chapter 7

Entire Solutions of Hydrodynamical Equations with Exponential Dissipation

In this Chapter we consider a modification of the three-dimensional Navier–Stokes equations and other hydrodynamical evolution equations with space-periodic initial conditions in which the usual Laplacian of the dissipation operator is replaced by an operator whose Fourier transform grows exponentially as $e^{|k|/k_d}$ at high wavenumbers $|k|$. By using estimates in suitable classes of analytic functions, we show that the solutions with initially finite energy become immediately entire in the space variables and that the Fourier coefficients decay faster than $e^{-C(k/k_d)\ln(|k|/k_d)}$ for any $C < 1/(2\ln 2)$. The same result holds for the one-dimensional Burgers equation with exponential dissipation but can be improved: heuristic arguments and very precise simulations, analyzed by the method of asymptotic interpolation of van der Hoeven, indicate that the leading-order asymptotics is precisely of the above form with $C = C_\star = 1/\ln 2$. The same behavior with a universal constant $C_\star$ is conjectured for the Navier–Stokes equations with exponential dissipation in any space dimension. This universality prevents the strong growth of intermittency in the far dissipation range. Such intermittency is obtained for ordinary Navier–Stokes

turbulence. This work was done in collaboration with C. Bardos, U. Frisch, W. Pauls, and E. Titi [1]. The rest of the Chapter follows closely Ref. [1].

7.1 Introduction

More than a quarter of a millenium after the introduction by Euler of the equations of incompressible fluid dynamics the question of their well-posedeness in three dimensions (3D), with sufficienty smooth initial data, is still moot [2, 3, 4, 5] (also many papers in [6] and references therein). Even more vexing is the fact that switching to viscous flow for the solution of the Navier–Stokes equations (NSE), barely improves the situation in 3D [7, 8, 9, 10, 11]. Finite-time blow up of the solution to the NSE can thus not be ruled out, but there is no numerical evidence that this happens.

In contrast, there is strong numerical evidence that, for analytic spatially periodic initial data, both the 3D Euler and NSE have complex-space singularities. Indeed, when such equations are solved by (pseudo-)spectral techniques the Fourier transforms of the solution display an exponential decrease at high wavenumbers, which is a signature of complex singularities [12]. This behavior was already conjectured by von Neumann [13] who pointed out that the solution should be analytic with an exponentially decreasing spectrum. Recently Li and Sinai used a Renormalization-Group method to prove that for certain complex-valued initial data the 3D NSE display finite-time blow up in the real domain (and, as a trivial corollary, also in the complex domain) [14].

For some PDEs in space dimensions lower than 3, explicit information about the position and type of complex singularities may be available. For example, complex singularities can sometimes be related to poles of elliptic functions in connection with the reaction-

diffusion equation [15] and the 2D incompressible Euler equations in Lagrangian coordinates [16]. The best-understood case is that of the 1D Burgers equation with ordinary (Laplacian) dissipation:[1] its singularities are poles located at the zeroes of the solutions of the heat equation to which it can be mapped by using the Hopf–Cole transformation (see, e.g., [17, 18] and references therein).

We now return to the 3D NSE with real analytic data. It is known that blow up in the real domain can be avoided altogether by modifying the dissipative operator, whose Fourier-space symbol is $\mu|k|^2$, to a higher power of the Laplacian with Fourier-space symbol $\mu|k|^{2\alpha}$ ($\alpha > 5/4$) [7, 19]. The numerical evidence is, however, that complex singularities cannot be avoided by this "hyperviscous" procedure, which is frequently used in geophysical simulations (see, for example, [20]).

Actually, we are unaware of any instance of a nonlinear space-time PDE, with the property that the Cauchy problem is well posed in the complex space domain for at least some time and which is guaranteed never to have any complex-space singularities at a finite distance from the real domain. In other words, such that the solution stays or becomes entire for all $t > 0$. Here we shall show that solutions of the Cauchy problem are entire for a fairly large class of pseudo-differential nonlinear equations, encompassing variants of the 3D NSE, which possess "exponential dissipation", that is dissipation with a Fourier-space symbol growing exponentially as $e^{|k|/k_d}$ with the ratio of the wavenumber $|k|$ to a reference wavenumber k_d.

The Chapter is organized as follows. In Section 7.2 we consider the forced 3D incompressible NSE in a periodic domain with exponential dissipation. The initial conditions are assumed just to have finite energy. The main theorem is established by using classes of analytic functions whose norms contain exponentially growing weights in the Fourier space [21, 22]. In Section 7.3 we show that the Fourier

---

[1]The case of the Burgers equation with modified dissipation will be considered in Section 7.5.

transform of the solution decays at high wavenumbers faster than $\exp(-C\tilde{k}\ln\tilde{k})$ for any $C < 1/(2\ln 2)$. Here, $\tilde{k} := |k|/k_{\mathrm{d}}$ is the nondimensionalised wavenumber. In Section 7.4 we briefly present extensions of the result to other instances: different space dimensions and dissipation rates, problems formulated in the whole space and on a sphere, and different equations. In Section 7.5 we then turn to the 1D Burgers equation with a dissipation growing exponentially at high wavenumbers, for which the same bounds hold as for the 3D Navier–Stokes case. However, in the Burgers case, simple heuristic considerations (Section 7.5.1) and very accurate numerical simulations performed by two different techniques (Sections 7.5.2 and **??**), indicate that the leading-order asymptotic decay is precisely $\exp((-1/\ln 2)\tilde{k}\ln\tilde{k})$. In the concluding Section 7.6 we discuss open problems and a possible application.

7.2 Proof that the solution is entire

We consider the following 3D periodic Navier–Stokes equations with an exponential dissipation (expNSE) :

$$\frac{\partial u}{\partial t} + u \cdot \nabla u = -\nabla p - \mu \mathcal{D} u + f, \qquad \nabla \cdot u = 0, \qquad (7.1)$$

$$u(x, 0) = u_0(x). \qquad (7.2)$$

Here, $\mathcal{D}$ is the (pseudo-differential) operator whose Fourier space symbol is $\mathrm{e}^{2\sigma|k|}$, that is a dissipation rate varying exponentially with the wavenumber $|k|$, u_0 is the initial condition, f is a prescribed driving force, and μ and σ are prescribed positive coefficients. The problem is formulated in a periodic domain $\Omega = [0, L]^3$ (for simplicity of notation we take $\Omega = [0, 2\pi]^3$). The driving force is assumed to be a divergence-free trigonometric polynomial in the spatial coordinates. For technical convenience we use σ in the statements and proofs of mathematical

results, whereas the use of the reference wavenumber $k_\mathrm{d} = 1/(2\sigma)$ is preferred when discussing the results.

The initial condition is taken to be a divergence-free periodic vector field with a finite L^2 norm (finite energy).

As usual the problem is rewritten as an abstract ordinary differential equation in a suitable function space, namely,

$$\frac{du}{dt} + \mu e^{2\sigma A^{1/2}} u + B(u, u) = f; \tag{7.3}$$

$$u(0) = u_0; \tag{7.4}$$

here $A := -\nabla^2$ and $B(u, u)$ is a suitable quadratic form which takes into account the nonlinear term, the pressure term and the incompressibility constraint (see, e.g. [7, 8, 10]). Note that the Fourier symbol of $A^{1/2}$ is $|k|$.

The problem is formulated in the space $H := \{\varphi \in (L^2(\Omega))^3 : \varphi$ is periodic, $\int \varphi\, dx = 0$, $\nabla \cdot \varphi = 0\}$. Here, for any $\lambda \geq 0$, the Fourier symbol of the operator $e^{\lambda A^{1/2}}$ is given by $e^{\lambda|k|}$, where $k \in \mathbb{Z}^3 \setminus \{(0, 0, 0)\}$.

To prove the entire character, with respect to the spatial variables, of the solution $u(t)$ of expNSE for $t > 0$, it suffices to show that its Fourier coefficients decrease faster than exponentially with the wavenumber $|k|$. This will be done by showing that, for any $\lambda > 0$, the L^2 norm of $e^{\lambda A^{1/2}} u$, the solution with an exponential weight in Fourier space, is finite. As usual, we here denote the L^2 norm of a real space-periodic function f by $|f| := \sqrt{\int_{[0,2\pi]^3} |f(x)|^2 dx}$. Moreover, H^m will be the usual L^2 Sobolev space of index m (i.e., functions which have up to m space derivatives in L^2).

The main result (Theorem 2.1) will make use of the following Proposition which was inspired from [21] (see also [22])

<u>Proposition 2.1</u> *Let $\alpha \geq 0$, $\beta > 0$, $\kappa > 3$ and $\varphi \in \mathrm{dom}\,(e^{(\alpha+\beta)A^{1/2}})$. Then*

$$\left| e^{\alpha A^{1/2}} B(\varphi, \varphi) \right| \leq C_\mathrm{A} [l_\kappa(\beta)]^{\mathsf{a}(\kappa)} \left| e^{\alpha A^{1/2}} \varphi \right|^{\mathsf{b}(\kappa)} \left| e^{(\alpha+\beta)A^{1/2}} \varphi \right|^{\mathsf{a}(\kappa)}, \tag{7.5}$$

where C_A is a universal constant and

$$l_\kappa(\beta) := \sup_{0 \le x < \infty} x^\kappa e^{-\beta x} = \left(\frac{\kappa}{\beta}\right)^\kappa e^{-1}. \tag{7.6}$$

Notation In Proposition 2.1 and also in the sequel we have made use of the following notation (to avoid fractions in exponents):

$$\mathsf{a}(\kappa) := \frac{5}{2\kappa}, \quad \mathsf{b}(\kappa) := \frac{4\kappa - 5}{2\kappa}, \quad \mathsf{c}(\kappa) := \frac{2\kappa + 5}{2\kappa}, \quad \mathsf{d}(\kappa) := \frac{2\kappa + 5}{2\kappa - 5}$$

$$\mathsf{e}(\kappa) := \frac{4\kappa - 5}{2\kappa - 5}, \quad \mathsf{f}(\kappa) := \frac{2\kappa}{2\kappa - 5}, \quad \mathsf{g}(\kappa) := \frac{10}{2\kappa - 5}. \tag{7.7}$$

Proof Let $w \in H$, by using the Fourier representations $\varphi(x) = \sum_l e^{i l \cdot x} \hat{\varphi}_l$ and $w(x) = \sum_k e^{i k \cdot x} \hat{w}_k$ and Parseval's theorem, we have

$$\frac{1}{(2\pi)^3} \left(e^{\alpha A^{1/2}} B(\varphi, \varphi), w \right) = \sum_{k \in \mathbb{Z}^3\, k \neq 0} e^{\alpha |k|} \left(\sum_{l+m=k;\, l,m \neq 0} (\hat{\varphi}_l \cdot i m) \hat{\varphi}_m \right) \cdot \hat{w}_k^*, \tag{7.8}$$

where the $*$ means complex conjugation.

Since $e^{\alpha |k|} \le e^{\alpha |m| + \alpha |l|}$, when $k = l + m$, we can estimate the absolute value of the right-hand side from above as

$$\le \sum_{k \neq 0} \sum_{l+m=k,\, l,m \neq 0} e^{\alpha |l|} |\hat{\phi}_l| \, |m| e^{\alpha |m|} |\hat{\phi}_m| \, |\hat{w}_k|$$

$$= \frac{1}{(2\pi)^3} \int \Phi(x) \Psi(x) W(x) dx \le \frac{1}{(2\pi)^3} \|\Psi\|_{L^\infty} |\Phi| \, |W|, \tag{7.9}$$

where the functions $\Phi(x)$, $\Psi(x)$ and $W(x)$ are given by

$$\Phi(x) = \sum_{l \neq 0} e^{\alpha |l|} |\hat{\varphi}_l| e^{i l \cdot x}, \tag{7.10}$$

$$\Psi(x) = \sum_{m \neq 0} |m| e^{\alpha |m|} |\hat{\varphi}_m| e^{i m \cdot x}, \tag{7.11}$$

and

$$W(x) = \sum_{k \neq 0} |\hat{w}_k| e^{i k \cdot x}, \tag{7.12}$$

and the last inequality follows from the Cauchy–Schwarz inequality.

By Agmon's inequality [23] (see also [8]) in 3D we have

$$
\|\Psi\|_{L^\infty} \le C_A \|\Psi\|_{H^1}^{\frac{1}{2}} \|\Psi\|_{H^2}^{\frac{1}{2}} \le C_A \left|A^{1/2}\Psi\right|^{\frac{1}{2}} |A\Psi|^{\frac{1}{2}} = C_A \left|Ae^{\alpha A^{1/2}}\varphi\right| \left|A^{3/2}e^{\alpha A^{1/2}}\varphi\right|,
$$
(7.13)

where $C_A > 0$ is a universal constant. By using (7.10), (7.13) and the fact that $|W| = |w|$, we obtain

$$
\left|(e^{\alpha A^{1/2}}B(\varphi,\varphi),w)\right| \le C_A \left|e^{\alpha A^{1/2}}\varphi\right| \left|Ae^{\alpha A^{1/2}}\varphi\right|^{\frac{1}{2}} \left|A^{\frac{3}{2}}e^{\alpha A^{1/2}}\varphi\right|^{\frac{1}{2}} |w|.
$$
(7.14)

And by using the interpolation inequality between L^2 and H^κ, where $\kappa > 3$, we obtain[2]

$$
\left|(e^{\alpha A^{1/2}}B(\varphi,\varphi),w)\right| \le C_A \left|e^{\alpha A^{1/2}}\varphi\right|^{b(\kappa)} \left|A^{\frac{\kappa}{2}}e^{\alpha A^{1/2}}\varphi\right|^{a(\kappa)} |w|.
$$
(7.15)

Now, to obtain the inequality in Proposition 2.1, we just need to estimate the operator norm (in the sense of the L^2-operator norm)

$$
\left\|A^{\frac{\kappa}{2}}e^{-\beta A^{1/2}}\right\|_{\mathcal{L}(H)} \le \sup_{0 \le x < \infty} x^\kappa e^{-\beta x} = \left(\frac{\kappa}{\beta}\right)^\kappa e^{-1} = l_\kappa(\beta).
$$
(7.16)

This concludes the proof of Proposition 2.1.

Next, we state and present the proof of the main theorem. The steps of the proof are made in a formal way; however, they can be justified rigorously by establishing them first for a Galerkin approximation system and using the usual Aubin compactness theorem to pass to the limit (see, e.g. [7, 8, 10]). Furthermore, we do not assume that the initial condition u_0 is entire; it is only assumed to be square integrable, although it will become entire for any $t > 0$. This is why in estimating L^2 norms of the solution with exponential weights we have to stay clear of $t = 0$.

---

[2]The simplest formulation is obtained for $\kappa = 5$ but the optimisation of the bound for the law of decay in Section 7.3 requires using arbitrary κ.

Theorem 2.1 *Let $u_0 \in H$, $T > 0$ and let $f(x,t)$ be an entire function with respect to the spatial variable. Then for every $n = 0, 1, 2 \dots$ there exist constants $C_n, \bar{C}_n, K_n$ and $\bar{K}_n$ which depend on $|u_0|, \mu, T, \sigma$ and on*

$$\int_0^T \left| e^{(n-1)\sigma A^{1/2}} f(s) \right|^2 ds; \tag{7.17}$$

moreover there exists integers $p_n, q_n \geq 1$ such that

$$\left| e^{n\sigma A^{1/2}} u(t) \right|^2 \leq \frac{K_n}{t^{p_n}} + C_n, \quad \textit{for all} \ \ t \in (0, T] \tag{7.18}$$

and

$$\int_t^T |e^{(n+1)\sigma A^{1/2}} u(s)|^2 ds \leq \frac{\bar{K}_n}{t^{q_n}} + \bar{C}_n, \quad \textit{for all} \ t \in (0, T]. \tag{7.19}$$

Corollary 2.1 *Let $u_0 \in H, T > 0$ and let $f(x, t)$ be an entire function with respect to the spatial variable x such that for every $M \geq 0$ we have $\int_0^T \left| e^{M\sigma A^{1/2}} f(s) \right|^2 ds < \infty$. Then, the solution $u(t)$ of (7.3)-(7.4) is an entire function with respect to the spatial variable on the interval $(0, T]$, and satisfies the estimates (7.18) and (7.19) in Theorem 2.1 for any $n = 1, 2, \dots$.*

Proof of Corollary 2.1 Consider the Fourier series representation

$$u(x, t) = \sum_k e^{i k \cdot x} \hat{u}(k, t). \tag{7.20}$$

From (7.18) and Parseval's theorem, we have, for any $n = 0, 1, 2 \dots$

$$\sum_k e^{2n\sigma|k|} |\hat{u}(k, t)|^2 < \infty, \tag{7.21}$$

for $t > 0$. In (7.20) we change x to a complex location $z = x + \mathrm{i} y$ and obtain

$$u(x + \mathrm{i} y, t) = \sum_k e^{i k \cdot (x + \mathrm{i} y)} \hat{u}(k, t) \tag{7.22}$$

$$= \sum_k \left[e^{i k \cdot x} e^{-|k|} \right] \left[e^{-k \cdot y + |k|} \hat{u}(k, t) \right]. \tag{7.23}$$

For any $n = 1, 2, \ldots$, the series (7.23) of complex analytic functions converges uniformly in the strip $|y| + 1 \leq 2n$. This is because the sum in (7.23) is shown to be bounded, for any y, by use of the Cauchy–Schwarz inequality applied to the two bracketed expressions and use of (7.21) with $2n > |y| + 1$. Hence the Fourier series representation converges in the whole complex domain. This concludes the proof of the entire character of the solution with respect to the spatial variables.

Remark This corollary just expresses the most obvious part of the Paley–Wiener Theorem.

Proof of Theorem 2.1 The proof of the theorem proceeds by mathematical induction.

Step $n = 0$ We prove the statement of the theorem for $n = 0$. We take the inner product of (7.3) with u and use the fact that $(B(u, u), u) = 0$ to obtain (when there is no ambiguity we shall henceforth frequently denote $u(t)$ by u)

$$\frac{1}{2}\frac{d}{dt}|u|^2 + \mu \left|e^{\sigma A^{1/2}}u\right|^2 = (f, u) = (e^{-\sigma A^{1/2}}f, e^{\sigma A^{1/2}}u) \qquad (7.24)$$

$$\leq \left|e^{-\sigma A^{1/2}}f\right| \left|e^{\sigma A^{1/2}}u\right|$$

$$\leq \frac{|e^{-\sigma A^{1/2}}f|}{2\mu} + \frac{\mu}{2}|e^{\sigma A^{1/2}}u|^2, \qquad (7.25)$$

where Young's inequality has been used to obtain the third line. Therefore

$$\frac{d}{dt}|u|^2 + \mu \left|e^{\sigma A^{1/2}}u\right|^2 \leq \frac{|e^{-\sigma A^{1/2}}f|}{\mu}. \qquad (7.26)$$

Integrating the above from 0 to T, we obtain

$$|u(t)|^2 + \mu \int_0^T \left|e^{\sigma A^{1/2}}u(s)\right|^2 ds \leq |u_0|^2 + \frac{1}{\mu} \int_0^T \left|e^{-\sigma A^{1/2}}f(s)\right|^2 ds = C_0. \qquad (7.27)$$

Hence

$$|u(t)|^2 \leq C_0. \qquad (7.28)$$

and

$$\mu \int_0^T \left| e^{\sigma A^{1/2}} u(s) \right|^2 ds \le C_0 \tag{7.29}$$

From (7.28) and (7.29) we obtain (7.18) and (7.19) for the case $n = 0$. Here C_0 is given by (7.27), $K_0 = 0$, $\bar{K}_0 = 0$ and $\bar{C}_0 = C_0$. Notice that since $K_0 = \bar{K}_0 = 0$ there is no need to determine the integers p_0 and q_0; however, for the sake of initializing the induction process we chose $p_0 = q_0 = 1$.

Step $n \to n+1$ Assume that (7.18) and (7.19) are true up to $n = m$ and we would like to prove them for $n = m + 1$. Let us take the inner product of (7.3) with $e^{2(m+1)\sigma A^{1/2}} u$ and obtain

$$\frac{1}{2}\frac{d}{dt}\left| e^{(m+1)\sigma A^{1/2}} u \right|^2 + \mu \left| e^{(m+2)\sigma A^{1/2}} u \right|^2$$

$$\le \left| (f, e^{2(m+1)\sigma A^{1/2}} u) \right| + \left| (B(u,u), e^{2(m+1)\sigma A^{1/2}} u) \right|$$

$$\le \left| e^{m\sigma A^{1/2}} f \right| \left| e^{(m+2)\sigma A^{1/2}} u \right| + \left| e^{m\sigma A^{1/2}} B(u,u) \right| \left| e^{(m+2)\sigma A^{1/2}} u \right|.$$

Now we use Proposition 2.1 to majorize the previous expression by

$$\le \left| e^{m\sigma A^{1/2}} f \right| \left| e^{(m+2)\sigma A^{1/2}} u \right| + C_A [l_\kappa(\beta)]^{a(\kappa)} \left| e^{m\sigma A^{1/2}} u \right|^{b(\kappa)} \left| e^{(m+2)\sigma A^{1/2}} u \right|^{c(\kappa)}. \tag{7.30}$$

By Young's inequality we have

$$C_A [l_\kappa(\beta)]^{a(\kappa)} \left| e^{m\sigma A^{1/2}} u \right|^{b(\kappa)} \left| e^{(m+2)\sigma A^{1/2}} u \right|^{c(\kappa)} \le$$

$$\frac{2\kappa - 5}{4\kappa} \mu^{-d(\kappa)} C_A^{2f(\kappa)} [l_\kappa(\beta)]^{g(\kappa)} \left(\frac{2\kappa + 5}{\kappa} \right)^{d(\kappa)} \left| e^{m\sigma A^{1/2}} u \right|^{2e(\kappa)} + \frac{\mu}{4} \left| e^{(m+2)\sigma A^{1/2}} u \right|^2, \tag{7.31}$$

from which follows

$$\frac{d}{dt}\left| e^{(m+1)\sigma A^{1/2}} u \right|^2 + \mu \left| e^{(m+2)\sigma A^{1/2}} u \right|^2 \le \frac{2}{\mu} \left| e^{m\sigma A^{1/2}} f \right|^2$$

$$+ \frac{2\kappa - 5}{2\kappa} \mu^{-d(\kappa)} C_A^{2f(\kappa)} [l_\kappa(\beta)]^{g(\kappa)} \left(\frac{2\kappa + 5}{\kappa} \right)^{d(\kappa)} \left| e^{m\sigma A^{1/2}} u \right|^{2e(\kappa)}. \tag{7.32}$$

Now we integrate this inequality on the interval $(s, t) \subset (0, T)$, obtaining

$$
\left| e^{(m+1)\sigma A^{1/2}} u(t) \right|^2 + \mu \int_s^t \left| e^{(m+2)\sigma A^{1/2}} u(s') \right|^2 ds'
$$
$$
\leq \left| e^{(m+1)\sigma A^{1/2}} u(s) \right|^2 + \frac{2}{\mu} \int_s^t \left| e^{m\sigma A^{1/2}} f(s') \right|^2 ds' + C \int_s^t \left| e^{m\sigma A^{1/2}} u(s') \right|^{2e(\kappa)} ds'
$$
$$
\leq \left| e^{(m+1)\sigma A^{1/2}} u(s) \right|^2 + \frac{2}{\mu} \int_0^T \left| e^{m\sigma A^{1/2}} f(s') \right|^2 ds' + C \int_s^t \left| e^{m\sigma A^{1/2}} u(s') \right|^{2e(\kappa)} ds',
$$

$$\tag{7.33}$$

where we have set for brevity

$$
C = C(\mu, \beta, \kappa) := \frac{2\kappa - 5}{2\kappa} \mu^{-d(\kappa)} C_A^{2f(\kappa)} [l_\kappa(\beta)]^{g(\kappa)} \left(\frac{2\kappa + 5}{\kappa} \right)^{d(\kappa)}, \tag{7.34}
$$

where $l_\kappa(\beta)$ is given by (7.6).

Now we come to the point where we use the actual induction assumptions. We use (7.18) and the midpoint convexity to estimate the integrand in the last integral:

$$
\left| e^{m\sigma A^{1/2}} u(t) \right|^{2e(\kappa)} \leq \left(\frac{K_m}{t^{p_m}} + C_m \right)^{e(\kappa)} \leq 2^{f(\kappa)} \left(\frac{K_m}{t^{p_m}} \right)^{e(\kappa)} + 2^{f(\kappa)} C_m^{e(\kappa)}. \tag{7.35}
$$

Therefrom follows

$$
C \int_s^t \left| e^{m\sigma A^{1/2}} u(s') \right|^{2e(\kappa)} ds' \leq 2^{f(\kappa)} C \frac{1}{e(\kappa) p_m - 1} K_m^{e(\kappa)} \left(\frac{1}{s^{e(\kappa) p_m - 1}} - \frac{1}{t^{e(\kappa) p_m - 1}} \right)
$$
$$
+ 2^{f(\kappa)} C C_m^{e(\kappa)} (t - s) \leq 2^{f(\kappa)} C \frac{1}{e(\kappa) p_m - 1} K_m^{e(\kappa)} \frac{1}{s^{e(\kappa) p_m - 1}} + 2^{f(\kappa)} C C_m^{e(\kappa)} (t - s).
$$

$$\tag{7.36}$$

Discarding the positive term $\mu \int_s^t \left| e^{(m+2)\sigma A^{1/2}} u(s') \right|^2 ds'$ in (7.33), we obtain from (7.33) and (7.36)

$$
\left| e^{(m+1)\sigma A^{1/2}} u(t) \right|^2 \leq \left| e^{(m+1)\sigma A^{1/2}} u(s) \right|^2 + \frac{2}{\mu} \int_0^T \left| e^{m\sigma A^{1/2}} f(s') \right|^2 ds'
$$
$$
+ 2^{f(\kappa)} C \frac{1}{e(\kappa) p_m - 1} K_m^{e(\kappa)} \frac{1}{s^{e(\kappa) p_m - 1}} + 2^{f(\kappa)} C C_m^{e(\kappa)} (t - s).
$$

$$\tag{7.37}$$

Integrating this inequality with respect to s over $(t/2, t)$ we get

$$\left| e^{(m+1)\sigma A^{1/2}} u(t) \right|^2 \leq \frac{2}{t} \int_{t/2}^t \left| e^{(m+1)\sigma A^{1/2}} u(s) \right|^2 ds + \frac{2}{\mu} \int_0^T \left| e^{m\sigma A^{1/2}} f(s') \right|^2 ds'$$

$$+ \frac{2^{\mathsf{f}(\kappa)} C K_m^{\mathsf{e}(\kappa)}}{(\mathsf{e}(\kappa)p_m - 1)(\mathsf{e}(\kappa)p_m - 2)} \left(\frac{2}{t} \right)^{\mathsf{e}(\kappa)p_m - 1} + 2^{\mathsf{f}(\kappa)} C C_m^{\mathsf{e}(\kappa)} \frac{t}{4}.$$

$$(7.38)$$

Note that $p_m \geq 1$ implies that

$$\frac{4\kappa - 5}{2\kappa - 5} p_m - 2 > 0. \tag{7.39}$$

By using (7.19), we have

$$\left| e^{(m+1)\sigma A^{1/2}} u(t) \right|^2 \leq \overline{K}_m \left(\frac{2}{t} \right)^{q_m + 1} + \overline{C}_m \frac{2}{t} + \frac{2}{\mu} \int_0^T \left| e^{m\sigma A^{1/2}} f(s') \right|^2 ds'$$

$$(7.40)$$

$$+ \frac{2^{\mathsf{f}(\kappa)} C K_m^{\mathsf{e}(\kappa)}}{(\mathsf{e}(\kappa)p_m - 1)(\mathsf{e}(\kappa)p_m - 2)} \left(\frac{2}{t} \right)^{\mathsf{e}(\kappa)p_m - 1} + 2^{\mathsf{f}(\kappa)} C C_m^{\mathsf{e}(\kappa)} \frac{T}{4}.$$

From this relation follows that (7.18) holds for $m + 1$ with

$$p_{m+1} = \max \left\{ \frac{4\kappa - 5}{2\kappa - 5} p_m - 1, q_m + 1 \right\}, \tag{7.41}$$

$$q_{m+1} = \max \left\{ \frac{4\kappa - 5}{2\kappa - 5} p_m - 1, q_m + 1 \right\}. \tag{7.42}$$

By the induction assumption we use (7.33) to estimate

$$\int_{\frac{t}{2}}^T \left| e^{(m+1)\sigma A^{1/2}} u(s) \right|^2 ds \leq \frac{2^{q_m} \bar{K}_m}{t^{q_m}} + \bar{C}_m. \tag{7.43}$$

From this estimate and the above we conclude the existence of the constants K_{m+1}, C_{m+1} and the integer p_{m+1} such that (7.18) holds for $n = m + 1$. Using the estimate that we have just established in (7.18) for $n = m+1$, and substituting this in (7.33), we immediately obtain the estimate (7.19) for $n = m + 1$. This concludes the proof of Theorem 2.1.

7.3 Rate of decay of the Fourier coefficients

The purpose of this section is to specify the behavior of various constants appearing in the preceding section to obtain the rate of decay with the wavenumber of the Fourier coefficients $\hat{u}(k,t)$ for $t > 0$. We again consider the 3D case in the periodic domain. Since the decay may depend on the rate of decay of the Fourier transform of the forcing term $f(x,t)$, for simplicity we assume zero external forcing. The adaptation to sufficiently regular forced cases, for example a trigonometric polynomial, is similar.[3] Furthermore, it is enough to prove the decay result up to a time T such that $1/N := TU/L < 1$, where L and U are a typical length scale and velocity of the initial data. Extending the results to later times is easy (by propagation of regularity).

We shall show that the bound for the square of the L^2 norm of the velocity weighted by $e^{n\sigma A^{1/2}}$ is a double exponential in n. Specifically, we have

Theorem 3.1 *Let $u(t)$ be the solution of* (7.3)-(7.4) *in* $[0,T]$ *with $f = 0$ and $0 < T < L/U$. Then for every $\kappa > 3$ and $\delta > 0$, there exists a large enough number Λ, depending on δ and κ, such that, for all integer $n \geq 0$*

$$\left| e^{n\sigma A^{1/2}} u(t) \right|^2 \ \leq \ \left(\frac{\Lambda L}{Ut} \right)^{a_n}, \qquad t \in (0,T], \qquad (7.44)$$

$$\int_t^T \left| e^{(n+1)\sigma A^{1/2}} u(s) \right|^2 ds \ \leq \ \left(\frac{\Lambda L}{Ut} \right)^{a_n}, \qquad t \in (0,T] \qquad (7.45)$$

$$a_n \ = \ \left((1+\delta) \frac{4\kappa - 5}{2\kappa - 5} \right)^n. \qquad (7.46)$$

Corollary 3.1 *For any $t > 0$ the function $u(t)$ of* (7.3)-(7.4) *is an entire function in the space variable and its (spatial) Fourier coefficients*

---

[3]It is conceivable that the results can be extended to forces entire in the space variables whose Fourier transforms decrease faster than $e^{-C|k|\ln|k|}$ with sufficiently large C.

tend to zero in the following faster-than-exponential way: there exists a constant Λ such that, for any $0 < \varepsilon < 1$, we have

$$|\hat{u}(k,t)| \leq e^{-\frac{\sigma(1-\varepsilon)}{\beta_{\kappa,\delta}}|k|\ln|k|}, \quad \text{for all} \quad |k| \geq \left(\sqrt{\frac{\Lambda L}{Ut}}\right)^{\frac{\beta_{\kappa,\delta}}{\varepsilon\sigma}}, \tag{7.47}$$

where

$$\beta_{\kappa,\delta} = \ln\left((1+\delta)\frac{4\kappa - 5}{2\kappa - 5}\right). \tag{7.48}$$

Proof of Corollary 3.1 Since we are dealing with a Fourier series, the modulus of any Fourier coefficient of the function $e^{(n+1)\sigma A^{1/2}}u(t)$ cannot exceed its L^2 norm, hence it is bounded by (7.44). Thus, discarding a factor $(2\pi)^{-3/2} < 1$, we have for all k and n

$$|\hat{u}(k,t)| \leq e^{-n\sigma|k|}\left(\sqrt{\frac{\Lambda L}{Ut}}\right)^{((1+\delta)\,e(\kappa))^n} = \exp\left(\ln\sqrt{\frac{\Lambda L}{Ut}}e^{n\beta_{\kappa,\delta}} - n\sigma|k|\right), \tag{7.49}$$

where notation such as $e(\kappa)$ is defined in (7.7). Now choosing

$$\ln|k| \geq \frac{1}{\varepsilon}\frac{\beta_{\kappa,\delta}}{\sigma}\ln\sqrt{\frac{\Lambda L}{Ut}}, \tag{7.50}$$

we obtain with $n = \ln|k|/\beta_{\kappa,\delta}$ the following estimate

$$|\hat{u}(k,t)| \leq \exp\left[-\frac{\sigma}{\beta_{\kappa,\delta}}|k|\ln|k|\left(1 - \frac{\beta_{\kappa,\delta}\ln\sqrt{\Lambda L/Ut}}{\sigma\ln|k|}\right)\right] \leq e^{-\frac{\sigma(1-\varepsilon)}{\beta_{\kappa,\delta}}|k|\ln|k|}. \tag{7.51}$$

Remark 3.1 Since ε and δ can be chosen arbitrarily small and κ arbitrarily large, Corollary 3.1 implies that, in terms of the dimensionless wavenumber $\tilde{k} = 2\sigma k$, the Fourier amplitude has a bound (at high enough $\tilde{k}$) of the form $e^{-C\tilde{k}\ln\tilde{k}}$ for any $C < 1/(2\ln 2)$. We shall see later that the upper bound for the constant C can probably be improved to $1/\ln 2$.

Proof of Theorem 3.1 We proceed again by induction. We assume that the following inequalities hold

$$\left|e^{n\sigma A^{1/2}}u(t)\right|^2 \leq \frac{K_n}{t^{a_n}}, \tag{7.52}$$

and

$$\int_t^T \left| e^{(n+1)\sigma A^{1/2}} u(s) \right|^2 ds \leq \frac{K_n}{t^{a_n}}, \tag{7.53}$$

where K_n and $a_n \geq 1$ are still to be determined. Starting from expNSE (7.3), we take the inner product with $e^{2(n+1)\sigma A^{1/2}} u$. Then we obtain from Proposition 2.1 with $\alpha = m\sigma$ and $\beta = 2\sigma$

$$\frac{1}{2}\frac{d}{dt} \left| e^{(n+1)\sigma A^{1/2}} u \right|^2 + \mu \left| e^{(n+2)\sigma A^{1/2}} u \right|^2 \leq \left| \left(B(u,u), e^{2(m+1)\sigma A^{1/2}} u \right) \right|$$
$$\leq \left| e^{m\sigma A^{1/2}} B(u,u) \right| \left| e^{(m+2)\sigma A^{1/2}} u \right| \leq C_A (l_\kappa(\beta))^{\mathsf{a}(\kappa)} \left| e^{m\sigma A^{1/2}} u \right|^{\mathsf{e}(\kappa)} \left| e^{(m+2)\sigma A^{1/2}} u \right|^{\mathsf{c}(\kappa)}$$
$$\leq \frac{2\kappa - 5}{4\kappa} \mu^{-\mathsf{d}(\kappa)} C_A^{\mathsf{b}(\kappa)} \left(l_\kappa(\beta) \right)^{\mathsf{g}(\kappa)} (\mathsf{c}(\kappa))^{\mathsf{d}(\kappa)} \left| e^{m\sigma A^{1/2}} u \right|^{2\mathsf{e}(\kappa)} + \frac{\mu}{2} \left| e^{(m+2)\sigma A^{1/2}} u \right|^2. \tag{7.54}$$

Then it follows that

$$\frac{d}{dt} \left| e^{(n+1)\sigma A^{1/2}} u \right|^2 + \mu \left| e^{(n+2)\sigma A^{1/2}} u \right|^2$$
$$\leq \frac{2\kappa - 5}{2\kappa} \mu^{-\mathsf{d}(\kappa)} C_A^{\mathsf{f}(\kappa)} \left(l_\kappa(\beta) \right)^{\mathsf{g}(\kappa)} \left(\frac{2\kappa + 5}{2\kappa} \right)^{\mathsf{d}(\kappa)} \left| e^{m\sigma A^{1/2}} u \right|^{2\mathsf{e}(\kappa)}. \tag{7.55}$$

By using the induction assumption we obtain

$$\frac{d}{dt} \left| e^{(n+1)\sigma A^{1/2}} u \right|^2 + \mu \left| e^{(n+2)\sigma A^{1/2}} u \right|^2 \leq C' \left(\frac{K_n}{t^{a_n}} \right)^{\mathsf{e}(\kappa)}, \tag{7.56}$$

where we have set

$$C' = \frac{2\kappa - 5}{2\kappa} \mu^{-\mathsf{d}(\kappa)} C_A^{2\mathsf{f}(\kappa)} \left(l_\kappa(\beta) \right)^{\mathsf{g}(\kappa)} \left(\frac{2\kappa + 5}{2\kappa} \right)^{\mathsf{d}(\kappa)}. \tag{7.57}$$

Renaming the time variable in (7.56) from t to s' and integrating over s' from s to t (with $0 < s < t \leq T$) we obtain

$$\left| e^{(n+1)\sigma A^{1/2}} u(t) \right|^2 + \mu \int_s^t \left| e^{(n+2)\sigma A^{1/2}} u(s') \right|^2 ds'$$
$$\leq \frac{1}{a_n \mathsf{e}(\kappa) - 1} C' K_n^{\mathsf{e}(\kappa)} \left(\frac{1}{s^{a_n \mathsf{e}(\kappa) - 1}} - \frac{1}{t^{a_n \mathsf{e}(\kappa) - 1}} \right) + \left| e^{(n+1)\sigma A^{1/2}} u(s) \right|^2 \tag{7.58}$$
$$\leq \frac{1}{a_n \mathsf{e}(\kappa) - 1} C' K_n^{\mathsf{e}(\kappa)} \frac{1}{s^{a_n \mathsf{e}(\kappa) - 1}} + \left| e^{(n+1)\sigma A^{1/2}} u(s) \right|^2.$$

Omitting the positive integral term on the left-hand side of the inequality we obtain

$$\left|e^{(n+1)\sigma A^{1/2}}u(t)\right|^2 \le \frac{1}{a_n\mathsf{e}(\kappa)-1}C'\,K_n^{\mathsf{e}(\kappa)}\frac{1}{s^{a_n\mathsf{e}(\kappa)-1}} + \left|e^{(n+1)\sigma A^{1/2}}u(s)\right|^2. \qquad (7.59)$$

Choosing $1 < \gamma \le N^\delta = (L/UT)^\delta$ and integrating over s from t/γ to t we obtain

$$(\gamma-1)\frac{t}{\gamma}\left|e^{(n+1)\sigma A^{1/2}}u(t)\right|^2 \le \frac{1}{a_n\mathsf{e}(\kappa)-1}\frac{1}{a_n\mathsf{e}(\kappa)-2}C'\,K_n^{\mathsf{e}(\kappa)}\left\{\left(\frac{\gamma}{t}\right)^{a_n\mathsf{e}(\kappa)-2} - \left(\frac{1}{t}\right)^{a_n\mathsf{e}(\kappa)-2}\right\}$$

$$+ \int_{t/\gamma}^{t}\left|e^{(n+1)\sigma A^{1/2}}u(s)\right|^2\,ds \le \frac{1}{a_n\mathsf{e}(\kappa)-1}\frac{1}{a_n\mathsf{e}(\kappa)-2}C'\,K_n^{\mathsf{e}(\kappa)}\left(\frac{\gamma}{t}\right)^{a_n\mathsf{e}(\kappa)-2} + K_n\left(\frac{\gamma}{t}\right)^{a_n}, \tag{7.60}$$

where we have used the induction assumption (7.53). We obtain thus the following estimate

$$\left|e^{(n+1)\sigma A^{1/2}}u(t)\right|^2 \le \frac{1}{\gamma-1}\frac{1}{a_n\mathsf{e}(\kappa)-1}\frac{1}{a_n\mathsf{e}(\kappa)-2}C'\,K_n^{\mathsf{e}(\kappa)}\left(\frac{\gamma}{t}\right)^{a_n\mathsf{e}(\kappa)-1} + \frac{1}{\gamma-1}K_n\left(\frac{\gamma}{t}\right)^{a_n+1}, \tag{7.61}$$

which holds for every $0 < t \le T$.

To estimate $\int_t^T \left|e^{(n+2)\sigma A^{1/2}}u(s)\right|^2\,ds$ we integrate (7.56) from t to T:

$$\left|e^{(n+1)\sigma A^{1/2}}u(T)\right|^2 + \mu\int_t^T\left|e^{(n+2)\sigma A^{1/2}}u(s)\right|^2\,ds$$

$$\le C'\frac{1}{a_n\mathsf{e}(\kappa)-1}C'\,K_n^{\mathsf{e}(\kappa)}\frac{1}{t^{a_n\mathsf{e}(\kappa)-1}} + \left|e^{(n+1)\sigma A^{1/2}}u(t)\right|^2. \tag{7.62}$$

Omitting the first term on the right-hand side and using (7.61) we obtain

$$\mu\int_t^T\left|e^{(n+2)\sigma A^{1/2}}u(s)\right|^2\,ds \le C'\frac{1}{a_n\mathsf{e}(\kappa)-1}C'\,K_n^{\mathsf{e}(\kappa)}\frac{1}{t^{a_n\mathsf{e}(\kappa)-1}}$$

$$+ \frac{1}{\gamma-1}\frac{1}{a_n\mathsf{e}(\kappa)-1}\frac{1}{a_n\mathsf{e}(\kappa)-2}C'\,K_n^{\mathsf{e}(\kappa)}\left(\frac{\gamma}{t}\right)^{a_n\mathsf{e}(\kappa)-1} + \frac{1}{\gamma-1}K_n\left(\frac{\gamma}{t}\right)^{a_n+1}. \tag{7.63}$$

We conclude that since $a_n \ge 1$ and

$$a_n + 1 \le a_n\left(2 + \frac{5}{2\kappa-5}\right) = a_n\mathsf{e}(\kappa), \tag{7.64}$$

for a suitable constant $E > 0$ we have

$$\left| e^{(n+1)\sigma A^{1/2}} u(t) \right|^2 \le E(K_n)^{e(\kappa)} \left(\frac{\gamma}{t} \right)^{a_n e(\kappa)} \tag{7.65}$$

and

$$\int_t^T \left| e^{(n+2)\sigma A^{1/2}} u(s) \right|^2 \le E(K_n)^{e(\kappa)} \left(\frac{\gamma}{t} \right)^{a_n e(\kappa)}. \tag{7.66}$$

Since, for $t \le T$,

$$\frac{\gamma}{t} \le \frac{N^\delta}{t} = \left(\frac{L}{UT} \right)^\delta \frac{1}{t} \le \left(\frac{L}{Ut} \right)^{1+\delta} \frac{U}{L},$$

it follows that

$$\left| e^{(n+1)\sigma A^{1/2}} u(t) \right|^2 \le E(K_n)^{e(\kappa)} \left(\frac{L}{Ut} \right)^{a_n(1+\delta)e(\kappa)} \left(\frac{U}{L} \right)^{a_n e(\kappa)} \tag{7.67}$$

and

$$\int_t^T \left| e^{(n+2)\sigma A^{1/2}} u(s) \right|^2 \le E(K_n)^{e(\kappa)} \left(\frac{L}{Ut} \right)^{a_n(1+\delta)e(\kappa)} \left(\frac{U}{L} \right)^{a_n e(\kappa)}. \tag{7.68}$$

This finishes the induction step.

From the above follows that we can take

$$a_{n+1} = a_n(1 + \delta)\frac{4\kappa - 5}{2\kappa - 5}, \qquad K_{n+1} = EK_n^{e(\kappa)}. \tag{7.69}$$

Note that in the induction step we use the assumption that $a_n \ge 1$. This fixes the value of $a_0 = 1$. The solution of the recursion relations is given by

$$a_n = \left((1 + \delta)\frac{4\kappa - 5}{2\kappa - 5} \right)^n, \qquad \ln K_n = \ln E \frac{a_n - 1}{(1 + \delta)\frac{4\kappa-5}{2\kappa-5} - 1} + a_n \ln K_0. \tag{7.70}$$

Finally, choosing a large enough number Λ we get the desired estimates (7.44) and (7.45). This concludes the proof of Theorem 3.1.

7.4 Remarks and extensions for the main results

Although our main theorems are stated for the case of the 3D expNSE, their statements and proofs are easily extended *mutatis mutandis* to

arbitrary space dimensions d: with exponential dissipation for any d the solution is entire in the space variables and the decay of Fourier coefficients is bounded by $\exp(-C|\tilde{k}|\ln|\tilde{k}|)$ for any $C < C_\star = 1/(2\ln 2)$. Some of the intermediate steps in the proof, such as the formulation of Agmon's inequality, change with d but not the result about the constant $1/(2\ln 2)$.

We can also easily change the functional form of the dissipation.[4] One instance is a dissipation operator $\mathcal{D}$ with a Fourier symbol $e^{2\sigma|k|^\alpha}$ with $0 < \alpha < 1$. One should then be able to prove that the solution in this case satisfies

$$\sum_{k\neq 0} e^{2n|k|^\alpha} |\hat{u}(k,t)|^2 \le \frac{K_n}{t^{p_n}} + C_n, \tag{7.71}$$

for all $t \in (0,T]$ and for all n. Hence the solution in this case belongs to C^∞ but is not necessarily an entire function. In fact it belongs to the Gevrey class $G_{1/\alpha}$. Gevrey regularity with $0 < \alpha < 1$ does not even imply analyticity.[5] Actually, with such a dissipation, the solutions are analytic even when $\alpha < 1$. We shall return to this case of dual Gevrey regularity and analyticity in Section 7.5.1.

Next, consider the case $\alpha > 1$. The dissipation has a lower bound of the ordinary exponential type, so that the entire character of the solution is easily established. However, for $\alpha > 1$ the bound $\exp(-C|k|\ln|k|)$ can be improved in its functional form, as we shall see in Section 7.5.1.

Obviously, the results of Sections 7.2 and 7.3 do still hold if we change the functional form of the Fourier symbol of the dissipation at low wavenumbers $|k|$ while keeping its exponential growth at high wavenumber. One particularly interesting instance, to which we shall come back in the next Section on the Burgers equation and in the Conclusion, is "cosh dissipation", namely a Fourier symbol $\mu(1-\cosh(k/k_{\rm d}))$.

---

[4]Note that the proof of Proposition 2.1 and Theorem 2.1 holds *mutatis mutandis* if we replace, in the argument of the exponential, $|k|$ by a subadditive function of $|k|$ subject to some mild conditions, such as $|k|^\alpha$ with $0 < \alpha < 1$.

[5]The special class when $\alpha = 1$ of analytic functions is considered by some authors as one of the Gevrey classes [21, 22].

The dissipation rate at wavenumber much smaller than k_d is then $\nu|k|^2$ with $\nu = \mu/(2k_d{}^2)$, just as for the ordinary Navier–Stokes equation.

It is worth mentioning that the key results of Sections 7.2 and 7.3 still hold when the problem is formulated in the whole space $\mathbb{R}^d$ rather than with periodicity conditions. Similarly they should hold on the sphere S^2, a case for which spherical harmonics can be used (see [24]).

Of course the result on the entire character of the solution, when exponential dissipation is assumed, holds for a large class of partial differential equations. Besides the Navier–Stokes equations it applies for example to the magnetohydrodynamical equations and to the complex Ginzburg–Landau equation

$$\frac{\partial}{\partial t}u - \alpha u_{xx} + \beta u + \gamma|u|^2 u = 0, \tag{7.72}$$

where

$$Re\ \alpha > 0\ , \quad Re\ \gamma > 0. \tag{7.73}$$

The main idea would be in proving the analogue of Proposition 2.1 for the corresponding nonlinear terms in the underlying equations following our proof combined with ideas presented in [22] and [25].

7.5 The case of the 1D Burgers equation

The (unforced) one-dimensional Burgers equation with modified dissipation reads:

$$\frac{\partial u}{\partial t} + u\frac{\partial u}{\partial x} = -\mu\mathcal{D}u, \tag{7.74}$$

$$u(x,0) = u_0(x). \tag{7.75}$$

We shall mostly consider the case of the cosh Burgers equation when $\mathcal{D}$ has the Fourier symbol $\mu(1 - \cosh(k/k_d))$. Since the cosh Burgers equation is much simpler than expNSE we can expect to obtain stronger results or, at least, good evidence in favor of stronger conjectures.

Let us observe that the cosh Burgers equation can be rewritten in the complexified space of analytic functions of $z := x + iy$ as

$$\frac{\partial u(z,t)}{\partial t} + u(z,t)\frac{\partial u(z,t)}{\partial x} = -\frac{\mu}{2}\left[u(z + i/k_\mathrm{d}, t) + u(z - i/k_\mathrm{d}, t) - 2u(z,t)\right]. \quad (7.76)$$

This is the ordinary Burgers equation with the dissipative Laplacian replaced by its centered second-order finite difference approximation, differences being taken in the pure imaginary direction with a mesh $1/k_\mathrm{d}$.

As already stated, Corollary 2.1 on the entire character of the solution and Corollary 3.1 on the bound of the modulus of the Fourier coefficients by $\exp(-C|\tilde{k}|\ln|\tilde{k}|)$ for any $C < 1/(2\ln 2)$ hold in the same form as for the expNSE. Of course, if the finite differences were taken in the real rather than in the pure imaginary direction, the solution would not be entire. Actually, (7.76) relates the values of the velocity on lines parallel to the real axis shifted by $\pm 1/k_\mathrm{d}$ in the imaginary direction. It thereby provides a kind of *Jacob's Ladder* allowing us to climb to complex infinity in the imaginary direction. This can be used to show, at least heuristically, that the complexified velocity grows with the imaginary coordinate y as $\exp\left(C 2^{|y|k_\mathrm{d}}\right)$.

Such a heuristic derivation turns out to be equivalent to another derivation by dominant balance which can be done on the Fourier-transformed equation, the latter being not limited to cosh dissipation. Section 7.5.1 is devoted to Fourier space heuristics for different forms of the dissipation. For exponential and cosh dissipation this suggests a leading-order behavior of the Fourier coefficients for large wavenumber of the form $\exp(-C_\star|k|\ln|k|)$ with $C_\star = 1/\ln 2$, a substantial improvement over the rigorous bound. Various numerical and semi-numerical results, discussed in Section 7.5.2 and **??**, support this improved result.

7.5.1 Heuristics: a dominant balance approach

We want to handle dissipation operators $\mathcal{D}$ with an arbitrary positive Fourier symbol, taken here to be $e^{G(k)}$ where $G(k)$ is a real even function of the wavenumber $k \in \mathbb{Z}$ which is increasing without bound for $k > 0$. It is then best to rewrite the Burgers equation in terms of the Fourier coefficients. We set

$$u(x, t) = \sum_{k \in \mathbb{Z}} e^{ikx} \hat{u}(k, t), \tag{7.77}$$

and obtain from (7.74)

$$\frac{\partial \hat{u}(k, t)}{\partial t} + \frac{ik}{2} \sum_{p+q=k} \hat{u}(p, t)\hat{u}(q, t) = -\mu e^{G(k)}\hat{u}(k, t). \tag{7.78}$$

This is the place where we begin our heuristic analysis of the large-wavenumber asymptotics. First, we drop the time derivative term since it will turn out not to be relevant to leading order. (A suitable Galilean change of frame may be needed before this becomes true.) For simplicity we now drop the time variable completely. The next heuristic step is to balance the moduli of the two remaining terms, taking

$$|\hat{u}(k)| \sim e^{-F(k)}, \tag{7.79}$$

where $F(k)$ is still to be determined but assumed sufficiently smooth and the symbol $\sim$ is used here to connect two functions "asymptotically equal up to contants and algebraic prefactors" (in other words, asymptotic equality of the logarithms). The convolution in (7.78) can be approximated for large wavenumbers by a continuous wavenumber integral $\sim \int e^{-F(p)-F(k-p)}dp$. Next we evaluate the integral by steepest descent, assuming that the leading order comes from the critical point $p = k/2$, where the p-derivative of $F(p) + F(k - p)$ obviously vanishes. This will require that this point be truly a minimum of $F(p) + F(k - p)$. Balancing the logarithms of the nonlinear term and of the dissipative

term we obtain the following simple equation for the function $F(k)$:

$$2F\left(\frac{k}{2}\right) = F(k) - G(k).$$ (7.80)

This is a linear first order finite difference equation (in the variable $\ln k$) which is easily solved for values of the wavenumber of the form $k = 2^n$:

$$F(2^n) = 2^n \left[F(1) + \frac{G(2)}{2} + \frac{G(4)}{4} + \cdots + \frac{G(2^n)}{2^n} \right].$$ (7.81)

For exponential dissipation (and for cosh dissipation when $|k|/k_d \gg 1$), we have $G(k) \simeq 2\sigma|k|$ and we obtain from (7.81), to leading order for large positive k

$$F(k) \simeq \frac{1}{\ln 2} \tilde{k} \ln \tilde{k}; \quad \tilde{k} := 2\sigma k = \frac{k}{k_d}.$$ (7.82)

If this heuristic result is correct – and the supporting numerical evidence is strong as we shall see in Sections 7.5.2 and **??** – the estimate given by Corollary 3.1 (adapted to the Burgers case) that $|\hat{u}(k)| < e^{-C|\tilde{k}|\ln|\tilde{k}|}$ for sufficiently large $|\tilde{k}|$ and any $C < C_\star = 1/(2\ln 2)$ still leaves room for improvement as to the value of $C_\star$. It can be shown that this dominant balance argument remains unchanged if we reinsert the time-derivative term, since its contribution is easily checked to be subdominant. Actually, the conjecture that the solution of NSE is entire with exponential or cosh dissipation was based on precisely this kind of dominant balance argument, which suggests a faster-than-exponential decay of the Fourier coefficients.

When $G(k) = 2\sigma|k|^\alpha$ with $\alpha > 1$ we obtain to leading order

$$F(k) \simeq \frac{2\sigma}{1 - 2^{1-\alpha}} |k|^\alpha.$$ (7.83)

This is an even faster decay of the Fourier coefficients than in the exponential case (7.3).[6]

---

[6]Actually, one can show, for the Burgers equation and the NSE that when $\alpha > 1$ the Fourier coefficients of the solution decay faster than $\exp(-C|k|^{\alpha-\epsilon})$ for any $\epsilon > 0$.

It is easily checked that for $\alpha \geq 1$ the condition of having a minimum of $F(p) + F(k - p)$ at $p = k/2$ is satisfied. If however we were to use (7.83) for $0 < \alpha < 1$ the condition would not be satisfied. In this case it is easily shown for the Burgers equation and the NSE, by using a variant of the theory present in Section 7.2, that the solution is in the Gevrey class $G_{1/\alpha}$ in the whole space $\mathbb{R}^d$. It is actually not difficult to show that the solution is also analytic when $0 < \alpha < 1$, in a finite strip in $\mathbb{C}^d$ about the real space $\mathbb{R}^d$. For this it suffices to adapt to the proof of analyticity given for the ordinary NSE under the condition of some mild regularity. Such regularity is trivially satisfied with the much stronger dissipation assumed here [21].[7]

It is of interest to point out that, although analyticity is a stronger regularity than Gevrey when $0 < \alpha < 1$, the Gevrey result implies a decay of the form $\exp(-C|k|^\alpha \ln |k|)$, independently of the viscosity coefficient μ, whereas analyticity in a finite strip gives a decay of the form $\exp(-\eta|k|)$ where η depends on μ [27].

7.5.2 Spectral simulation for the Burgers case

Here we begin our numerical tests on the 1D Burgers equation. So far we have a significant gap in the value of the constant C appearing in the $e^{-C|\tilde{k}| \ln |\tilde{k}|}$ estimate of Fourier coefficient, between the bounds and a heuristic derivation of the asymptotic behavior. In this section we shall exclusively consider the case of the unforced Burgers equation with initial condition $u_0(x) = -\sin x$ and dissipation with a rate $1 - \cosh k$. (Thus, $\mu = 1$ and $k_{\mathrm{d}} = 1$.) The numerical method is, however, very easily extended to other functional forms of the dissipation and other initial conditions. The spectral method is actually quite versatile. Its main drawback will be discussed at the end of this section.

---

[7]The first results on analyticity, derived in the more complex setting of flow with boundaries, were obtained in [26].

The standard way of obtaining a high-order scheme when numerically integrating PDE's with (spatial) periodic boundary conditions is by the (pseudo)-spectral technique with the 2/3 rule of alias removal [28]. The usual reason this is more precise than finite differences is that the truncation errors resulting from the use of a finite number N of collocation points (and thus a finite number $N/3$ of Fourier modes) decreases exponentially with N if the solution is analytic in a strip of width δ around the real axis. Indeed this implies a bound for the Fourier coefficients at high $|k|$ of the form $|\hat{u}(k)| < \mathrm{e}^{-C|k|}$ for any $C < \delta$. In the present case, the solution being entire, the bound is even better.

There are of course sources of error other than spatial Fourier truncation, namely rounding errors and temporal discretization errors. Temporal discretization is a non-trivial problem here because the dissipation grows exponentially with $|k|$ and thus the characteristic time scale of high-$|k|$ modes can become exceedingly small. Fortunately, these modes are basically slaved to the input stemming from nonlinear interaction of lower-lying modes. It is possible to take advantage of this to use a slaving technique which bypasses the stiffness of the equation (a simple instance of this phenomenon is described in Appendix B of [29]). We use here the slaved scheme *Exponential Time Difference Runge Kutta 4* (ETDRK4) of [30] with a time step of 10^{-3} .[8]

As to the rounding noise, it is essential to use at least double precision since otherwise the faster-than-exponential decrease of the Fourier coefficients would be swamped by rounding noise beyond a rather modest wavenumber. Even with double precision, rounding noise problems start around wavenumber 17, as we shall see. Hence it makes no sense to use more than, say, 64 collocation points, as we have done.

Fig. 7.1 shows the discrepancy

$$\mathrm{Discr}\,(k) := -\frac{\ln |\hat{u}(k,1)|}{|k| \ln |k|} - \frac{1}{\ln 2}, \qquad (7.84)$$

[8]This is far larger than would have have been permitted without the slaving. Actually it can still be increased somwehat to 5×10^{-3} without affecting the results.

which, according to heuristic asymptotic theory (7.79)-(7.82), should converge to 0 as $|k| \to \infty$.

It is seen that the discrepancy falls to about 3.5% of the nominal value $1/\ln 2$ before getting swamped by rounding noise around wavenumber 17.

It is actually possible to decrease significantly the discrepancy by using a better processing of the numerical output, called *asymptotic interpolation*, developed recently by van der Hoeven [31] and which is related to the theory of transseries [32, 33]. The basic idea is to perform on the data a succession of transformations which successively strip off the leading and subleading terms in the asymptotic expansion (here for large $|k|$). Eventually, the transformed data allow a very simple interpolation (mostly by a constant). The procedure can be carried out until the transformed data become swamped by rounding noise or display lack of asymptoticity, whichever occurs first. After the interpolation stage, the successive transformations are undone. This determines the asymptotic expansion of the data up to a certain order of subdominant terms. An elementary introduction to this method may be found in [34], from which we shall also borrow the notation for the various transformations: **I** for "inverse", **R** for "ratio", **SR** for "second ratio", **D** for "difference" and **Log** for "logarithm". The choice of the successive transformations is dictated by various tests which roughly allow us to find into which broad asymptotic class the data and their transformed versions fall.

In the present case, the appropriate set of transformations is: **Log**, **D**, **D**, **I**, **D**. Because of the relatively low precision of the data it is not possible to perform more than five transformations, so that the method gives us access only to the leading-order asymptotic behavior, namely $|\hat{u}(k,1)| \simeq e^{-C_\star |k| \ln |k|}$. It may be shown that the constant $C_\star = -1/u^{(5)}$, where $u^{(5)}$ is the constant value of the high-$|k|$ interpolation $u^{(5)}(|k|)$ after the 5th stage of transformation. Fig. 7.2 shows
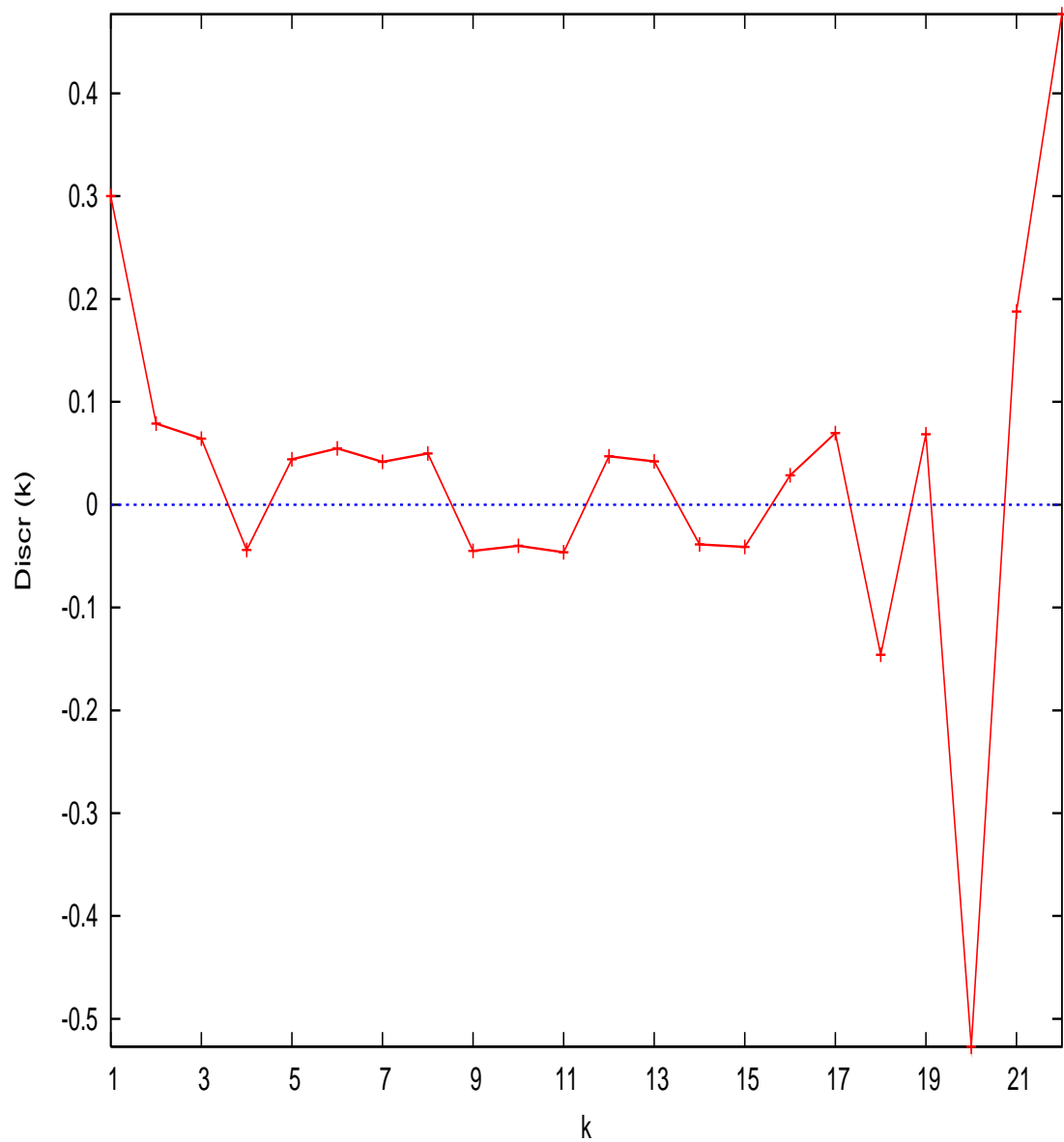
Figure 7.1: Discrepancy Discr, as predicted by (7.84), vs wavenumber k for data obtained by spectral simulation in double precission; rounding noise becomes significant beyond wavenumber 17.
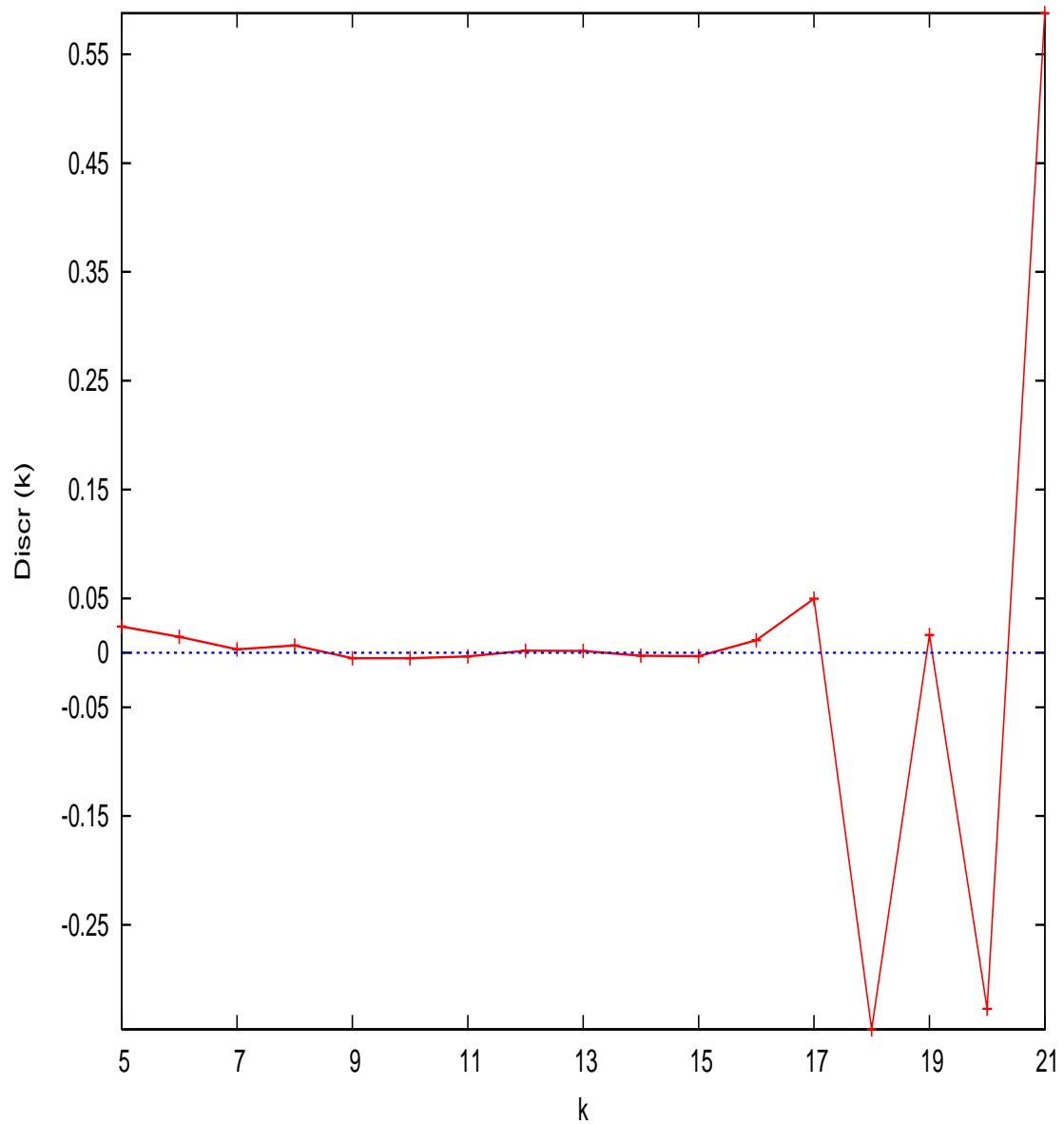
Figure 7.2: Discrepancy Discr vs wavenumber k for the same data as in Fig. 7.1, but proccessed by a 5-stage asymptotic interpolation method.

the discrepancy $u^{(5)}(|k|) + \ln 2$. The absolute value of the discrepancy lingers around 0.002 to 0.005 before being swamped by rounding noise at wavenumber 17. Thus with asymptotic interpolation the discrepancy does not exceed 0.7% of the nominal value $\ln 2$. The accuracy of the determination has thus improved by about a factor 5, compared to the naive method without asymptotic interpolation.

To improve further on this result and get some indication as to the type of subdominant corrections present in the large-wavenumber expansion of the Fourier coefficients it would not suffice to increase the spatial resolution, since rounding noise would still swamp the signal beyond a wavenumber of roughly 17. Higher precision spectral calculations are doable but not very simple because high-precision fast Fourier transform packages are still in the experimental phase.

It is possible to use an alternative method which is significantly less versatile as to the choice of the initial condition because it exploits the algebraic structure of a certain special class of solutions, but which also allows to work easily in arbitrary precision and thus to make better use of asymptotic interpolation for determining the constant $C_\star$. We refer the reader to Ref. [1] for a discussion on this.

7.6 Conclusions

In this Chapter we have proven that, for a large class of evolution PDE's, including the 3D NSE, exponential or faster-growing dissipation implies that the solution remains an entire function in the space variables at all times. Exponential growth constitutes a threshold: subexponential growth with a Fourier symbol $\mathrm{e}^{|k|^\alpha}$, where $0 < \alpha < 1$ makes the solution analytic (but not entire) as is the case in 2D (and generally conjectured in 3D). Furthermore, for the 3D NSE and the 1D Burgers equation with a dissipation having the Fourier symbol $\mu \mathrm{e}^{|k|/k_\mathrm{d}}$, we have shown that the amplitude of the Fourier coefficients

is bounded by $\mathrm{e}^{-C|\tilde{k}|\ln|\tilde{k}|}$ (where $\tilde{k} := k/k_\mathrm{d}$) for any $C < 1/(2\ln 2)$. For the case of the 1D Burgers equation we have good evidence that this can be improved to $C < C_\star = 1/\ln 2$ since the high-$|k|$ asymptotics seems to have a leading term precisely of the form $\mathrm{e}^{-C_\star|\tilde{k}|\ln|\tilde{k}|}$; the evidence comes from a heuristic dominant-balance argument and from high-precision simulations. The heuristic argument can actually be carried over somewhat loosely to the expNSE in any dimension: again the dominant nonlinear interaction contributing to wave vector k comes from the wave vectors $p = q = k/2$; actually the condition of incompressibility kills nonlinear interactions between exactly parallel wave vectors but this is only expected to modify algebraic prefactors in front of the exponential term.

We thus conjecture that $C_\star = 1/\ln 2$ also holds for expNSE in any space dimension $d \geq 2$. Of course there is a substantial gap between the bound and the conjectured asymptotic behavior. It seems that such a gap is hard to avoid when using L^2-type norms. For proving the entire character of the solution such norms were appropriate. Beyond this, it is appears more advisable to try bounding directly the moduli of Fourier coefficients by using the power series method [14, 35]. A first step in this direction would be to prove that $C_\star = 1/\ln 2$ for initial conditions whose Fourier coefficients are compactly supported in a product of half-spaces, of the kind considered in Section **??**.

Exponential dissipation differs from ordinary dissipation (with a Laplacian or a power thereof) not only by giving a faster decay of the Fourier coefficients but by doing so in a *universal* way: with ordinary dissipation the decay of the Fourier coefficient is generally conjectured to be, to leading order, of the form $\mathrm{e}^{-\eta|k|}$, where η depends on the viscosity ν and on the energy input or on the size of the initial velocity; with exponential dissipation the decay is $\mathrm{e}^{-C_\star|\tilde{k}|\ln|\tilde{k}|}$, where $C_\star = 1/\ln 2$ and thus depends neither on the coefficient μ, which plays the role

of the viscosity, nor on the initial data.[9] As a consequence, it is expected that exponential dissipation will not exhibit the phenomenon of dissipation-range intermittency, which for the usual dissipation can be traced back either to the fluctuations of η [37] or to complex singularities of a velocity field that is analytic but not entire [38].

Finally some comments on the practical relevance of modified dissipation. First, let us comment on "hyperviscosity", the replacement of the (negative) Laplacian by its power of order $\alpha > 1$. Of course we know that specialists of PDE's have traditionally been interested in the hyperviscous 3D NSE, perhaps to overcome the frustration of not being able to prove much about the ordinary 3D NSE. But scientists doing numerical simulations of the NSE, say, for engineering, astrophysical or geophysical applications, have also been using hyperviscosity because it is often believed to allow effectively higher Reynolds numbers without the need to increase spatial resolution. We have shown in Chapter 4 and in Ref. [39] that, when using a high power α of the Laplacian in the dissipative term for 3D NSE or 1D Burgers, one comes very close to a Galerkin truncation of Euler or inviscid Burgers, respectively [39]. This produces a range of nearly thermalized modes which shows up in large-Reynolds number spectral simulations as a huge bottleneck in the Fourier amplitudes between the inertial range and the far dissipation range. Since the bottleneck generates a fairly large eddy viscosity, the hyperviscosity procedure with large α actually *decreases* the effective Reynolds number.

Next, consider exponential dissipation. In 1996 it was noticed that when used in the 1D Burgers equation, cosh dissipation produces almost no bottleneck although it grows much faster than a power of the wavenumber at high wavenumbers [40]. It is now clear that such a dissipation will produce a faster-than-exponential decay at the high-

---

[9]It does, however, depend on the type of nonlinearity. For example, with a cubic nonlinearity the same kind of heuristics as presented earlier predicts a constant $C_\star = 1/\ln 3$.

est wavenumbers. But at wavenumbers such that $|k| \ll k_{\mathrm{d}}$ a dissipation rate $\mu(1 - \cosh k/k_{\mathrm{d}})$ reduces to $\mu|k|^2/(2k_{\mathrm{d}}^2)$, to leading order in k/k_d, which is the ordinary (Laplacian) dissipation. With the ordinary 1D Burgers equation it may be shown analytically that there is no bottleneck. For the ordinary 3D NSE, experimental and numerical results show the presence of a rather modest bottleneck (for example the "compensated" three-dimensional energy spectrum $|k|^{+5/3}E(|k|)$ overshoots by about 20%.). If in a simulation with cosh dissipation μ and k_{d} are adjusted in such a way that dissipation starts acting at wavenumbers slighter smaller than k_{d}, the beginning of the dissipation range will be mostly as with an ordinary Laplacian, that is with no or little bottleneck.[10] At higher wavenumbers, where the exponential growth of the dissipation rate is felt, faster than exponential decay will be observed. In principle this can be used to avoid wasting resolution without developing a serious bottleneck. Faster than exponentially growing dissipation, e.g. $\mu\left(e^{(|k|/k_{\mathrm{d}})^2} - 1\right)$, may be even better because the prediction is that the Fourier coefficients will display Gaussian decay.[11] Testing the advantages and drawbacks of different types of faster-than-algebraically growing dissipations for numerical simulations is left for future work.

---

[10]If μ and k_{d} are not carefully chosen, effective dissipation can start well beyond k_{d}. One may then observe the same kind of thermalization and of bottleneck than with a high power of the Laplacian [41].

[11]Here we mention that this may be related to the use of Gaussian filters at each time step, a procedure described to one of us (UF) as allowing to absorbe energy near the maximum wavenumber without having it reflected back to lower wavenumbers [42].

Appendix D

Inequalities

D.1 Cauchy-Schwarz Inequality

The CauchySchwarz inequality is commonly used in a variety of mathematical problems. The inequality for sums was published by Augustin Cauchy (1821); the corresponding inequality for integrals was first stated by Viktor Yakovlevich Bunyakovsky (1859) and rediscovered by Hermann Amandus Schwarz (1888)

The CauchySchwarz inequality states that for all vectors $\mathbf{x}$ and $\mathbf{y}$

$$|\langle x, y \rangle|^2 \leq \langle x, x \rangle \cdot \langle y, y \rangle, \tag{D.1}$$

where $\langle \cdot, \cdot \rangle$ is the inner product. This can be rewritten, by taking square roots and using the norms of the vectors, as

$$|\langle x, y \rangle| \leq \|x\| \cdot \|y\|. \tag{D.2}$$

The equality holds if and only if $\mathbf{x}$ and $\mathbf{y}$ are linearly dependent (parallel) or if one of the vectors is equal to zero).

If $x_1, \cdots, x_n \in \mathbb{C}$ and $y_1, \cdots, y_n \in \mathbb{C}$ are the components of $\mathbf{x}$ and $\mathbf{y}$ in an orthonormal basis one can write:

$$\left| \sum_{i=1}^{n} x_i \overline{y_i} \right|^2 \leq \sum_{j=1}^{n} |x_j|^2 \sum_{k=1}^{n} |y_k|^2. \tag{D.3}$$

For square-integrable complex-valued functions the Cauchy-Schwarz inequality states

$$\left| \int f(x)g(x)\,dx \right|^2 \le \int |f(x)|^2\,dx \cdot \int |g(x)|^2\,dx. \tag{D.4}$$

D.2 Young's Inequality

Young's Inequality states that if a and b are nonnegative real numbers then for any p and q which are positive real numbers and satisfy the condition $1/p + 1/q = 1$ then

$$ab \le \frac{a^p}{p} + \frac{b^q}{q}. \tag{D.5}$$

The equality holds if and only if $ap = bq$.

A special case of Young's inequality is

$$ab \le \frac{a^2}{2} + \frac{b^2}{2}. \tag{D.6}$$

This can be generalised to

$$ab \le \frac{a^2}{2\varepsilon} + \frac{\varepsilon b^2}{2}, \tag{D.7}$$

which is valid for any positive ε.

In real analysis, we use Young's inequality in the following form. For any function f in L^p and g in L^q and where

$$\frac{1}{p} + \frac{1}{q} = \frac{1}{r} + 1 \tag{D.8}$$

for $1 \le p, q, r \le r$, we have

$$|f * g|_r \le |f|_p |g|_q. \tag{D.9}$$

The star denotes convolution, L^p is Lebesgue space, and

$$|f|_p = \left(\int |f(x)|^p , dx \right)^{1/p} \tag{D.10}$$

denotes the usual L^p norm.

For the special case $p, q > 1$ we obtain

$$|f * g|_r \le c_{p,q} |f|_p |g|_q, \tag{D.11}$$

where the constant $c_{p,q} < 1$.

D.3 Agmon's Inequality

Agmon's inequalities, which consists of closely related inequalities between the Lebesgue space L^∞ and the Sobolev spaces H^s, are used in the study of partial differential equations.

The result, obtained in $\mathbb{R}^3$, states that for u, a vector-valued function, such that $u \in (H^2(\Omega) \cap H_0^1(\Omega))^3$, where $\Omega \subset \mathbb{R}^3$, there exists a constant C such that

$$\|u\|_{L^\infty(\Omega)} \le C \|u\|_{L^2(\Omega)}^{1/4} \|u\|_{H^2(\Omega)}^{3/4} \tag{D.12}$$

and

$$\|u\|_{L^\infty(\Omega)} \le C \|u\|_{H^1(\Omega)}^{1/2} \|u\|_{H^2(\Omega)}^{1/2}. \tag{D.13}$$

Bibliography

[1] C. Bardos, U. Frisch, W. Pauls, S. S. Ray, E. S. Titi, Comm. Math. Phys., in press (DOI 10.1007/s00220-009-0916-z) (2009).

[2] Majda, A.J.; Bertozzi, A.L. *Vorticity and Incompressible Flow*. Cambridge Texts in Applied Mathematics, Cambridge University Press, Cambridge, 2001.

[3] Frisch, U.; Matsumoto, T.; Bec, J. Singularities of Euler flow? Not out of the blue! *J. Stat. Phys.* **113** (2003), 761–781.

[4] Bardos, C.; Titi, E.S. Euler equations of incompressible ideal fluids. *Uspekhi Mat. Nauk* **62**(2007), 5–46. English version *Russian Math. Surv.* **62** (2007), 409–451.

[5] Constantin, P. On the Euler equations of incompressible fluids. *Bull. Amer. Math. Soc.* **44** (2007), 603–621.

[6] Eyink, G.; Frisch, U.; Moreau, R.; Sobolevskii, A. Proceedings of *Euler Equations: 250 Years On*, Aussois, June 18–23, 2007. *Physica D* **237** (2008), no. 14–17.

[7] Lions, J.L. *Quelques Méthodes de Résolution des Problèmes aux Limites non Linéaires*, Gauthier-Villars, Paris, 1969.

[8] Constantin, P.; Foias, C. *Navier-Stokes equations*. Chicago Lectures in Mathematics. University of Chicago Press, Chicago, 1988.

[9] Fefferman, C. Existence & smoothness of the Navier–Stokes equation. Millenium problems of the Clay Mathematics Institute (2000). Available at www.claymath.org/millennium/Navier-Stokes_Equations/Official_Problem_Description.pdf.

[10] Temam, R. *Navier-Stokes equations. Theory and numerical analysis*. Revised edition. With an appendix by F. Thomasset. Published by AMS Bookstore, 2001.

[11] Sohr, H. *The Navier-Stokes equations*. Birkhäuser, Basel, 2001.

[12] Brachet, M.-E.; Meiron, D.I.; Orszag, S.A.; Nickel, B.G.; Morf, R.H.; Frisch, U. Small-scale structure of the Taylor-Green vortex, *J. Fluid Mech.* **130** (1983), 411–452.

[13] Neumann, J. von. Recent theories of turbulence (1949). In *Collected works (1949–1963)* **6**, 37–472, ed. A.H. Taub. Pergamon Press, New York, 1963.

[14] Li, D.; Sinai, Ya. G. Blow-ups of complex solutions of the 3D Navier–Stokes system and renormalization group method. *J. Eur. Math. Soc.* **10** (2008), 267–313 .

[15] Oliver, M; Titi, E.S. On the domain of analyticity for solutions of second order analytic nonlinear differential equations. *J. Differ. Equations* **174** (2001), 55–74.

[16] Pauls, W.; Matsumoto, T. Lagrangian singularities of steady two-dimensional flow. *Geophys. Astrophys. Fluid. Dyn.* **99**, (2005), pp. 61–75,

[17] Senouf, D.; Caflisch, R.; Ercolani, N. Pole dynamics and oscillation for the complex Burgers equation in the small-dispersion limit. *Nonlinearity* **9** (1996), 1671–1702.

[18] Polá*vc*ik, P.; *vS* verák, V. Zeros of complex caloric functions and singularities of complex viscous Burgers equation. Preprint. 2008. arXiv:math/0612506v1 [math.AP].

[19] Ladyzhenskaya, O.A. *The Mathematical Theory of Viscous Incompressible Flow* (1st ed.) Gordon and Breach, New York, 1963.

[20] Holloway, G. Representing topographic stress for large-scale ocean models. *J. Phys. Oceanogr.* **22** (1992), 1033–1046.

[21] Foias, C.; Temam, R. Gevrey class regularity for the solutions of the Navier–Stokes equations. *J. Funct. Anal.* **87** (1989), 359–369.

[22] Ferrari, A.; Titi, E.S. Gevrey regularity for nonlinear analytic parabolic equations. *Commun. Part. Diff. Eq.* **23** (1998), 1–16.

[23] Agmon, S. *Lectures on Elliptic Boundary Value Problems*. Mathematical Studies, Van Nostrand, 1965.

[24] Cao, C.; Rammaha, M.; Titi, E.S. The Navier–Stokes equations on the rotating $2 - D$ sphere: Gevrey regularity and asymptotic degrees of freedom. *Zeitschrift für Angewandte Mathematik und Physik (ZAMP)* **50** (1999), 341–360.

[25] Doelman, A; Titi, E.S. Regularity of solutions and the convergence of the Galerkin method in the Ginzburg–Landau equation, *Numerical Functional Analysis and Optimization* **14** (1993), 299–321.

[26] Masuda, K. On the analyticity and the unique continuation theorem for solutions of the Navier–Stokes equation. *Proc. Japan Acad.* **43** (1967), 827–832.

[27] Doering, C.R.; Titi, E.S. Exponential decay rate of the power spectrum for solutions of the Navier–Stokes equations. *Phys. Fluids* **7** (1995), 1384–1390.

[28] Gottlieb, D.; Orszag, S.A. *Numerical Analysis of Spectral Methods*. SIAM, Philadelphia, 1977.

[29] Frisch, U.; She, Z.S.; Thual, O. Viscoelastic behaviour of cellular solutions to the Kuramoto-Sivashinsky model. *J. Fluid Mech.* **168** (1986), 221–240.

[30] Cox, C.M.; Matthews, P.C. Exponential time differencing for stiff systems. *J. Comput. Phys.* **76** (2002), 430–455.

[31] van der Hoeven, J. Algorithms for asymptotic interpolation, preprint 2006-12 Dep. Math. Univ. Paris-Sud, submitted to *J. Symbolic Computation* (2006); see also http://www.math.u-psud.fr/˜vdhoeven/Publs/2006/interpolate.ps.gz

[32] Ecalle, J. *Introduction aux Fonctions Analysables et Preuve Constructive de la Conjecture de Dulac*. Actualités mathématiques. Hermann, Paris, 1992.

[33] van der Hoeven, J. *Transseries and Real Differential Algebra*. Lecture Notes in Math. **1888**, Springer, Berlin, 2006.

[34] Pauls, W.; Frisch, U. A Borel transform method for locating singularities of Taylor and Fourier series, *J. Stat. Phys.* **127** (2007), 1095–1119. arXiv:nlin/0609025v2 [nlin.CD]

[35] Sinai, Ya. G. Diagrammatic approach to the 3D Navier-Stokes system. *Russ. Math. Surv.* **60** (2005), 849–873.

[36] Caflisch, R.E. Singularity formation for complex solutions of the 3D incompressible Euler equations. *Physica* D **67** (1993), 1–18.

[37] Kraichnan, R.H. Intermittency in the very small scales of turbulence. *Phys. Fluids* **10** (1967) 2080–2082.

[38] Frisch, U; Morf, R. Intermittency in nonlinear dynamics and singularities at complex times. *Phys. Rev.* A **10** (1981), 2673–2705.

[39] Frisch, U.; Kurien, S.; Pandit, R.; Pauls, W.; Ray, S.S.; Wirth, A.; Zhu, J.-Z. Hyperviscosity, Galerkin truncation and bottlenecks in turbulence, *Phys. Rev. Lett.* **101** (2008), 144501. arxiv:0803.4269 [nlin.CD].

[40] Wirth, A. Private communication (1996).

[41] Zhu, J.-Z. Private communication (2008).

[42] Orszag, S.A. Private communication (1979).